

JERZY HABER INSTITUTE OF CATALYSIS AND SURFACE CHEMISTRY PAS  
XRD AND THERMOANALYSIS LABORATORY

# **Hybrid organic-inorganic layered materials precursors of semiconducting nanostructures**

---

DOCTORAL THESIS

Katarzyna Luberda-Durnaś  
Supervisor: Prof. Dr hab. Wiesław Łasocha

CRACOW 2013

*First and foremost I would like to express my gratitude to my supervisor Prof. Dr hab. Wiesław Łasocha for scientific support, patience, understanding, constructive conversations and motivation during the PhD period.*

*Marcin Oszejca and Marcin Koziel for their valuable advice and help, Anna Szymańska, Marta Grzesiak – Nowak and Dariusz Mucha for creating a great atmosphere at work, successful cooperation, inspiration, support and friendship.*

*I would like also to thank Prof. Janusz Szklarzewicz and Elżbieta Bielańska, for the opportunity of making some measurements necessary for this thesis.*

*Furthermore, I would like to thank Dr Alicja Rafalska - Łasocha for her warmth and great kindness. Also, I gratefully acknowledge all people, who contribute to the development of this PhD thesis.*

*Finally, I would like to thank my family and friends for encouragement and faith in me. I am especially grateful for my husband's love, which every day was a great support for me.*

*This work was supported by the Krakow Interdisciplinary PhD-Project in Nanoscience and Advanced Nanostructures, operated within the Foundation for Polish Science MPD Programme co-financed by the EU European Regional Development Fund. The support of the Polish Government program MNiSW, grant NN204546439, is also kindly acknowledged.*

# Contents

<b>Introduction .....</b>	<b>1</b>
<b>1. Structure solution from powder diffraction data .....</b>	<b>4</b>
1.1 Powder X-ray diffraction .....	4
1.2 Mathematical and physical basis of X-ray diffraction .....	5
1.3 Methodology for determining structures from X-ray powder data .....	8
<b>2. Hybrid organic-inorganic materials .....</b>	<b>30</b>
2.1 Introduction.....	30
2.2 General knowledge about hybrid organic-inorganic materials .....	30
2.3 Hybrid organic-inorganic semiconductor nanomaterials.....	32
2.4 Synthesis methods of hybrid organic-inorganic materials.....	38
2.5 Properties of hybrid organic-inorganic materials .....	38
2.6 Hybrid organic-inorganic materials as the precursors of pure nanometric semiconductors .....	44
2.7 Potential applications .....	45
<b>3. Basic knowledge about ZnS and its application in photocatalysis .....</b>	<b>47</b>
3.1 ZnS – basic features .....	47
3.2 ZnS as a catalyst .....	48
3.3 The basis of photodegradation on ZnS.....	49
<b>The goal of work.....</b>	<b>53</b>
<b>4. Measurement conditions and parameters .....</b>	<b>54</b>
<b>5. Hybrid organic-inorganic materials based on a ZnS semiconductor.....</b>	<b>56</b>
5.1 Materials and synthesis.....	56
5.2 Characterization of $(\text{ZnS})_n\text{I-ap}$ .....	57
5.3 Characterization of $(\text{ZnS})_n\text{I,2-pda}$ .....	60
5.4 Characterization of $\text{ZnS(pda)}_{1/2}$ .....	62
5.5 Comparison of $(\text{ZnS})_n\text{I-ap}$ , $(\text{ZnS})_n\text{I,2-pda}$ and $\text{ZnS(pda)}_{1/2}$ .....	68
<b>6. Hybrid composites of the types <math>\text{Zn}_x\text{Cd}_{1-x}\text{Se(pda)}_{1/2}</math> and <math>\text{ZnS}_x\text{Se}_{1-x}(\text{pda})_{1/2}</math> .....</b>	<b>70</b>
6.1 Materials and synthesis.....	70
6.2 Characterization of hybrid material of the type $\text{Zn}_x\text{Cd}_{1-x}\text{Se(pda)}_{1/2}$ .....	71
6.3 Characterization of hybrid material of the type $\text{ZnS}_x\text{Se}_{1-x}(\text{pda})_{1/2}$ .....	80
6.4 Conclusion .....	85
<b>7. Hybrid composites of the type (amine)<math>\text{MSO}_4</math>.....</b>	<b>87</b>
7.1 Introduction.....	87
7.2 Materials and synthesis.....	87

7.3 Characterization of (MXDA)MSO <sub>4</sub> and (PXDA)MSO <sub>4</sub> .....	88
7.4 Conclusion .....	103
<b>8. Obtaining pure semiconducting nanostructures from hybrid organic-inorganic precursors .....</b>	<b>105</b>
8.1 Method of formation of semiconducting nanostructures.....	105
8.2 XRD analysis of obtained II-VI semiconductors.....	105
8.3 Optical properties of obtained semiconductors .....	111
8.4 SEM images of obtained materials.....	118
8.5 Conclusion .....	122
<b>9. Synthesis of nanometric ZnS using microwave radiation .....</b>	<b>124</b>
9.1 Materials and synthesis procedure .....	124
9.2 Analysis of the samples .....	125
9.3 Preliminary tests of photodegradation activity .....	126
9.4 Conclusion .....	128
<b>Summary .....</b>	<b>129</b>
<b>List of Figure.....</b>	<b>131</b>
<b>List of Tables.....</b>	<b>135</b>
<b>List of References .....</b>	<b>136</b>

## Introduction

My PhD thesis is devoted to the study of hybrid organic-inorganic materials, which epitomise perfectly arranged structures with interesting electronic, optical and magnetic properties. The most promising future applications of these composites are related to semiconductor monolayers present in their structure and to their arrangement, which produces a quantum confinement effect.

The main goal of the research was the synthesis and characterisation of new hybrid organic-inorganic compounds. Using different techniques such as X-ray diffraction, chemical analysis, scanning electron microscopy, TG-DSC and UV-vis spectroscopy, detailed information about these materials was obtained. Furthermore, for the newly-obtained hybrid compounds, crystal structures were determined.

Thus, in the first chapter, the theoretical basis of X-ray diffraction methods and the structure solution process are described. Crucial steps, such as sample preparation, measurement, indexing, space group determination, finding a structure model and, finally, refinement, are presented in more detail. There are many methods and algorithms related to this matter, but only those employed in the experimental part have been introduced.

The focus then moves to hybrid organic-inorganic materials. Since their discovery in 2000, the number of papers devoted to these materials has grown considerably. They are composed of two main groups: organic, which are amines, and inorganic, which are semiconductors. Because of their structure, hybrid materials exhibit quantum confinement effects. The physical basis for this phenomenon is briefly considered. Depending on the type of semiconductor (linear or layered) and amines used, these materials are classified into three different groups: 1D, 2D and 3D. The optical properties of hybrid organic-inorganic materials determine the future applications of these materials. Therefore, a great deal of attention has been devoted to this topic.

In the course of the research, a new hybrid organic-inorganic material based on ZnS was obtained. 1,3-pda (1,3-propylenediamine) was used as a solvent (and one of the reagents), and finally  $\text{ZnS}(1,3\text{-pda})_{1/2}$  was created, using a new synthesis method under reflux. In comparison to the routinely-employed solvothermal technique, this method is cheaper and shorter and does not require sophisticated equipment such as an autoclave. The structure has been solved, showing that the synthesised compounds belong to the class of 3D hybrid

organic-inorganic materials. The analyses prove that unique optical properties can also be observed in this case.

Doped hybrid organic-inorganic materials were also investigated. Different cations ( $\text{Zn}^{2+}$ ,  $\text{Cd}^{2+}$ ) or anions ( $\text{S}^{2-}$ ,  $\text{Se}^{2-}$ ) were built in to the semiconductor layers at different percentages, which should cause changes in optical properties. However, the expected changes are rather slight. Systematic studies were carried out based on ten samples:  $\text{Zn}_x\text{Cd}_{1-x}\text{Se}(\text{1.3-pda})_{1/2}$  and  $\text{ZnSe}_x\text{S}_{1-x}(\text{pda})_{1/2}$  where  $x = 0, 0.25, 0.5, 0.75, 1$ .

As previously mentioned, the main aim of my research was to obtain new members of the family of hybrid MQ(diamine) $_{1/2}$  materials. In the course of my studies of the MTe(diamine) $_{1/2}$  system, a group of new chemical compounds were obtained. Their diffraction patterns and unit cell parameters are similar to those of typical MQ(amine) $_{1/2}$  compounds. Only spatially resolved SEM/EDX analysis and X-ray crystal structure analysis indicated the formation of a novel complex compound with the formula (diamine)MSO<sub>4</sub>.

Finally, the possibilities of forming hybrid materials from pure II-VI semiconductors were studied. Two different methods were involved: temperature treatment and boiling in alcohol. It turns out that both techniques can remove amines from the structures, so that pure semiconductors, in an interesting form (not in the typical form of massive crystals), were obtained. Also, in the course of the studies, ZnS was obtained using microwave radiation in the synthesis route.

In summary, hybrid organic-inorganic materials are interesting scientific objects with promising future applications in optoelectronics and catalysis. Thus their full characterisation is extremely important. All tests performed in my research led to a better understanding of the relationship, so important from the point of view of the above-mentioned applications, between structural diversity and optical properties.

# **LITERATURE PART**

## Structure solution from powder diffraction data

### 1.1 Powder X-ray diffraction

In 1912 when Max von Laue discovered the phenomenon of crystal diffraction, no one imagined that it would become the basis for one of the most powerful methods: X-ray diffraction.<sup>1</sup> Today, this technique is used in many fields of science: chemistry, solid state physics, and material science, not to mention biochemistry. Using X-ray diffraction measurement it is possible to obtain information on the chemical composition, presence of different phases, and most importantly, crystal structure of various materials. Based on this technique a number of breakthroughs have been made, such as solving the structure of ribosomes<sup>2</sup> and HIV proteins<sup>3</sup> as well as the discovery of quasicrystals.<sup>4</sup> Since the beginning of the twentieth century, the Nobel Prize has been awarded 26 times for research on crystallography.<sup>5</sup> Thus there is no doubt that X-ray diffraction is one of the most powerful research tools of recent times.

Due to the size of crystalline grains, two main techniques can be distinguished: X-ray diffraction on single crystals and powder X-ray diffraction (XRPD). In the first case, the size of the crystal must fall in the range 0.05 mm to 0.4 mm; in the second, the sizes of the crystallites can be much smaller, ranging from 0.1  $\mu\text{m}$  to 10  $\mu\text{m}$ . The type of the materials to be examined (single-crystal or polycrystalline compound) determines the type of diffractometer used and actual geometry of measurement. As a result, from single-crystal diffraction, three-dimensional crystallographic information is obtained, while from powder diffraction, only a single dimension (powder diffraction pattern) is available. Therefore, what was easy in single-crystal technique poses some difficulties in the case of powder studies. The problem is not only to determine the lattice parameters of the unit cell, but also to apply direct methods or Patterson techniques to find the structure model.

Despite these drawbacks, in the last 20 years more and more structures have been solved by powder diffraction, mainly due to the tremendous progress in instrumentation and algorithms, computing power and the general development of XRDP<sup>6</sup> techniques. A particularly great impact on the improved popularity of XRDP techniques was made by the development of the Rietveld refinement method,<sup>7</sup> invented in response to a growing demand of crystallographers. Most structures have been solved from powder diffraction data in recent years. The most spectacular result was the solution of a structure containing more than one hundred atoms in

an asymmetric unit.<sup>8</sup> Until now, this has been possible using exclusively single-crystal methods. However, a representative single crystal is not always available, and that is the reason powder diffraction plays such a crucial role in crystallography.

In the case of organic-inorganic hybrid compounds, situations in which single crystals cannot be obtained are very frequent. Usually, those materials have a greasy or powdery consistency. That is why so much attention in this section will be devoted to powder X-ray diffraction.

## 1.2 Mathematical and physical basis of X-ray diffraction

As previously mentioned, the diffraction measurement technique is dependent on the form of the objects studied (single-crystal or polycrystalline sample). Nevertheless, the fundamental idea of X-ray diffraction is the same in both cases and is based on a combination of two physical concepts: scattering and interference.

An electromagnetic wave is coherently scattered on atoms (precisely on electrons) in the sample. In the electric field derived from X-ray beams, electrons oscillate and radiate electromagnetic waves. These secondary X-rays have the same frequency as the primary beam but are shifted in phase.<sup>9</sup> Interference is a phenomenon in which electromagnetic waves are superimposed to form a resultant wave of greater or lower amplitude, depending on their phases; if waves are consistent in phase, they will be strengthened; if not, they will be extinguished.

Given these concepts, diffraction in a crystal can be explained. Many different, mutually parallel planes can be hypothetically led by atoms in the crystal. From these planes, X-rays will be partially reflected.

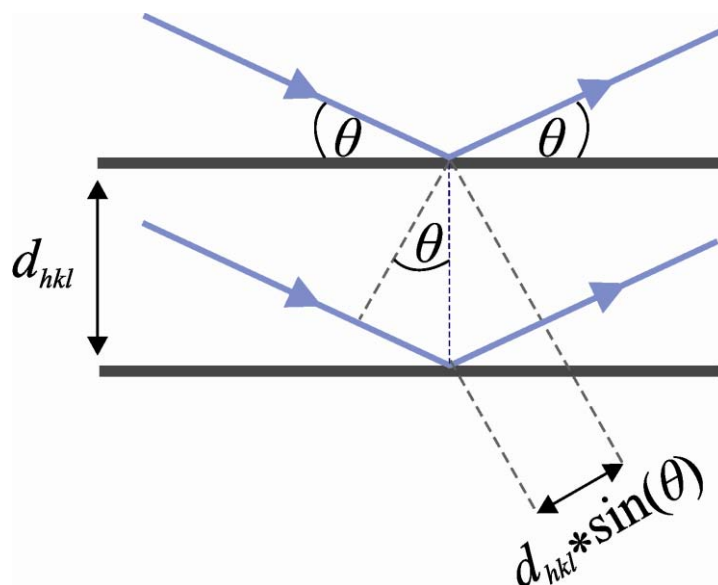


Figure 1. Bragg law

In Figure 1, X-ray reflection is shown on two parallel planes. Constructive interference occurs when the path difference is equal to a whole number of wavelengths. Taking into account geometrical conditions, the following equation can be written:

$$2d_{hkl} \sin(\theta) = n\lambda \quad (1)$$

where:  $d_{hkl}$  – plane spacing,  $\lambda$  – wavelength,  $\theta$  – the angle between the primary beam of rays and the crystal plane,  $n$  – an integer. This is the content of Bragg's law.

Noteworthy is that diffraction occurs only with the specific combination of these three factors:  $d$ ,  $\lambda$  and  $\theta$ . In diffraction measurement  $\lambda$  is a constant (monochromatic source of X-ray diffraction), while  $\theta$  systematically increases during measurement.<sup>9</sup>

Here Ewald's construction, a geometrical interpretation of Bragg's law, needs to be discussed. This concept is associated with the reciprocal lattice, a mathematical construction coupled spatially and dimensionally with the crystal lattice. The following equations show the relationship between them:

$$|\vec{a}^*| = a^* = \frac{1}{d_{(100)}} = \frac{bc \sin \alpha}{V}, |\vec{b}^*| = b^* = \frac{1}{d_{(010)}} = \frac{ac \sin \beta}{V}, |\vec{c}^*| = c^* = \frac{1}{d_{(001)}} = \frac{ba \sin \gamma}{V} \quad (2)$$

$$V = abc \sqrt{1 - (\cos \alpha)^2 - (\cos \beta)^2 - (\cos \gamma)^2 + 2 \cos \alpha \cos \beta \cos \gamma} \quad (3)$$

where:  $\vec{a}^*$ ,  $\vec{b}^*$ ,  $\vec{c}^*$  – translation unit vectors in the reciprocal lattice,  $a^*$ ,  $b^*$ ,  $c^*$  – length of translation unit vectors in the reciprocal lattice,  $a$ ,  $b$ ,  $c$  – length of translation unit vectors in the crystal lattice,  $\alpha$ ,  $\beta$ ,  $\gamma$  – angles between vectors in the crystal lattice.<sup>10</sup>

The reciprocal lattice is constructed as follows: for each set of planes, the normal with the length  $d^* = \frac{1}{d_{hkl}}$ , is drawn from the origin.<sup>11</sup>

The use of Ewald's construction and the concept of the reciprocal lattice is an elegant way to show the conditions which must be fulfilled in order for diffraction to occur (Figure 2).

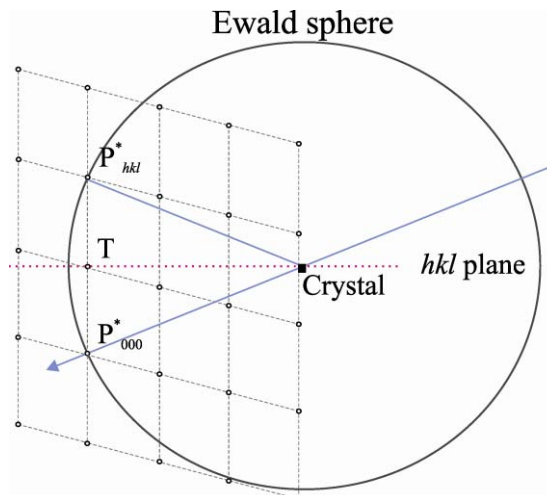


Figure 2. Ewald's construction

In the center of the Ewald sphere, whose radius is  $1/\lambda$ , a crystal is placed. The primary beam is scattered on plane  $(hkl)$ —in the picture, orientation of the plane is shown by a red dotted line. The surface of the sphere is intersected by the primary beam at point  $P^*_{000}$ , which is also the starting point of the reciprocal lattice. From this point, the normal to the  $(hkl)$  plane is drawn. Its length is  $1/d_{hkl}$ , and the end is located at point  $P^*_{hkl}$ . An analysis of the geometric condition ( $|TP^*_{hkl}|=1/(2d_{hkl})$ ,  $|P^*_{hkl}C|=1/\lambda$  and the angle between  $P^*_{hkl}-C-T=\theta$ ) yields the Bragg equation:

$$\frac{1}{\frac{2d_{hkl}}{\lambda}} = \sin \theta.$$

To sum up, if the point  $P^*_{hkl}$ , coupled with plane  $(hkl)$ , is on the Ewald surface, then X-rays are reflected from the plane according to the conditions contained in the Bragg equation and diffraction occurs. By changing the position of the crystal or the direction of the primary beam, different lattice planes are exposed, and so different points connected with them will be on the Ewald sphere.

In the polycrystalline samples, there are a large number of randomly-oriented crystallites. Therefore, Bragg conditions for a set of planes will always be met for some group of properly-oriented crystallites. The diffraction reflections (from different crystallites but the same family of planes) lie on a cone defined by the X-rays reflected at an angle  $2\theta$  for the incident beam. This diffraction geometry is shown in Figure 3.

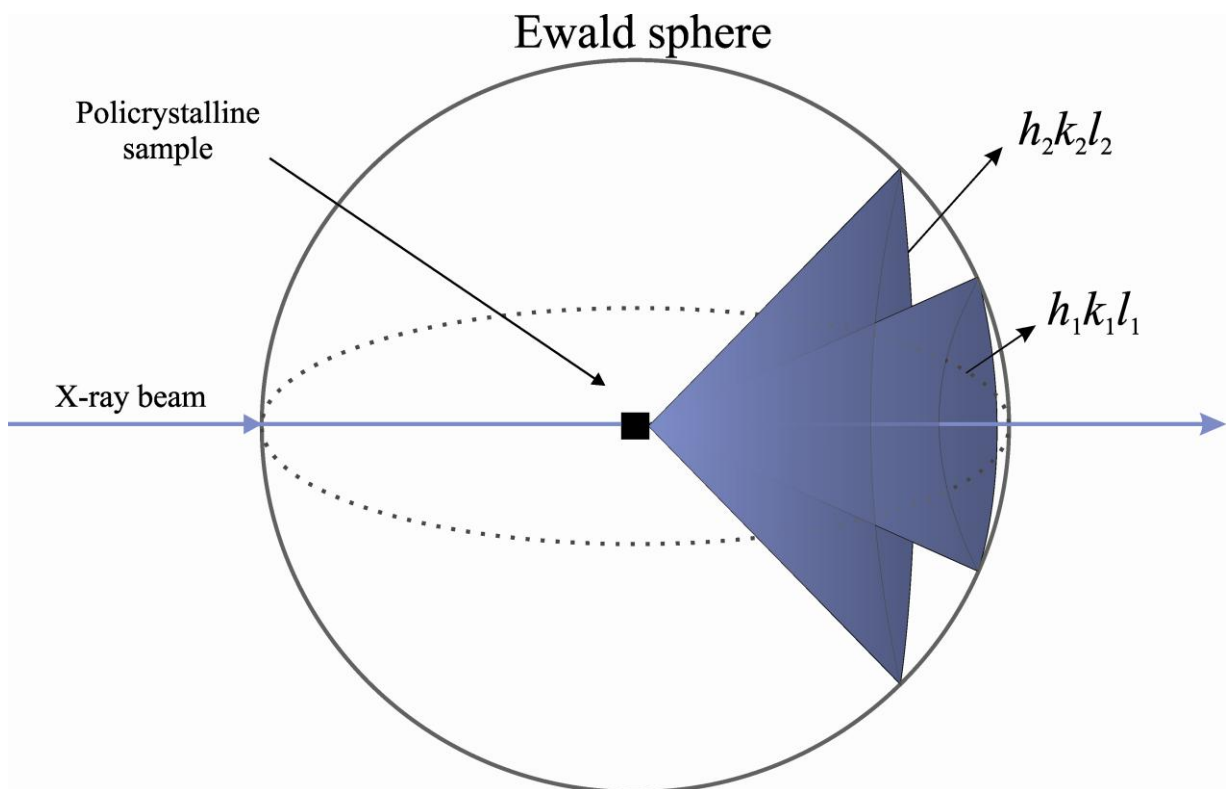


Figure 3. X-ray reflection from a polycrystalline sample

During measurement, the reflection intensities from a different set of planes, as a function of  $2\theta$ , are recorded. The intensities in a powder diffraction pattern contain information about the type of scattering atoms, their positions and displacements. Intensities are proportional to the square of the structure factor:

$$I(hkl) \sim |F(hkl)|^2, F(hkl) = |F(hkl)| \exp[i\varphi(hkl)] \quad (4)$$

where:  $I(hkl)$  – measured intensities,  $F(hkl)$  – structure factor,  $\varphi(hkl)$  – phase. Diffraction measurement provides the value of  $|F(hkl)|$  but not of  $\varphi(hkl)$ . There is a so-called phase problem, which will be discussed later. A structure factor can also be described by the following equation:

$$F(hkl) = \sum_{j=1}^N f_j \exp[2\pi i(hx_j + ky_j + lz_j)] \quad (5)$$

where:  $f_j$  – scattering factor of  $j$ -atom,  $x_j, y_j, z_j$  – co-ordinations of  $j$ -atom,  $N$  – atoms in the unit cell.

The important parameter calculated from the powder diffraction pattern is  $\rho(xyz)$  – electron density:

$$\rho(xyz) = \frac{1}{V} \sum_{hkl} F(hkl) \exp[-2\pi i(hx + ky + lz)] \quad (6)$$

As can be seen, in this equation  $F(hkl)$  (not  $|F(hkl)|$ ) is presented. Therefore, knowledge of  $\varphi(hkl)$  is necessary and should be found in the structure solution process. The solution of the phase problem is quite difficult, complicated and arduous. Therefore, many methods have been dedicated to this issue, for example, the Patterson or direct methods, use of anomalous dispersion etc. This problem arises from the fact that the crystal is described in real space while the powder diffraction pattern is described in the reciprocal lattice. To obtain electron density the inverse transform needs to be done. The schematic approach is shown in Figure 4.



Figure 4. Application of Fourier transform and inverse Fourier transform in diffraction

### 1.3 Methodology for determining structures from X-ray powder data

The structure determination process can be illustrated as a choice of the best path through the maze shown in Figure 5.

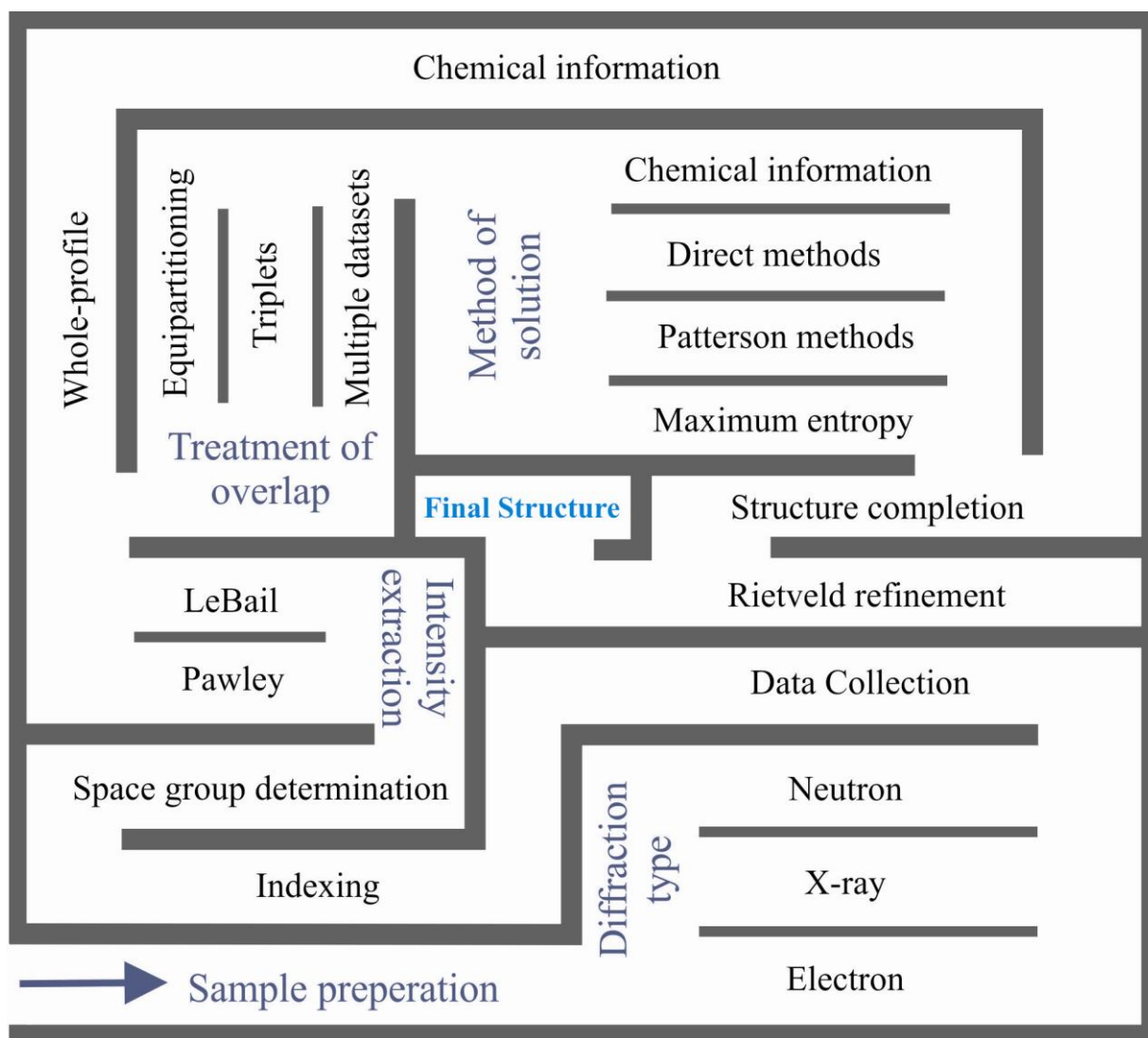


Figure 5. The structure determination graph<sup>6</sup>

As we can see, there are multiple pathways leading to the final structure. Which one will be selected depends on the sample itself and the availability of the equipment. There is no universal method that can be recommended for each tested material.<sup>6</sup>

Structure determination from powder data should be done in a number of steps: sample preparation, indexing the powder diffraction pattern, determining the cell parameters, identifying the space group from systematic absences and the decomposition of the powder diffraction pattern into integrated intensity data, finding the model structure and finally refining.<sup>12</sup> In this chapter, all of these steps and the most commonly used techniques will be discussed.

### 1.3.1 Sample preparation: key issues

The first stage, sample preparation, seems to be the least demanding. Nevertheless, it is crucial for the proper solution of the structure. Data obtained from the measurement should be

of the highest quality, which can only be achieved through proper sample preparation. This can minimize the effects associated with the size of the grains or texture in the studied materials.

To obtain reproducible measurements, the smallest possible particle sizes are required (the sample should contain crystallites in the range 0.1 to 10  $\mu\text{m}$ ). With such a specimen, one can be sure that each orientation is properly represented (stochastic distribution), and that scattering will occur in many grains. Therefore, the sample is triturated with a special agate mortar or mill, whichever is the easiest and at the same time the most effective way to reduce particle size. Obtaining a high-quality powder diffraction pattern depends not only on the crystallite size but also on grains, which must be arranged in a random manner. Otherwise, the preferred orientation of grains is observed (texture).<sup>13</sup> To prevent this phenomenon, side or rear sample loading can be applied.<sup>14</sup> If this proves to be insufficient, capillary measurement can be done. In this method, the sample is loaded into a specially-prepared, very fine glass tube. Capillary filling must be carried out correctly: the sample must be precisely compacted. Moreover, methods such as sieving, spray drying or adding amorphous materials to the sample can be used.<sup>6</sup>

However, texture, which is a serious limitation in the study of structural powder diffraction can be also a valuable and useful tool in this field of structural research.<sup>8,15,16</sup> The method for determining the intensity of overlapping reflections, which involves full texture analyses, is well known and widely used. In this technique, several different but related data sets are collected on the same polycrystalline sample, enabling us to obtain more information about the relative intensities. Given the function describing the texture and its direction, the following equations can be created:

$$\begin{aligned} I(n,1) &= a_{11}I_1 + a_{12}I_2 + \dots + a_{1k}I_k \\ I(n,2) &= a_{21}I_1 + a_{22}I_2 + \dots + a_{2k}I_k \\ &\vdots \\ I(n,k) &= a_{k1}I_1 + a_{k2}I_2 + \dots + a_{kk}I_k \end{aligned}$$

Where:  $I(n,k)$  – affected by the texture intensity of overlapping peaks,  $I_1, I_2 \dots I_k$  – searches, overlapping intensities,  $a_{11}I_1 = I_1'$ ,  $a_{12}I_2 = I_2'$ ,  $a_{1k}I_k = I_k'$  – intensities modified by texture.

Therefore, it is no wonder that special techniques to prepare textured samples have been developed. The type of method used depends on the kind of sample. The preferred orientation of grains in magnetic or electrostatic materials can be achieved by applying an appropriate field.<sup>17,18</sup> However, in most cases morphological features are used in the preparation process;

for example, for plate-like crystallites sedimentation can be used, whereas for needles, smoothing is sufficient.

### 1.3.2 Measurement: X-ray diffractometers and synchrotrons

The second step in determining the structure solution is measurement. In this stage also, a few important factors will have an impact on the diffraction pattern and on the structure determination process. Firstly, two sources of radiation can be used: X-ray laboratory powder diffractometers and synchrotron facilities.

**X-ray diffractometers** Despite the fact that higher resolution and higher count rates are offered in the latter case, availability to this source is limited. Therefore, much more attention will be devoted to X-ray powder diffractometers, which are commonly used in laboratory practice. The quality of diffraction patterns depends on many parameters related to characteristics of the instrument and sample microstructure.

The main problem in structure solution is peak overlap. This phenomenon is, among others, the result of two interpenetrating effects called instrumental broadening and sample broadening. Instrumental broadening is dependent on the wavelengths in the incident beam, beam divergence, finite width of source, receiving slit and residual misalignment. The factor related to instrumental aspects can be optimized to a certain extent. One technique which could minimize an impact from the sample was discussed above, in the section ‘Sample preparation’ and also in Table 1. Another determinant of the quality of diffraction patterns is the shape of the peaks. In the older type of diffractometers, the obtained shapes had a Gaussian or Lorentzian profile, but in modern instruments, with high resolution, the shape can be approximated by Pearson VII or pseudo-Voigt functions. A high-quality diffraction pattern is also characterized by a very precise peak position. The most frequent errors connected with this are zero-point shift and displacement of specimen.<sup>6</sup> In Table 1, the most significant problems and its sources are shown.

*Table 1. A list of the most common problems which could reduce the quality of powder diffraction data and the possible solution<sup>6</sup>*

<b>Observed effects in powder diffraction pattern</b>	<b>Cause</b>	<b>Possible solution</b>
Inappropriate peak intensities	Not enough crystallites or improper size  Preferred orientation  Incident beam divergence	Reduce the crystallite size, spin sample, increase beam divergence Use special technique of sample preparation or capillary measurement Change the beam divergence by appropriate slit selection, use the shorter wavelength of radiation
High background	Sample fluorescence or incoherent scattering	Change of wavelength

Peak overlaps	Not enough crystallites or improper size Wavelengths in the incident beam, beam divergence, the finite width of source, receiving slit and residual misalignment	Reduce the crystallite size  Change the beam divergence by appropriate slits selection, use the shorter wavelength of radiation
Asymmetry of peaks	Flat specimen error Axial divergence	Reduce the sample length Appropriate slit selection
Shifts of peak position	Sample displacement  Zero-shift error	Sample must be positioned at the center of the diffractometer and properly prepared for measurement  Calibration

One very important factor which has some impact on diffraction pattern quality is diffractometer geometry. Nowadays reflection and transmission geometries are available for laboratory diffractometers. A transmission technique requiring a small amount of sample, which is undoubtedly a great advantage, is used for thin film or capillary samples, but rarely. This is because this type of geometry is not suitable for highly absorbing samples. Much more popular is the reflection mode based on parafocusing Bragg-Brentano geometry.

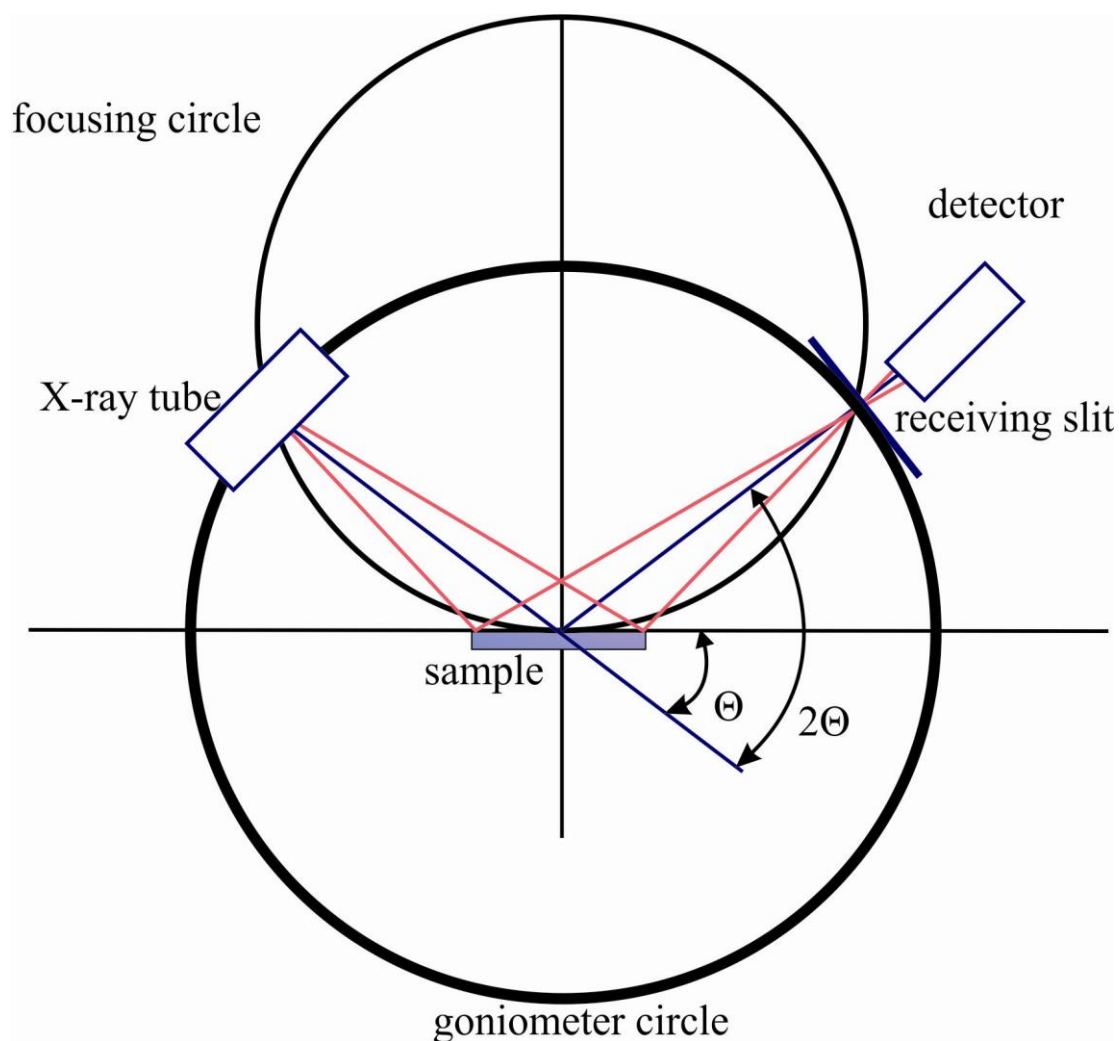


Figure 6. Geometry of a Bragg-Brentano diffractometer

As can be seen in Figure 6, in this geometry the X-ray tube, sample and receiving slit lie on the circle with a radius dependent on  $\theta$ . This circle is called a “focusing circle”.<sup>6</sup> X-rays produced by the tube reach the monochromator, which cuts off residual  $K_{\alpha 2}$  and the continuous component of the spectrum. Then the beam is focused, its geometry formed by a number of slots with which the goniometer is equipped, enabling us to reduce its divergence, eliminate the scattered radiation and adjust the beam width to the size of the sample. Finally, radiation reflected from different areas of the sample surface is focused on the receiving slot and once more passes through the collimated and antiscattered slits (Soller slits) in order to reach the detector window.<sup>19</sup> The detector rotates around the goniometer axis with an angular speed of rotation the same as the X-ray tube ( $\theta/\theta$  geometry).

The diffractometers can be equipped with different types of X-ray tube. Table 2 lists typical wavelengths of used X-ray tubes.

Table 2. Length of X-rays depending on anode type<sup>20</sup>

Anode type	$K_{\alpha 1}$ [Å]	$K_{\alpha 2}$ [Å]
Cr	2.28970	2.29361
Fe	1.93604	1.93998
Co	1.78897	1.79285
Cu	1.54056	1.54439
Mo	0.70930	0.71395

In the X-ray tubes a characteristic component of radiation is used. The sample spectrum and its components are shown in Figure 7.

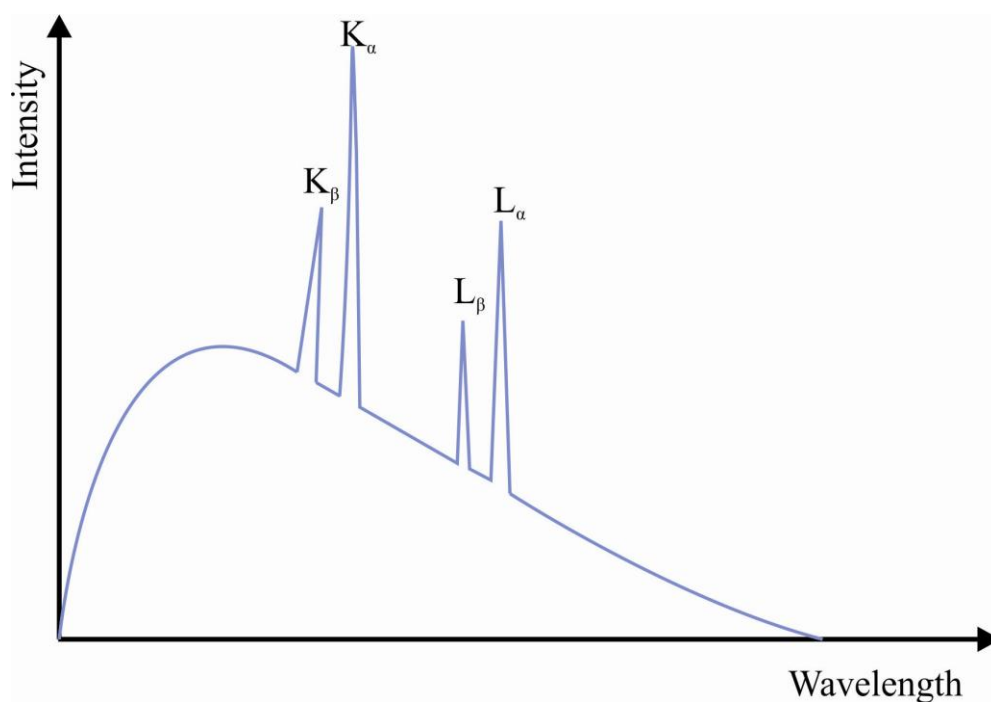


Figure 7. Spectrum of the X-ray diffraction tube

The type of X-ray tube used is often dependent on the kind of examined materials. This is connected with Ewald's construction and reciprocal lattice. The shortest wavelength is more appropriate for samples with smaller cell parameters, the longest for structures with larger (for example, protein) crystals.<sup>21</sup> Also, for transmission geometry, where the beam path and effects of absorption should be minimal, a short wavelength is recommended.<sup>6</sup>

**Synchrotron** To study powder samples one can also use synchrotron radiation. It has many advantages, but one key disadvantage: it is not widely available. Fortunately, nowadays more and more of such objects are built, including, in the near future, in Krakow. Therefore, the availability of this type of research will be much greater.<sup>22</sup>

Essentially, synchrotron is built of four main modules. "Linac" is where electrons are produced and initially accelerated. In the "booster," they are constantly accelerated and finally injected into a "storage ring" where electrons circle at close to the speed of light. In the storage ring, the electron paths are deflected with special magnets while X-ray beams are emitted. Then, they are directed to laboratories called "beamlines" that surround the storage ring. Each beamline is a specific type of laboratory, in which the beam is used for different research.<sup>23</sup> A schematic diagram of a synchrotron is given in Figure 8.

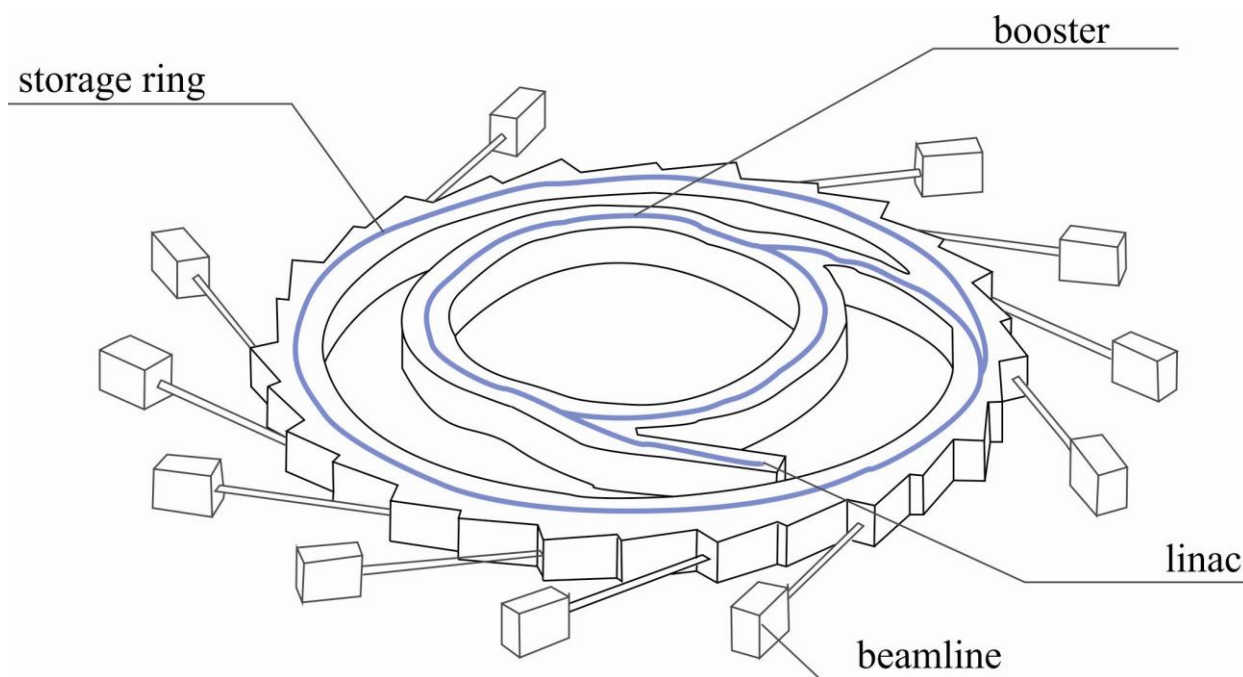


Figure 8. Schematic construction of synchrotron

In comparison to X-rays traditionally obtained in the laboratory, synchrotron radiation is characterized by higher intensities, better collimation, polarization and continuous wavelength spectrum. Examples of synchrotron spectra are presented in Figure 9.

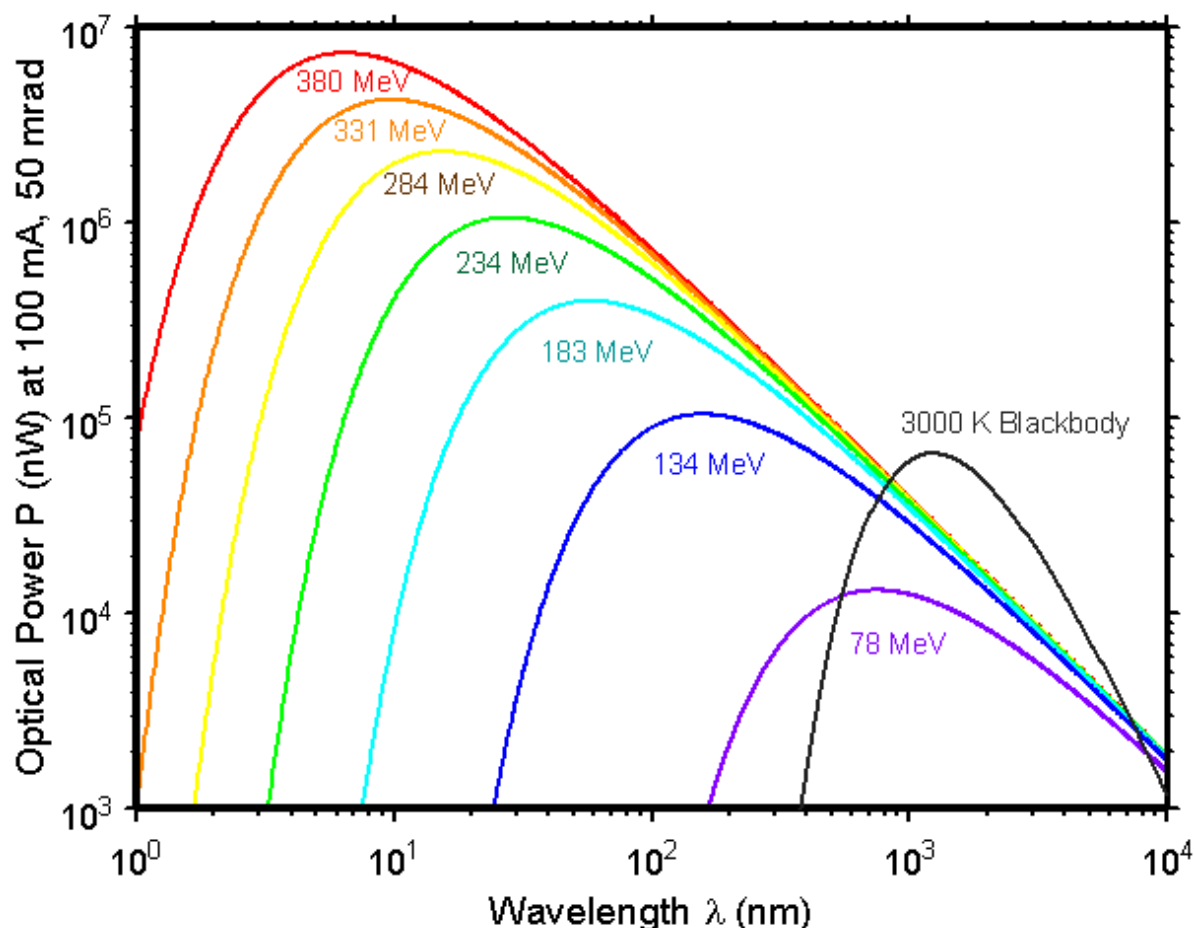


Figure 9. Synchrotron Radiation Spectrum emitted by SURF III<sup>24</sup>

All of the above features make the synchrotron the most powerful and most appropriate tool for powder diffraction experiments. Moreover, powder diffraction patterns recorded in ‘synchrotron laboratories’ are of much better quality. The problems in structure solution typical of laboratory X-ray diffractometers are less severe here. Peaks are better-resolved, sharper, and their positions are determined more accurately, thus significantly simplifying the structure-solving process.<sup>6</sup>

### 1.3.3 Indexing: a process in which cell parameters are found

Two types of information contained in powder diffraction pattern are relevant in structure determination: peak position and integrated intensities. The indexing is related to the first one-peak position.<sup>6</sup> From the powder diffraction pattern,  $d_{hkl}$  can be calculated (Bragg equation) and given the fundamental relationship between crystal lattice and reciprocal lattice, the following equation can be written:

$$\frac{1}{d_{hkl}^2} = h^2 a^{*2} + k^2 b^{*2} + l^2 c^{*2} + 2hka^*b^* \cos \gamma^* + 2klb^*c^* \cos \alpha^* + 2hla^*c^* \cos \beta^* \quad (7)$$

This expression is often presented more clearly and conveniently:

$$Q_{hkl} = h^2 Q_A + k^2 Q_B + l^2 Q_C + kl Q_D + lh Q_E + hk Q_F \quad (8)$$

where:  $Q_{hkl} = \frac{1}{d_{hkl}^2}$ ,  $Q_A = a^{*2}$ ,  $Q_B = b^{*2}$ ,  $Q_C = c^{*2}$ ,  $Q_D = b^* c^* \cos \alpha^*$ ,  $Q_E = a^* c^* \cos \beta^*$ ,  $Q_F = a^* b^* \cos \gamma^*$ . As can be seen,  $Q$ -values are a function of reciprocal lattice parameters ( $a^*$ ,  $b^*$ ,  $c^*$ ,  $\alpha^*$ ,  $\beta^*$ ,  $\gamma^*$ ) and thus, in turn, of crystal lattice parameters ( $a$ ,  $b$ ,  $c$ ,  $\alpha$ ,  $\beta$ ,  $\gamma$ ). The number of  $Q$ -values varies from one to six, depending on the symmetry. Generally, in the indexing process, for each observed  $Q_{hkl}$ , three Miller indices and all parameters need to be found.

Nowadays, this is carried out by computer programs and the correctness of the solutions is verified by two figures of merit  $M_{20}$  and  $F_N$ . The first is defined by the following equation:

$$M_{20} = \frac{Q_{20}}{2 \langle Q \rangle N_{20}} \quad (9)$$

where  $Q_{20}$  is the  $Q$ -value for the 20<sup>th</sup> observed and indexed line,  $\langle Q \rangle$  is the average ( $Q_{i,obs} - Q_{i,calc}$ ) of the first 20 lines and  $N_{20}$  is the total number of different  $Q$ -values calculated up to  $Q_{20}$ . When  $M_{20}$  exceeds than 10 and the number of unindexed lines is lower than three, the solution can be accepted. Of course, unindexed lines may indicate error, but in most cases they are associated with impurities in the sample.  $M_{20}$  increases with the symmetry of the unit cell.<sup>6</sup>

The second factor is defined as follows:

$$F_N = \frac{1}{\langle \Delta 2\theta \rangle} \frac{N}{N(\theta_g)} \quad (10)$$

where:  $N$  is the number of observed lines,  $\langle \Delta 2\theta \rangle$  is the average discrepancy in  $2\theta$  for the first  $N$  lines,  $N(\theta_g)$  is the number of different calculated  $Q$  values up to  $\theta_g$  (limit value of  $\theta$ ).<sup>6</sup>

In the majority of cases, these factors are sufficient to determine the correct solution, but it sometimes happens that the correct solution is not indicated in the list of probable alternatives. This situation may occur when a dominant zone is present in the diffraction pattern. It is characteristic for compounds with a unit cell for which one period is much smaller (or longer) than the two others. Then, in the diffraction pattern, one Miller index equals zero for most of the low-angle lines. It is possible even for more than 20 lines; therefore  $M_{20}$  is more susceptible to this phenomenon (in most cases the first 20 lines are considered in the indexing procedure). The second situation in which figures of merit can fail arises due to the fact that from the powder diffraction pattern only the length ( $d$ ), not the three-dimensional vectors, are known. This can result in finding a unit cell which is a sub- or super cell in comparison to a

true one. It is typical for crystals with symmetry higher than orthorhombic. Most indexing programs deal with these problems through the use of specific tests at the beginning of the indexing procedure.<sup>6</sup>

Of course, these factors are not the only indicators of the correctness of the indexing procedure. Important features which also need be considered are: lattice symmetry (should be as high as possible), unit cell volume, similarity to compounds belonging to the same group. Finally, in the unit cell, the total number of molecules should be found.<sup>25</sup>

The most frequently applied programs are ITO, DICVOL and TREOR. They will be briefly discussed in more detail below. All indexing programs can be split into two main groups: those working either in the parameter space or in the Miller indices space. In the first case, the parameters of the unit cell are found in the first step and then *hkl*-indexes are assigned to the individual peaks. In the second, the exact opposite procedure is used: first, the *hkl*-indexes are found and then the unit cell parameters. Some of these programs can be operated by deductive or exhaustive algorithms. What does this mean? For example, in the parameter space, using deductive methods, the dependences between parameters and *hkl* as well as the differences between the positions of the lines are analyzed and used for indexing, while in the exhaustive methods, the parameters are successively changed and tested. This classification is shown in Table 3.

Table 3. Algorithm for finding the cell parameters<sup>24</sup>

Operating space Working method	Miller index space	Parameter space
Deductive methods	TREOR	ITO
Exhaustive methods	POWDER	DICVOL

#### 1.3.4 Space group determination

Space group determination, the next stage in the structure solution process, is based on the analysis of the powder diffraction pattern for systematic absences (systematically absent reflections). Unfortunately, a single space group is not always defined by a specific set of systematic absences. It may happen that different groups will share them, as in case of  $P2_1$  and  $P2_1/m$ . Also, it is possible that some groups will not have any systematic absences at all, for example:  $P222$ ,  $Pmm2$ . In such cases, an approach based on an intensity statistic must be used.

On the other hand, even if the space group is related to specific systematic absences, Bragg peak overlap can cause some difficulties in searching for a space group. This problem is especially significant for higher Miller indices (higher value of  $2\theta$ ), where reflections that may be absent often overlap with those present for other possible space groups. This means that the space group is practically determined on the basis of the low-angle part of the diffraction pattern. Thus, to exclude mistakes and to have numerical indications, a profile fit of the low-angle part of the diffraction pattern using Le Bail or Pawley methods should be used.<sup>6</sup>

### 1.3.5 Extracting integrated intensities from a powder diffraction pattern

Extraction of integrated intensities is a significant step in the structure solution process. Nowadays, two main methods are used: the iterative Le Bail technique based on modified Rietveld approaches and the method originally proposed by Pawley, which is the linear least squares analysis of powder diffraction patterns.<sup>6</sup>

In order to understand the theoretical bases of Le Bail methods, the Rietveld approach to the evaluation of an observed structure factor magnitudes needs to be analyzed. As was discussed in chapter 1.2, intensity is proportional to the square of the structure factor magnitude ( $I(hkl) \approx |F(hkl)|^2$ ). In the Rietveld approach the square of the structure factor magnitude is proportional to the peak area. Thus, the following relationship can be expressed:

$$I(hkl) \sim |F(hkl)|^2 \sim \text{peak area observed in powder diffraction pattern}$$

For an isolated peak, the observed peak area is easy to determine by adding together the background-subtracted profile points. The situation becomes more complicated for overlapping reflexes. For two overlapping peaks, the sum of the integrated intensities can be presented as:

$$I_{1(\text{obs})} + I_{2(\text{obs})} = \sum_i (\text{obs}(i) - \text{back}(i)) \quad (11)$$

and  $I_{1(\text{obs})}$ ,  $I_{2(\text{obs})}$  can be defined as:

$$I_{1(\text{obs})} = \sum_i \frac{I_{1(\text{calc})} \times q_1(i)}{(I_{1(\text{calc})} \times q_1(i) + I_{2(\text{calc})} \times q_2(i))} (\text{obs}(i) - \text{back}(i)) \quad (12)$$

$$I_{2(\text{obs})} = \sum_i \frac{I_{2(\text{calc})} \times q_2(i)}{(I_{1(\text{calc})} \times q_1(i) + I_{2(\text{calc})} \times q_2(i))} (\text{obs}(i) - \text{back}(i)) \quad (13)$$

where:  $I_p = j_p |F_{h_p k_p l_p}|$  integrated intensities ( $j_p$ -reflection multiplicity,  $|F_{h_p k_p l_p}|$  – structure factor magnitude),  $q_p(i) = c_p(i) H_p(i)$  ( $c_p(i)$  is the function of Lorentz polarization, adsorption and extinction terms and  $H_p(i)$  is the normalized  $p^{\text{th}}$  peak shape) and finally  $\text{obs}(i) - \text{back}(i)$  is the observed peak contribution at the  $p^{\text{th}}$  point in the diffraction pattern.

This result demonstrates that the sum of the peak area as estimated by the Rietveld algorithm is similar to the background-subtracted area of the observed Bragg peaks.<sup>6</sup>

The same assumptions are used in the Le Bail methods. Only a few modifications are implemented. Because no model of the structure exists, the calculated structure factors cannot be generated. Thus, in the  $(r+1)^{\text{th}}$  iteration the observed peak area for the  $r^{\text{th}}$  iteration is used as a calculated value of structure factors. Furthermore, all the integrated intensities are set as the same until the first iteration. Then, for isolated peaks observed intensities equal to the observed area under the Bragg peaks are fitted. For  $N$ -overlapping reflections, the integrated intensities can be mathematically presented as:

$$I_{m(\text{obs})}^{(r+1)} = \sum_i \frac{I_{m(\text{obs})}^{(r)} \times q_m(i)}{\sum_{n=1}^N I_{n(\text{obs})}^{(r)} \times q_n(i)} (\text{obs}(i) - \text{back}(i)) \quad (14)$$

The Le Bail technique is a powerful tool for extracting integrated intensities; however, it has some disadvantages. One of these is the problem of incorporating prior knowledge about structure factor magnitudes before the first iteration. Another involves the occasional instabilities which occur in a situation when the peaks are weak and the background is overestimated. In general, however, the Le Bail method offers a fast, certain and successful algorithm to extracting intensities from powder diffraction.<sup>6</sup>

The second technique is the so-called Pawley method, which is based on a simple linear least squares procedure. In this approach, the sum ( $\chi^2$ ) of the squares of the differences between the observed ( $y(i)$ ) and the calculated ( $M(i)$ ) diffraction pattern is minimized:

$$\chi^2 = \sum_{i=1}^N \frac{1}{\sigma_i^2} (y(i) - M(i))^2 \quad (15)$$

The calculated profile can be described by the following equation:

$$M(i) = \text{back}(i) + \sum_{\{p\}_i} I_p q_p(i) \quad (16)$$

where:  $M(i)$  – calculated value for  $i^{\text{th}}$  point in the diffraction pattern,  $I_p$  – integrated intensities,  $q_p(i)$  – includes the Lorenz polarization, adsorption and information about the  $p^{\text{th}}$  peak shape.

In the first step of the minimization procedure, the derivatives with respect to  $I_p$  are evaluated and set to zero ( $\frac{\partial \chi^2}{\partial I_p} = 0$ ). This procedure gives the best fit for the peak areas. In the next step,

the peak areas and the indexed intensities can be obtained by a matrix inversion:

$$I_p = (H_{hp})^{-1} B_h \quad (17)$$

where:

$$H_{hp} = \sum_{i=1}^N \frac{1}{\sigma_i^2} q_h(i) q_p(i), \quad B_h = \sum_{i=1}^N \frac{1}{\sigma_i^2} q_h(i) y(i) \quad (18)$$

All symbols were described above.

In the Pawley method, the most serious problem is the degenerate nature of the matrix (two or more rows are identical), which is the result of overlapping peaks. Two different approaches are used to deal with it (one based on equipartition, the second on the so-called Wasser constraints), but they will be not discussed in detail here.

Although the Pawley technique was elaborated first, Le Bail fitting has become more popular. In my work, only the Le Bail method was used.

### 1.3.6 Finding the structure model

The main goal of the structure solution process is to find the approximate structure model — in other words, the positions of atoms in the unit cell need to be extracted. The procedure of the model search, based only on the diffraction pattern, is relatively difficult and complicated, especially without prior knowledge of the “atom connectivity” of the investigated compound. This is mainly because of the phase problem. Obtaining information on the electron density distribution in the unit cell, while relying only on the data contained in the diffraction pattern seems extremely difficult (structure phase  $\varphi(hkl)$  is unknown). Nevertheless, several methods have been developed to enable us to find the structure model. Among them, two groups can be distinguished: classic methods and direct space methods. The following presents a detailed classification of these techniques (Figure 10):

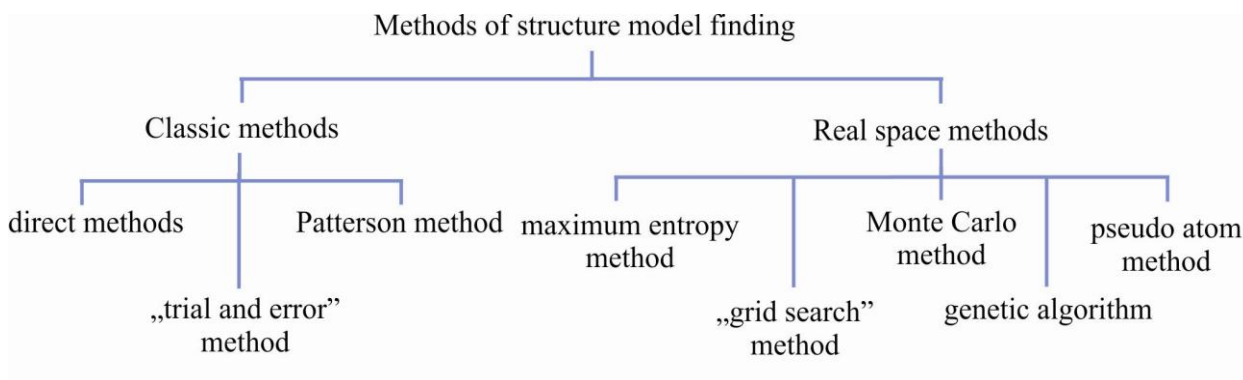


Figure 10. Classification of structure solution methods

Among classic methods, direct methods and the Patterson method deserve the greatest attention. In this group, one can also include the “trial and error” method, but it requires information about structure (the model is found through the use of analogy with known, solved structures and through extensive knowledge of crystallography). Therefore, it will not be discussed in detail here. Methods working in real space include the maximum entropy method, the “grid search” method, the Monte Carlo method, genetic algorithm, the pseudo atom method, etc.

To solve the structure described in this paper, two techniques were used: the direct method and the Monte Carlo method. Therefore, this section will be devoted to these two algorithms.

**Direct methods** One of the most powerful techniques, which was implemented in program EXPO,<sup>26</sup> is the direct method. It is based on the assumption that phases  $\varphi(hkl)$  can be found directly from measured intensities by using mathematic dependences between them.

Structure factor amplitudes are related to phases and also indirectly to electron density. This relation is shown in Figure 11.

$$|F(hkl)| \quad \times \quad \exp(i\varphi(hkl)) \quad = \quad F(hkl)$$

$\updownarrow$  *Fourier transform*  
**electron density  $\rho(xyz)$**

Figure 11. Relation between structure factor amplitudes, phases and electron density<sup>9</sup>

From the above diagram, it is clear that phases can be evaluated if structure factor amplitudes and electron densities are known. It is also obvious that in the process of finding the structure model, the electron density and search parameter and phases are unknown. Therefore, some fundamental assumptions should be made.<sup>9</sup>

First of all, atoms are discrete; thus the value of electron density is high inside atoms while the value outside is nearly zero. The result of the use of this knowledge is the evaluation of the normalized structure factor  $E(hkl)$ . This procedure allows us to eliminate the effect of the atomic shape from  $F(hkl)$ .  $E$ -values can be expressed as:

$$|E(hkl)|^2 = \frac{|F(hkl)|^2}{\varepsilon_{hkl} \sum_{j=1}^N f_j^2} \quad (19)$$

where:  $E(hkl)$  – normalized structure factor,  $\varepsilon_{hkl}$  – factor which describes the impact of the space group symmetry on the observed intensities,  $f_j$  – scattering factor of the  $j^{\text{th}}$  atom.

The next assumption, that the electron density is always non-negative, leads to the Karle-Hauptman determinant and inequality so that the solution gives some constraint to the phases. In fact, it gives a group of phases, which, if  $\rho(xyz)$  is negative, will be excluded.

More restrictions regarding phases can be obtained by using the information that atoms are distributed in the unit cell randomly. For a non-centrosymmetric structure, the probability distribution (for the Karle-Hauptman determinant 3×3) can be expressed mathematically as:

$$P(\varphi(\mathbf{H}_1, \mathbf{H}_2)) = \frac{\exp[\kappa(\mathbf{H}_1, \mathbf{H}_2) \cos(\varphi(\mathbf{H}_1, \mathbf{H}_2))]}{2I_0(\kappa(\mathbf{H}_1, \mathbf{H}_2))} \quad (20)$$

where:  $\kappa(\mathbf{H}_1, \mathbf{H}_2) = 2N^{1/4}|E(-\mathbf{H}_1)E(\mathbf{H}_1 - \mathbf{H}_2)E(\mathbf{H}_2)|$ ,  $\varphi(\mathbf{H}_1, \mathbf{H}_2) = \varphi(-\mathbf{H}_1) + \varphi(\mathbf{H}_1 - \mathbf{H}_2) + \varphi(\mathbf{H}_2)$ ,  $N$  – number of atoms in the unit cell,  $\varphi(\mathbf{H}_1)$ ,  $\varphi(\mathbf{H}_2)$  – are phases of  $E(\mathbf{H}_1)$  and  $E(\mathbf{H}_2)$ , respectively.

Depending on the  $\kappa$  value,  $P(\varphi(\mathbf{H}_1, \mathbf{H}_2))$  may look different from what is shown in Figure 12.

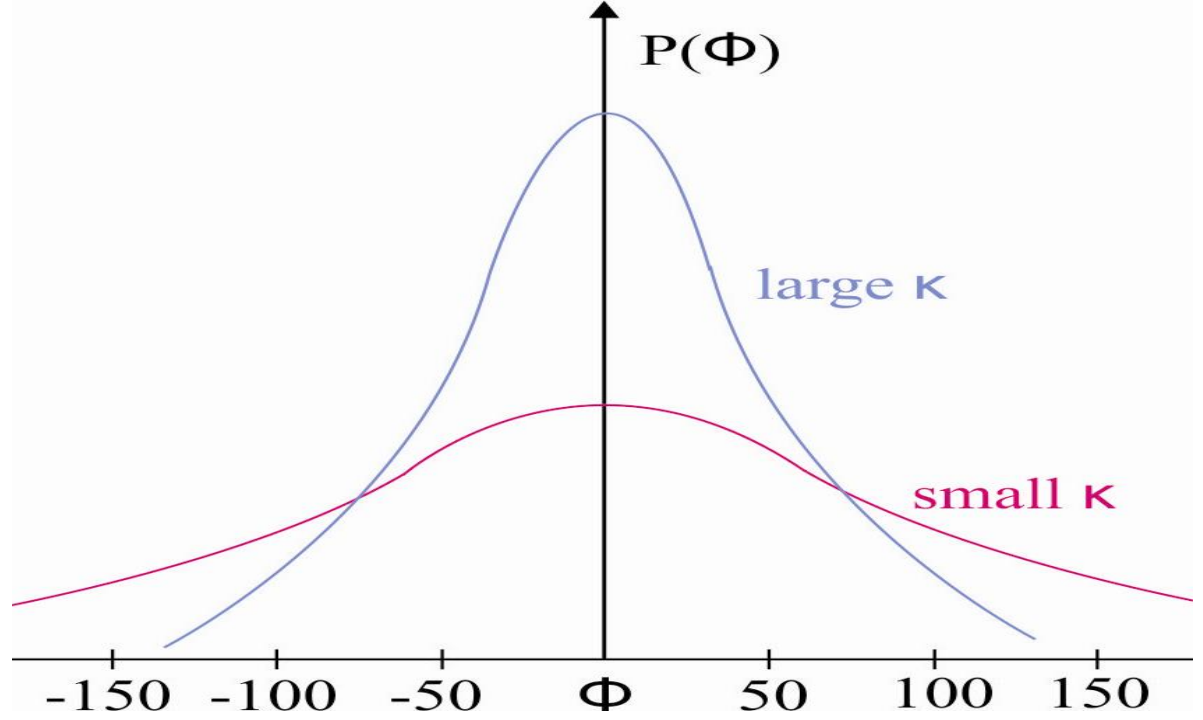


Figure 12. The probability density of  $\varphi(\mathbf{H}_1, \mathbf{H}_2)$

It can be seen that the value of  $\varphi(\mathbf{H}_1, \mathbf{H}_2)$  is more probably 0 than  $\pi$ . Thus, the following relation between phases can be expressed as follows:

$$\varphi(\mathbf{H}_1) \approx \varphi(\mathbf{H}_1 - \mathbf{H}_2) + \varphi(\mathbf{H}_2) \quad (21)$$

Significant information can be obtained by considering the condition that  $\int \rho^3(xyz)dV$  will adopt the maximum value. Following a mathematical calculation, the tangent formula describing dependencies between phases can be derived:

$$\tan(\varphi(\mathbf{H}_1)) \approx \frac{\sum_{\mathbf{H}_2} |E(\mathbf{H}_2)E(\mathbf{H}_1 - \mathbf{H}_2)| \sin(\varphi(\mathbf{H}_2) + \varphi(\mathbf{H}_1 - \mathbf{H}_2))}{\sum_{\mathbf{H}_2} |E(\mathbf{H}_2)E(\mathbf{H}_1 - \mathbf{H}_2)| \cos(\varphi(\mathbf{H}_2) + \varphi(\mathbf{H}_1 - \mathbf{H}_2))} \quad (22)$$

This result shows the most likely value of  $\varphi(\mathbf{H}_1)$ .

All the above methods of phase determination are implemented and fully automated in programs using the direct method. Steps which are commonly performed in all these programs are shown in Figure 13.

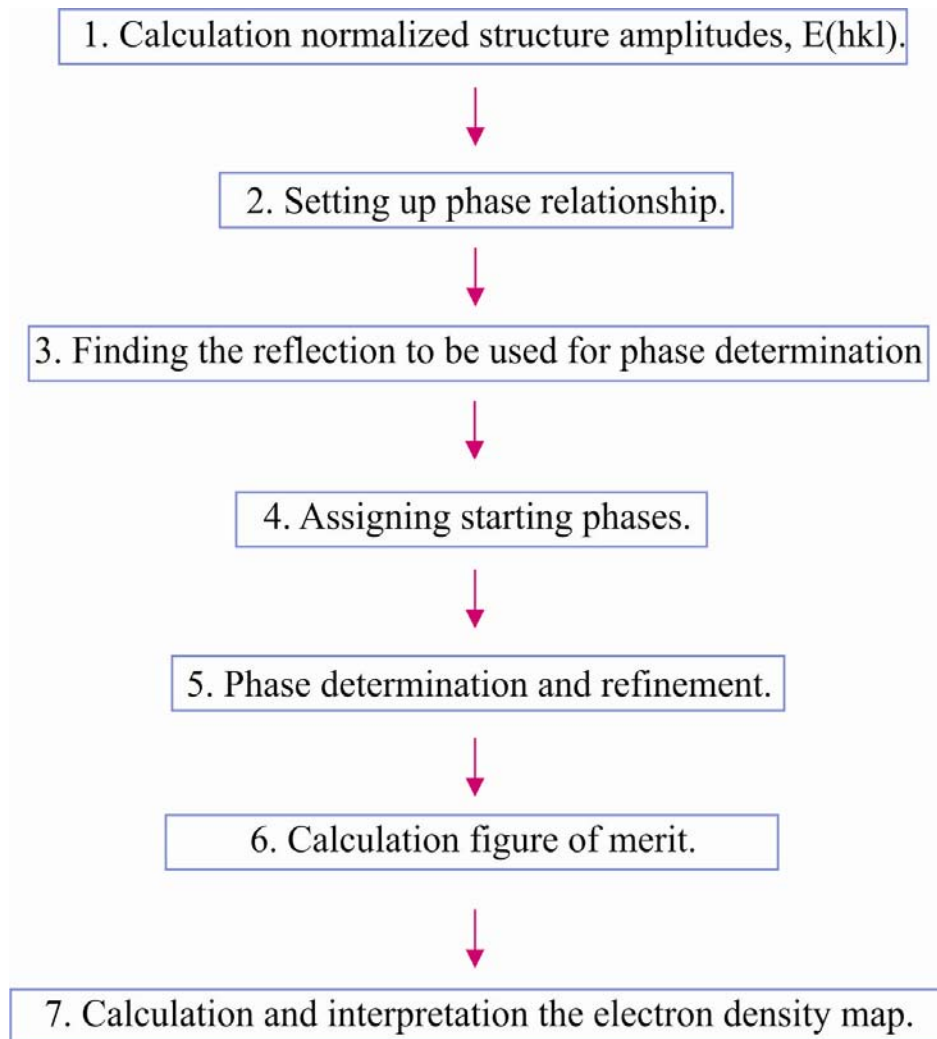


Figure 13. Operation used in programs based on the direct method<sup>9</sup>

1. For the calculation of  $E(hkl)$ , the expected intensity, expressed as  $\varepsilon_{hkl} \sum_{j=1}^N f_j^2$  needs to be found. In practice, this value is obtained by estimating the spherical average of the actual intensities. Strong reflections at a low angle deserve special care, because they have the strongest influence on finding the proper solution.<sup>9</sup>
2. In this step, the structure factor related as  $\varphi(\mathbf{H}_1) \approx \varphi(\mathbf{H}_1 - \mathbf{H}_2) + \varphi(\mathbf{H}_2)$  is found and saved for later use.<sup>9</sup>
3. Two main criteria are used for finding useful reflections: structure factors  $|E(hkl)|$  need to be the strongest and they should be presented in the highest possible number of phase relations.<sup>9</sup>
4. The random values are assigned to phases and then tested. It is not very probable that starting phases obtained in this way will lead to a correct set of phases after the first refinement. However, this procedure is repeated a number of times.<sup>9</sup>
5. The starting phases are implemented in a tangent formula and new phase values are obtained. These procedures are repeated until the phases have achieved stable values.

In programs using direct methods, the weight terms in the tangent formula are applied:<sup>9</sup>

$$\varphi(\mathbf{H}_1) = \text{phase of } \sum_{\mathbf{H}_2} w(\mathbf{H}_2)w(\mathbf{H}_1 - \mathbf{H}_2)E(\mathbf{H}_2)E(\mathbf{H}_1 - \mathbf{H}_2) \quad (23)$$

Where  $w(\mathbf{H}_1)$  is the weight associated with  $\varphi(\mathbf{H}_1)$ .

6. The correct set of phases is identified by specified figures of merit. The most often used is:

$$R_\alpha = \frac{\sum_{\mathbf{H}_1} |\alpha(\mathbf{H}_1) - \alpha_e(\mathbf{H}_1)|}{\sum_{\mathbf{H}_1} \alpha_e(\mathbf{H}_1)} \quad (24)$$

where  $\alpha(\mathbf{H}_1)$  the trustworthiness of the evaluated phase,  $\alpha_e(\mathbf{H}_1)$  approximation to the estimated  $\alpha(\mathbf{H}_1)$ . They can be described by the following equations:

$$\alpha(\mathbf{H}_1) = 2N^{-1/2} |E(\mathbf{H}_1)| |\sum_{\mathbf{H}_2} E(\mathbf{H}_2) E(\mathbf{H}_1 - \mathbf{H}_2)| \quad (25)$$

$$\alpha_e(\mathbf{H}_1) = \sum_{\mathbf{H}_2} 2N^{-1/2} |E(\mathbf{H}_1)E(\mathbf{H}_2)E(\mathbf{H}_1 - \mathbf{H}_2)| \frac{I_1(2N^{-1/2} |E(\mathbf{H}_1)E(\mathbf{H}_2)E(\mathbf{H}_1 - \mathbf{H}_2)|)}{I_0(2N^{-1/2} |E(\mathbf{H}_1)E(\mathbf{H}_2)E(\mathbf{H}_1 - \mathbf{H}_2)|)} \quad (26)$$

7. In the final step the electron density map is calculated based on the best phases determined during the above stages.<sup>9</sup>

**The global optimization method: Monte Carlo and simulated annealing** When direct methods are unsuccessful, due mainly to peaks overlapping in the diffraction pattern, then real space global optimization should be implemented.

In this technique, the starting model is created based on some knowledge about the structure, even though the probability of obtaining the correct distribution of atoms in the unit cell in the first step is marginal. Therefore, the next structure models need to be generated so as to minimize the difference between the calculated and the measured diffraction data. This procedure is repeated until the proper structure is found.<sup>6</sup>

That can be visualized as localization of the minimum on the N-dimensional hypersurface (Figure 14), where  $N$  is the number of parameters defining structure. In cases where the optimization procedure applies to the full diffraction pattern, the surface can be described by Rietveld  $\chi^2$  (goodness-of-fit indicator), which can be shown as:

$$\chi^2 = \frac{(y_i^{\text{obs}} - y_i^{\text{calc}})^2}{\sigma^2} \quad (27)$$

where  $y_i^{\text{calc}}$  – calculated value of intensity at the  $i^{\text{th}}$  point of diffraction pattern,  $y_i^{\text{obs}}$  – observed value of intensity at the  $i^{\text{th}}$  point of the diffraction pattern,  $\sigma^2$  – standard deviation.

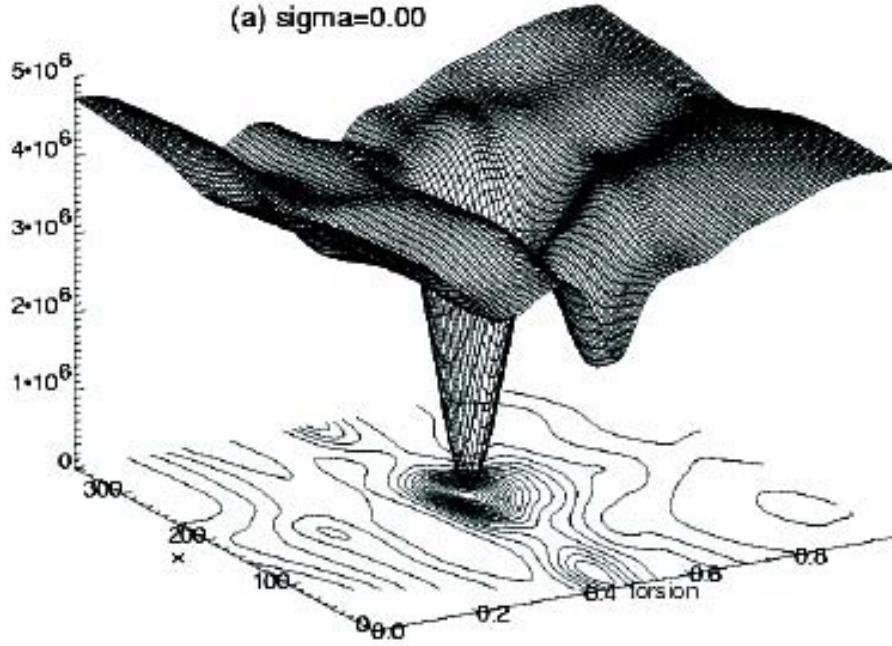


Figure 14.  $N$ -hypersurface with local and global minimum

In the process of finding the correct structure, the local minima positioned on the  $N$ -hypersurface can act as traps. Hence, the initial model in the global optimized technique should be chosen as close to the true position as possible to avoid this danger. In addition, special procedures are elaborated for the same purpose (see below).

In programs which use this technique to solve structure, the following stages have been implemented:

1. From the starting structure  $\Gamma_j$ , as a result of small, random changes of parameters describing the model, the new structure  $\Gamma_{j,T}$  is generated. The agreement between the calculated and obtained diffraction pattern is tested by the  $R_{wp}$  factor, which is presented as:

$$R_{wp} = \sqrt{\frac{\sum w_i (y_i^{obs} - y_i^{calc})^2}{\sum w_i (y_i^{obs})^2}} \quad (28)$$

where:  $w_i = 1/y_i^{obs}$  – weight of the  $i^{\text{th}}$  measured point.

2. In the next step, the analysis of the differences between the value of  $R_{wp}(\Gamma_{j,T})$  and  $R_{wp}(\Gamma_j)$  is performed. The structure is automatically accepted if  $R_{wp}(\Gamma_{j,T}) - R_{wp}(\Gamma_j) \leq 0$  while  $R_{wp}(\Gamma_{j,T}) - R_{wp}(\Gamma_j) > 0$  structure can be approved with probability  $\exp(-Z/S)$  and discarded with probability  $1 - \exp(-Z/S)$  where  $S$  is the scaling factor and  $Z = R_{wp}(\Gamma_{j,T}) - R_{wp}(\Gamma_j)$ . The larger it is, the higher the probability

that the structure with  $R_{wp}(\Gamma_{j,T}) - R_{wp}(\Gamma_j) > 0$  will be accepted. In the Monte Carlo methods, the scaling factor is set at a constant level or changed manually, while in simulated annealing it is systematically decreased.

3. In cases where the structure is accepted, it becomes  $\Gamma_j$ , and the procedure is repeated.
4. The idea of global optimization is shown in chart 15.

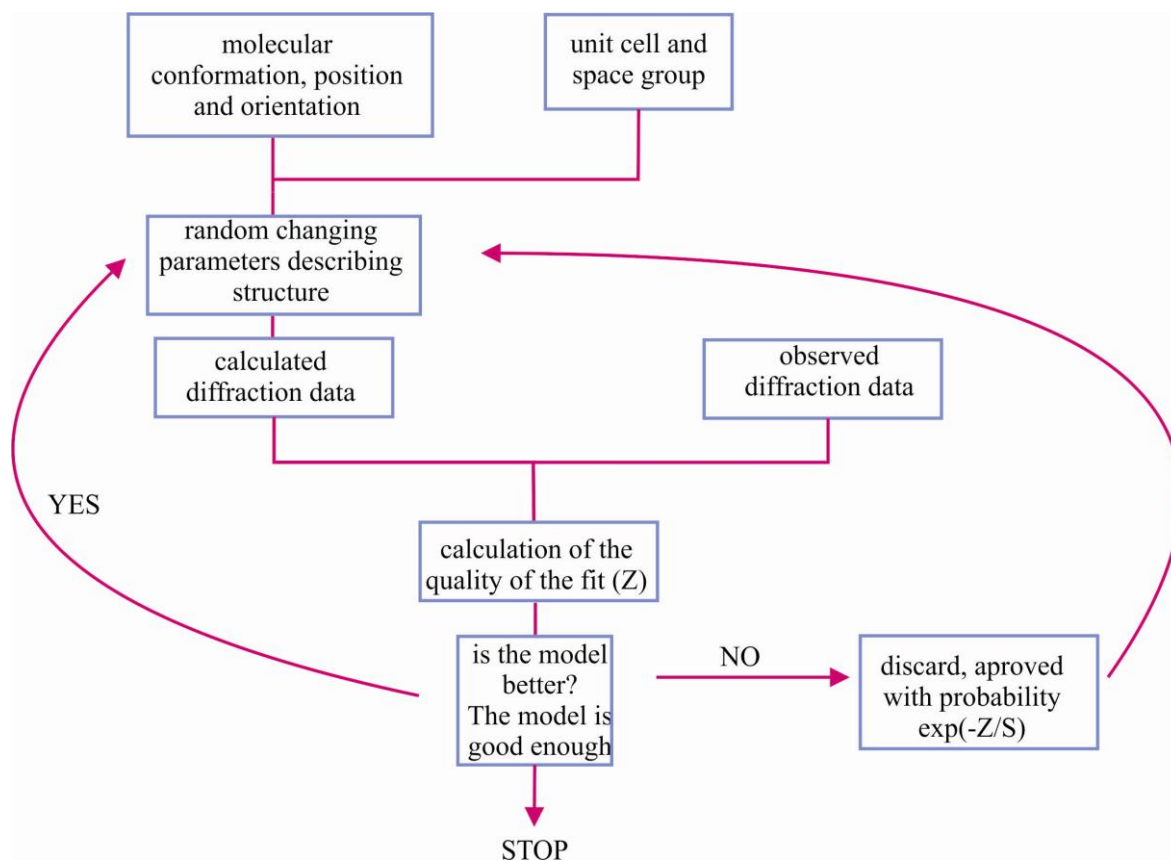


Figure 15. Applying a global optimization to crystal structure determination

In program FOX,<sup>27</sup> which is mainly designed for powder diffraction data, the reverse Monte Carlo method is implemented. First, the initial model is defined (type and number of atoms, bond length, values of angles, cell parameters and space group). Therefore, as can be seen, prior knowledge about the structure is required. In the next step, the positions of atoms are randomly changed. The quality of the new configuration is evaluated based on the so-called cost function ( $CF$ ), which is precisely determined by the experimental data and is characteristic for the structure. A new model is approved, if the cost function coupled with them is smaller than for an earlier structure. Otherwise, the model is saved with probability ( $P$ ) equals  $\exp(-\Delta CF/T)$ , ( $T$ -parameter is equivalent to the above-mentioned  $S$ -parameter). Fundamentally, the process of acceptance of the new structure is quite similar to that of the typical Monte Carlo method. Nevertheless, in the FOX program, a parallel tempering algorithm is implemented. In the typical Monte Carlo method, the  $T$ -parameter during the

optimization process is gradually decreased. In the FOX program, instead of testing one series of configuration after another, several simultaneous models are optimized. Such an approach is more effective, especially for more complicated structures.

Both the classic methods and the real space methods possess advantages and disadvantages. In the case of the classic technique, a crucial role is played by the quality of the obtained diffraction pattern. The necessity of extracting intensities requires data with high resolution, in which peak overlapping is not as severe. Therefore, it is clear that data obtained in synchrotron facilities is the best for classic methods. In real space methods, by contrast, a well-defined peak profile and reliable intensities are more important than high resolution. Furthermore, the complexity of the structure solution in both methods depends on different factors. In classic methods, the larger the number of atoms in asymmetric units, the more difficult finding a structure solution can be, while in the case of direct methods, the main limitation is the number of degrees of freedom in the optimization process. Following this line of thought, it becomes clear that solving a rigid structure, even one with a large number of atoms, is much easier using the real space technique, while small and flexible structures should be solved by direct methods. Also, direct methods do not require prior knowledge about the structure.

### 1.3.7 Rietveld refinement

Rietveld refinement<sup>7</sup> is based on the least squares approach. It is used to obtain the best fit between the experimental diffraction pattern ( $y_i^{\text{obs}}$ ) and the correlated profile calculated from the test structure ( $y_i^{\text{calc}}$ ). Thus, the minimized quantity is given as:

$$g = \sum_i w_i (y_i^{\text{obs}} - y_i^{\text{calc}})^2 \quad (29)$$

where:  $w_i = 1/y_i^{\text{obs}}$  – weight of the  $i^{\text{th}}$  measured point.

In practice, the powder diffraction pattern is shared into  $i$  stages to obtain an intensity function  $y_i^{\text{obs}}$ . In turn,  $y_i^{\text{calc}}$  can be described as:

$$y_i^{\text{calc}} = S \sum_j L_j M_{i,j} |F_j(hkl)| f(2\theta_i - 2\theta_j) P_j A + y_{bi} \quad (29)$$

where:  $S$  – scale factor,  $L_j$  – Lorentz-polarization factor for the  $j^{\text{th}}$  peak,  $M_{i,j}$  – multiplicity of reflections,  $F_j(hkl)$  – structure factor,  $f(2\theta_i - 2\theta_j)$  – profile function,  $P_j$  – function describing texture in the sample,  $A$  – absorption factor,  $y_{bi}$  – background on the  $i^{\text{th}}$  point. The profile ( $f(2\theta_i - 2\theta_j)$ ) describing diffraction peaks may be different depending on the type of measurement. The most popular for X-ray diffraction is a pseudo-Voight, which is:

$$P(x)_{p-v} = \eta L(x) + (1 - \eta)G(x) \quad (30)$$

where:  $\eta = f(2\theta)$ ,  $L(x)$  – Lorentzian distribution,  $G(x)$  – Gaussian distribution. They can be described by the following formulas:

$$L(x) = \frac{2}{\pi H_j} \left[ 1 + 4 \frac{(2\theta_i - 2\theta_j)^2}{H_j^2} \right]^{-1} \quad (31)$$

$$G(x) = \sqrt{\frac{4 \ln 2}{\pi H_j^2}} \exp \left[ -4 \ln 2 \frac{(2\theta_i - 2\theta_j)^2}{H_j^2} \right] \quad (32)$$

$H_j^2$  – full width of the peak at half-maximum height in the  $j^{\text{th}}$  reflection,  $\theta_i$  – the value of the function at the  $i^{\text{th}}$  point,  $\theta_j$  – Bragg angle. The better the match with the profile, the better a fit of structure parameters can be achieved.

In Rietveld refinement the whole diffraction pattern, point by point, is taken into account, which eliminates the problems associated with peak overlap, texture and decreasing intensity along with increasing  $2\theta$  value. The following factors (variables of the models) are refined: background coefficients, zero shift, space group (selected), unit cell parameters, positions of atoms, function describing texture, temperature factors and parameters of the shape of reflections. Quite interesting is the fact that to obtain a close fit between an observed and calculated diffraction pattern, the sequence of refinement steps is significant. Furthermore, restraints play a crucial role. They are defined as:

$$r = \sum_i w_i (r_i^{\text{obs}} - r(\text{xyz})_i^{\text{calc}})^2 \quad (33)$$

where:  $r_i^{\text{obs}}$  – observed value of bond, angle or position,  $r(\text{xyz})_i^{\text{calc}}$  – value calculated on the basis of the model structure. If restraints are used in refinement process, the final minimized quantity is:

$$m = g + wr \quad (34)$$

where  $w$  – weight of restraints,  $w > 0$ .

The quality of fit is evaluated by several factors:

1. Conventional R-factor:

$$R_F = \frac{\sum_i ||F_i^{\text{obs}}| - |F_i^{\text{calc}}||}{\sum_i |F_i^{\text{obs}}|} \quad (35)$$

2. Profile R-factor:

$$R_p = \frac{\sum_i |y_i^{\text{obs}} - y_i^{\text{calc}}|}{\sum_i y_i^{\text{obs}}} \quad (36)$$

3. The weight profile factor and goodness-of fit indicator are also described on pages 24 and 25 (equations 27 and 28) but they are quite important for the evaluation of the Rietveld refinement, so they will be repeated one more time:

$$R_{\text{wp}} = \sqrt{\frac{\sum w_i (y_i^{\text{obs}} - y_i^{\text{calc}})^2}{\sum w_i (y_i^{\text{obs}})^2}}$$

4. A goodness-of fit indicator is defined as:

$$\chi^2 = \left(\frac{R_{\text{wp}}}{R_e}\right)^2 \quad (37)$$

where:

$$R_e = \left(\frac{N-P}{\sum_i w_i (y_i^{\text{obs}})^2}\right)^{1/2} \quad (38)$$

$N$  is the number of data points  $i$  in the observed powder profile, and  $P$  is the number of refinement parameters.

The weight profile factor most often used is considered as the most reliable. If its value (for a simple structure) is lower than 15%, it indicates a high-quality fit and the correctness of the structure.

Rietveld refinement calculations can be performed using many well-written and quite sophisticated programs. The Rietveld method algorithm implemented in the JANA<sup>28</sup> program package was used to performed refinement of all structures described in this work.

## **Hybrid organic-inorganic materials**

### **2.1 Introduction**

Progress in many fields of science is still associated with the growing demand for new, sophisticated products. The need to miniaturize electronic devices necessitates the search for innovative, advanced materials and solutions which will be able to replace expensive transistor technology. Finding this type of compound is quite difficult, mainly due to the specific properties expected of it, such as resilience, non-toxicity or high efficiency of the synthesis process.<sup>29</sup>

One material which meets the above requirements is periodically arranged quantum dots (QDs). On a nanoscale, they exhibit different optical and electronic features than bulk phase, which is to their undoubted advantage and makes them interesting scientific objects. One example might be InP quantum dots with diameters of 2–6 nm, for which the band gap changes about 1 eV.<sup>29</sup> This phenomenon is caused by a quantum confinement effect (QCE) which will be discussed in more detail in this chapter. Unfortunately, it is a great challenge to obtain uniform arrays of quantum dots of repeatable size. This is very serious issue which may delay the applications of these materials.

This is not a problem for perfectly ordered hybrid organic-inorganic compounds, which were first described in 2000.<sup>30</sup> Similarly to QD, these semiconducting materials possess extraordinary optical and electronic properties, but in contrast to them, the synthesis procedure is much easier. In this chapter, this type of material will be presented, especially its structure, properties and possible modification.

### **2.2 General knowledge about hybrid organic-inorganic materials**

The interest in hybrid compounds has grown based on the assumption that through the combination of different building blocks into a single material, one can combine and sometimes enhance selected properties (advantages). Because hybrid materials are fused from organic and inorganic parts, they possess features typical for both. Thus, they combine the structural diversity, processability, tunability and flexibility characteristic of the organic part with the rigidity and thermal stability of the inorganic component. Furthermore, the inorganic fragment, depending on its structure, may add unusual and interesting optical, electronic and magnetic properties.

The class of hybrid organic-inorganic materials is very wide, from MOFs through functionalized nanotubes, organically-modified gold nanoparticles to semiconductor nanocrystals with organic matrices.<sup>31</sup> Examples are plentiful. Nevertheless, to be classified in this group, one specific condition needs to be fulfilled. A detailed definition was formulated by C. Janiak.<sup>32</sup> According to him, “infinite metal-ligand assemblies where the metal-organic connectivity is interrupted by ‘inorganic’ bridges (...) or where an extended inorganic metal-ligand network is lined by only terminal organic ligands are called organic–inorganic hybrid-materials.” Furthermore, ligands need to be connected to metal atoms by covalent bonds. Schematic structures are presented in Figures 16 and 17.

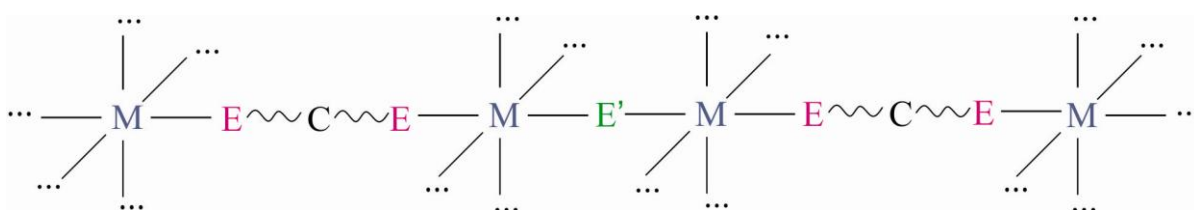


Figure 16. Schematic structures of hybrid organic inorganic materials, where organic and inorganic ligands are presented in the structure. E', E can be O, N, S, Se<sup>32</sup>

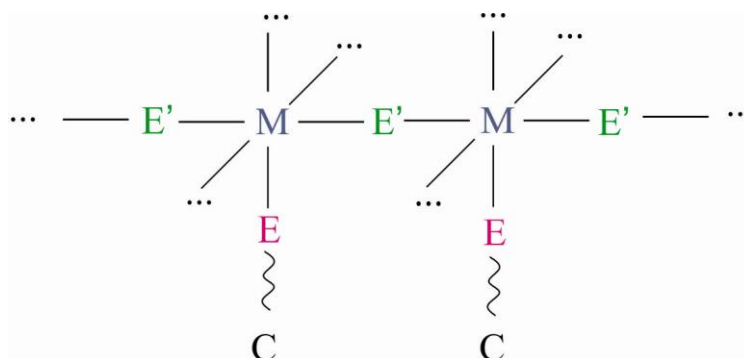


Figure 17. Schematic structures of hybrid organic inorganic materials, where inorganic and terminal organic ligands are presented in the structure. E', E can be O, N, S, S<sup>32</sup>

The dimensionality of hybrid compounds depends on two factors: the extent of inorganic part and type of inorganic fragment. The information about the way of classification to different dimensional class and used symbolism are presented in Table 4.

Table 4. Proposed classification of dimensionality hybrid organic-inorganic materials<sup>33</sup>

Metal-organic-metal connectivity (O <sup>n</sup> , n=0-3)	Dimensionality of inorganic connectivity (I <sup>n</sup> , n=0-3)	0	1	2	3
0		Molecular complexes (I <sup>0</sup> O <sup>0</sup> )	Hybrid inorganic chains (I <sup>1</sup> O <sup>0</sup> )	Hybrid inorganic layers (I <sup>2</sup> O <sup>0</sup> )	3-D inorganic hybrids (I <sup>3</sup> O <sup>0</sup> )

1	Chain coordination polymers ( $I^0O^1$ )	Mixed inorganic-organic layers ( $I^1O^1$ )	Mixed inorganic-organic 3-D framework ( $I^2O^1$ )	-
2	Layered coordination polymers ( $I^0O^2$ )	Mixed inorganic-organic 3-D framework	-	-
3	3-D coordination polymers ( $I^0O^3$ )	-	-	-

### 2.3 Hybrid organic-inorganic semiconductor nanomaterials

The most promising hybrid organic-inorganic materials for future applications are those based on semiconductors. In the case of compounds studied in this paper, semiconducting components (MQ) adopt the form of layers separated by organic linkers (L). The MQ sheets are built of elements from the second (M - Zn, Cd, Mn) and sixth (Q - S, Se, Te) groups of the periodic table, while the organic parts are aliphatic<sup>34</sup> or aromatic<sup>35</sup> amines. The metal-ligand covalent bond typical for hybrid materials is formed between the nitrogen atom from the amino group and the metal atom (M) built into an inorganic plane.

Hybrid organic-inorganic materials have been successfully synthesized, characterized and classified. In accordance with the adopted systematics, such compounds can be expressed by the following equations:  $MQ(L)_{1/2n}$  for diamine,  $(H_2N - (C \dots C) - NH_2)$  and  $(MQ)_nL$  for monoamine  $(H_2N - (C \dots C))$ . In both equations  $n$  indicates the number of semiconducting layers in a single package separated by amines. The idea of a semiconducting package is shown on Figure 18.

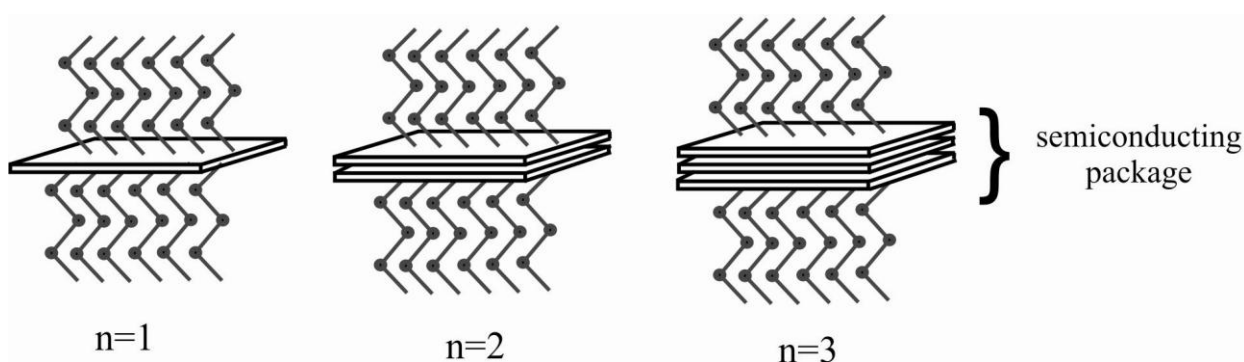


Figure 18. Semiconducting package

Depending on the structure, semiconducting hybrid compounds can be split into three classes: 1-, 2- and 3-dimensional (1D, 2D, 3D).<sup>36</sup>

### 2.3.1 1D-MQ(L) hybrid organic-inorganic materials

These hybrid organic-inorganic materials are built of semiconducting rods and di- or monoamines (Figure 19A, B).

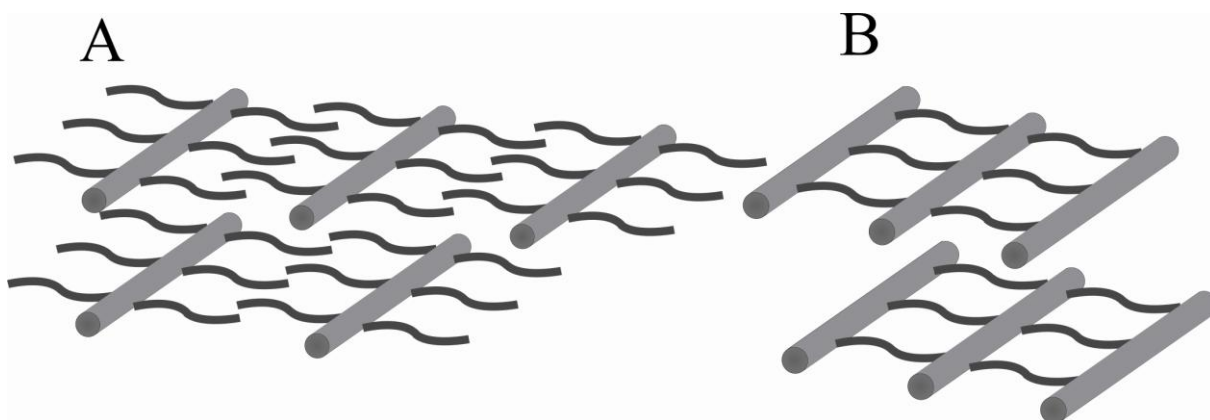


Figure 19. 1D hybrid organic-inorganic materials with **A**) monoamines, **B**) diamines

The most interesting representative is compound  $\text{ZnTe}(\text{pda})$  (pda indicates 1,3-propylenediamine) crystallized in an orthorhombic crystal system, space group Pbcm. One-dimensional Zn-Te chains, surrounded by amine, are extended along the b-axis. This way of linking organic spacers is unique. The propylenediamine is connected by both amine groups to the same tellurium atom, forming a sort of loop (Figure 20).<sup>37</sup>

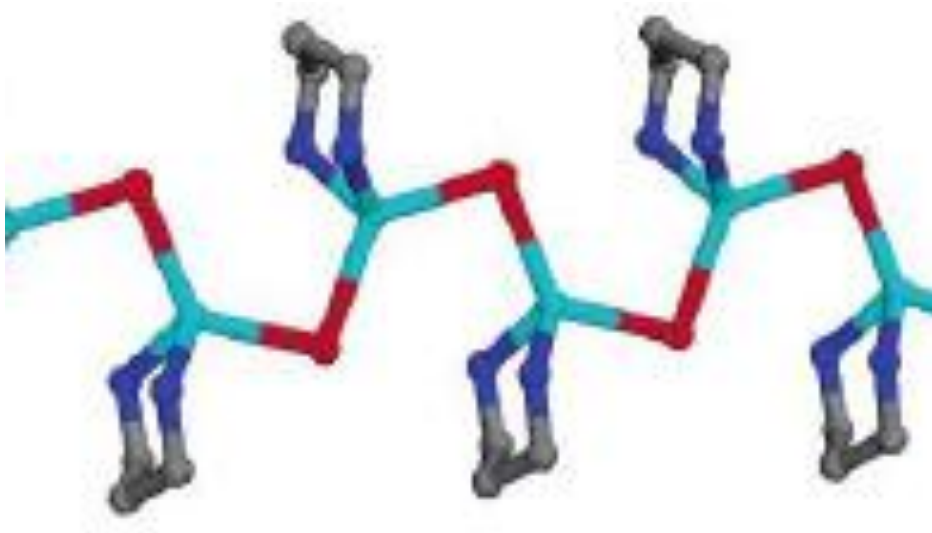


Figure 20. Structure of  $\text{ZnTe}(\text{pda})$ <sup>37</sup>

### 2.3.2 2D-(MQ)<sub>n</sub>L hybrid organic-inorganic materials

In two-dimensional (2D) hybrid materials, layers of semiconductors are separated by monoamines. The schematic arrangement is presented in Figure 21.

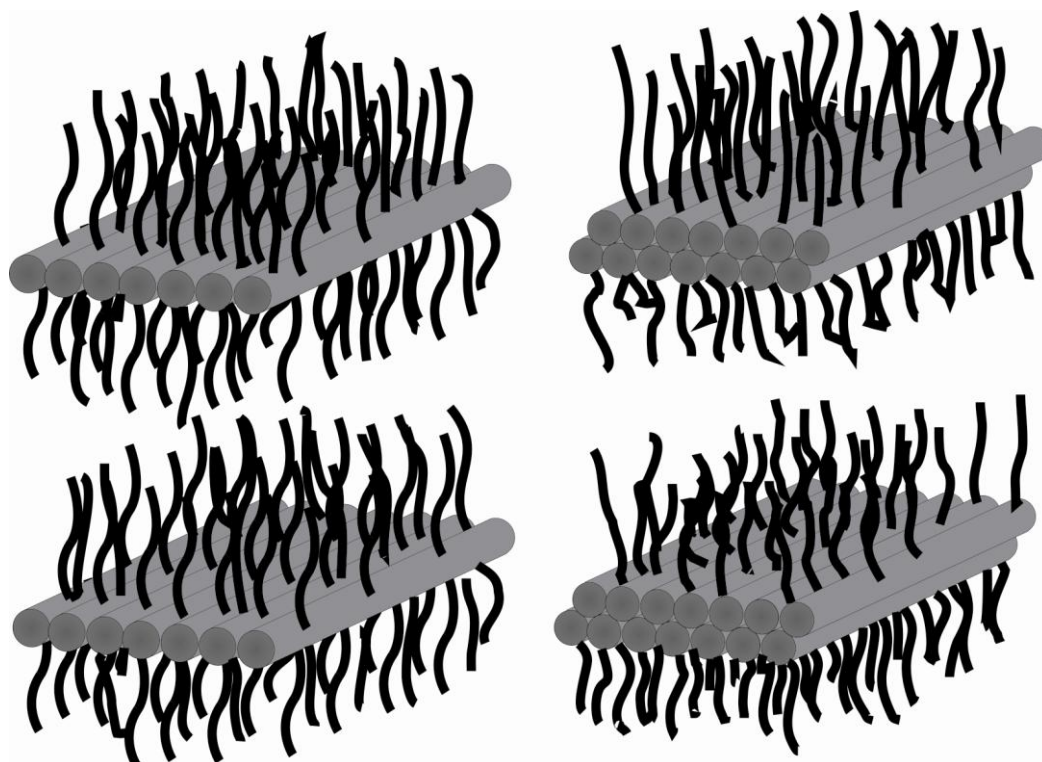


Figure 21. 2D hybrid organic-inorganic hybrid materials

2D hybrid compounds are interesting due to the possibility of obtaining double semiconducting layers, which have not been achieved for compounds based on diamines. The examples are described in Table 5 and Table 6.

Table 5. 2D-MQ(L) hybrid organic-inorganic materials<sup>37</sup>

M/Q	S	Te	Se
Zn	C <sub>1</sub> H <sub>3</sub> N <sub>1</sub> (ma) C <sub>3</sub> H <sub>7</sub> N <sub>1</sub> (pa) C <sub>4</sub> H <sub>9</sub> N <sub>1</sub> (ba) C <sub>6</sub> H <sub>13</sub> N <sub>1</sub> (ha)	C <sub>3</sub> H <sub>8</sub> N <sub>2</sub> (pda) N <sub>2</sub> H <sub>4</sub> (hd) MeNH <sub>2</sub>	C <sub>1</sub> H <sub>3</sub> N <sub>1</sub> (ma) C <sub>2</sub> H <sub>5</sub> N <sub>1</sub> (ea) C <sub>3</sub> H <sub>7</sub> N <sub>1</sub> (pa) C <sub>4</sub> H <sub>9</sub> N <sub>1</sub> (ba) C <sub>6</sub> H <sub>13</sub> N <sub>1</sub> (ha)

\*ma – metylamine, ea – etylamine, pa – propylamine, ba – butylamine, ha – hexaneamine, pda – propanediamine, hd – hydrazine;

Table 6. 2D-(MQ)<sub>2</sub>L hybrid organic-inorganic materials<sup>37</sup>

M/Q	S	Te	Se
Zn	C <sub>2</sub> H <sub>5</sub> N <sub>1</sub> (ea) C <sub>3</sub> H <sub>7</sub> N <sub>1</sub> (pa) C <sub>4</sub> H <sub>9</sub> N <sub>1</sub> (ba) C <sub>5</sub> H <sub>11</sub> N <sub>1</sub> (aa) C <sub>6</sub> H <sub>13</sub> N <sub>1</sub> (ha)	-	C <sub>2</sub> H <sub>5</sub> N <sub>1</sub> (ea) C <sub>3</sub> H <sub>7</sub> N <sub>1</sub> (pa) C <sub>4</sub> H <sub>9</sub> N <sub>1</sub> (ba) C <sub>5</sub> H <sub>11</sub> N <sub>1</sub> (aa) C <sub>6</sub> H <sub>13</sub> N <sub>1</sub> (ha)
Cd	C <sub>3</sub> H <sub>7</sub> N <sub>1</sub> (pa) C <sub>4</sub> H <sub>9</sub> N <sub>1</sub> (ba) C <sub>6</sub> H <sub>13</sub> N <sub>1</sub> (ha)	-	C <sub>3</sub> H <sub>7</sub> N <sub>1</sub> (pa) C <sub>4</sub> H <sub>9</sub> N <sub>1</sub> (ba) C <sub>6</sub> H <sub>13</sub> N <sub>1</sub> (ha)

\*ma – metylamine, ea – etylamine, pa – propylamine, ba – butylamine, ha – hexaneamina, pda – propanediamine, hd – hydrazine;

The crucial role in the synthesis of systems with single or double inorganic sheets is played by temperature. By precisely selecting a proper temperature range, a single-phase product can be successfully prepared. Normally, higher temperatures (above 160 °C) promote the formation of binary II-VI compounds (monolayer), whereas medium temperatures (in the range 50 °C – 150 °C) are more suitable for obtaining double-layer 2D-(MQ)<sub>2</sub>(L) hybrid materials.

The differences and similarities between 2D-(MQ)<sub>2</sub>L and 2D-(MQ)<sub>1</sub>L hybrid materials can be clearly depicted based on the following examples: ZnSe(ba) and Zn<sub>2</sub>Se<sub>2</sub>(ba), where ba means butylamine.<sup>37</sup> Both compounds crystallize in orthorhombic crystal system and in space group Pbcn. In single inorganic layers, each Zn atom is connected to three Se atoms and one N atom, while in the second case, Zn atoms can also be found surrounded only by four Se atoms. Furthermore, cell periods are longer for Zn<sub>2</sub>Se<sub>2</sub>(ba), which seems obvious because of the presence of double semiconducting layers in Zn<sub>2</sub>Se<sub>2</sub>. Both compounds were synthesized in solvothermal conditions, Zn<sub>2</sub>Se<sub>2</sub>(ba) in the temperature range 120–150 °C, ZnSe(ba) at temperatures higher than 160 °C.

### 2.3.3 3D-MQ(L)<sub>1/2</sub> hybrid organic-inorganic materials

The most stable type of organic-inorganic hybrid compound is composed of single layers of semiconductor separated by diamines. Two amino groups are linked to the two different, mutually parallel inorganic (MQ) planes by covalent bonds. A schematic representation of 3D hybrids is shown in Figure 22.

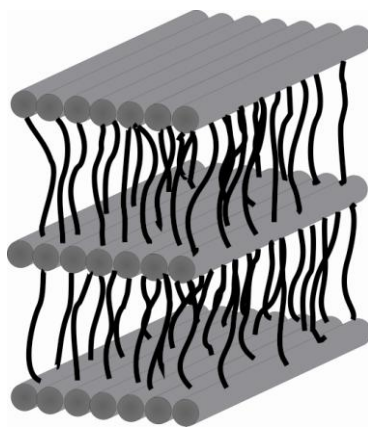


Figure 22. 3D-MQ(L)<sub>1/2</sub> hybrid organic inorganic materials – schematic representation

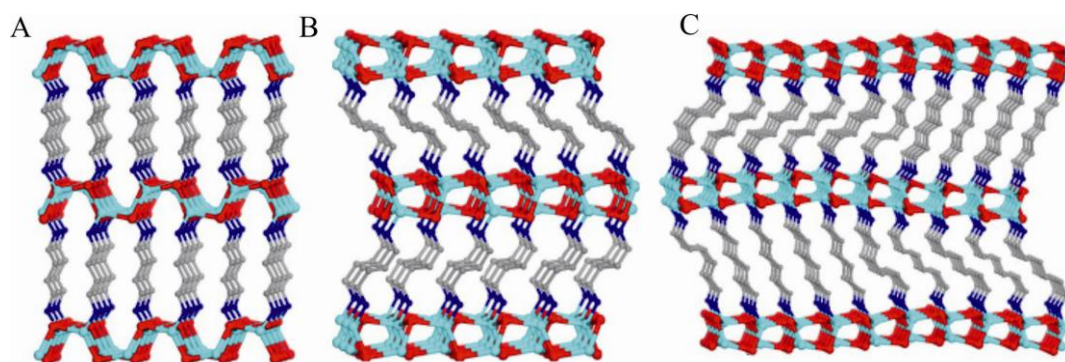
In some papers, authors postulate the possibility of synthesizing 3D double-layer systems, but until now it has never been done.<sup>36</sup> 3D hybrid materials are represented by the formula MQ(L)<sub>1/2</sub>. Typical for them is the presence of one long period in the unit cell. The other two are much shorter and possess nearly the same value. Table 7 shows crystallographic data for a few compounds which belong to this group.

Table 7. Crystallographic data of 3D-MQ(L)<sub>1/2</sub> hybrid organic-inorganic materials

Type of compounds/parameters	Space group	a[Å]	b[Å]	c[Å]	V[Å <sup>3</sup> ]	Z
<b>α2-CdSe(en)</b> <sub>1/2</sub> <sup>36,38</sup>	Pbca (61)	7.0949(3)	6.795(3)	16.7212(8)	806.17(2)	4
<b>CdSe(pda)</b> <sub>1/2</sub> <sup>36</sup>	Cmc2 <sub>1</sub> (36)	20.6660(12)	6.8900(4)	6.7513(4)	961.31(14)	4
<b>MnSe(en)</b> <sub>1/2</sub> <sup>29</sup>	Pbca (61)	6.711(1)	6.614(1)	17.720(4)	786.5(2)	4
<b>MnSe(pda)</b> <sub>1/2</sub> <sup>29</sup>	Cmc2 <sub>1</sub> (36)	20.384(4)	6.719(1)	6.565(1)	899.1(3)	4
<b>ZnSe(en)</b> <sub>1/2</sub> <sup>29</sup>	Pbca (61)	6.6298(9)	6.4608(9)	17.350(2)	744.0(2)	4
<b>ZnSe(pda)</b> <sub>1/2</sub> <sup>29</sup>	Cmc2 <sub>1</sub> (36)	19.9731(18)	6.6268(7)	6.44394(6)	852.31(14)	4
<b>α1-ZnTe(en)</b> <sub>1/2</sub> <sup>40</sup>	Pbca (61)	7.061(1)	6.927(1)	17.524(4)	857.1(3)	4
<b>β-ZnTe(en)</b> <sub>1/2</sub> <sup>40</sup>	Pnnm(58)	5.660(1)	17.156(3)	4.336(1)	421.04(14)	2
<b>ZnTe(pda)</b> <sub>1/2</sub> <sup>36</sup>	Cmc2 <sub>1</sub> (36)	20.169(4)	7.038(1)	6.882(1)	976.9(3)	4
<b>α-ZnTe(hda)</b> <sub>1/2</sub> <sup>42</sup>	Pbca (61)	7.0714(13)	6.9201(13)	27.051(5)	1323.7(4)	8
<b>γ-ZnTe(hda)</b> <sub>1/2</sub> <sup>42</sup>	Pbca (61)	7.1353(5)	6.9616(5)	23.7318(18)	1178.83(15)	8
<b>δ-ZnTe(hda)</b> <sub>1/2</sub> <sup>42</sup>	P2 <sub>1</sub> 2 <sub>1</sub> 2 <sub>1</sub> (19)	7.1091(14)	34.612(7)	25.091(5)	6174(2)	8

As can be seen, the type of amine used has an effect on space group, namely: compounds with amines containing an even number of carbon atoms in most cases crystallized in centrosymmetric space group Pbca (no. 61), those with odd numbers of carbon atoms in noncentrosymmetric space group Cmc2<sub>1</sub> (no. 36).<sup>39</sup> Furthermore, the differences in the conformation of the diamines in 3D hybrid materials lead to structural variants: α-, γ- and δ-<sup>41</sup>, α1, α2, β.<sup>40</sup>

For example, ZnTe(hda)<sub>1/2</sub> (1,6-hexadamine) can occur in three forms, α-, γ- and δ-. These are presented in Figure 23.

Figure 23. 3D-MQ(L)<sub>1/2</sub> **A**) α-ZnTe(hda)<sub>1/2</sub> **B**) γ-ZnTe(hda)<sub>1/2</sub> **C**) δ-ZnTe(hda)<sub>1/2</sub><sup>41</sup>

The first form ( $\alpha$ ) is the most frequently obtained. Here, the amines are perpendicular to the ZnTe slabs while in the two others cases ( $\gamma$ ,  $\delta$ ), organic molecules are arranged obliquely to the layers. In  $\gamma$ -ZnTe(hda)<sub>1/2</sub> all C-C bonds possess trans conformation, whereas in  $\delta$ -ZnTe(hda)<sub>1/2</sub>, besides pure trans, a mixture of trans and gauche conformations can also be observed.  $\alpha$ -ZnTe(hda)<sub>1/2</sub> and  $\delta$ -ZnTe(hda)<sub>1/2</sub> are synthesized routinely using solvothermal technique at temperatures 200–210 °C, whereas the  $\gamma$ -form can be obtained by phase transitions. Noteworthy is the fact that phase transitions take place only for structures in which diamines contain an even number of carbon atoms.<sup>41</sup>

Hybrid organic-inorganic compounds crystallize in the most preferred structural form, as, for example, CdSe(en)<sub>1/2</sub> in  $\alpha$ 2, ZnTe(en)<sub>1/2</sub> in  $\alpha$ 1. Despite careful investigations, no explanation for such behavior has been found.<sup>40</sup> It is also unclear whether the formation of these phases is determined by parameters of growth or by their ground-state total energies. There is no doubt that finding the answer is significant, more so given that the physical features of hybrids are closely related to the type of structure. This will be discussed in the next section.

Resolving the structural diversity of 3D hybrid materials, it should be mentioned that semiconducting layers can be obtained in two different allotropic forms (zinc blende and wurtzite). Generally inorganic slabs [MQ] are formed like a slightly deformed honeycomb (6<sup>3</sup>) in which three-coordinated metal atoms and halogen atoms are alternately placed (as is typical for both cases). However, the topology of nets is varied and thus relative orientation of the adjacent layers and connectivity with organic molecules. This phenomenon was actually observed for the ZnTe(pda)<sub>1/2</sub> structure (Figure 24).

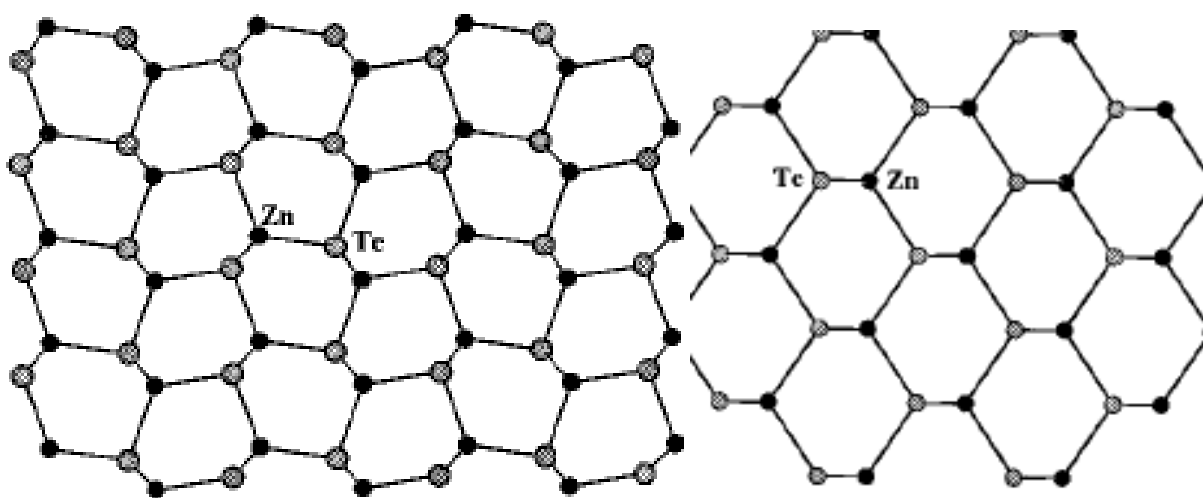


Figure 24. The semiconducting layers typical for compound  $\alpha$ -ZnTe(en)<sub>1/2</sub> and  $\beta$ -ZnTe(en)<sub>1/2</sub>

### 2.3.4 3D- $M_{1-x}N_xQ(L)_{1/2}$ hybrid organic-inorganic materials

It is also possible to obtain doped hybrid organic-inorganic materials  $M_{1-x}N_xQ(L)_{1/2}$ , where two different metal atoms (M, N) are built into the semiconducting layers. This modification can significantly change the properties of hybrid compounds, especially when Mn atoms are added, thus radically modifying magnetic features.<sup>42,43,44</sup> Such modifications in semiconducting layers have been performed only for 3D hybrids.

## 2.4 Synthesis methods of hybrid organic-inorganic materials

The most favorable, and actually the most frequently used, synthesis method for hybrid materials is the solvothermal technique.<sup>45,46,47,48</sup> It requires specialist equipment: microprocessor-controlled autoclaves, thanks to which suitable temperature, pressure and stable syntheses conditions can be achieved. As mentioned before, the key factor which determines the quality of the obtained compounds is temperature. Using the same substrates in the same ratio but at different temperatures very often leads to the creation of different products. This phenomenon is readily noticeable in the case of 2D hybrid materials with single or double semiconductor layers (higher synthesis temperatures are reserved for binary II-VI layers, while at a moderate temperature range, the acquisition of double layers is preferable). Of course, the type of substrate is not without significance. 3D compounds based on ZnTe semiconducting slabs required higher temperatures in the range 180–210 °C, while for ZnS and CdS much lower temperatures, 120–150 °C, are needed. It should be noted that the amine does not affect the temperature of the synthesis.

The most frequently used substrates as a source of Zn atoms are  $ZnCl_2$ <sup>29</sup> and  $Zn(NO_3)_2 \cdot 6H_2O$ ;<sup>36</sup> as a source of Cd atoms,  $CdCl_2$ ;<sup>36</sup> and as a source of Mn atoms,  $MnCl_2$ .<sup>29</sup> S, Se and Te are used in elemental form. The ratio M:Q is 2:1 or 1:1. Amines act as a solvent and usually are used with a large excess, even up to seventyfold. The final products are always washed with 30% ethanol, which enables the removal of residues.

## 2.5 Properties of hybrid organic-inorganic materials

Due to their uniform and highly arranged structures, in which semiconductor monolayers are divided by organic linkers, hybrid organic-inorganic materials possess interesting electronic, optical and magnetic properties. It should be emphasized that the features characteristic of nanomaterials are slightly different than those observed for the corresponding bulk compounds. As examples of such behavior, changing the melting point or increasing the band

gap in semiconductors, together with the transition to the nanoscale, may be indicated. This last phenomenon is related to the quantum confinement effect.

### 2.5.1 Quantum confinement effect

Generally bulk semiconductor materials are built of a large number of atoms ordered in three-dimensional networks. In such arrangements, sets of similar energy molecular orbitals form continuums called valence and conduction bands. They are split by an energy gap ( $E_g$ ) with typical values in the range 0.3–3.8 eV.<sup>49</sup> At a temperature of absolute zero ( $T=0$  K), semiconductors behave like insulators, the valence band (lower energy levels) is filled with electrons and the conduction band (higher energy levels) is unoccupied.<sup>50</sup> The electron can be excited to the conduction band at a higher temperature (small conductivity appears) or by the absorption of a photon with proper energy. In both cases, in the valence band the hole  $h^+$  and in the conduction band electron  $e^-$  are produced. Because of the Coulomb attraction between electron ( $e^-$ ) and hole ( $h^+$ ), they cannot move independently and therefore can be treated as a ‘pair’ called an exciton. The  $e^-/h^+$  pair is characterized by its energy and the Bohr radius, which can be defined as:

$$r_B = \frac{\hbar^2 \epsilon}{e^2} \left[ \frac{1}{m_e^*} + \frac{1}{m_h^*} \right] \quad (39)$$

where:  $\hbar$  – Planck's constant divided by  $2\pi$ ,  $\epsilon$  – the bulk optical dielectric coefficient,  $e$  – the elementary charge, and  $m_e^*, m_h^*$  effective mass of the electron and hole.<sup>31,49</sup>

The different behavior of nanosemiconductors compared to the equivalent bulk semiconducting materials is related to the size of the particle. Specifically, decreasing the particle size to the nanometer range generates an extraordinary situation in which the exciton radius can exceed the dimension of the grain. Then the charge carriers gain higher kinetic energy, which can be discussed on the basis of quantum theory. In isolated, thin semiconductor layers, separated by insulators (in the case of hybrid materials by the amines), movement of electrons and holes is unlimited along two perpendicular directions in the layers, but quantized in the third direction, perpendicular to the plane. Such a system may be approximate to a quantum well of finite depth. The reduction of dimensionality leads to quantization energy levels of discrete values and an increasing band gap, which now can be described as (effective band gap):

$$E_g^{ef} = E_g + \frac{\hbar^2}{8m_e^*T^2} + \frac{\hbar^2}{8m_h^*T^2} \quad (40)$$

where:  $E_g$  – band gap of corresponding bulk materials.  $T$  – thickness of the layer. Obviously, this is a straightforward approximation of the real situation in the crystals, where such phenomena as surface effects and coupling the electronic states were not considered. Thus the many other theories (more detailed) are employed to obtain the best fit between experimental and theoretical values for semiconductor nanocrystals.<sup>49</sup>

### 2.5.2 Fundamental knowledge about semiconductors

To observe electronic transition in the semiconductor (generation of an  $h^+$  and  $e^-$  pair), a photon with the adequate energy  $h\nu \geq E_g$  needs to be absorbed. This process in semiconductor materials can be described by the following equation, similar to the well-known Beer's Law:

$$A = \alpha T \quad (41)$$

where  $\alpha$  is defined as the adsorption coefficient of the solid. It can be expressed as follows:

$$\alpha(h\nu) \sim \sum P_{if} n_i n_f \quad (42)$$

The particular symbols are:  $P_{if}$  – the probability of optical transition between initial and final states,  $n_i$  – density of the initial states,  $n_f$  – density of the final states.

If the value of the absorbed energy greatly exceeds the width of  $E_g$ , the excitation may lead to higher states in conduction bands. Then the excess of energy of the electron can be lost through the radiation-free process.

Two different types of semiconductors are known: those with direct and those with indirect band gaps. In the former, during the optical transition, the wave vector is conserved. Furthermore, this type of semiconductor possesses a large absorption coefficient, which is associated with the energy of the photon in the following relationship:

$$\alpha(h\nu) \sim (E_g - h\nu)^{1/2} \quad (43)$$

In semiconductors with the indirect band gap, the absorption coefficient is small and the optical transitions occur with unpreserved wave vectors. The relation between the absorption coefficient and photon energy is:<sup>51</sup>

$$\alpha(h\nu) \sim (E_g - h\nu)^2 \quad (44)$$

Using the above equations for the estimation of an experimentally obtained optical spectrum, the band gap energy of semiconductors can be found.

The excitations in both types of semiconductors are presented in Figure 25.

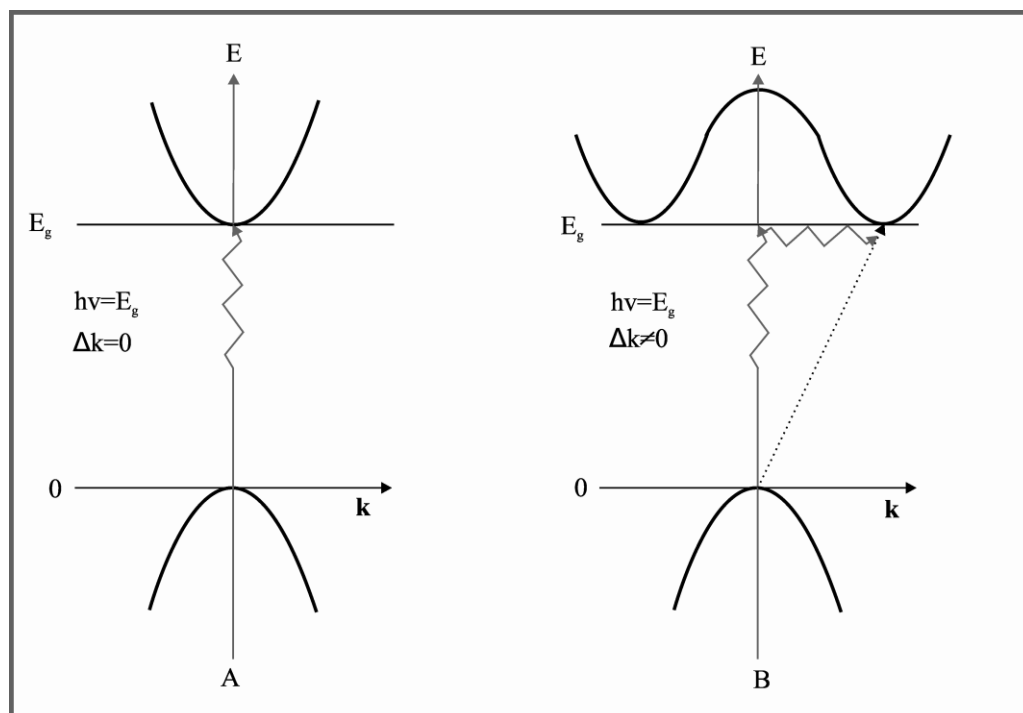


Figure 25. Excitation in the case of **A**) a direct semiconductor, **B**) an indirect semiconductor

### 2.5.3 Optical properties of hybrid organic inorganic materials

In the case of nanocrystalline material, the value of calculated band gap energy is higher than for the analogous macrocrystalline compound. This phenomenon is related to the quantum size effect and is commonly called “blue shift,” which was discussed in the previous section. It can be also observed for hybrid organic-inorganic materials.

The value of the band gap energy for most 3D-MQ(L)<sub>1/2</sub> hybrids is high, mostly because of the thickness of the semiconductor layer around 3 Å, which is a very low value. An example is a family of compounds based on ZnTe slabs ( $\alpha$ -ZnTe(en)<sub>1/2</sub>,  $\beta$ -ZnTe(en)<sub>1/2</sub>, ZnTe(pda)<sub>1/2</sub>, ZnTe(ptda)<sub>1/2</sub> and ZnTe(hda)<sub>1/2</sub>), for which the absorption edges are in the range 3.3–3.7 eV. For comparison, the band gap for pure bulk phase ZnTe is 2.1 eV. A quite similar situation occurs for the other 3D hybrid materials (Table 8).

Table 8. The band gap energy for selected 3D-MQ(L)<sub>1/2</sub> compounds

Type of compound	Blue Shift [eV]
$\alpha$ -ZnTe(en) <sub>1/2</sub> <sup>29</sup>	1.4
$\beta$ -ZnTe(en) <sub>1/2</sub> <sup>29</sup>	1.2
ZnTe(pda) <sub>1/2</sub> <sup>29</sup>	1.3
ZnTe(bda) <sub>1/2</sub> <sup>38</sup>	1.4
ZnTe(ptda) <sub>1/2</sub> <sup>38</sup>	1.5

$\text{CdS(en)}_{1/2}$ <sup>38</sup>	0.7
$\text{CdS(pda)}_{1/2}$ <sup>38</sup>	0.7
$\text{MnSe(en)}_{1/2}$ <sup>42</sup>	0.2
$\text{MnSe(pda)}_{1/2}$ <sup>42</sup>	0.1
$\text{ZnSe(en)}_{1/2}$ <sup>42, 28</sup>	1.5
$\text{ZnSe(pda)}_{1/2}$ <sup>42, 28</sup>	1.4

The only exception is a group of compounds based on MnQ semiconducting slabs, for which quantum confinement effect is actually nearly undetectable (in the case of  $\text{MnSe(en)}_{1/2}$  and  $\text{MnSe(pda)}_{1/2}$  the blue shift is in the range 0.1–0.2 eV). This is related to the fact that in Mn atoms 3d bands are highly localized, thus the quantum confinement effect induced by organic linkers leads to much smaller changes.<sup>42</sup> In this context the “optical behavior” of mixing semiconductor layers with Mn atoms seems quite interesting. As was observed in the case of  $\text{Zn}_{1-x}\text{Mn}_x\text{Se(pda)}_{1/2}$ , even with a high Mn concentration, a strong quantum confinement effect is exhibited. Furthermore, the linear increase in the Mn percentage does not correspond to the linear shift in the band gap energy. The authors explain this in terms of the differences in localization of Mn and Zn 3d bands (the Zn 3d bands are delocalized while Mn 3d bands are highly localized).<sup>42</sup>

$\text{ZnTe(pda)}$  is an example of a 1D hybrid compound. It possesses a very high blue shift value: 1.7 eV.<sup>36</sup> As can be seen, this is slightly higher than that usually observed in the case of 3D and 2D hybrid materials. This may be correlated to the fact that quantization here is in two directions.<sup>50</sup> In turn, the ‘optical behavior’ of 2D materials is similar to 3D compounds. Hybrid materials with single semiconductor layers are characterized by larger energy band gaps (in the range 1.2–1.6 eV), those with double semiconductor layers by smaller gaps (0.7–1.2 eV). The blue shifts for selected compounds are presented in Table 9.

Table 9. The blue shifts for selected 2D-(MQ)<sub>n</sub>L hybrid organic-inorganic materials<sup>37</sup>

2D-MQ (L)	Blue shift	2D-(MQ) <sub>2</sub> L	Blue shift
-	-	$\text{Zn}_2\text{Se}_2(\text{ea})$	1.0
-	-	$\text{Zn}_2\text{Se}_2(\text{pa})$	1.0
$\text{ZnSe}(\text{ba})$	1.6	$\text{Zn}_2\text{Se}_2(\text{ba})$	1.0
$\text{ZnS}(\text{ba})$	1.3	$\text{Zn}_2\text{S}_2(\text{ba})$	0.7

\*ea – ethylamine, pa – propylamine, ba – butylamine;

#### 2.5.4 Magnetic properties of hybrid organic-inorganic materials

Mn-based materials are known as dilute magnetic semiconductors (DMS). They are characterized by unusual magneto-optical features; thus, the study of magnetic properties of hybrid organic-inorganic compounds will be considered in relation to this group. Hybrids with incorporated Mn atoms possess strong Faraday rotation, a magnetic polaron state and giant exciton Zeeman splitting. This last feature results from the s, s-p exchange interaction between band electron/hole and  $\text{Mn}^{2+}3d^5$  electron.<sup>43,44</sup>

The in-depth study on magnetic properties of hybrid materials was performed based on  $\text{Zn}_{1-x}\text{Mn}_x\text{Se}(\text{en})_{1/2}$  ( $0 < x \leq 1$ ). As it turns out, all compounds belonging to this group reveal paramagnetic behavior. Nevertheless, the measurements of the dependency  $\chi(T) = C/(T + T_C)$ , where  $\chi(T)$  – magnetic susceptibility, C – Curie-Weiss constant,  $T_C$  – Curie temperature, indicates that a strong antiferromagnetic correlation between the  $\text{Mn}^{2+}$  ions occurs. Also quite interesting is that the value of  $\chi(T)$  is larger in the case of the smaller Mn-atom concentration than in the lower, in all temperature ranges. The effective magnetic moment  $\mu_{eff} = 5.11\mu_B$  for  $\text{MnSe}(\text{en})_{1/2}$  is weaker than that obtained for the bulk MnSe phase, which is  $\mu_{eff} = 5.88\mu_B$ .<sup>42</sup>

#### 2.5.5 Thermal properties of hybrid organic-inorganic materials

Three different types of material response to changing temperature are known. Positive thermal expansion (PTE) takes place when volume grows along with increasing temperature. In the case of negative thermal expansion (NTE), materials contract upon heating. And finally, zero thermal expansion (ZTE) can be defined as a case in which neither contraction nor expansion occur in response to a rise in temperature. The last case is extremely rare and also desirable. Therefore, many materials are designed so as to provide ZTE. Because in most cases they are constructed of materials characterized by adversarial thermal behavior, the most serious problems are cracks between grains. Such a situation does not occur for hybrid organic-inorganic materials, even though they are also built of two compounds with antagonist thermal responses (amines exhibit NTE, semiconductors PTE).<sup>39</sup> Nevertheless, in the case of hybrid compounds, these two building blocks form the same material: crystals without any boundary or grains. Thus, the compensation of NTE and PTE effects do not cause any cracks.

For the group  $\alpha\text{-ZnTe}(\text{L})_{1/2}$  compounds, where L – en-ethylenediamine, pda – propyldiamine, bda – butyldiamine and ptda – pentyldiamine, a systematic study on thermal behavior was performed. For all materials, near-ZTE behavior was observed. Quite interestingly, along with

an increase in the number of carbon atoms in the amine chains, the NTE becomes dominant. Only for  $\text{ZnTe}(\text{en})_{1/2}$  was PTE observed.<sup>39</sup>

### 2.5.6 The amine impact on the features of hybrid organic-inorganic materials

There is no doubt that amines play a crucial role in the formation of hybrid organic-inorganic materials: they act as a structure-directing coordination template.<sup>52</sup> In synthesis, amines are used as the solvent, but finally they are built into the structure, in the form of linkers between layers of semiconductors. As mentioned previously, this construction provides a strong quantum confinement effect. Using a different type of amine (mono- or diamines) a different value of blue shift can be achieved due to the fact that different thicknesses of semiconductor layers are obtained (it is unquestionable that the amine type is one of the most important factors affecting the creation of binary, or double layer, systems).

Furthermore, the length of amines has a significant impact on features of hybrid organic-inorganic materials. Firstly, the longer the amines built into the structures, the weaker the interaction between adjacent semiconductor layers.<sup>53</sup> In a few cases it can be observed that the band gap energy increases together with an increasing number of carbon atoms in the inorganic spacer. Such a situation occurs for hybrid compounds based on ZnTe slabs; nevertheless, this cannot be considered a rule for the others.

In comparison to corresponding bulk counterpart, hybrid organic-inorganic compounds are lighter and more flexible. With increased length of amines, the strength of the strain grows too.  $\text{ZnTe}(\text{had})_{1/2}$  undergoes an even larger strain (at the same pressure) than polystyrene.<sup>41</sup> Furthermore, the incorporation of amines changes the thermal properties of hybrids. Both thermal conductivity and thermal diffusivity decrease as the length of amines increases. In turn, thermal conductivity is inversely related to amine length.<sup>41</sup>

## 2.6 Hybrid organic-inorganic materials as the precursors of pure nanometric semiconductors

The possibilities of the application of semiconductors II-VI are strongly related to their morphology. Therefore, it is no wonder that so much attention is focused on the synthesis route, which enables control of the shape, size composition and assembly properties of the obtained nanostructures. In the last few years, new techniques using hybrid organic-inorganic materials as precursors have turned out to be quite popular and also successful. Nanobelts,<sup>54</sup> nanosheets,<sup>55</sup> nanoparticles,<sup>56</sup> nanowires and nanotubes<sup>57</sup> have been formed in a simple way.

As can be observed, even slight differences in the reaction conditions suffice to change the morphology of the obtained semiconductor nanoparticles. A great example of such behavior is preparation of CdSe nanostructures from  $\text{Cd}_2\text{Se}_2(\text{pa})$  (pa – propylamine), in which, through the use of nitrogen and ambient atmosphere, nanosheets and nanoparticles, respectively, were prepared. Furthermore, as was proved, temperature plays an important role, too: namely, at a lower temperature regime morphologically different molds, or actually intermediate forms (between hybrid materials and pure semiconductor), can be obtained.<sup>55</sup> There is also no doubt that solvent impacts substantially on the creation of nanoparticles with various sizes, shapes and morphologies. In the case of  $\text{Zn}_{1-x}\text{Mn}_x\text{Se}(\text{deta})_{1/2}$  (deta-diethylenetriamine) two different forms of  $\text{Zn}_{1-x}\text{Mn}_x\text{Se}$  were prepared. The use of 1-octadecane as a reaction medium resulted in the molding of nanobelts, whereas in the case of ethylene glycol the only obtained phase was nanotubes (because diethylenetriamine is less inert in comparison to 1-octadecane).<sup>57</sup> Moreover, the possibility of preparing modified semiconductor nanostructures is quite interesting. An example is N-doped ZnS nanoparticles, which were prepared through  $\text{ZnS}(\text{pp})_{1/2}$  (pp-piperazine).<sup>56</sup>

Depending on the morphology of the final products, various mechanisms have been proposed. In most situations, there is a multi-step process, in which coupled stages follow one by one. For example, the above-mentioned nanotubes are prepared in four main steps. Briefly, the initial compound  $\text{ZnSe}(\text{deta})_{1/2}$  decomposes to nanoparticles, which in turn become the seeds for the walls. Then, through the oriented-attachment and the Oswald ripening process, nanotubes grow. In a few cases, the presence of a transition complex with solvent molecules is suggested.<sup>55,57</sup>

From a technical point of view, the formation of a pure semiconductor from hybrid organic-inorganic materials is fairly simple. In most cases, starting material is boiled at a properly selected temperature (100–300 °C), in a properly chosen reacting (or non-reacting) medium and atmosphere. This procedure is accompanied by mixing and sonification. Also quite popular is the use of the solvothermal or hydrothermal technique.<sup>38,57</sup>

## 2.7 Potential applications

The potential functionalities of the hybrid-organic inorganic compounds discussed in this thesis are closely related to their unusual optical and magnetic properties. Furthermore, the simplicity of the synthesis route and the possibility of using the compounds as the precursors

of pure, well-defined semiconductors make them interesting scientific objects with wide applications.

In one interesting application, Mn-doped 2D-(MQ)<sub>2</sub>L hybrid compounds (where L – monoamine) were used as materials that emit direct white light. As reported by J. Li et al., a commercial LED (360 nm) was coated with a thin layer of 2D-Cd<sub>2</sub>S<sub>2</sub>(ba) (ba – butylamine) and Mn-doped 2D-Cd<sub>2</sub>S<sub>2</sub>(ba). Upon illumination, they generated white light. The strongest PL (photoluminescence) emission was achieved in the case of the presence of Mn<sup>2+</sup> ions. Furthermore, the longest amine is built between adjacent semiconductor layers, the more distinguished 2D confinement led to strengthening the photoluminescence.<sup>58</sup>

Despite the fact that hybrid organic-inorganic materials possess unique optical features, until now there have been no experimental trials of their employment within photonic applications. Nevertheless some studies of the theoretical aspects have been done, which is undoubtedly the first step.

On the other hand, the possibilities of application hybrid organic-inorganic materials can be related to their processability. The formation of a pure semiconductor type II-VI with the well-defined morphology and optical properties of these compounds make them very promising materials for optoelectronic, catalysis and sensor devices. Potential applications of selected semiconductor II-VI are summarized in Table 10.

Table 10. Potential applications of semiconductors II-VI

Semiconductor	Optical properties	Potential applications
ZnS	$E_g=3,6$ eV (wurtzite), $E_g=3,8$ eV (zinc blende), direct <sup>49</sup> .	Infrared windows <sup>49</sup> , UV-light sensors, field emitters <sup>59</sup>
ZnSe	$E_g=2,58$ eV (zinc blende), direct <sup>49</sup> .	Infrared windows <sup>49</sup> , photocatalysis <sup>60</sup> , optoelectronic devices <sup>61</sup>
ZnTe	$E_g=2,28$ eV (zinc blende), direct <sup>49</sup> .	Infrared windows <sup>49</sup> , LED, detectors <sup>62</sup>
CdS	$E_g=2,53$ eV (wurtzite), direct <sup>49</sup> .	Photovoltaic cells <sup>49</sup> , photocatalysis <sup>63</sup>
CdSe	$E_g=1,74$ eV (wurtzite), direct <sup>49</sup> .	Photovoltaic cells <sup>49</sup> , electronic devices (field effect transistor) <sup>64</sup>

## Basic knowledge about ZnS and its application in photocatalysis

In this work, special attention has been devoted to hybrid organic-inorganic materials based on ZnS. Furthermore, synthesis of pure ZnS and preliminary photocatalytic tests for the resulting samples were performed. Accordingly, in this section some fundamental information about ZnS and its photocatalytic applications will be presented.

### 3.1 ZnS – basic features

ZnS, with its promising potential applications, is an interesting scientific subject. Despite the fact that its bulk phases are well characterized, new morphological forms in nanometer scale (nanotubes, nanoribbons, nanorods) are still being obtained and investigated.

Two allotropic structures of bulk ZnS are known: zinc blende (zb) and wurtzite (wz). The first form is stable at lower temperatures, the second at higher ( $\sim 1000$  °C).<sup>59</sup> Both structures are shown in Figure 26.

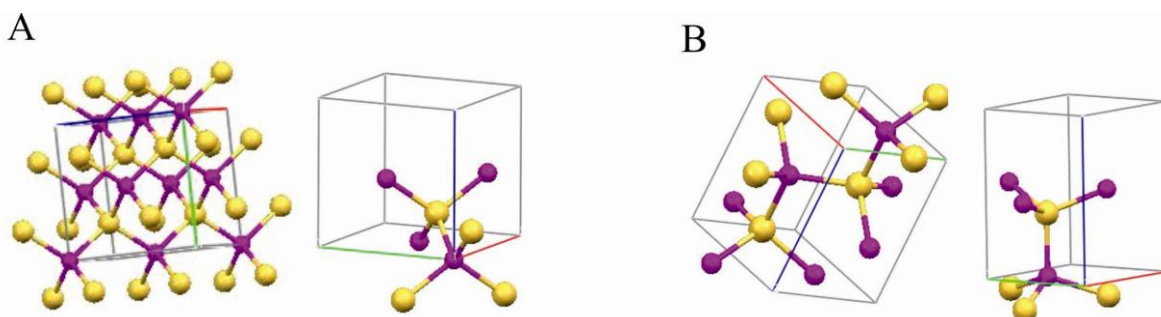


Figure 26. Zinc blende structure of ZnS: **A)** zinc blende structure **B)** wurtzite structure. Colors: Zn – pink, S – yellow

The zinc blende structure (zb-ZnS) crystallizes in cubic crystal system with cell parameters  $a=b=c=5.41$  Å and in the space group  $F4-3m$ . The wurtzite form (w-ZnS) crystallizes in hexagonal crystal system with cell parameters  $a=b=3.82$  Å,  $c=6.26$  Å and in the space group  $P6_3mc$ . In both cases, zinc atoms are tetrahedrally coordinated, but their arrangement is different.<sup>59</sup>

ZnS is an interesting material because of its optical properties, which differ between its two forms. The band gap of zb-ZnS is 3.6 eV, while for w-ZnS, it is 3.8 eV.<sup>49</sup> According to X.S. Fang et al. “the valence band comprises three regions: a lower region consisting of the s bands of Zn and S, a higher-lying region containing well-localized Zn 3d bands, and a top broader band originating from the s-p states hybridized with 3d Zn states.” Because the minima of the

conduction band are much more dispersive than the maxima of the valence band, electrons are more mobile than holes.<sup>59</sup> The Bohr radius for an exciton is 2,5 nm.<sup>65</sup> Of course, in the nanometer regime the optical properties were changed, which is related to the quantum confinement effect discussed in section 2.5.1.

Due to the above-mentioned features, ZnS can be applied as a material in optoelectronic devices, sensors, IR-windows or as a catalyst.<sup>49,59</sup> Taking my research into account, especially interesting is the application of ZnS in photocatalysis.

### **3.2 ZnS as a catalyst**

Bulk phase ZnS is resistant to oxidation and hydrolysis; however, this changes in the case of transition to the nanometer scale. Thus, ZnS nanoparticles can be used successfully as photocatalysts. Moreover, they are characterized by additional advantages such as nontoxicity and ease of synthesis, and their electronic features can be modified simply by doping with different elements. Furthermore, in ZnS, electron-hole pairs are generated relatively quickly and excited electrons possess highly negative reduction potential, which is a favorable feature. Thus, ZnS is considered to be a promising catalyst. ZnS is most frequently used in photocatalytic degradation of water pollutants.<sup>59</sup> Hence, eosin B,<sup>59,66</sup> p-nitrophenyl,<sup>67</sup> or dyes (methyl orange, methylene blue)<sup>59,68</sup> have been successfully removed using ZnS. It should be emphasized that the degradation of eosin B with ZnS nanoparticles gives even better results than those obtained with commercially available Degussy P25 (TiO<sub>2</sub>).<sup>59</sup> Furthermore, ZnS can be employed also in the reduction of atmospheric CO<sub>2</sub>.<sup>69</sup> These are only a few selected cases from the very wide range of possibilities for the application of nano-ZnS in photocatalysis. Nevertheless, many more examples can be shown, especially if the doped forms of ZnS are taken into account, for instance, Zn<sub>1-x</sub>Mn<sub>x</sub>S, which has been used for the photodegradation of the modeled dye methylene blue.<sup>70</sup>

Since in my research ZnS was used for the photoreduction of methyl orange (MO) from solutions, special attention will be devoted to this reaction. In their paper, L. Zang et al. discuss the few parameters relevant to the photodegradation of MO.<sup>71</sup> Their catalytic experiments were performed for ZnS sols prepared as follows: polyphosphate (Na<sub>5</sub>P<sub>3</sub>O<sub>10</sub>) and zinc nitrate (Zn(NO<sub>3</sub>)<sub>2</sub>) solutions were mixed. Next, Na<sub>2</sub>S was added, and the mixture was vigorously stirred. Illumination was provided with a 500 W Hg lamp with a 290 nm cutoff filter. As the authors observed, no linear dependency between concentration of MO and irradiation time occurred. Thus, it can be explained that the reduction rate is determined by

several factors, including the diffusion of the MO molecules in the solutions (the experiments were performed without stirring), surface charge effect and pH.

Considering the following assumptions: a) the greater part of the reduction takes place near the irradiation source (reaction zone), b) the reduction occurs very rapidly, so the concentration of MO in the reaction zone is nearly zero, then the dependency of the reduction rate on the diffusion effect can be described by the equation:

$$\frac{dc}{dt} = -kct^{-n} \quad (45)$$

where:  $c$  – concentration of MO,  $k$  – constant,  $t$  – time of irradiation,  $n$  – parameter related to the diffusion of the kinetic reaction (in real conditions its value is always lower than  $\frac{1}{2}$ ).<sup>71</sup>

The second important factor with an impact on the photoreduction of MO by ZnS is the presence in the solution of different ions. Under such conditions, these ions are absorbed on the surface of the semiconductor, which can accelerate, but also retard, the photodegradation process. Anions always act as inhibitors while cations, in most cases, cause the reaction rate to increase (especially at the beginning). The author gives several explanations of such behavior. The anions form a negative electric field around the ZnS particle while the cations can act as a trap for electrons. The latter situation may have a positive impact given a low concentration of cations.<sup>71</sup>

Finally, the influence of pH was investigated. The results indicate that the best conditions are obtained at pH levels higher than 4. At a lower pH the acid degradation of ZnS may occur:<sup>71</sup>



### 3.3 The basis of photodegradation on ZnS

According to IUPAC terminology, photocatalysis is defined as “change in the rate of a chemical reaction or its initiation under the action of ultraviolet, visible or infrared radiation in the presence of a substance and the photocatalyst that absorbs light and is involved in the chemical transformation of the reaction partners.”<sup>72</sup> Two main types of photocatalysis can be indicated: heterogeneous and homogeneous.

In the former case, the whole process can be split into five parts. First, reactants are transferred to the semiconductor-catalyst (1) and are absorbed on its surface (2). Then in the absorbed phase certain reactions occur (3), which are shown in detail in Figure 27. Finally, the products are desorbed (4) and removed from the interface region (5).<sup>73</sup> It should be emphasized that heterogeneous photocatalysis occurs on the phase boundary.

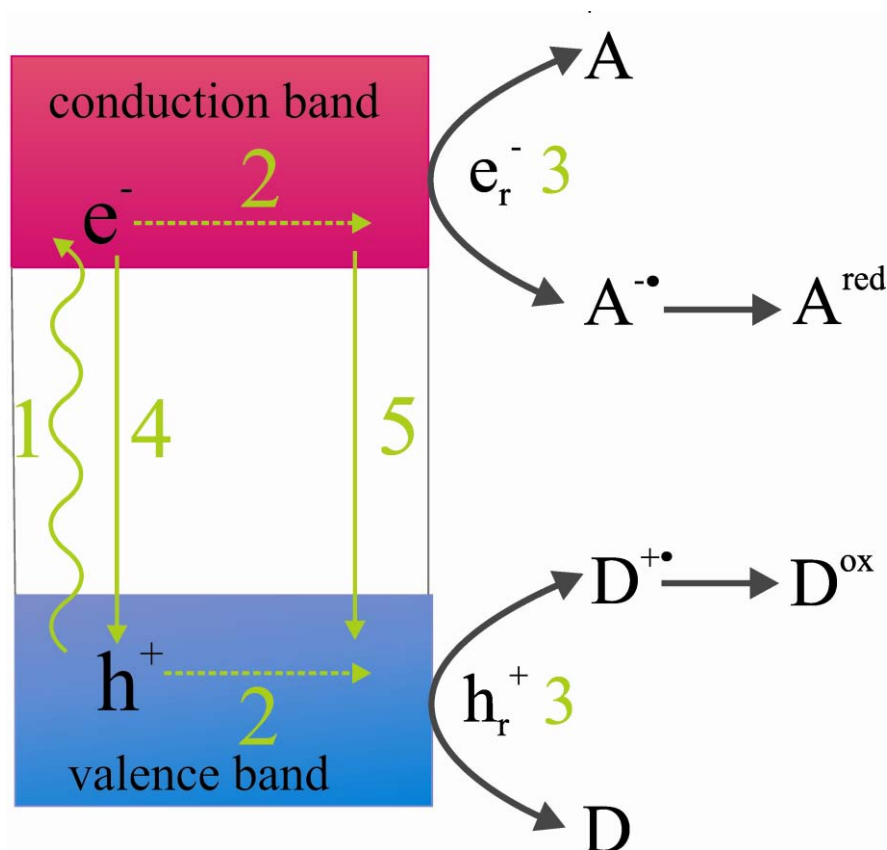


Figure 27. Schematic of the photocatalytic effect in a semiconductor

Through the absorption of the photon with energy equal or higher than the band gap in the semiconductor, the electron is excited to the conduction band, and in the valence band a hole is generated (1):



Then, the charge carriers can diffuse to the phase boundary (2) where they can take part in reduction or oxidation reactions (3) with electron acceptors (A) or donors (D) adsorbed on the surface of photocatalysts:



Unfortunately, electrons and holes can recombine, non-radiatively or radiatively (4,5), and the intermediate forms ( $\text{A}^{\cdot-}$ ,  $\text{D}^{\cdot+}$ ) can react with each other. Both of these processes are adverse because they reduce photocatalytic efficiency.<sup>73</sup>

As was previously mentioned, many factors can have an impact on photocatalysis. In the previous section only three of them were discussed; nevertheless, many more can be listed, for example:<sup>73</sup>

1. Mass of the catalyst: The initial rates of the reaction are proportional to the mass of the catalyst. Nevertheless, after exceeding a certain level of catalyst mass, the screening

effect starts to play a crucial role and in the situation described above this relationship cannot be assumed.

2. Wavelength and intensity of the radiations: it is obvious that to absorb the radiation the following condition needs to be met:  $h\nu \geq E_g$ . This provides some restraints on wavelength.
3. Concentration of the substrate: in photocatalysis the reaction rate ( $r$ ) depends on the concentration of substrate ( $C$ ) as follows:

$$r = k \left( \frac{KC}{1+KC} \right) \quad (50)$$

where  $k$  – the reaction rate constant,  $K$  – ratio of the absorption rate constant to desorption rate constant and  $C$  – concentration of the substrate  $S$ .

If the solution is very diluted, the first order reaction in relation to  $S$  will take place ( $r = kC$ ); otherwise the zero order reaction will occur ( $r = k$ ).

4. Temperature.
5. Presence of oxygen.
6. pH and the presence of ions: their influence was discussed in the previous section.

As can be observed, the photocatalysis process is affected by many factors. Thus, all of them need to be taken into account in the analysis of the results.

# **EXPERIMENTAL PART**

## **The goal of work**

The main goal of my work was to obtain new hybrid organic – inorganic materials and their detailed characterisation including structure determination, morphology, optical and thermal properties. The most frequently used synthesis technique is solvothermal route. However, in my opinion, the other synthesis methods, faster and cheaper, are possible (under reflux, using unstable substrates etc). Thus, alternative to solvothermal methods will be tested and compare. Furthermore, according to my best knowledge, the studies of hybrid materials were limited to compounds containing aliphatic amines only. Therefore, the use of the aromatic amines as the spacers may bring interesting and surprising results.

Hybrid organic- inorganic materials are promising compounds to application in optoelectronic and photocatalysis. Furthermore, they can be treated as the precursors for pure nanometric semiconducting aggregates. Therefore, their thermal decomposition (supported by microwave or chemical treatment) will be tested. Such procedure may result in formation of interesting semiconducting nanometric MQ aggregates with different optical properties than their bulk counterpart.

### Measurement conditions and parameters

In most cases, X-ray powder diffraction patterns (XRPD) were recorded using an X'PERT PRO MPD diffractometer. Depending on sample types and their requirements (amount, stability), either Bragg-Brentano or Debye-Scherrer geometry was used. To standardize the results, the same measurement conditions were maintained. Therefore, the incident and anti-scatter slits were  $1/4^\circ$  and  $1/2^\circ$ , respectively, and the beam mask was 10 mm. A  $\text{CuK}\alpha$  X-ray tube with working conditions 40 kV, 30 mA was used as a source of radiation. In the case of Bragg-Brentano geometry, the measurement range was from  $4^\circ$  to  $75^\circ 2\theta$ , while for Debye-Scherrer it was from  $4^\circ$  to  $85^\circ 2\theta$ . For both, the interpolated step size was  $0.02^\circ$ . A more detailed list of parameters of diffraction experiments is given in Table 11.

Table 11. Detailed information about measurement parameters

Parameters	Values of parameters
X-ray tube (wave length)	$\text{CuK}\alpha$ (1.540593 Å)
Incident beam slits	$1/4^\circ$
Incident beam mask	10 mm
Soller slits	0.04 rad
Anti-scatter	$1/2^\circ$
Monochromator	PW3122/00 (graphite)
Detector	X'Celerator
Capillary size	0.7 mm

Several samples were investigated using a Bruker D8 Advance diffractometer (Bruker AXS) working in Bragg-Brentano geometry. As a source of X-ray radiation a Co tube, operated at 30 kV and 25 mA, was used. The samples were scanned from  $20^\circ$  to  $75^\circ 2\theta$  with a step size of  $0.03^\circ$ . A fast position-sensitive detector, VANTEC 1, was employed.

Using an XRK chamber produced by Anton Paar, thermal analysis was performed. The heat rate was  $10^\circ\text{C}/\text{min}$ . After reaching the desired temperature, the sample was stabilized for 10 min and X-ray measurement was performed. The initial temperature was  $20^\circ\text{C}$ , whereas subsequent temperatures were  $100^\circ\text{C}$ ,  $200^\circ\text{C}$ ,  $300^\circ\text{C}$ , and so on up to  $800^\circ\text{C}$ . Samples were measured in air or helium atmospheres.

Simultaneous Thermogravimetry and Differential Scanning Calorimetry (TG-DSC) studies were performed on a computer-controlled STA 409 PC Luxx system. All samples were

investigated in air. The heating rate was 10 °C/min, the temperature range from 20 °C to 1000 °C.

Using a JEOL JSM-7500F scanning electron microscope, the morphology of the samples was investigated. The samples were placed on special brass stubs and covered with a thin layer of chrome. The images were obtained with an accelerating voltage of 15 kV. Furthermore, EDS analysis was performed (using the X-ray radiation generated in the samples).

UV-vis spectra were collected on a Shimadzu UV 2101 PC. This measurement was carried out at room temperature. As a “white standard”, BaSO<sub>4</sub> was used.

Chemical analysis was performed on a EuroVector EA 300 Elemental Analyzer.

## Hybrid organic-inorganic materials based on a ZnS semiconductor

### 5.1 Materials and synthesis

Zinc sulfate hydrate [ $\text{ZnSO}_4 \cdot 7\text{H}_2\text{O}$ ] was purchased from POCH S.A., Gliwice; thioacetamide [ $\text{CH}_3\text{CSNH}_2$ ], toluene [ $\text{C}_6\text{H}_5\text{CH}_3$ ], 1-aminopropane /denoted as (**1-ap**)/ [ $\text{C}_3\text{H}_7\text{NH}_2$ ], 1,2-diaminopropane /(**1,2-pda**)/ and 1,3-diaminopropane /(**1,3-pda**), (**pda**)/ [ $\text{C}_3\text{H}_6(\text{NH}_2)_2$ ] were purchased from Sigma-Aldrich. All reactants were used without prior purification.

In the course of my research a new synthesis method, under reflux, was utilized. This method does not require sophisticated equipment such as autoclaves and thus is inexpensive. Furthermore, synthesis time can be even several days shorter than in the routinely-used solvothermal technique. These unquestionable advantages make this synthesis method competitive with others. The original system which was used in my research is presented in Figure 28.



*Figure 28. A set of equipment for synthesis under reflux used in the synthesis of hybrid organic-inorganic materials*

All samples ( $(\text{ZnS})_n\text{1-ap}$ ,  $(\text{ZnS})_n\text{1,2pda}$  and finally  $\text{ZnS}(\text{pda})_{1/2}$ ) were obtained at atmospheric pressure at  $120\text{ }^\circ\text{C}$ . In the first step, three substrates — 10 mmol of hydrated zinc sulphate, 50 ml of toluene and 15 ml of appropriate amines — were combined. The mixture was boiled for 1 hour and then 20 mmol of thioacetamide was added. The resulting mixture was boiled under reflux for 12 h and finally cooled naturally to room temperature. In the final stage, the solution was washed with n-hexane and filtered. All syntheses using 1-ap, 1,2-pda and pda were carried out under the same conditions.

In cases involving small amounts of reagents, toluene is recommended as an inert medium for mass and heat transfer. Nevertheless, as was confirmed, all of the above compounds can be prepared using only amine as a solvent and substrate. In all syntheses zinc sulphate was the source of zinc atoms, thioacetamide of sulfur atoms.

The obtained materials are stable and do not decompose even after a long time in air. All three samples, after drying, take the form of a white grease. Nevertheless, even for sticky products, diffraction patterns with sharp, strong lines were obtained.

## 5.2 Characterization of $(\text{ZnS})_n\text{1-ap}$

The X-ray diffraction pattern of  $(\text{ZnS})_n\text{1-ap}$  is shown in Figure 29.

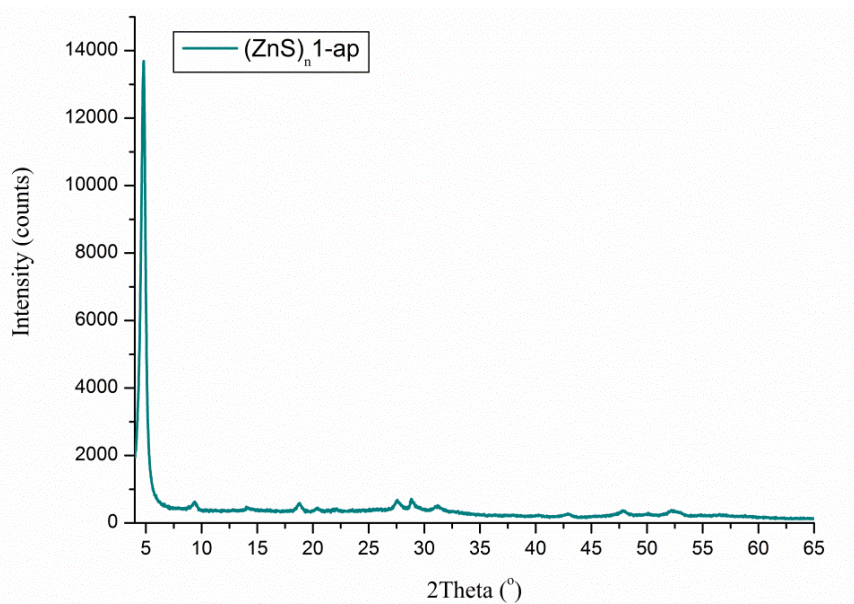


Figure 29. XRD-pattern of  $\text{ZnS}(1\text{-ap})$

As can be seen, in the XRD-pattern only the first maximum is strong and clearly visible. The others are weak and barely visible against the background. This is typical for layered compounds, which do not exhibit strong interaction between adjacent layers. Furthermore, based on the first peak position, the distance between the layers can be calculated, in this case  $\sim 18.7 \text{ \AA}$ . This value is consistent with the double length of 1-ap, suggesting that 2D hybrid organic-inorganic material was obtained.

Chemical analyses confirm this assumption. For  $(\text{ZnS})_n\text{1-ap}$  (n-number of semiconducting layers with the value of 1 or 2), the obtained (and calculated) data are: C – 21.06% (23.02%), H – 5.20% (5.79%), N – 7.75% (8.95%), S – 21.25% (20.48%). Despite a slight but noticeable excess of amine, those results correspond closely to the model of a structure in which double semiconducting layers are attached from both sides by amines (Figure 30).

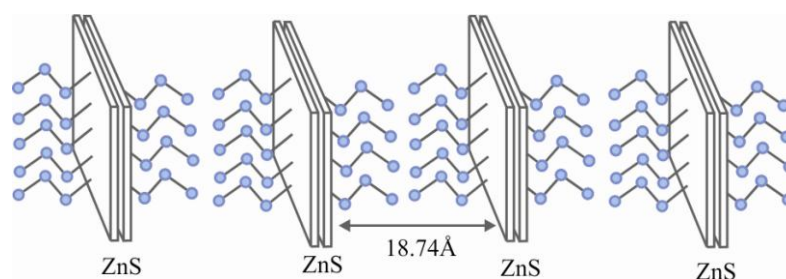


Figure 30. Model of the 2D-  $Zn_2S_2(1-ap)$  – double semiconductor layer ( $n=2$ )

Based on this model, the disorder between the ZnS sheets can be explained. Namely, amines connected to the semiconductor layers interact with amines of adjacent layers. Those interactions between hydrophobic amine tails ( $-C_2H_5-CH_3$ ) cause weak ordering in the structure.

The thermal behavior of  $(ZnS)_n1-ap$  was investigated using XRD (XRD vs. temperature). The measurement was performed in air. The results are presented in Figure 31.

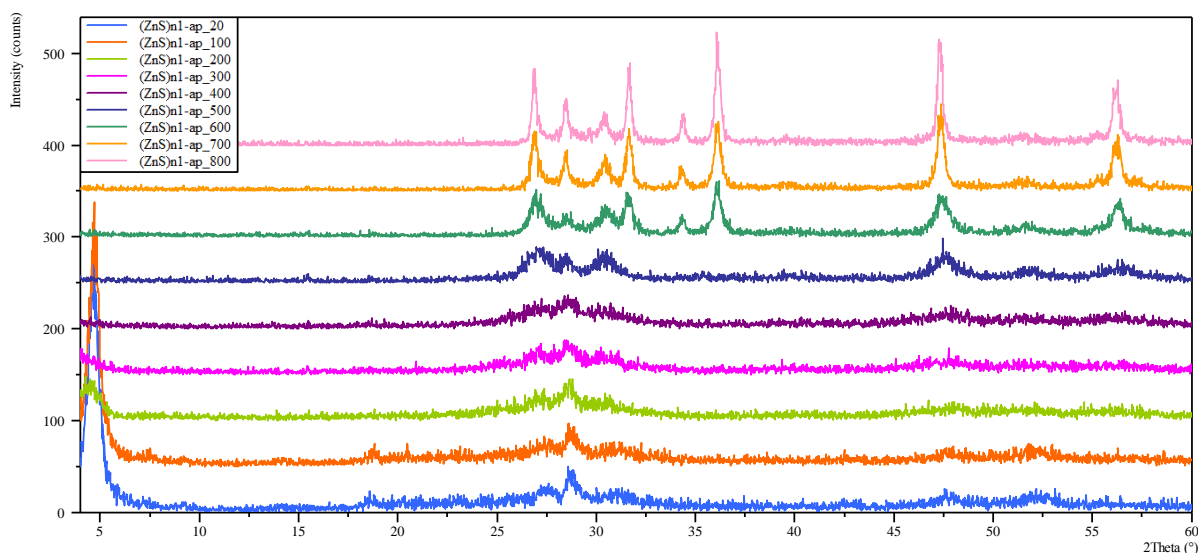


Figure 31. XRD patterns of  $(ZnS)_n1-ap$  obtained during heat treatment in air

At 300 °C, the studied compound decomposed to ZnS (PDF 04-003-4429). Then at 600 °C the second phase ZnO (PDF 04-008-8198) appeared, with both remaining up to 800 °C. The presence of ZnO is caused by the oxidation of fine-crystalline ZnS. The detailed investigation of diffraction patterns show that crystalline size increases with an increase in temperature. This change can be estimated using a Scherrer equation implemented in the diffractometer software HighScore:

$$L_C = \frac{K \cdot \lambda}{\vartheta \cdot \cos \theta} \quad (51)$$

where:  $L_C$  is the crystallite diameter,  $K$  is a constant equal to 0.9,  $\lambda$  is the X-ray wave length 1.54178 Å,  $\vartheta$  is the halfwidth and  $\theta$  is the diffraction angle. The instrumental broadening was evaluated using silicon powder (NIST-640d).

The size of ZnS crystallites in the temperature range 300 °C to 600 °C increases from about 70 Å to 100 Å. Between 600 °C and 700 °C, the crystallites increase to 200 Å, thus essentially doubling their size. Finally, ZnS crystallites achieve a size of about 270 Å. The same behavior in response to rising temperature can be observed in the case of the second phase, ZnO. At 600 °C, the size of crystallites is 200 Å, then increases to about 460 Å (800 °C).

The morphology of the sample was investigated using a scanning electron microscope. The obtained images are presented in Figure 32. As can be seen, the crystallites' surface is heterogeneous, and the edges are ragged. The aggregates of  $(\text{ZnS})_n\text{I-ap}$  are quite large, with diameters about 50  $\mu\text{m}$  (one of them is shown in Figure 32A).

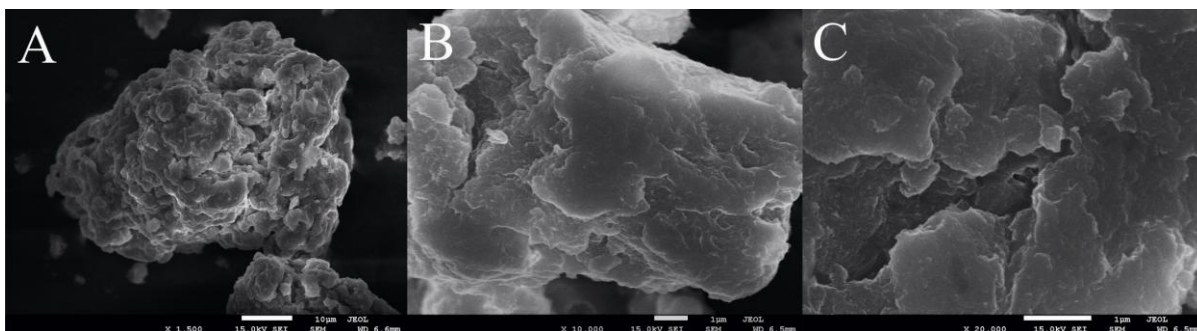


Figure 32. SEM images of  $(\text{ZnS})_n\text{I-ap}$

Given the specific arrangement of semiconductor layers and amines, the optical properties should be very interesting. The obtained UV-vis spectra is presented in Figure 33.

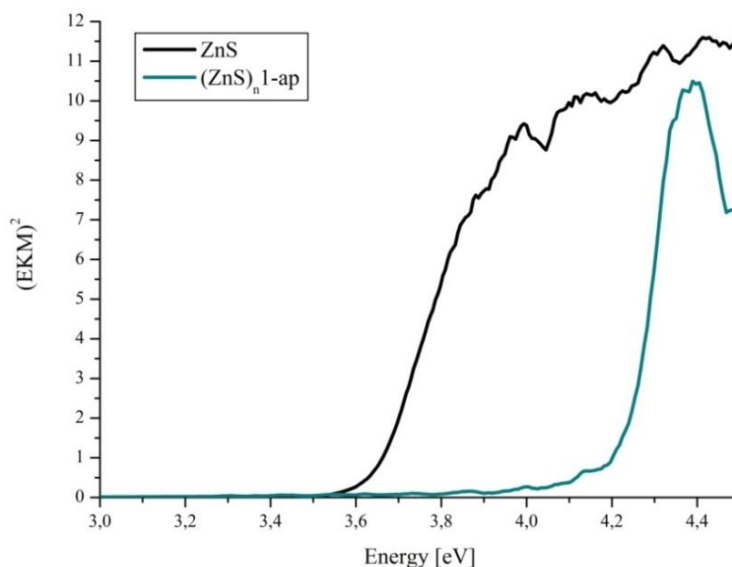


Figure 33. UV-vis spectra of  $(\text{ZnS})_n\text{I-ap}$ , compared with spectrum of ZnS

In comparison to bulk phase ZnS, the band gap changes from 3.6 eV to 4.25 eV. This phenomenon is caused by the quantum confinement effect discussed earlier. In this case, the blue shift is 0.65 eV. This value is close to that obtained for 2D-(MQ)<sub>2</sub>L hybrid materials.

Therefore, based on this result, a structure with a double semiconductor layer can be postulated as more likely. Also the Urbach tail is visible.

### 5.3 Characterization of $(\text{ZnS})_n1,2\text{-pda}$

The obtained (and calculated) results of chemical analysis of  $(\text{ZnS})_n1,2\text{-pda}$  are given below: C – 22.93% (21.00%), H – 6.41% (5.87%), N – 15.03% (16.33%), S – 16.49% (18.69%). These data suggest that, as in the previous case, a double semiconducting layer has been obtained.

The crucial role in the formation of hybrid compounds with a specific dimensionality is played by molecules of amines. Namely, in the case of 1,2-diaminepropane (1,2-pda), theoretically two linking (amine) groups are sufficient to form the expected 3D layered materials. However, this is difficult due to the position of these groups, which are connected to the first and second carbon atoms in the chain. This location can be a serious obstacle in the formation of 3D hybrid structures. Nevertheless, a 2D hybrid compound can be successfully obtained if one or both amine groups create covalent bonds with the Zn atoms from the same layer.

The XRD pattern of  $(\text{ZnS})_n1,2\text{-pda}$  is presented in Figure 34. The presence of three reflections — (001)  $d_1$  – 8.96 Å, (002)  $d_2$  – 4.47 Å, (003)  $d_3$  – 2.97 Å — suggest that this material also has a layered structure. Furthermore, the second phase of nano-ZnS was probably obtained in the samples, as suggested by the presence of three barely visible peaks [(111), (220), (311)]. These peaks indicate the zinc blende structure.

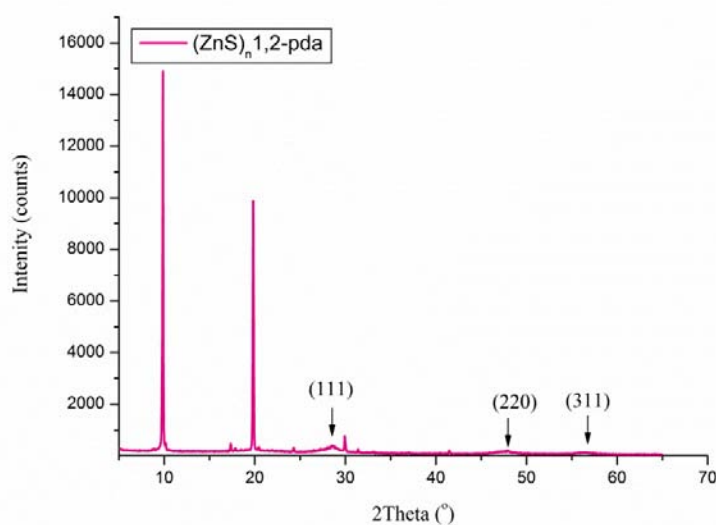


Figure 34. XRD pattern of  $(\text{ZnS})_n1,2\text{-pda}$

The thermal study (XRK) of  $(\text{ZnS})_n1,2\text{-pda}$  was carried out in air. The results (Figure 35) show that this compound is stable up to 200 °C. Above this temperature, 2D hybrid material is

decomposed and at 300 °C only ZnS (PDF 01-007-8756) is present. Between 500–600 °C crystallites of ZnS are oxidized to ZnO (PDF 04-007-9805), which is stable at 800 °C. As in the case of  $(\text{ZnS})_n1\text{-ap}$ , the crystallite size was calculated using the Scherrer formula implemented in the diffractometer software (HighScore). The size of crystallites of the ZnS phase increases slightly from 35 Å (300 °C) to about 50 Å (500 °C). As a result of oxidation of ZnS at 600 °C, crystallites of ZnO almost 400 Å are created, growing to about 500 Å at 800 °C.

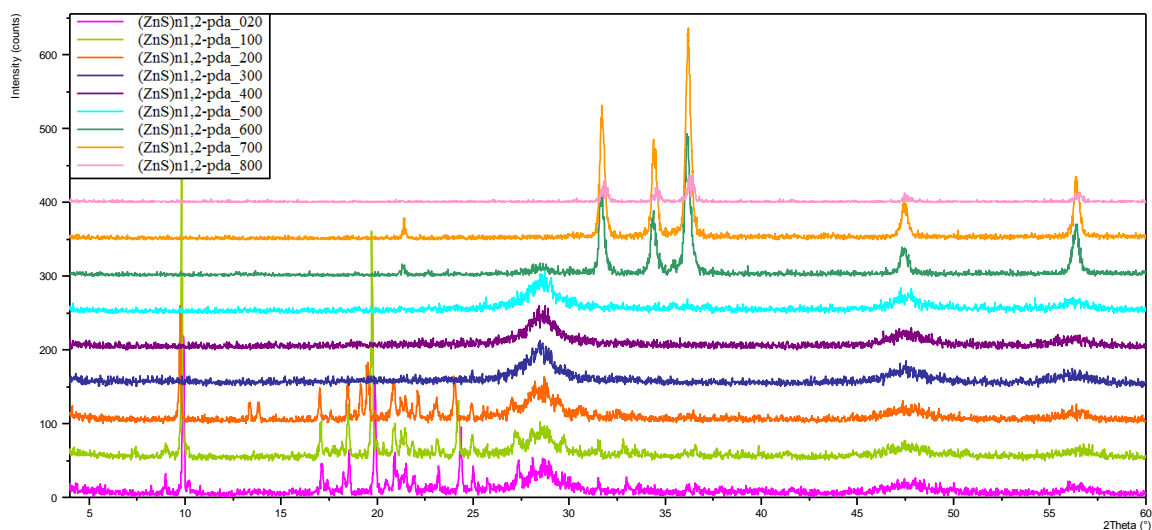


Figure 35. XRD patterns of  $(\text{ZnS})_n1\text{-ap}$  obtained during heat treatment in air

The SEM images of  $(\text{ZnS})_n1,2\text{-pda}$  are presented in Figure 36. As can be seen, the compound assumes the form of a rectangular prism. The crystallites possess regular edges and layered structures which are clearly visible in the pictures. In the sample, the second phase, morphologically different, can also be observed, characterized by irregular edges and a heterogeneous surface (Figure 36 E, F).

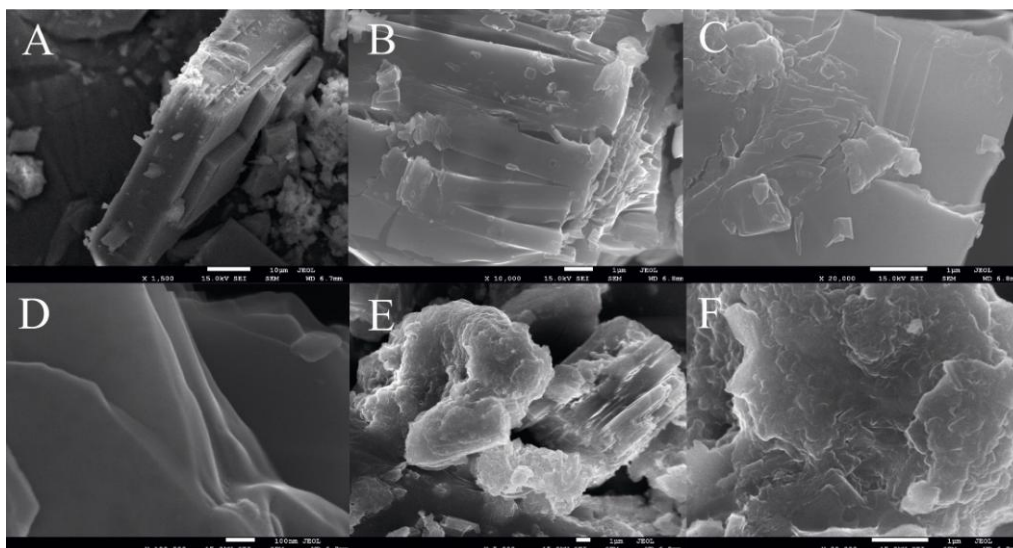


Figure 36. SEM images of  $(\text{ZnS})_n1,2\text{-pda}$

Finally, the optical properties of the samples were investigated. The obtained UV-vis spectra is depicted in Figure 37.

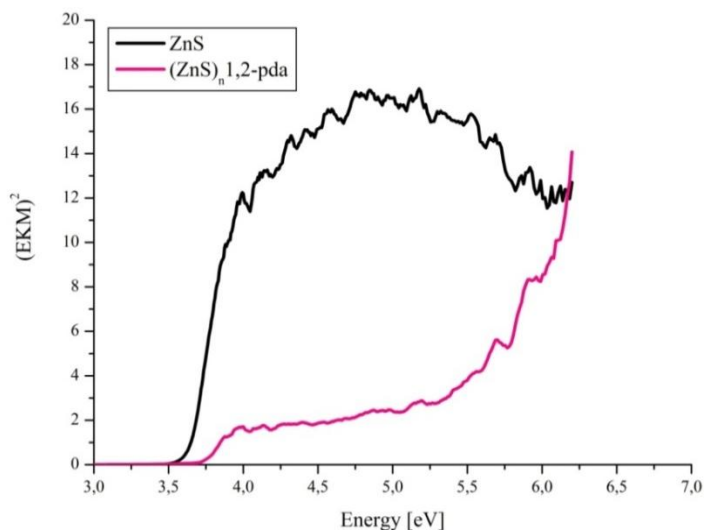


Figure 37. UV-vis spectra of  $(\text{ZnS})_n1,2\text{-pda}$ , compared with spectrum of ZnS

The analysis of UV-vis spectra suggests that the two-phase sample was obtained. For the first phase, the calculated band gap occurs about  $\sim 3.6$  eV, the typical value for bulk ZnS. The evaluation of the second band gap is very difficult. From the above UV-vis spectra, only an approximate value can be extrapolated. It appears higher than 4.5 eV but, due to the presence of the second phase, this is probably an overestimate. Nevertheless, one can speculate that this band gap is related to the second phase, which is hybrid organic-inorganic material type  $(\text{ZnS})_n1,2\text{-pda}$ . It should be emphasized that estimation of the second band gap in this area of energy is questionable. However, in my opinion, this second increase (band gap) in UV-vis spectra can be related to the second phase, which presence in the sample is confirmed by the XRD pattern.

#### 5.4 Characterization of $\text{ZnS}(\text{pda})_{1/2}$

In the third case, 1,3-diaminopropane was used as an organic template, which enabled the acquisition of 3D hybrid organic-inorganic material type  $\text{ZnS}(\text{pda})_{1/2}$ . Based on the XRD pattern, the crystal structure was determined. First, the cell parameters were found, using an exhaustive program working in the parameter space and implemented in the PROSZKI<sup>74</sup> package. Then, global optimization techniques (FOX program)<sup>27</sup> and direct methods (EXPO program)<sup>26</sup> were used to find the position of heavy atoms and atoms of the organic part. Finally, the program JANA2006<sup>28</sup> (employing the Rietveld method) was applied. For refining the background, zero shift, unit cell and profile parameters (including asymmetry), the LeBail fitting procedure was used. Next, the positions of atoms were refined using isotropic thermal

displacement parameters. Geometric restraints (bond lengths, angles and constraints on atomic displacement parameters) were utilized to prevent instability in the refinement. Figure 38 depicts the Rietveld refinement plot.

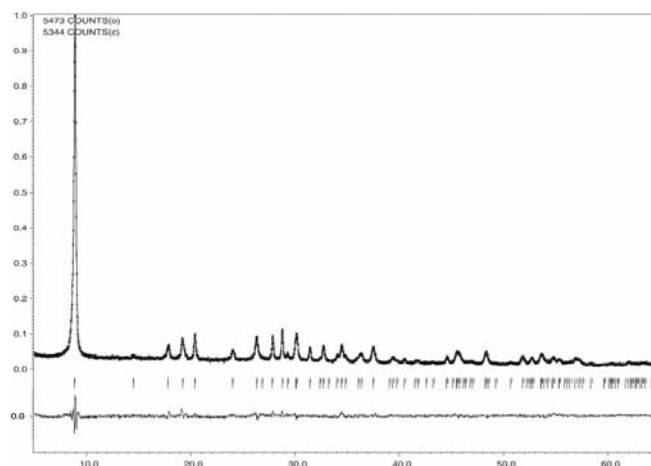


Figure 38. Rietveld plot of  $\text{ZnS}(\text{pda})_{1/2}$

The diffraction pattern consists of a few sharp peaks. The first maximum is the strongest and corresponds to the distance between the ZnS layers equal to 9.87 Å.

Detailed crystallographic data of  $\text{ZnS}(\text{pda})_{1/2}$  are presented in Table 12, atomic parameters in Table 13 and selected interatomic distances in Table 14.

Table 12. Crystallographic data for  $\text{ZnS}(\text{pda})_{1/2}$

Empirical formula	$\text{Zn}_2 \text{S}_2 \text{C}_3 \text{N}_2 \text{H}_{10}$
Formula weight	269
System	Orthorhombic
Space group	$C m c 2_1 (36)$
a [Å]	19.899(2)
b [Å]	6.3980(8)
c [Å]	6.1951(7)
V [Å <sup>3</sup> ]	788.6(3)
R <sub>p</sub> [%]	6.61
R <sub>wp</sub> [%]	8.51

Table 13. Atomic parameters

Atom	x	y	z	U <sub>iso</sub>
Zn(1)	0.2888(4)	0.1547(3)	0.8762 <sup>*</sup>	0.006(3)
S(1)	0.3068(8)	0.191(3)	1.255(3)	0.014(9)
N(1)	0.3779(2)	0.3332(12)	0.7103(11)	0.045(17)
C(3)	0.4334(18)	0.2238(7)	0.8382(8)	0.045(17)
C(4)	0.50000	0.2801(11)	0.7327(2)	0.045(17)
H(1) <sub>C(3)</sub> <sup>**</sup>	0.42686	0.07524	0.83142	0.0536
H(2) <sub>C(3)</sub>	0.43305	0.27324	0.98449	0.0536
H(1) <sub>C(4)</sub>	0.50000	0.42571	0.69537	0.0536
H(2) <sub>C(4)</sub>	0.50000	0.23291	0.58559	0.0536
H(1) <sub>N(1)</sub>	0.38041	0.29660	0.57533	0.0536
H(2) <sub>N(1)</sub>	0.37648	0.46459	0.74632	0.0536

Table 14. Selected interatomic distances

Atom1	Atom2 symm.code*	d(Å)
Zn(1)	S(1)	2.385(18)
Zn(1)	S(1) $-x+1/2, -y+1/2, z-1/2$	2.270(18)
Zn(1)	S(1) $x, -y, z-1/2$	2.366(17)
Zn(1)	N(1)	2.347(6)
N(1)	C(3)	1.5285(7)
N(1)	H(1) <sub>N(1)</sub>	0.870(7)
N(1)	H(2) <sub>N(2)</sub>	0.870(7)
C(3)	C(4)	1.5215(7)
C(3)	H(1) <sub>C(3)</sub>	0.960(5)
C(3)	H(2) <sub>C(3)</sub>	0.960(5)
C(4)	H(1) <sub>C(4)</sub>	0.960(8)
C(4)	H(2) <sub>C(4)</sub>	0.960(8)

ZnS(pda)<sub>1/2</sub> belongs to the 3D class of hybrid organic-inorganic materials. The layers of ZnS (wurtzite type) are linked by organic spacers, which in this case are 1,3-pda molecules. The inorganic layers are constructed in a specific way: the network topology is 6<sup>3</sup>. In this situation, the sulfur and zinc atoms are arranged alternately and create slightly deformed honeycomb rings. This layer is presented in Figure 39.

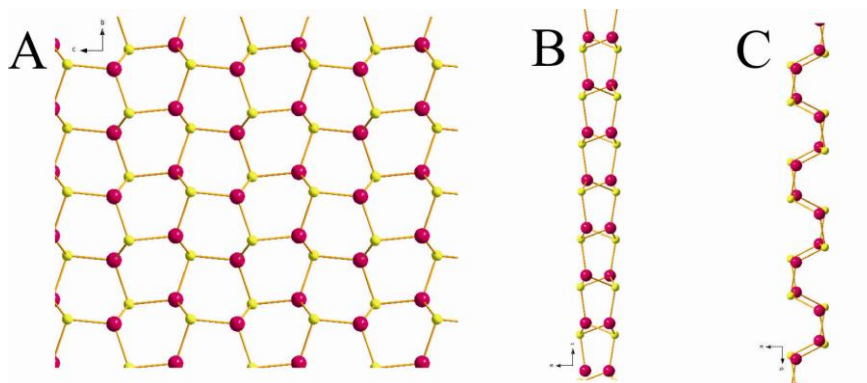


Figure 39. Layer of ZnS **A**) view along the *a*-axis **B**) view along the *b*-axis **C**) view along the *c*-axis; (Zn-pink, S-yellow)

The zinc atom is tetrahedrally coordinated. It is bonded to three sulfur atoms and one nitrogen atom originating from the amino group. The covalent bond between zinc and nitrogen ensures the stability of the structure. The immediate neighborhood of the metal atom and the means of connection with the organic part are presented in Figure 40.

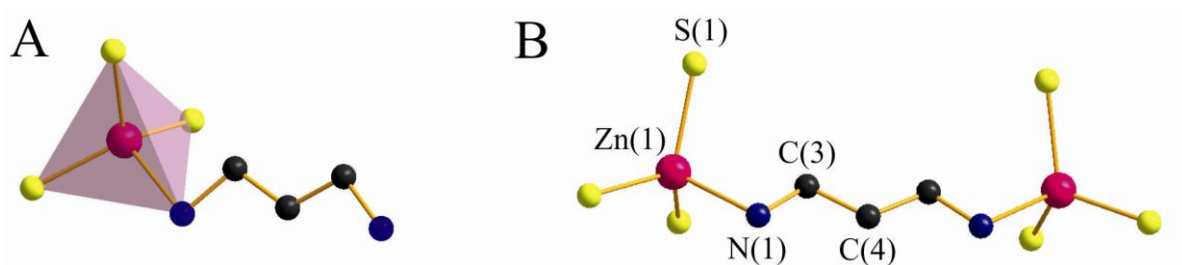


Figure 40. **A**) Tetrahedral coordination of Zn atom, **B**) amine as a linker between two zinc atoms; (Zn-pink, S-yellow, N-blue, C-black)

$\text{ZnS}(\text{pda})_{1/2}$  is a layered material in which adjacent semiconductor ZnS slabs are linked by amines. This lamellar structure is presented in Figure 41.

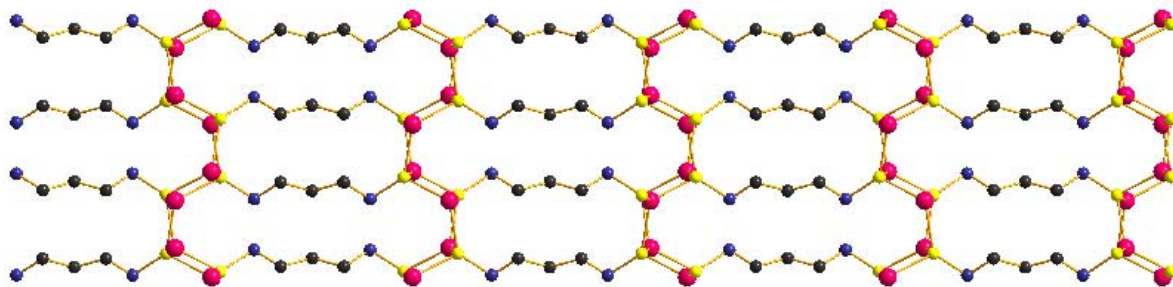


Figure 41. Layered structure of  $\text{ZnS}(\text{pda})_{1/2}$ ; (Zn-pink, S-yellow, N-blue, C-black)

The results of chemical analysis are consistent with the results of crystal structure solution and confirm that one amine is linked to two adjacent semiconducting layers. The obtained (and calculated) results are: C – 16.84% (13.39%), H – 4.60% (3.75%), N – 11.70% (10.41%), S – 21.01% (23.84%). As can be seen, an excess of amine is present in the sample. Probably 1,3-pda was absorbed on the crystalline surface.

In the case of  $\text{ZnS}(\text{pda})_{1/2}$ , powder diffraction measurements as a function of temperature in air and helium atmospheres were carried out. Both results are shown in Figures 42 and 43. The size of the grains was calculated using HighScore software and the TOPAS program.<sup>75</sup>

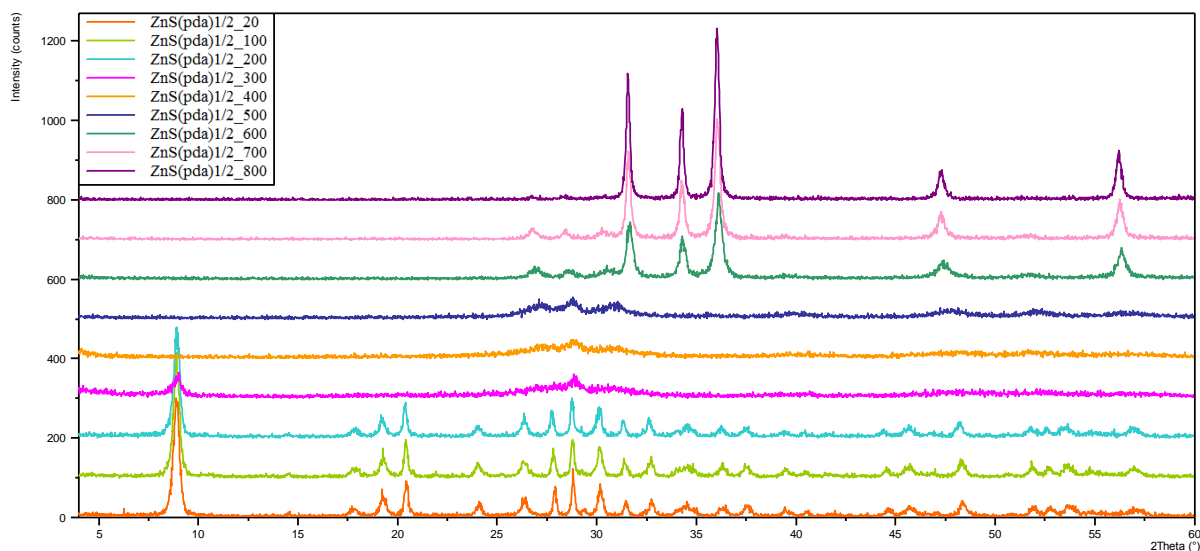


Figure 42. XRD patterns of  $\text{ZnS}(\text{pda})_{1/2}$  obtained during heat treatment in air

In the case of measurement in air, at 300 °C the studied compound decomposed to ZnS (PDF 10-0434). At 600 °C ZnO (PDF 79-0208), as the second phase, appeared as a result of the oxidation of fine-crystalline ZnS. At a low temperature range (about 300–400 °C) the estimated size of the grains is about 150 Å. At higher temperatures, 600–700 °C, the size of ZnS aggregates increases to about 220 Å. This result was confirmed by TOPAS. The

estimated grain size was similar to that obtained using diffractometer software and no microstrains were observed.

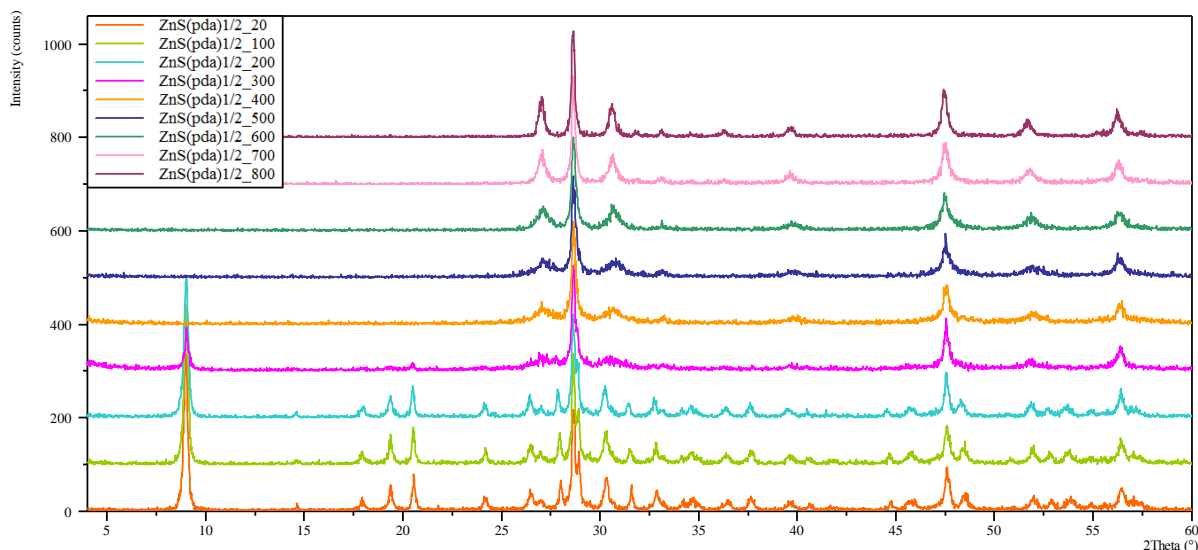


Figure 43. XRD patterns of  $\text{ZnS}(\text{pda})_{1/2}$  obtained during heat treatment in helium

The helium atmosphere prevented the oxidation of ZnS to ZnO. At 300 °C, a ZnS phase of the wurtzite type is observed. This phase remains stable at higher temperatures, 400–800 °C (PDF 04-006-2556). The size of crystalline grains increases along with growing temperature, from 180 Å to 380 Å. Furthermore, another kind of ZnS-sphalerite can be found in the sample (PDF 01-071-5971). Nevertheless, it occurs in small amounts, and the size of the grains does not change, remaining about 300 Å.

The thermal stability of  $\text{ZnS}(\text{pda})_{1/2}$  was also studied using TG/DSC. The measurement was performed in air. The result is shown in Figure 44.

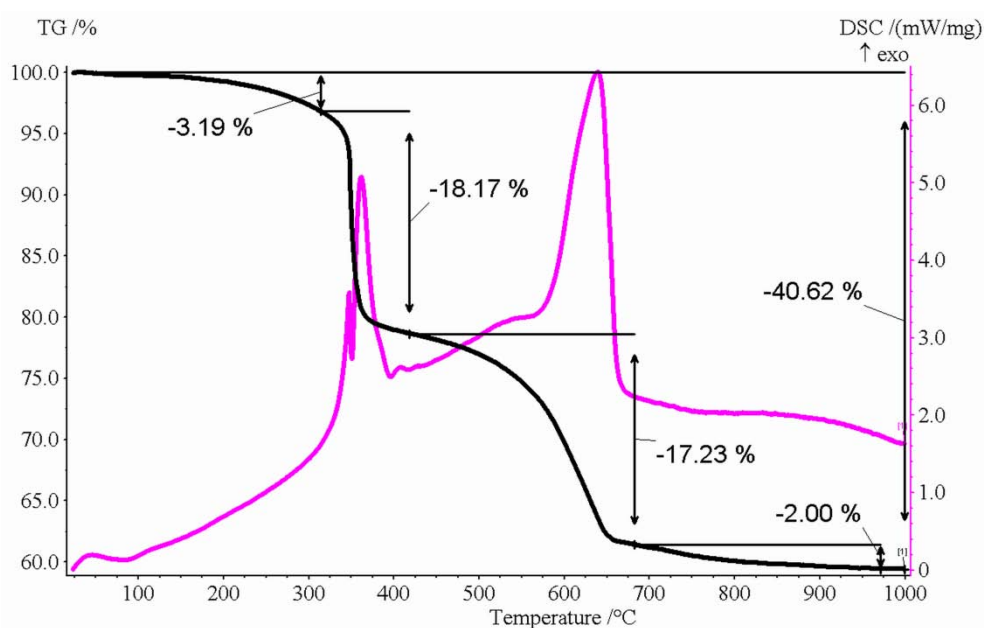


Figure 44. TG/DSC analysis of  $\text{ZnS}(\text{pda})_{1/2}$

The first small loss of weight (3.19%) is connected with weakly-bonded amines or amines adsorbed at the surface. Part of this could be also the water presented in the sample. At the temperature range 300 °C to 400 °C, the next loss of weight (18.17%) is observed, corresponding to the amine release. The last (400–700 °C) is related to oxidation and removal of sulfur. The final product is ZnO, and the total loss of weight is 40.62%.

As can be observed from SEM images (Figure 45), crystallites of  $\text{ZnS}(\text{pda})_{1/2}$  possess very uniform morphology, namely, prisms based on triangles, with a height in the range of 50–100 nm. The thickness of the prism is about 10 nm.

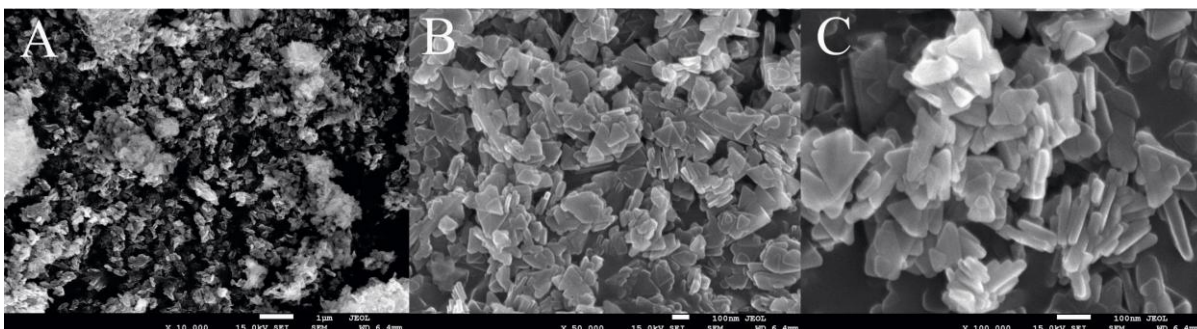


Figure 45. SEM images of  $\text{ZnS}(\text{pda})_{1/2}$

Due to the separated semiconductor monolayers present in the structure and correlated with the quantum confinement effect,  $\text{ZnS}(\text{pda})_{1/2}$  is characterized by interesting optical features, which were studied using UV-vis spectroscopy. Based on the obtained spectra (Figure 46), the band gap of  $\text{ZnS}(\text{pda})_{1/2}$  was calculated as equal to 4.76 eV. In comparison to bulk ZnS, it varied by about 1.1 eV.

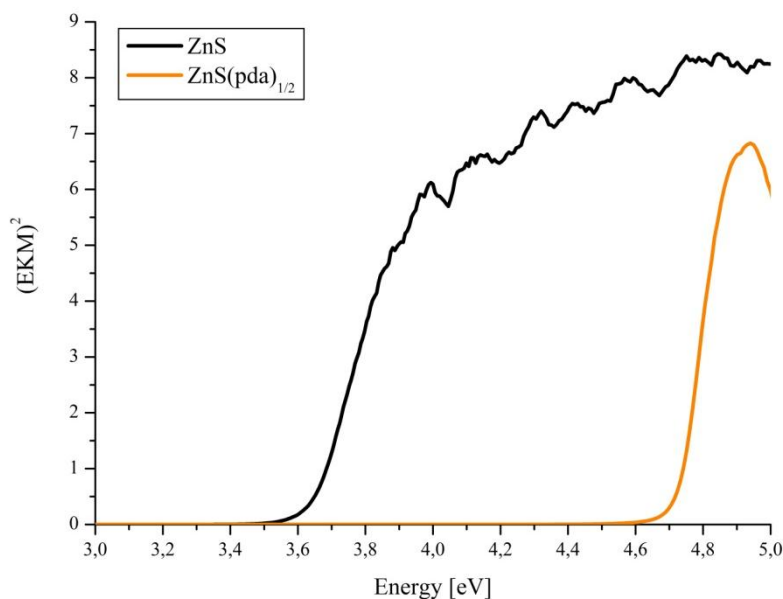


Figure 46. UV-vis spectra of  $\text{ZnS}(\text{pda})_{1/2}$

### 5.5 Comparison of $(\text{ZnS})_n\text{1-ap}$ , $(\text{ZnS})_n\text{1,2-pda}$ and $\text{ZnS(pda)}_{1/2}$

The hybrid materials discussed in this thesis are built of an inorganic part which comprises semiconductors and an organic part which comprises amines. As shown in the above studies, the dimensionality (1D, 2D or 3D) of the obtained compounds is strongly related to the type of spacers used. In my research, three different amines were applied as linkers: 1-ap, 1,2-pda and 1,3-pda (Figure 47).

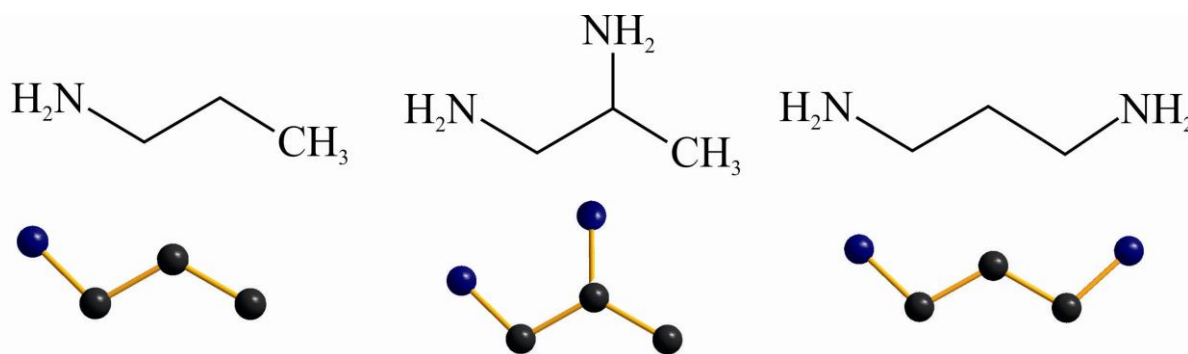


Figure 47. Amine used in synthesis: 1-aminopropane (1-ap), 1,2-propanediamine (1,2-pda), 1,3-propanediamine (1,3-pda), respectively

In the case of 1-ap, which has only one linking group (amine group), a 2D structure was obtained. Each organic molecule was connected to inorganic slabs through one covalent bond, created between a nitrogen atom and a zinc atom. For this type of amine it should also be possible to synthesize 1D hybrid materials. Nevertheless, probably because of reaction conditions (temperature, pressure), only the 2D phase was observed.

The second amine, 1,2-diaminepropane, possesses two amine groups which in principle are able to form two covalent bonds with metal atoms in neighboring semiconductor layers. As it turns out, however, this is still difficult because of the position of those amino groups (first and second carbon atom in the chain). The research shows that, as in the previous case, 2D compounds were obtained. The obtained sample is contaminated; the second phase present in the sample is ZnS.

Finally, in the case of 1,3-diaminepropane, 3D hybrid organic-inorganic material was synthesized. Two factors related to the structure of the amine have an impact on this: 1) the presence of two amino groups and 2) their availability (both were terminal amino groups, located at the first and third carbon atom in the chain). For  $\text{ZnS(pda)}_{1/2}$ , the crystal structure solution was found using powder data.

The thermal stability of all obtained compounds is quite similar. Regardless of the type of spacer and dimensionality, obtained hybrid materials decomposed to ZnS at 300 °C. Only in the case of  $\text{ZnS(pda)}_{1/2}$  was a small quantity of hybrid material still present in the sample. The

size of crystallites increases along with increasing temperatures. In air, ZnO appears as the result of the oxidation of ZnS.  $(\text{ZnS})_{\text{n}1\text{-ap}}$  and  $\text{ZnS}(\text{pda})_{1/2}$  decomposed to ZnS of the wurtzite type. This is a stable phase. It is interesting because the bulk phase of the wurtzite form of ZnS is a high-temperature form which is stable above 1000 °C.

Due to the potential application of hybrid materials in optoelectronics, their electronic and optical properties seem especially interesting. Therefore, they were investigated using UV-vis spectroscopy, which shows that all materials exhibit the quantum confinement effect, revealing itself in the changing band gap energy. A shift towards shorter wavelengths, the so-called blue shift, is observed. In the case of  $\text{ZnS}(\text{pda})_{1/2}$  the shift is 1.1 eV, while for  $(\text{ZnS})_{\text{n}1\text{-ap}}$  about 0.6 eV. The evaluation of the band gap energy in the case of  $\text{ZnS}(1,2\text{-pda})$  is difficult due to the occurrence of the second phase in the sample.

To conclude, three different hybrid materials were prepared using synthesis under reflux. To the best of my knowledge, heretofore only the solvothermal technique had been used to synthesize hybrid materials. In comparison, the reflux method takes much less time, which is undoubtedly its great advantage. For  $\text{ZnS}(\text{pda})_{1/2}$  the crystal structure solution was performed.

## Hybrid composites of the types $Zn_xCd_{1-x}Se(pda)_{1/2}$ and $ZnS_xSe_{1-x}(pda)_{1/2}$

### 6.1 Materials and synthesis

Zinc sulphate hydrate [ $ZnSO_4 \cdot 7H_2O$ ], cadmium sulphate hydrate [ $CdSO_4 \cdot 8H_2O$ ] and sulfur [S] were purchased from POCH S.A. Gliwice, while selenium [Se] and 1,3-diaminopropane (pda) [ $C_3H_6(NH_2)_2$ ] were bought from Sigma-Aldrich. All of the above reagents were used without further purification.

As in the previous chapter, most compounds were synthesized under reflux, mostly because this method is shorter than the routinely-used solvothermal technique. Nevertheless, for three samples, solvothermal methods were applied, because, as it turned out, the reaction conditions under reflux were insufficient to create mixed-hybrid compounds (mainly based on Se and S).

#### 6.1.1 Synthesis of $Zn_xCd_{1-x}Se(pda)_{1/2}$

To synthesize  $Zn_xCd_{1-x}Se(pda)_{1/2}$ , zinc sulphate hydrate and cadmium sulphate hydrate were used in stoichiometric proportions. Five syntheses were performed with  $ZnSO_4 \cdot 7H_2O$  in the following amounts: 10 mmol (1), 7.5 mmol (2), 5 mmol (3), 2.5 mmol (4) and 0 mol (5), with  $CdSO_4 \cdot 8H_2O$  in quantities complementary to 10 mmol. In each synthesis 10 mmol of selenium and 30 ml of 1,3-diaminepropane were used. All substrates were boiled under reflux to 12 h, then cooled naturally to room temperature. The precipitate was filtered and washed with water. The products were brown greases. Samples (1) and (5) do not require 12 h of synthesis: in these two cases, even 2 hours sufficed to obtain well-formed hybrid materials.

#### 6.1.2 Synthesis of $ZnS_xSe_{1-x}(pda)_{1/2}$

$ZnS_xSe_{1-x}(pda)_{1/2}$  compounds were obtained using zinc sulfate hydrate (as a source of zinc atoms); sulfur and selenium elements were applied in amounts complementary to 10 mmol ( $x - 0$  (1), 0.25 (6), 0.5 (7), 0.75 (8), 1 (9)). 1,3-pda in a quantity of 20 ml was used as a substrate and at the same time as the reaction medium. Materials (1), (7) and (9) were obtained under reflux over 12 h. However, samples (6) and (8) were prepared using solvothermal methods (the autoclave used in the syntheses is shown in Figure 48). The temperature was 160 °C. All products were washed with water. Samples (6–8) had the consistency of grease and a brown color. Sample (9) was white. All samples (1–9) required prolonged drying.



Figure 48. Autoclave used for synthesis

## 6.2 Characterization of hybrid material of the type $Zn_xCd_{1-x}Se(pda)_{1/2}$

All compounds of the type  $Zn_xCd_{1-x}Se(pda)_{1/2}$  (1–5) were characterized using XRPD. The obtained diffraction patterns are presented in Figure 49.

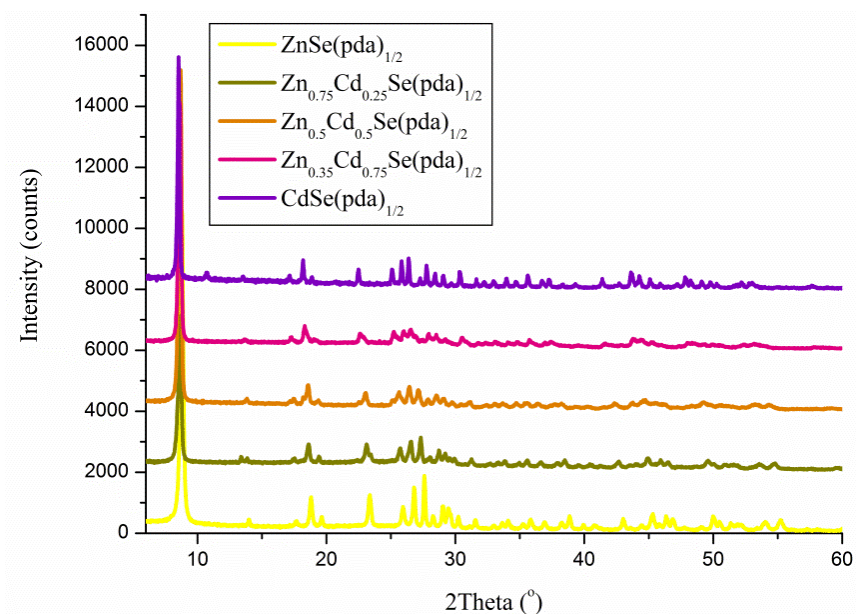


Figure 49. XRD patterns of  $Zn_xCd_{1-x}(pda)_{1/2}$

As can be seen, along with the increase in percentage of Cd atoms (and at the same time as the decrease in Zn atoms) in the inorganic slabs, the peak positions were slightly shifted towards a lower value of  $2\theta$ . This is correlated with an increase in the unit cell parameters as the result of the incorporation of atoms with larger diameters. The above-mentioned

phenomenon proves simply that mixed semiconducting layers were obtained. In more detailed studies, cell parameters were found using the WinPLOTR program package.<sup>76</sup> As it turned out, all materials crystallized in orthorhombic crystal system. Furthermore, the cell parameters of  $ZnSe(pda)_{1/2}$  and  $CdSe(pda)_{1/2}$ , which were calculated based on diffraction patterns, are quite similar to the values found by J. Li's group.<sup>29,36</sup> This indicates the creation of 3D hybrid organic-inorganic compounds. The obtained cell parameters are shown in Table 15.

Table 15. Indexing results of powder X-ray diffraction of  $Zn_xCd_{1-x}Se(pda)_{1/2}$  ( $x = 0, 0.25, 0.5, 0.75, 1$ )

Compound	a (Å)	b (Å)	c (Å)	V(Å <sup>3</sup> )
$ZnSe(pda)_{1/2}$	20.002(8)	6.6352(7)	6.4473(7)	855.6(5)
$Cd_{0.25}Zn_{0.75}Se(pda)_{1/2}$	20.094(7)	6.6794(9)	6.5027(9)	872.6(5)
$Cd_{0.50}Zn_{0.50}Se(pda)_{1/2}$	20.256(9)	6.7355(8)	6.5719(9)	896.4(6)
$Cd_{0.75}Zn_{0.25}Se(pda)_{1/2}$	20.652(8)	6.8714(7)	6.7318(6)	955.1(6)
$CdSe(pda)_{1/2}$	20.666(7)	6.8917(8)	6.7523(9)	961.5(5)

Surprisingly, the cell parameters do not change continuously along with changes in the compositions of the semiconductor layers. Significant discontinuities in cell volumes can be observed between  $Cd_{0.50}Zn_{0.50}Se(pda)_{1/2}$  and  $Cd_{0.75}Zn_{0.25}Se(pda)_{1/2}$ , as is clearly visible in Figure 50.

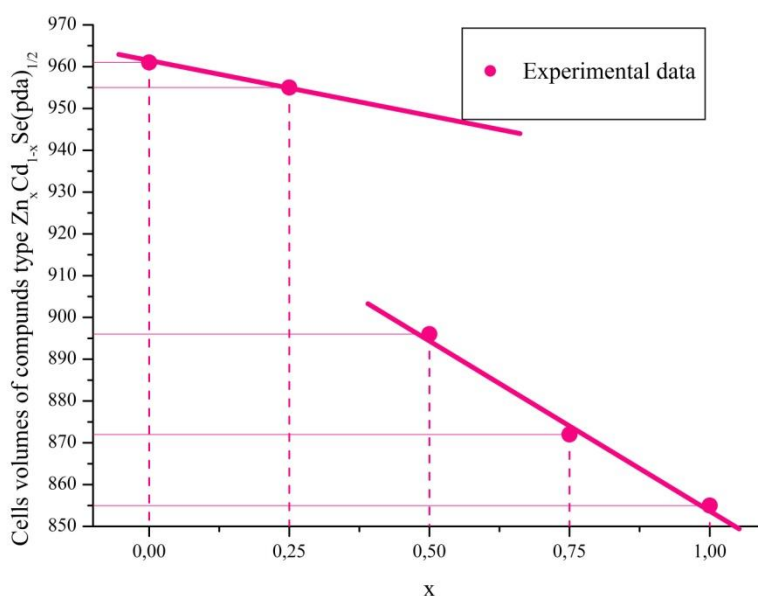


Figure 50. Obtained volumes as a function of the amount of zinc and cadmium ( $x = 0, 0.25, 0.5, 0.75, 1$ ) in compounds type  $Zn_xCd_{1-x}Se(pda)_{1/2}$  (pink line – calculated volumes)

The analyses of diffraction patterns also indicate that all samples are pure monophase. On the other hand, the chemical analyses show a slight excess of amines in those materials. The obtained (and calculated) results are presented below; for compounds (1): 15.39% (9.93%), H – 3.82% (2.78%), N – 10.37% (7.72%), (2) C – 16.95% (9.33%), H – 4.34% (2.61%), N – 11.53% (7.25%) (3) C – 9.71% (8.79%), H – 2.67% (2.46%), N – 7.20% (6.84%), (4) C –

20.58% (8.32%), H – 5.18% (2.33%), N – 13.35% (6.46%) (5) C – 11.74% (7.86%), H – 3.81% (2.21%), N – 8.25% (6.13%). Such discrepancies between the results obtained from XRD and those obtained from chemical analysis are difficult to explain. Probably amine was absorbed on the surface of the samples; additionally, the samples were greasy and required prolonged drying.

Hybrid organic-inorganic layered materials are scientifically interesting objects mainly due to their optical properties. The incorporation into the semiconducting layers of different metal atoms should modify the band gap, which thus makes them even more noteworthy. The optical properties of mixed-hybrid materials were investigated using UV-vis spectroscopy. The results are presented in Figure 51. To make the drawings clearer, only the mixed samples are present, i.e.  $Zn_{0.25}Cd_{0.75}Se(pda)_{1/2}$ ,  $Zn_{0.5}Cd_{0.5}Se(pda)_{1/2}$ ,  $Zn_{0.75}Cd_{0.25}Se(pda)_{1/2}$ . For  $ZnSe(pda)_{1/2}$  and  $CdSe(pda)_{1/2}$ , band gaps were calculated and are shown in Table 16.

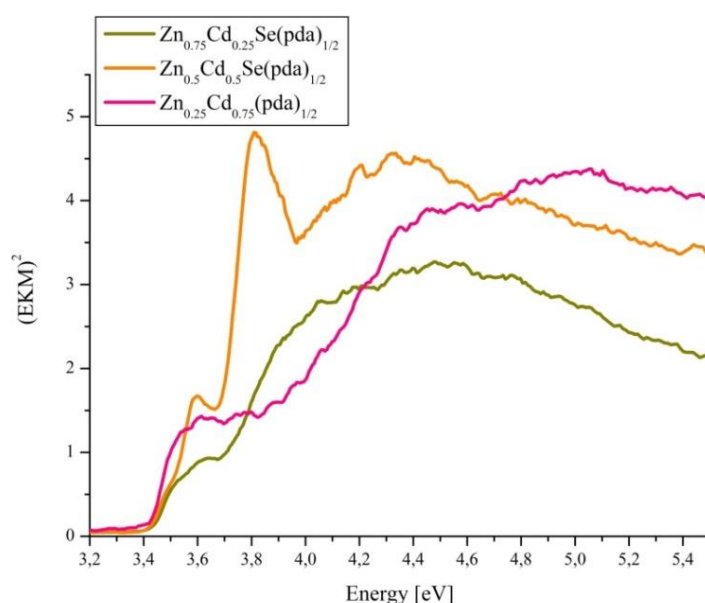


Figure 51. UV-vis spectra of  $Zn_xCd_{1-x}Se(pda)_{1/2}$  compounds

In comparison to homogenous hybrid materials ( $ZnSe(pda)_{1/2}$  and  $CdSe(pda)_{1/2}$ ) the mixed compounds possess two different band gaps. The first increases along with a decrease in percentage of Cd atoms, whereas in the second the dependence is reversed (the changes are very small, in the margin of standard deviation).

Table 16. The calculated band gaps of hybrid materials of the type  $Zn_xCd_{1-x}Se(pda)_{1/2}$

Compound	BG <sub>1</sub> [eV]	BG <sub>2</sub> [eV]
$ZnSe(pda)_{1/2}$	3.99	-
$Zn_{0.75}Cd_{0.25}Se(pda)_{1/2}$	3.43	3.55
$Zn_{0.5}Cd_{0.5}Se(pda)_{1/2}$	3.42	3.65
$Zn_{0.25}Cd_{0.75}Se(pda)_{1/2}$	3.41	3.70
$CdSe(pda)_{1/2}$	3.38	-

Unexpectedly, contrary to the changes in cell parameters (for which the biggest shift was between  $Zn_{0.5}Cd_{0.5}Se(pda)_{1/2}$  and  $Zn_{0.25}Cd_{0.75}Se(pda)_{1/2}$ ) the largest difference in band gaps is observed between compounds  $Zn_{0.75}Cd_{0.25}Se(pda)_{1/2}$  and  $ZnSe(pda)_{1/2}$ .

The thermal properties of compounds of the type  $Zn_xCd_{1-x}Se(pda)_{1/2}$  were studied using two methods: XRD vs. temperature (XRK) and TG/DSC. The first was performed in a helium atmosphere, the second in air. The analyses were carried out only for three samples, (1), (3) and (5), which are, in my opinion, representative of the whole group.

### 6.2.1 Thermal properties of $ZnSe(pda)_{1/2}$

In Figure 52, XRD patterns vs. temperature are depicted.

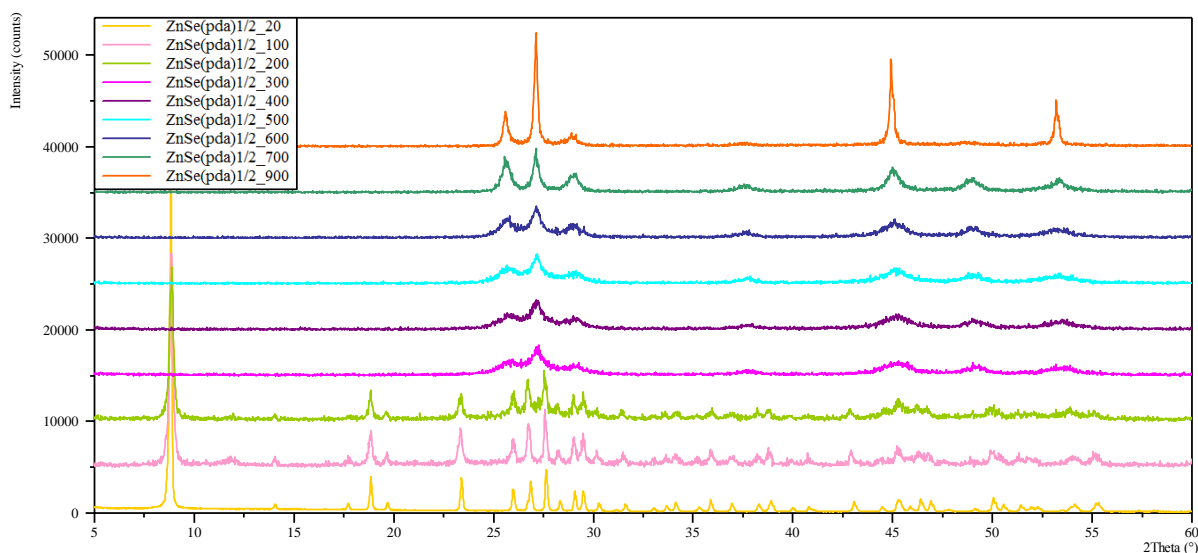


Figure 52. XRD patterns as a function of temperature of  $ZnSe(pda)_{1/2}$  obtained in helium atmosphere

$ZnSe(pda)_{1/2}$  decomposes between 200–300 °C. At 300 °C, pure ZnSe (PDF 04-004-5646) is observed. It is stable to 600 °C, when a new phase of ZnSe (PDF 04-004-5647) arises. However, the second phase occurs in smaller quantities than the previous one. Along with the increase in temperature, the size of crystallites increases. At 300 °C, the estimated size of the grains is about 160 Å. For crystallites obtained in the temperature range 400–700 °C, the size of ZnSe increases from 180 Å to 260 Å and at 800 °C reaches 470 Å. Crystallite size was calculated for the main phase ZnSe (PDF 04-004-5646).

As was mentioned above, the thermal behavior of the samples were also studied using TG/DSC. The result obtained for  $ZnSe(pda)_{1/2}$  (Figure 53) shows that the compound is stable to 300 °C. This is consistent with the data obtained in XRK (XRD as a function of temperature).

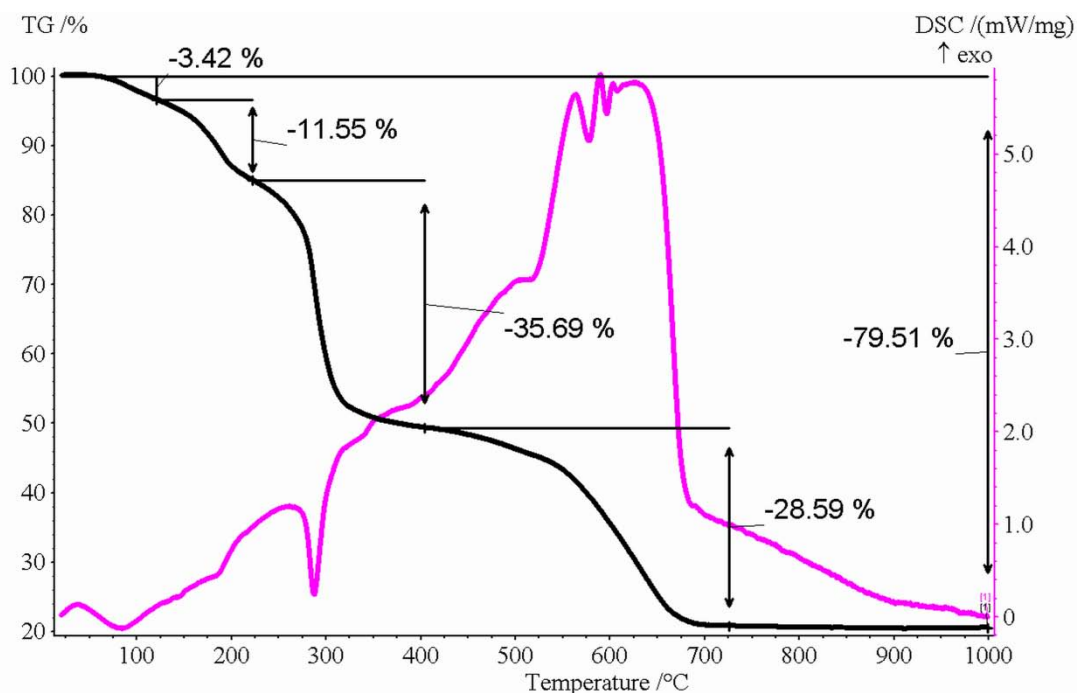


Figure 53. TG/DSC analysis for  $ZnSe(pda)_{1/2}$

Between 20–300 °C three weight losses, equaling 25.59% of the total, are clearly visible. They are correlated with water on the sample and with the weak-bonded amines on the crystalline surface (this result is confirmed by chemical analysis, which also indicates an excess of amine). Next, amine incorporated in the structure is released, which in turn, is connected to a 17.55% weight loss (the calculated mass change corresponding to the release of one molecule of amine is 20%). Finally, Se is oxidized and released. Total weight loss is 67.73%. ZnO remains as the only phase. These results were confirmed by XRPD measurements, which were performed using the sample after heating.

### 6.2.2 Thermal properties of $Zn_{0.5}Cd_{0.5}Se(pda)_{1/2}$

XRPD measurements as a function of temperature were carried out in a helium atmosphere (Figure 54). The studied material  $Zn_{0.5}Cd_{0.5}Se(pda)_{1/2}$  decomposes to  $Zn_{0.56}Cd_{0.44}Se$  (PDF 04-005-3557) through a release of amines at 300 °C. As it turns out, this phase is stable up to 800 °C. However, the size of the crystallites changes along with the temperature increase. At 300 °C, grain size is about 90 Å, while at temperatures between 400–500 °C, it increases from 120 Å to 150 Å. Then, between 600–700 °C, grain size progressively increases, from 290 Å to 400 Å. At last, at 800 °C, it reaches a value of 500 Å. These results confirm the formation of a mixed layer, because hybrid materials decompose to doped-type compounds ( $Zn_{0.56}Cd_{0.44}Se$ ). Furthermore, the proportion of metal atoms (Zn to Cd) are quite similar to those established through synthesis.

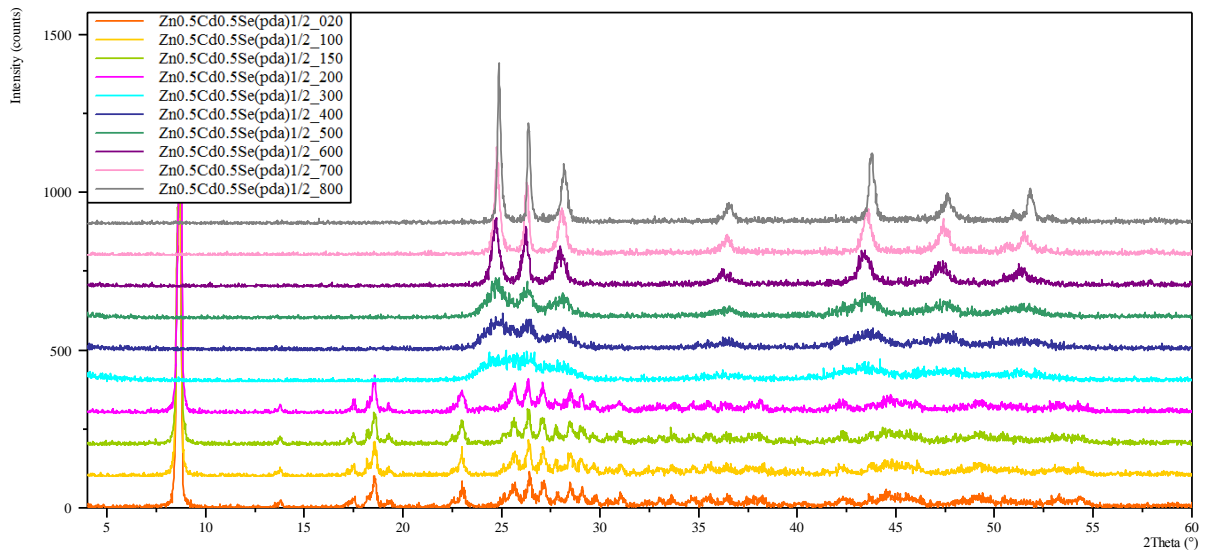


Figure 54. XRD patterns at the function of temperature of  $Zn_{0.5}Cd_{0.5}Se(pda)_{1/2}$  obtained in helium atmosphere

In Figure 55, the TG/DSC analysis for  $Zn_{0.5}Cd_{0.5}Se(pda)_{1/2}$  is presented. The measurement was carried out in air.

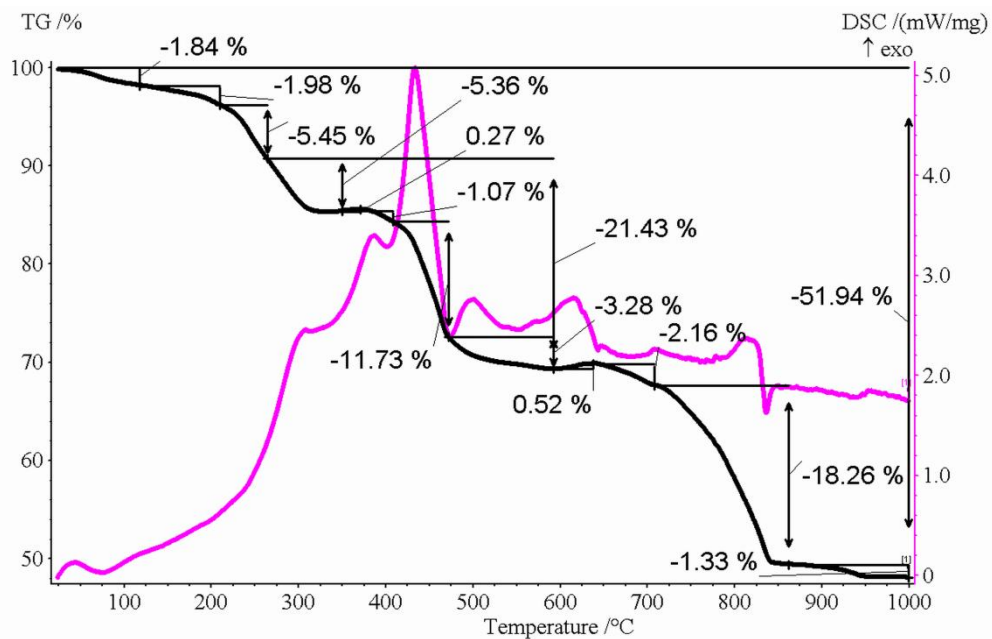


Figure 55. TG/DSC analysis for  $Zn_{0.5}Cd_{0.5}Se(pda)_{1/2}$

In the temperature range 100–300 °C, three weight losses are observed. They may correspond to the removal of amines which are adsorbed at the crystalline surface and water present in the structure. The following mass change, 21.43% (250–600 °C), is related to the release of amines which are linked to semiconductor slabs. Next, Se is probably oxidized and released, as observed in the temperature range 600–850 °C. The weight loss which corresponds to this step is 18.26%. The total loss of mass is 51.94%. The final products after TG-DSC analysis are CdO and ZnO. Powder X-ray diffraction measurement performed for the products confirms these findings.

### 6.2.3 Thermal properties of $CdSe(pda)_{1/2}$

The investigated material is stable to 300 °C, which is consistent with the previously investigated compounds. As a consequence of amine release, at 400 °C only CdSe (PDF 04-001-7283) is presented. This phase does not change at higher temperatures, 400–800 °C; however, the size of grains increases. At 300 °C, the estimated size of crystallites is about 210 Å; at a temperature range of 400–700 °C, about 215 Å. Finally, at 800 °C, the size of grains rapidly increases to 430 Å. Figure 56 shows XRD patterns as a function of temperature.

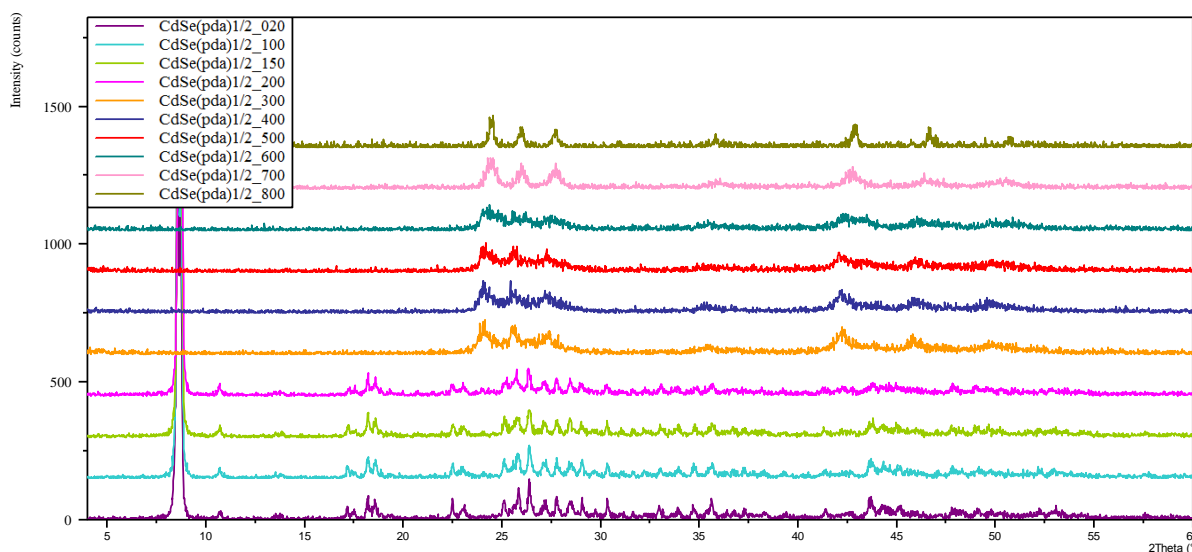


Figure 56. . XRD patterns as a function of temperature of  $CdSe(pda)_{1/2}$  obtained in helium atmosphere

The TG/DSC analysis was performed in air (Figure 57).

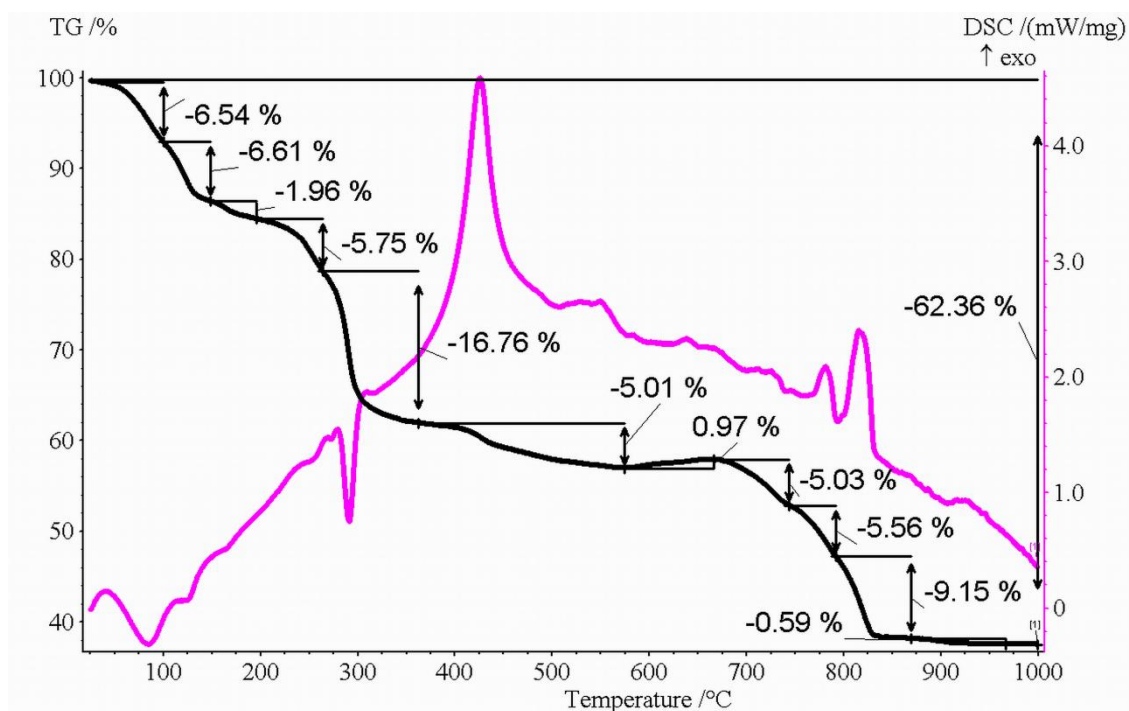


Figure 57. TG/DSC analysis for  $CdSe(pda)_{1/2}$

The first weight losses may correspond to the evaporation of weak-bonded amines absorbed on the crystalline surface and surface water. The following two (5.75% and 16.76%) losses of weight correspond to the removal of amine incorporated between semiconductor slabs. Selenium [Se] is oxidized and released from the structure in the succeeding steps. The total mass loss in the TG-DSC analysis is 62.36%. The final product is cadmium oxide (CdO).

#### 6.2.4 SEM and EDS analysis for $Zn_xCd_{1-x}Se(pda)_{1/2}$ compounds

The morphology of all samples was investigated using scanning electron microscopy. In Figure 58, SEM images of  $ZnSe(pda)_{1/2}$  are depicted.

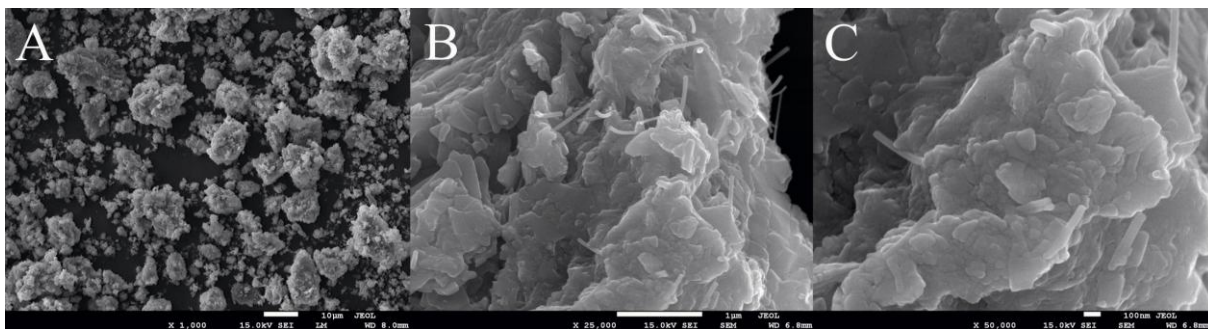


Figure 58. SEM images of  $ZnSe(pda)_{1/2}$

As can be seen, this hybrid material is composed of two morphologically different types of crystallites: layers and needles. The surface of the obtained layers is ragged and rough, but the edges are quite regular. Its thickness is in the range of 100–200 nm. The ratio of the surface to the thickness seems large. The second type of crystallite, needles, occurs as a minority phase. Its diameter is about 50 nm.

In Figure 59,  $Zn_{0.75}Cd_{0.25}Se(pda)_{1/2}$  is presented. It is a layered material with homogenous surface and quite regular smooth edges. The mean thickness of the layers is about 100 nm.

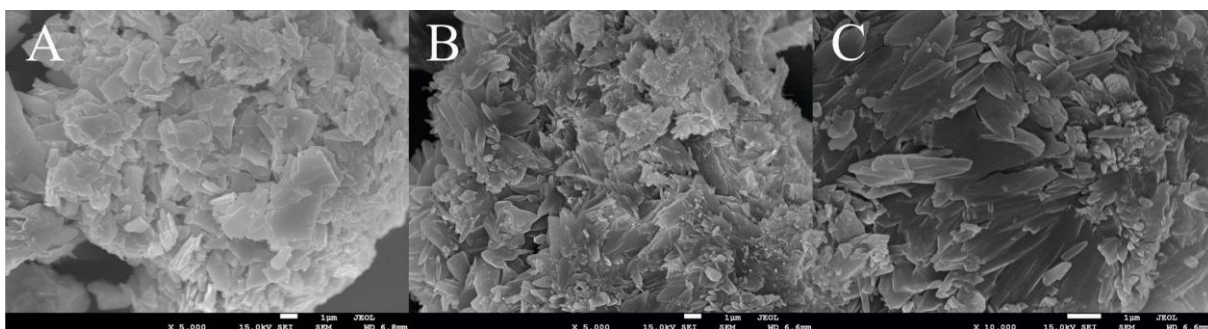


Figure 59. SEM images of  $Zn_{0.75}Cd_{0.25}Se(pda)_{1/2}$

In the sample of  $Zn_{0.5}Cd_{0.5}Se(pda)_{1/2}$  layers are well developed and surfaces are smooth; however, edges are irregular. The thickness of obtained crystallites is in the range of 100 nm to 0.5  $\mu\text{m}$ . The SEM images of this sample are presented in Figure 60.

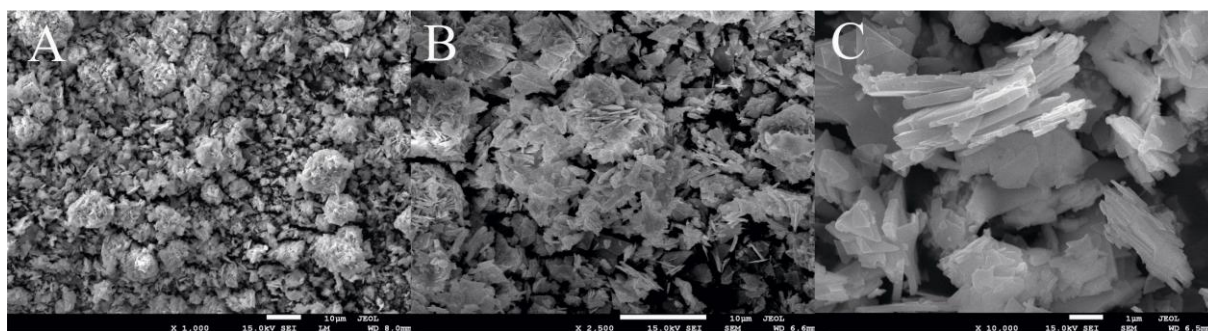


Figure 60. SEM images of  $Zn_{0.5}Cd_{0.5}Se(pda)_{1/2}$

$Zn_{0.25}Cd_{0.75}Se(pda)_{1/2}$  (Figure 61) is also a layered material with a thickness of about 10 nm. The surface of these slabs is homogenous and the edges are regular.

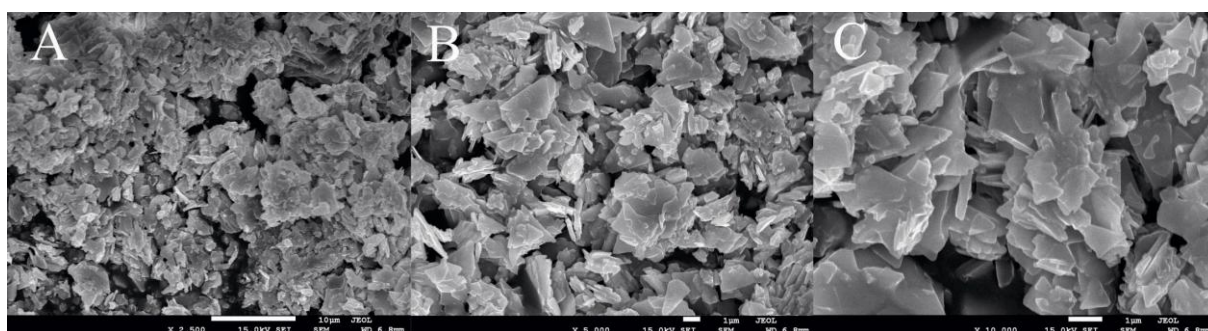


Figure 61. SEM images of  $Zn_{0.25}Cd_{0.75}Se(pda)_{1/2}$

Hybrid material  $CdSe(pda)_{1/2}$  is composed of one type of layered crystallites, which differ in size. The thicknesses of obtained prisms are about 100 nm. The obtained images are presented in Figure 62.

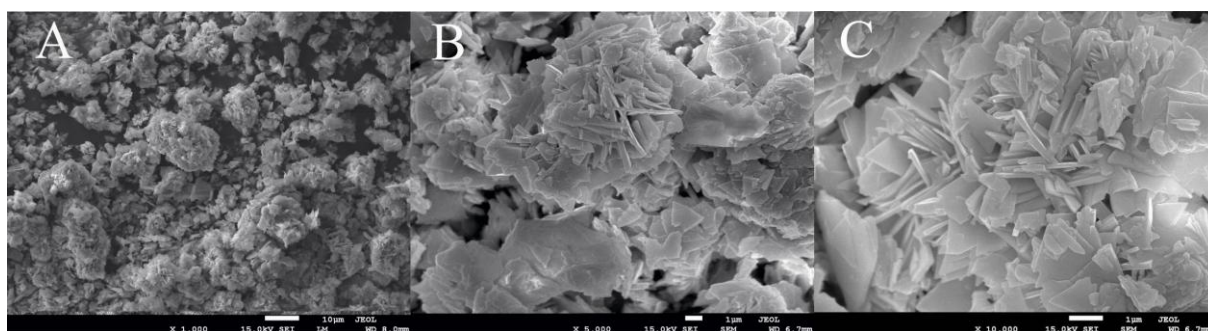


Figure 62. SEM images of  $CdSe(pda)_{1/2}$

As can be seen, all obtained hybrid organic-inorganic materials of  $Zn_xCd_{1-x}Se(pda)_{1/2}$  type are composed of platy crystallites. They differ in size and thickness. The most distinctive in the whole group is  $ZnSe(pda)_{1/2}$ , in which two types of crystallites occur. It is also the most heterogeneous in terms of morphology (the surface and edges of crystallites are irregular).

To confirm that mixed hybrid materials were obtained, an EDS analysis was performed. The results show that the desired compounds were obtained. For  $Zn_{0.5}Cd_{0.5}Se(pda)_{1/2}$ , the obtained

result is 51.8% Zn atoms and 48.2% Cd atoms. In Figure 63, the surface of the analyzed sample is shown. Areas scanned during EDS analysis are marked as rectangles.

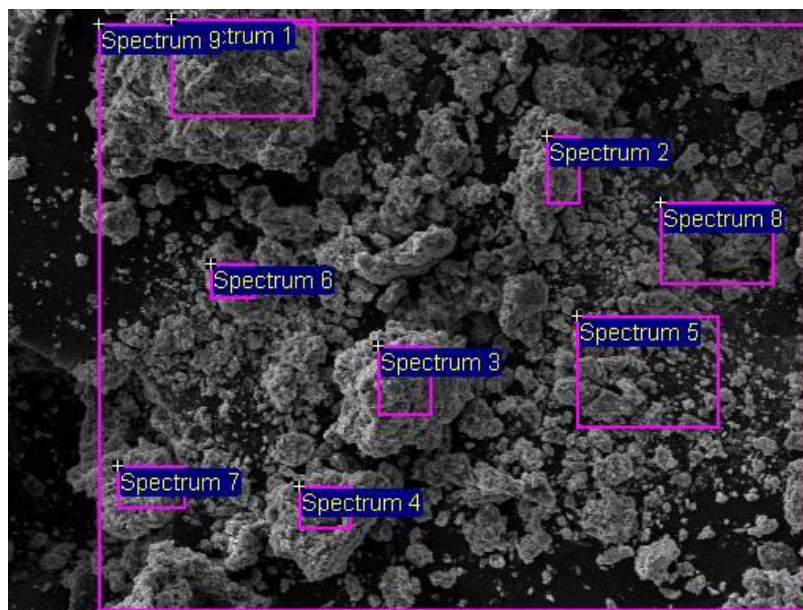


Figure 63. The data collection area of  $Zn_{0.5}Cd_{0.5}Se(pda)_{1/2}$

In the cases of  $Zn_{0.75}Cd_{0.25}Se(pda)_{1/2}$  and  $Zn_{0.25}Cd_{0.75}Se(pda)_{1/2}$  also, the percentage of Zn and Cd atoms is close to the relative amounts of Zn and Cd salts used in the synthesis.

### 6.3 Characterization of hybrid material of the type $ZnS_xSe_{1-x}(pda)_{1/2}$

Compounds of the type  $ZnS_xSe_{1-x}(pda)_{1/2}$  were investigated using XRD methods. The results confirm that as in the previous case, mixed layers were obtained (Figure 64).

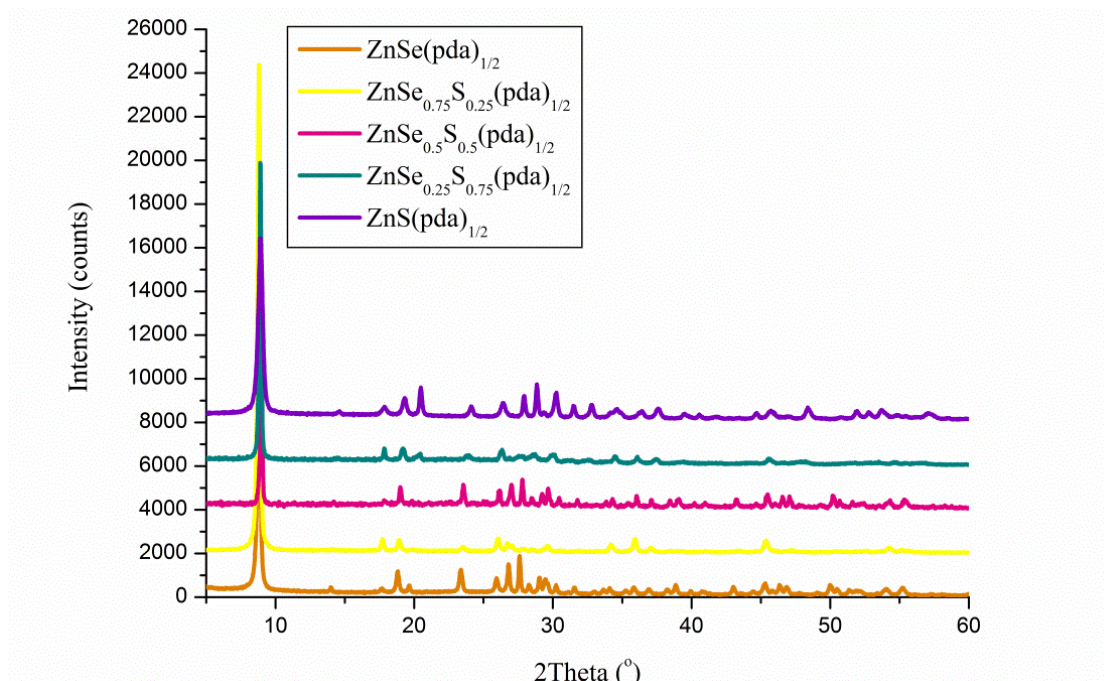


Figure 64. XRD patterns of  $ZnS_xSe_{1-x}(pda)_{1/2}$

Cell parameters calculated using program DICVOL06 are shown in Table 17. The compounds of type  $ZnS_xSe_{1-x}(pda)_{1/2}$  are 3D hybrid organic-inorganic materials, all of which crystallized in orthorhombic crystal system.

Table 17. Indexing results of powder X-ray diffraction of  $ZnS_xSe_{1-x}(pda)_{1/2}$  ( $x = 0, 0.25, 0.5, 0.75, 1$ )

Compound	a (Å)	b (Å)	c (Å)	V(Å <sup>3</sup> )
ZnSe(pda) <sub>1/2</sub>	20.002(7)	6.6351(9)	6.4478(6)	855.6(5)
ZnS <sub>0.25</sub> Se <sub>0.75</sub> (pda) <sub>1/2</sub>	19.995(8)	6.6024(6)	6.4016(8)	844.9(5)
ZnSe <sub>0.50</sub> S <sub>0.5</sub> (pda) <sub>1/2</sub>	19.989(8)	6.5173(5)	6.3334(9)	824.9(5)
ZnS <sub>0.75</sub> Se <sub>0.25</sub> (pda) <sub>1/2</sub>	19.948(5)	6.4557(8)	6.3303(6)	814.9(4)
ZnS(pda) <sub>1/2</sub> *	19.899(2)	6.3980(7)	6.1951(9)	788.6(3)

\*more detailed information about this compound is in chapter 5.

The obtained (and calculated) data of chemical analysis are presented below: **(6)** C – 21.47% (10.62%), H – 5,51% (2.97%), N – 13.91% (8.25%), S – 4.84% (4.72%), **(7)** C – 23.72% (11.41%), H – 6.22% (3.19%), N – 15.40% (8.87%), S – 9.99% (10.15%), **(8)** C – 21.20% (12.32%), H – 6.62% (3.45 %), N – 14.01% (9.58%), S – 9.23% (16.45%). They indicate that the obtained samples are contaminated by amine, which is difficult to remove by washing or drying. The results of chemical analysis are confirmed by TG/DSC studies.

As in the previous case, as well as in the cell parameters of  $ZnS_xSe_{1-x}(pda)_{1/2}$  compounds, discontinuity is observed. To illustrate this phenomenon, volume as a function of percentage of selenium and sulfur atoms is shown (Figure 65).

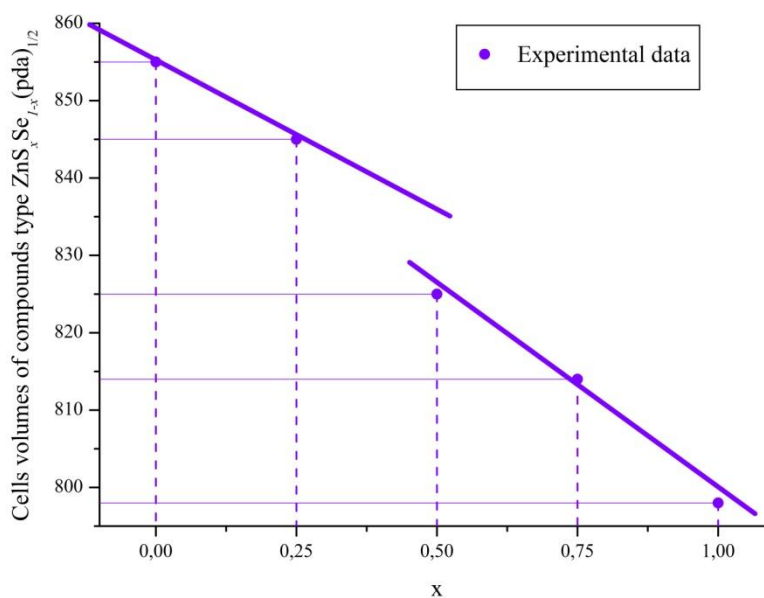


Figure 65. Obtained volumes as a function of the number of sulfur and selenium atoms ( $x = 0, 0.25, 0.5, 0.75, 1$ ) in compounds of the type  $ZnS_xSe_{1-x}(pda)_{1/2}$  (violet line – calculated volumes)

The biggest change occurs between  $ZnS_{0.5}Se_{0.5}(pda)_{1/2}$  and  $ZnS_{0.25}Se_{0.75}(pda)_{1/2}$ . Therefore, it is quite similar to  $Zn_xCd_{1-x}Se(pda)_{1/2}$ , where the most visible volume increase falls between  $Zn_{0.5}Cd_{0.5}Se(pda)_{1/2}$  and  $Zn_{0.25}Cd_{0.75}Se(pda)_{1/2}$ .

The optical features of  $ZnS_xSe_{1-x}(pda)_{1/2}$  compounds were studied. The UV-vis spectra are presented in Figure 66.

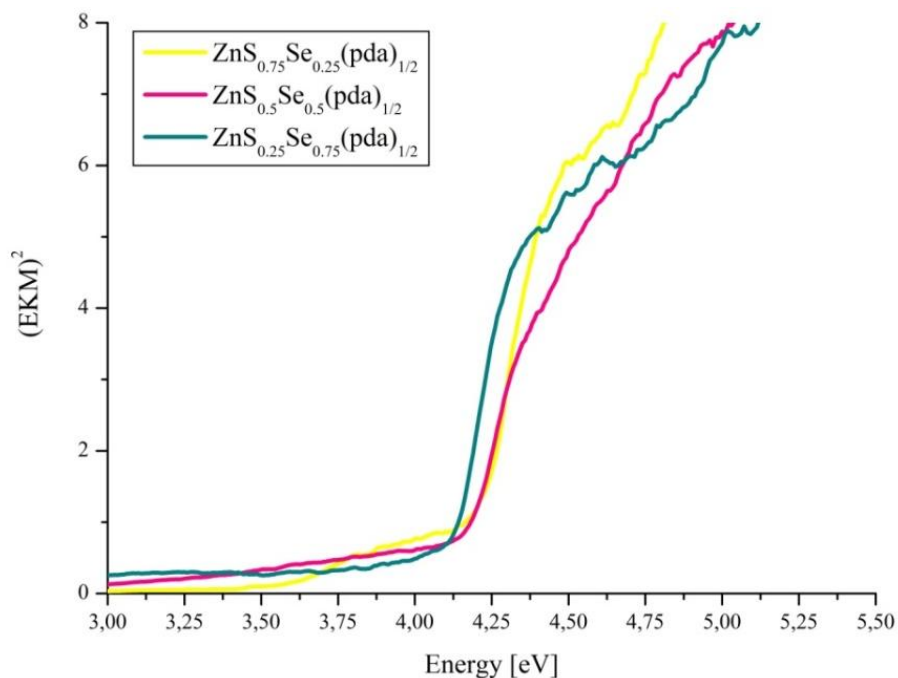


Figure 66. UV-vis spectra of  $ZnS_xSe_{1-x}(pda)_{1/2}$  compounds

Changing the composition of semiconducting layers caused very slight changes in the band gap. The calculated values are presented in Table 18.

Table 18. The calculated band gaps of hybrid materials of the type  $ZnS_xSe_{1-x}(pda)_{1/2}$

Compound	BG [eV]
$ZnSe(pda)_{1/2}$	3,99
$ZnS_{0.25}Se_{0.75}(pda)_{1/2}$	4,10
$ZnS_{0.50}Se_{0.5}(pda)_{1/2}$	4,15
$ZnS_{0.75}Se_{0.25}(pda)_{1/2}$	4,20
$ZnS(pda)_{1/2}$	4,75

The largest difference between the band gaps, about 0.5 eV, occurs between  $Zn_{0.75}Se_{0.25}(pda)_{1/2}$  and  $ZnS(pda)_{1/2}$ . Unexpectedly, it is not correlated with the step change in the cell parameters. Furthermore, a more detailed analysis of UV-vis spectra shows that ZnS and ZnSe could also be obtained. In the case of  $ZnS_{0.5}Se_{0.5}(pda)_{1/2}$ , both additional phases are present in the sample, whereas for  $ZnS_{0.75}Se_{0.25}(pda)_{1/2}$  only ZnS occurs.

### 6.3.1 Thermal properties of $ZnS_{0.5}Se_{0.5}(pda)_{1/2}$

Thermal properties of hybrid materials of the type  $ZnS_xSe_{1-x}(pda)_{1/2}$  were examined using TG/DSC in air and XRD vs. temperature in a helium atmosphere. As the representative of all hybrid materials with mixed semiconductor layers,  $ZnS_{0.5}Se_{0.5}(pda)_{1/2}$  was chosen; therefore thermal analysis was performed only for this compound.

In Figure 67, the results of XRD vs. temperature are shown. As it turns out,  $ZnS_{0.5}Se_{0.5}(pda)_{1/2}$  is stable to 300 °C, at which point pure  $ZnS_{0.5}Se_{0.5}$  (PDF 04-001-6856) appears. This phase remains stable to 800 °C. Along with an increase in temperature, the size of the crystallites increases. At 300 °C it is about 30 Å and then increases slowly to about 100 nm at 700 °C. At 800 °C their size reaches 200 Å.

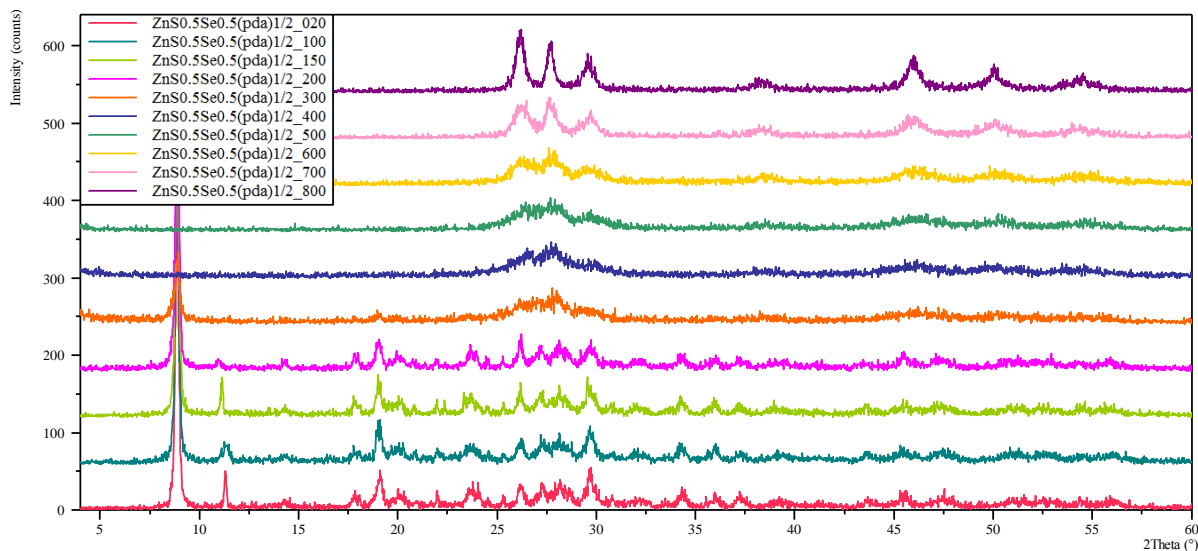


Figure 67. XRD patterns as a function of temperature of  $ZnS_{0.5}Se_{0.5}(pda)_{1/2}$  obtained in helium atmosphere

In Figure 68, TG/DSC analysis of  $ZnS_{0.5}Se_{0.5}(pda)_{1/2}$  is presented.

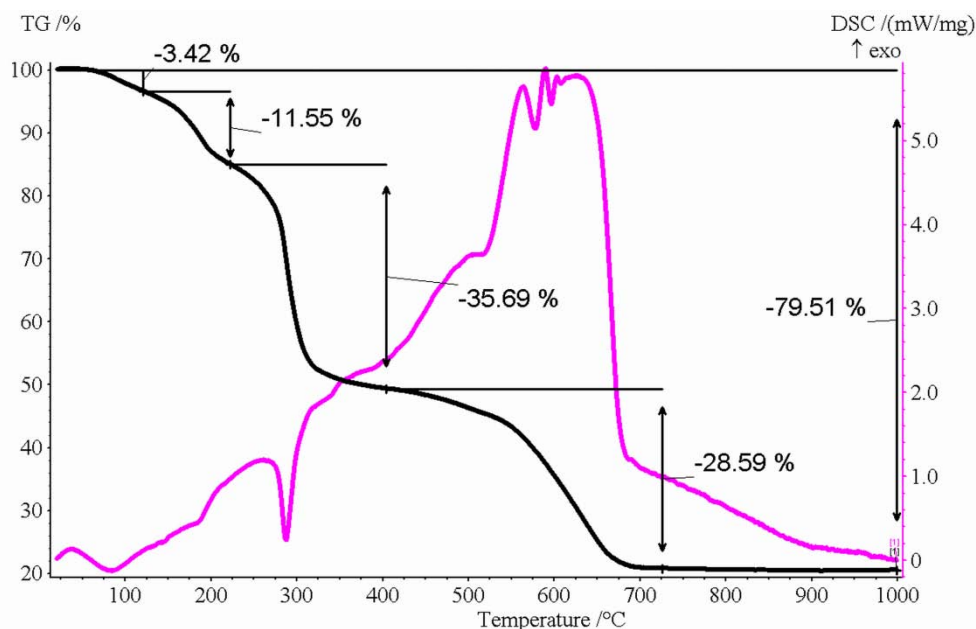


Figure 68. TG/DSC analysis for  $Zn_{0.5}Cd_{0.5}Se(pda)_{1/2}$

The first two losses of weight (3.42% and 11.54%) are related to the release of weak-bonded amines and surface water; the third (36.96%) to amines built into the structure. Probably the oxidation and removal of sulfur and selenium start at the same time as the removal of amines (these two phenomena overlap). The total loss of mass is 79.51%. The final product is ZnO.

6.3.2 SEM and EDS analysis for  $ZnS_xSe_{1-x}(pda)_{1/2}$  compounds

SEM analysis shows that all materials from the group with mixed semiconductor layers possess a platy (layered) structure. The edges are irregular and the surface is heterogeneous.

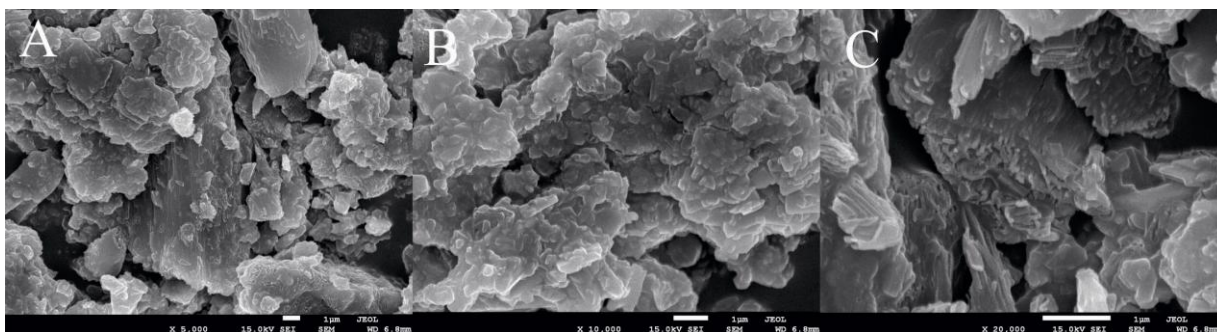


Figure 69. SEM images of  $ZnS_{0.75}Se_{0.25}(pda)_{1/2}$

However, in addition to these typical morphological forms, for  $ZnS_{0.75}Se_{0.25}(pda)_{1/2}$ , a second one can be distinguished. As can be seen in Figure 69C, these crystallites took the form of rods with diameters about 10 nm. In Figure 69B, plate-like crystals are presented. Both forms occur as aggregates.

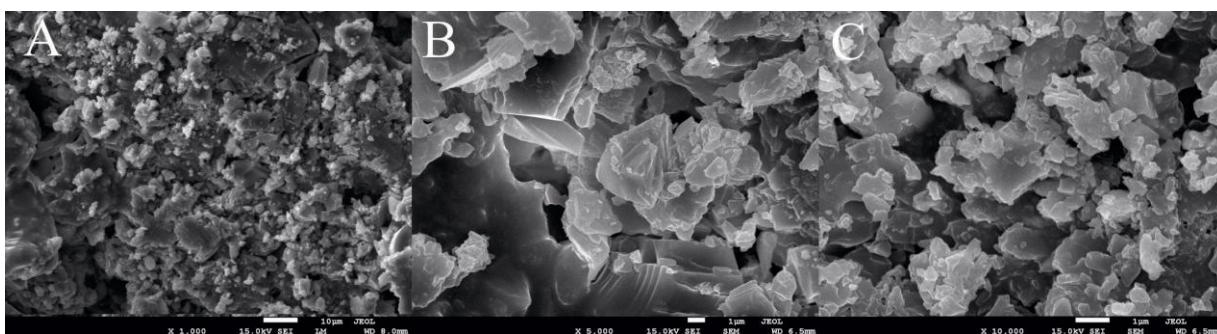


Figure 70. SEM images of  $ZnS_{0.5}Se_{0.5}(pda)_{1/2}$

In the case of  $ZnS_{0.5}Se_{0.5}(pda)_{1/2}$ , the surface is less heterogeneous, and the crystallites' edges are more regular. However, the sizes of the crystallites are much more diverse. SEM images of  $ZnS_{0.5}Se_{0.5}(pda)_{1/2}$  are presented in Figure 70.

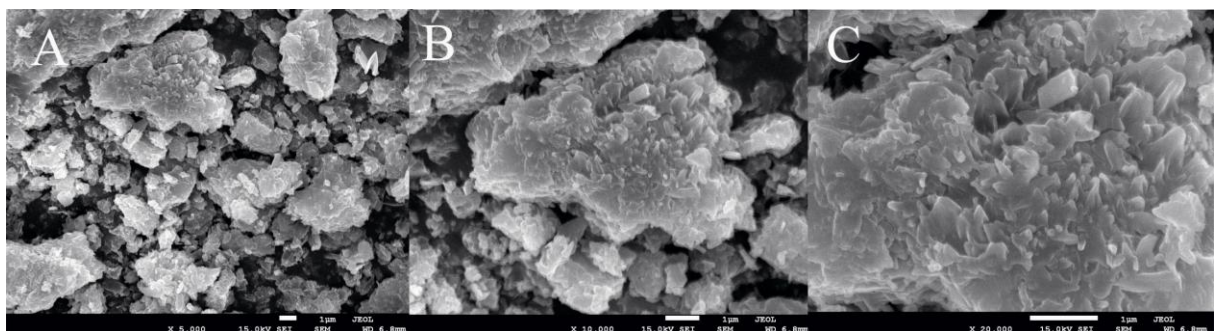


Figure 71. SEM images of  $ZnS_{0.25}Se_{0.75}(pda)_{1/2}$

In Figure 71, SEM images of  $ZnS_{0.25}Se_{0.75}(pda)_{1/2}$  are presented. The crystallites are aggregated but layered morphology can still be noted. The edges of crystallites are irregular and their surface is rough.

EDS analysis was carried out for all three samples with mixed semiconducting layers. The results confirm that 3D hybrid materials with two different anions built into the structure were obtained. However, the proportions of those anions, in comparison to those established in the synthesis, are slightly altered: namely, in each case about 10% more sulfur was incorporated into the semiconducting layer. Therefore, instead of contributions of sulfur of 25%, 50% and 75%, contributions of 35%, 60% and 85%, respectively, were found. This effect could be caused by sulfur coming from hydrated zinc sulfate, which is used in the synthesis as a source of zinc atoms.

#### 6.4 Conclusion

3D hybrid organic-inorganic layered materials with mixed semiconducting layers were obtained. In the first case, two different cations in varying percentages were used ( $Zn^{2+}$ ,  $Cd^{2+}$ ) to synthesize compounds of the type  $Zn_xCd_{1-x}Se(pda)_{1/2}$  ( $x = 0, 0.25, 0.5, 0.75, 1$ ), while in the second, the anions ( $S^{2-}$ ,  $Se^{2-}$ ) were mixed, which resulted in materials of the type  $ZnS_xSe_{1-x}(pda)_{1/2}$  ( $x = 0, 0.25, 0.5, 0.75, 1$ ). All analyses confirmed the creation of hybrid materials with mixed layers. However, in the case of  $ZnS_xSe_{1-x}(pda)_{1/2}$ , about 10% more sulfur atoms were incorporated into the semiconducting layers than had been planned in the synthesis. Based on the XRD diffraction patterns, the cell parameters of all compounds were determined. According to the assumptions, these parameters change along with changes in the composition (the volume grows with an increase in the percentage of atoms with higher radii).

The thermal behavior of all compounds was investigated. As it turns out, 3D hybrid materials are stable to 300 °C. In air, compounds with the general formula  $(Zn,Cd)(Se,S)$  were oxidized and, finally, ZnO and CdO were obtained. In a helium atmosphere this cannot occur; therefore, pure nanocompounds of the type ZnS, CdS,  $Zn_{0.5}Cd_{0.5}Se$  and  $ZnS_{0.5}Se_{0.5}$  were the final products. Both TG/DSC and chemical analysis indicated that amines exist in two forms: built into the structure and bonded on crystallite surfaces.

The important aim of my work was to examine the optical properties of mixed hybrid materials. Due to the fact that in semiconducting layers, two different anions and cations were incorporated, the optical properties should change. The performed analysis indicated that for compounds of the type  $Zn_xCd_{1-x}Se(pda)_{1/2}$ , significant modification took place: namely, in

comparison to pure hybrid materials, two values of band gaps were observed. However, surprisingly, the band gaps were not modified proportionally to the changes in composition. A very big transition (about 0.5 eV) occurs between  $Zn_{0.75}Cd_{0.25}Se(pda)_{1/2}$  (3.43 eV) and  $ZnSe(pda)_{1/2}$  (3.99 eV), while within the group of mixed compounds ( $Zn_{0.75}Cd_{0.25}Se(pda)_{1/2}$ ,  $Zn_{0.5}Cd_{0.5}Se(pda)_{1/2}$ ,  $Zn_{0.25}Cd_{0.75}Se(pda)_{1/2}$ ) it is about 0.01eV, which basically is in the range of standard deviation. Exactly the same result was observed in the second group of mixed hybrid materials, with the exception that in this case only one band gap is observed. Here, the greatest change (also about 0.5 eV) occurs between  $ZnS_{0.75}Se_{0.25}(pda)_{1/2}$  (4.20 eV) and  $ZnS(pda)_{1/2}$  (4.75 eV). In general, in both cases, the greatest change in band gaps occurs between contents of 75% and 100% of atoms with smaller radii (S (not Se) and Zn (not Cd)). It is also quite interesting that the second calculated band gaps in  $Zn_xCd_{1-x}Se(pda)_{1/2}$  compounds decrease along with an increase in the percentage of Zn atoms, that is, exactly the reverse of the first.

## Hybrid composites of the type (amine)MSO<sub>4</sub>

### 7.1 Introduction

The main aim of my research was to obtain new members of the family of 3D hybrid materials MQ(L)<sub>1/2</sub>, or to optimize their synthesis routes. In the course of my studies of the MTe(diamine)<sub>1/2</sub> system, to my great astonishment, a new group of chemical compounds was obtained. These compounds were synthesized using solvothermal methods. Their diffraction patterns and unit cell parameters are quite similar to “typical” MQ(L)<sub>1/2</sub> hybrid materials. Only through spatially-resolved SEM/EDX analysis and X-ray crystal structure analysis was the formation of a novel type of complex compounds with the formula (diamine)MX” (where X” means divalent anion) indicated.

As shown by the experiments, even relatively simple inorganic salts (in this case, sulfates), under solvothermal conditions and in the presence of amines, can form three-dimensional layered compounds. A number of such materials have been described recently in the literature.<sup>77,78,79</sup> These compounds are interesting mainly due to their potential applications in catalysis as sorption or ion exchange materials.

### 7.2 Materials and synthesis

In my syntheses two aromatic amines were used: *p*-xylylenediamine and *m*-xylylenediamine [C<sub>8</sub>H<sub>12</sub>N<sub>2</sub>]. Both were purchased from Sigma-Aldrich. Zinc sulphate hydrate [ZnSO<sub>4</sub>\*7H<sub>2</sub>O] and cadmium sulphate hydrate [CdSO<sub>4</sub>\*8H<sub>2</sub>O] were bought from POCH S.A Gliwice. All chemicals were used without further purification.

#### 7.2.1 Synthesis of (MXDA)MSO<sub>4</sub>

Compound (MXDA)ZnSO<sub>4</sub> was prepared using the solvothermal technique. First, 0.01 mol of hydrated zinc sulfate and 0.01 mol of *m*-xylylenediamine (MXDA) were placed into a 63-ml teflon-lined stainless steel autoclave. The mixture was heated at 160 °C for 2 days and then slowly cooled to room temperature. The precipitate was washed with a 30% solution of 2-propanol in water, and then dried at room temperature for 24 h. The same synthesis conditions were used for (MXDA)CdSO<sub>4</sub>; however, in this case the source of M atoms was hydrated cadmium sulfate.

### 7.2.2 Synthesis of (PXDA)MSO<sub>4</sub>

Synthesis was carried out using 0.01 mol of hydrated zinc sulfate and 0.0125 mol of *p*-xylylenediamine (PXDA). As can be seen, in comparison to the synthesis described above (in which (MXDA)MSO<sub>4</sub> compounds were synthesized) a greater quantity of amine was used, because a lower amount of this substrate resulted in insufficiently crystallized material. The zinc sulfate hydrate and *p*-xylylenediamine were mixed and placed in a 63-ml teflon-lined stainless steel autoclave. The reaction mixture was heated at 160 °C for 2 days and then cooled naturally (by switching off the heater) to room temperature. The precipitate was washed with a mixture of 30% 2-propanol and water and dried at room temperature in an air atmosphere. Exactly the same conditions, apart from the source of the metal, were employed to synthesize (PXDA)CdSO<sub>4</sub>. In this case, hydrated cadmium sulfate was used instead of hydrated zinc sulfate.

### 7.3 Characterization of (MXDA)MSO<sub>4</sub> and (PXDA)MSO<sub>4</sub>

All compounds crystallize as very fine powders, which enabled the use of X-ray powder diffraction methods (XRPD). The measurements were performed using a diffractometer working in Bragg-Brentano geometry. However, in the case of (MXDA)MSO<sub>4</sub>, further analyses showed the presence of texture. Therefore, additional measurements had to be done in DSH geometry (the samples were loaded into a capillary, size 2r=0.7mm).

#### 7.3.1 Structure description

Cell parameters were determined using the WinPLOTR program package. The space group was found by the EXPO2009 program, which calculates normalized structure factors, prepares intensity statistics, and then, based on these, suggests space groups and orders them according to their probability. Positions of heavy atoms and atoms of organic parts were found using direct methods implemented within this program (EXPO2009) and the global optimization method implemented in the FOX program.

The structure models were refined with the use of the JANA2006 program, which employs the Rietveldt algorithm. Using LeBail fitting, background, zero shift, unit cell parameters, profile parameters and asymmetry were refined in the initial runs of the program. Bond length, angles and atomic displacement parameters were limited by geometric restraints. Finally, the positions of atoms were fitted with the application of isotropic atomic thermal displacement parameters.

In the case of (MXDA)MSO<sub>4</sub> compounds, due to the cylindrical shape of the sample, an absorption correction had to be introduced. The obtained Rietveld plots for (MXDA)ZnSO<sub>4</sub> and (MXDA)CdSO<sub>4</sub> are shown in Figure 72 and Figure 73, respectively.

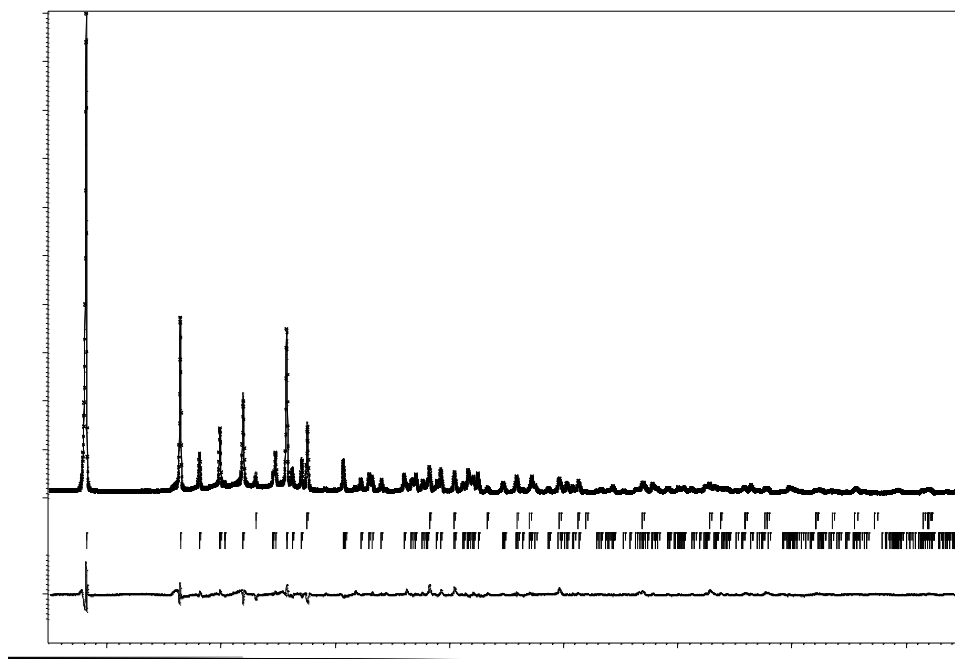


Figure 72. Rietveld plot for (MXDA)ZnSO<sub>4</sub>

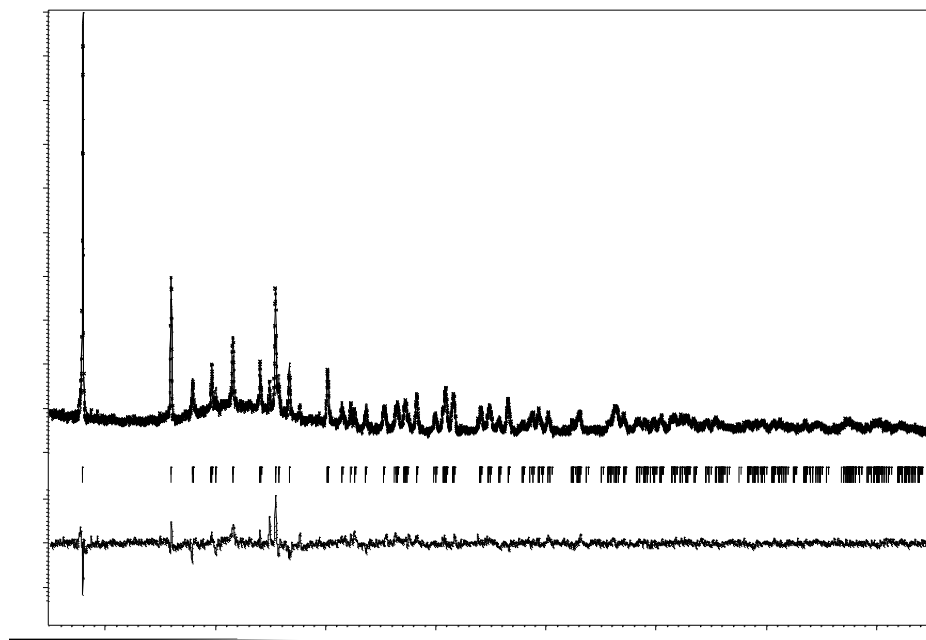


Figure 73. Rietveld plot for (MXDA)CdSO<sub>4</sub>

The compounds with MXDA molecules used as a spacer crystallize in the space group P2<sub>1</sub>ma. Selected crystallographic data of (MXDA)MSO<sub>4</sub> are summarized in Table 19, selected interatomic distances in Table 20 and Table 21, and atomic positions in Table 22 and Table 23.

Table 19. Crystallographic data for (MXDA)ZnSO<sub>4</sub> and (MXDA)CdSO<sub>4</sub>

Empirical formula	ZnSO <sub>4</sub> C <sub>8</sub> H <sub>12</sub> N <sub>2</sub>	CdSO <sub>4</sub> C <sub>8</sub> H <sub>12</sub> N <sub>2</sub>
Formula weight	297.65 g/mol	344.57 g/mol
Crystal system	Orthorhombic	Orthorhombic
Space group	P2 <sub>1</sub> ma	P2 <sub>1</sub> ma
a[Å]	9.8004(4)	9.8824(10)
b[Å]	10.7829(3)	11.0907(7)
c[Å]	4.88473(19)	4.9663(5)
V[Å <sup>3</sup> ]	516.21(3)	544.32(9)
R <sub>p</sub>	6.9	7.8
R <sub>wp</sub>	9.2	10.0
R <sub>F</sub>	6.1	8.7
Color	white	white

Table 20. Selected interatomic distances for (MXDA)ZnSO<sub>4</sub>

Atom 1	Atom2(symm. code)	distance (Å)
Zn1	O1	2.111(16)
Zn1	O2	2.199(15)
Zn1	N1	2.203(12)
Zn1	N1 (x, -y+2, z)	2.203(12)
Zn1	O3	2.427(9)
Zn1	O3 (x, -y+2, z)	2.427(9)
Zn1	N1 (x, -y+2, z)	2.203(12)
Zn1	O3	2.427(9)
Zn1	O3 (x, -y+2, z)	2.427(9)

Table 21. Selected interatomic distances for (MXDA)CdSO<sub>4</sub>

Atom 1	Atom2(symm. code)	d (Å)
Cd1	O1	2.77(5)
Cd1	O1 (x, -y+2, z+1)	2.69(6)
Cd1	O2	2.84(6)
Cd1	O2	2.97(6)
Cd1	N1	2.297(14)
Cd1	N1 (x, -y+2, z)	2.297(14)
Cd1	O3	2.35(3)
Cd1	O3 (x, -y+2, z+1)	2.35(3)

Table 22. Atomic positions of (MXDA)ZnSO<sub>4</sub>

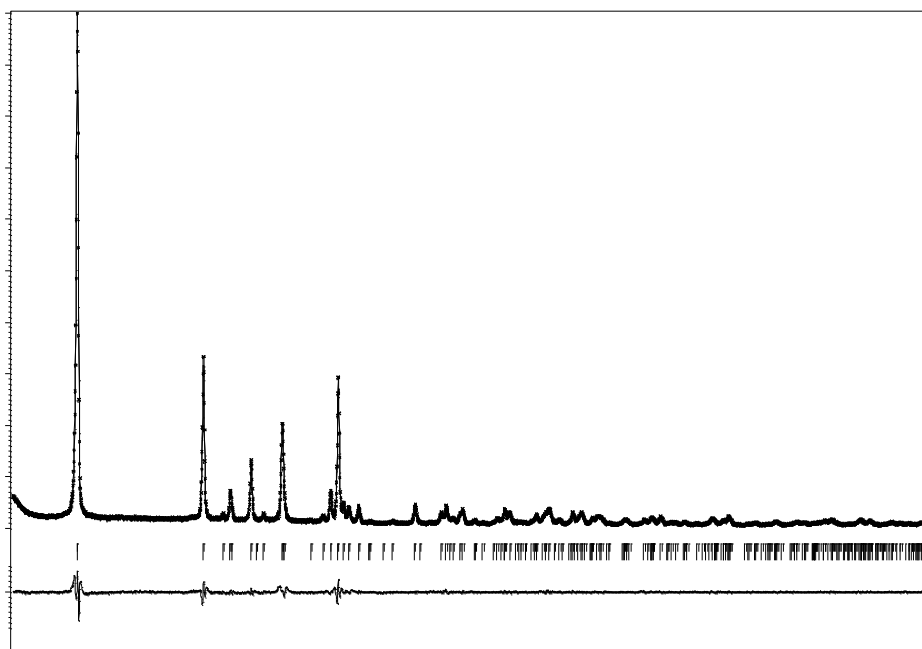
Atom	x	y	z	U <sub>iso</sub>
Zn1	0.8666	1	1.1241(9)	-0.0002(7)
S1	1.0700(8)	1	0.5682(16)	-0.0002(7)
O1	1.0346(15)	1	0.854(4)	0.028(4)
O2	1.2164(17)	1	0.541(3)	0.028(4)
O3	0.50000	0.2801(11)	0.7327(2)	0.045(17)
N1	0.7823(14)	0.8317(9)	0.933(3)	0.025(7)
C1	0.6963(14)	0.6149(6)	0.687(3)	0.018(3)
C2	0.6439(18)	0.5	0.582(4)	0.018(3)
C4	0.8001(12)	0.6121(5)	0.895(2)	0.018(3)
C5	0.8595(13)	0.7315(8)	1.014(3)	0.018(3)
C6	0.8489(15)	0.5	0.993(3)	0.018(3)

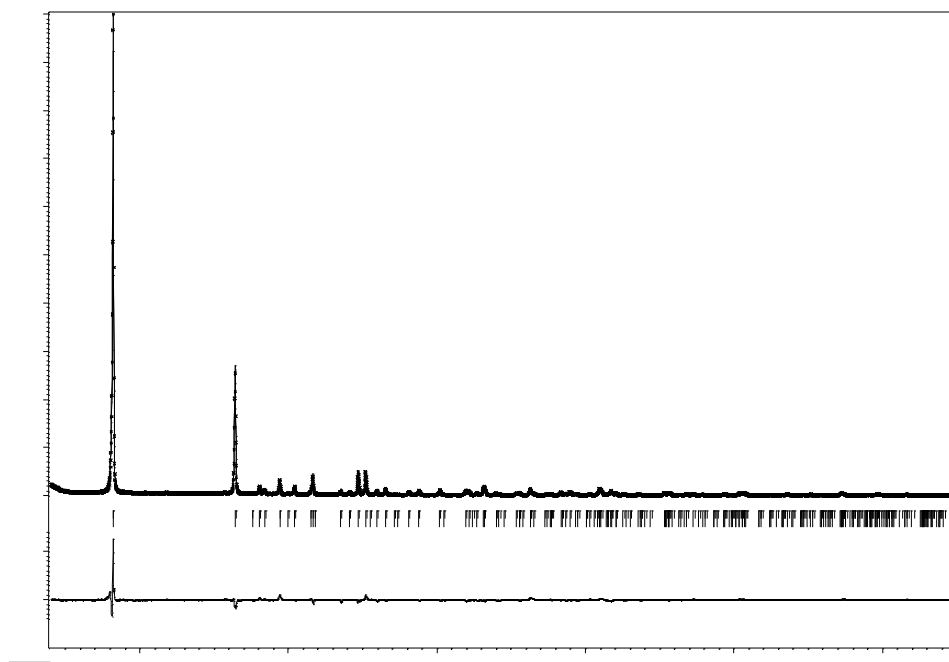
Table 23. Atomic positions of (MXDA)CdSO<sub>4</sub>

Atom	x	y	z	U <sub>iso</sub>
Cd1	0.8666	1	1.1189(8)	0.0103(9)
S1	1.0849(4)	1	0.519(2)	0.029(8)
O1	1.0564(6)	1	0.816(2)	0.068(11)
O2	1.2353(6)	1	0.4734(2)	0.068(11)
O3	1.0240(9)	0.88952(5)	0.393(3)	0.068(11)
N1	0.757(3)	0.8317(9)	1.009(5)	0.032(9)
C1	0.671(3)	0.6149(6)	1.191(4)	0.032(9)
C2	0.621(4)	0.5	1.290(6);	0.032(9)
C4	0.770(2)	0.60858(5)	0.992(4)	0.032(9)
C5	0.825(3)	0.72887(9)	0.882(5)	0.032(9)
C6	0.820(3)	0.5	0.893(5)	0.032(9)

On the other hand, the compounds with PXDA as a spacer crystallize in space group Pnma. In comparison to (MXDA)MSO<sub>4</sub> materials, the measurements in Bragg-Brentano geometry were sufficient to solve the structures of (PXDA)MSO<sub>4</sub> compounds. However, a correction related to preferred orientation had to be introduced. The texture direction was [010].

The Rietveld plots for (PXDA)ZnSO<sub>4</sub> and (PXDA)CdSO<sub>4</sub> are shown in Figure 74 and Figure 75, respectively. Selected crystallographic data for (PXDA)MSO<sub>4</sub> are summarized in Table 24, selected interatomic distances in Table 25 and Table 26, and atomic positions in Table 27 and Table 28.

Figure 74. Rietveldt plot for (PXDA)ZnSO<sub>4</sub>

Figure 75. Rietveld plot for (PXDA)CdSO<sub>4</sub>Table 24. Crystallographic data for (PXDA)ZnSO<sub>4</sub> and (PXDA)CdSO<sub>4</sub>

Empirical formula	ZnSO <sub>4</sub> C <sub>8</sub> H <sub>12</sub> N <sub>2</sub>	CdSO <sub>4</sub> C <sub>8</sub> H <sub>12</sub> N <sub>2</sub>
Formula weight	297.65 g/mol	344.57 g/mol
Crystal system	Orthorhombic	Orthorhombic
Space group	Pnma	Pnma
a[Å]	9.8496(3)	10.1136(4)
b[Å]	21.2419(5)	21.6625(3)
c[Å]	4.89556(17)	4.9562(2)
V[Å <sup>3</sup> ]	1024.27(5)	1086.83(7)
R <sub>p</sub>	6.8	9.6
R <sub>wp</sub>	9.1	12.3
R <sub>F</sub>	5.1	6.5
Colour	white	white

Table 25. Selected interatomic distances for (PXDA)ZnSO<sub>4</sub>.

Atom 1	Atom2(symm. code)	d (Å)
Zn1	O1	2.250(8)
Zn1	O2	2.399(4)
Zn1	O2 (x-1/2, y, -z-1/2)	2.399(4)
Zn1	N1	2.112(6)
Zn1	N1 (x, -y+1/2, z)	2.112(6)
Zn1	O3	2.263(9)

Table 26. Selected interatomic distances for (PXDA)CdSO<sub>4</sub>.

Atom 1	Atom2(symm. code)	Distance (Å)
Cd1	O1	2.432(15)
Cd1	O2	2.469(10)
Cd1	O2 (x-1/2, y, -z-1/2)	2.469(10)
Cd1	N1	2.368(14)

Cd1	N1 (x, -y+1/2, z)	2.368(14)
Cd1	O3	2.414(17)

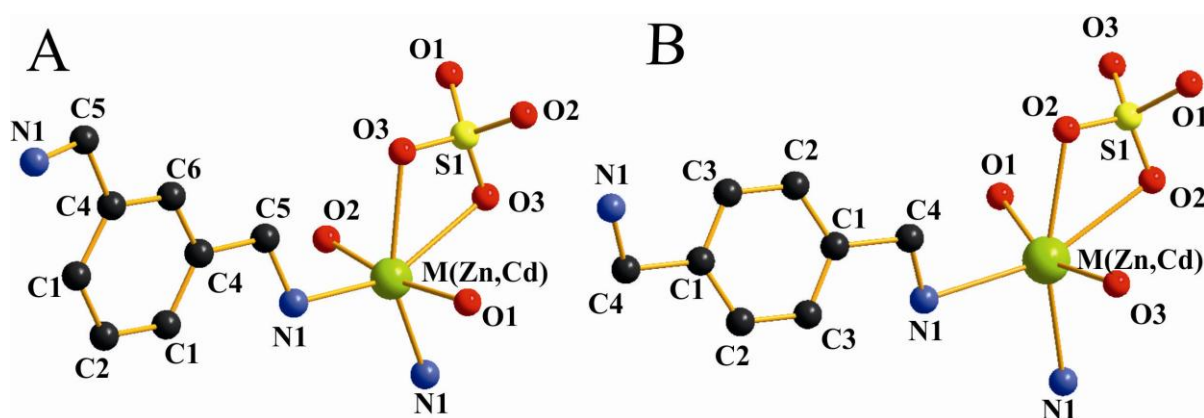
Table 27. Atomic positions of (PXDA) $ZnSO_4$ .

Atom	x	y	z	$U_{iso}$
Zn1	0.3691(4)	0.25	0.1143(9)	0.0264(17)
S1	0.6686(5)	0.25	-0.1742(12)	0.018(4)
O1	0.5159(18)	0.25	-0.238(2)	0.013(4)
O2	0.7319(7)	0.1929(4)	-0.2934(17)	0.013(4)
O3	0.6877(10)	0.25	0.103(4)	0.013(4)
N1	0.4472(11)	0.1691(4)	0.318(3)	0.001
C1	0.4479(15)	0.0547(3)	0.370(3)	0.007(4)
C2	0.3987(10)	-0.0055(4)	0.304(2)	0.007(4)
C3	0.4498(13)	-0.0597(3)	0.433(2)	0.007(4)
C4	0.3877(14)	0.1129(4)	0.221(3)	0.007(4)

Table 28. Atomic positions of (PXDA) $CdSO_4$ .

Atom	x	y	z	$U_{iso}$
Cd1	0.3394(4)	0.25	0.1129(7)	0.0552(12)
S1	0.6329(9)	0.25	-0.1793(16)	0.038(4)
O1	0.4918(11)	0.25	-0.267(3)	0.038(4)
O2	0.7001(10)	0.19374(18)	-0.286(2)	0.038(4)
O3	0.6395(19)	0.25	0.1211(19)	0.038(4)
N1	0.409(2)	0.1618(4)	0.357(4)	0.045(6)
C1	0.4661(10)	0.0519(2)	0.3499(13)	0.045(6)
C2	0.4035(13)	-0.0041(4)	0.301(3);	0.045(6)
C3	0.770(2)	0.60858(5)	0.992(4)	0.045(6)
C4	0.428(2)	0.1104(5)	0.180(3)	0.045(6)

As it turns out, all compounds crystallize in orthorhombic crystal system. Compounds (MXDA) $ZnSO_4$ , (MXDA) $CdSO_4$  and (PXDA) $ZnSO_4$ , and (PXDA) $CdSO_4$  are isostructural and show significant similarities. All are 3D materials consisting of  $-M-(SO_4)-$  layers, linked by aromatic diamines (MXDA or PXDA), through covalent bonds with the metal atoms (M) from the layer. Fragments of the basic structures are shown in Figure 76.

Figure 76. Basic structure fragments of: A) (MXDA) $MSO_4$ , B) (PXDA) $MSO_4$ 

In each compound, atoms M (Zn, Cd) show octahedral coordination. Each M atom is surrounded by six ligands, two nitrogen atoms (in *cis*-position to each other) and four oxygen

atoms. The sulfur atoms are tetrahedrally coordinated by oxygen atoms. For comparison, in “typical” semiconducting hybrid materials, metal atoms show tetrahedral coordination, with three sulfurs and one nitrogen linked to each metal atom.

From the viewpoint of topology, the  $-M-SO_4-$  layers are similar to the layers in semiconductor hybrid compounds. In all cases, they are built of six-member rings, alternately occupied by three M atoms and three anions ( $SO_4^{2-}$  in my studies, or, in the case of semiconductor layers, by  $S^{2-}$ ,  $Se^{2-}$  or  $Te^{2-}$ ). Each vertex is common to three rings. Nevertheless, as mentioned above, each M atom is coordinated by two amines, which results in different stoichiometry. Octahedrally-coordinated metal centers can be more easily incorporated in flat  $M-SO_4$  layers, whereas in  $MQ(\text{amine})_{1/2}$  hybrid materials such layers are more puckered. However, this does not change the fact that in both classes of hybrid materials the topology of the layers is  $6^3$ . A  $-M-SO_4-$  layer is shown in Figure 77.

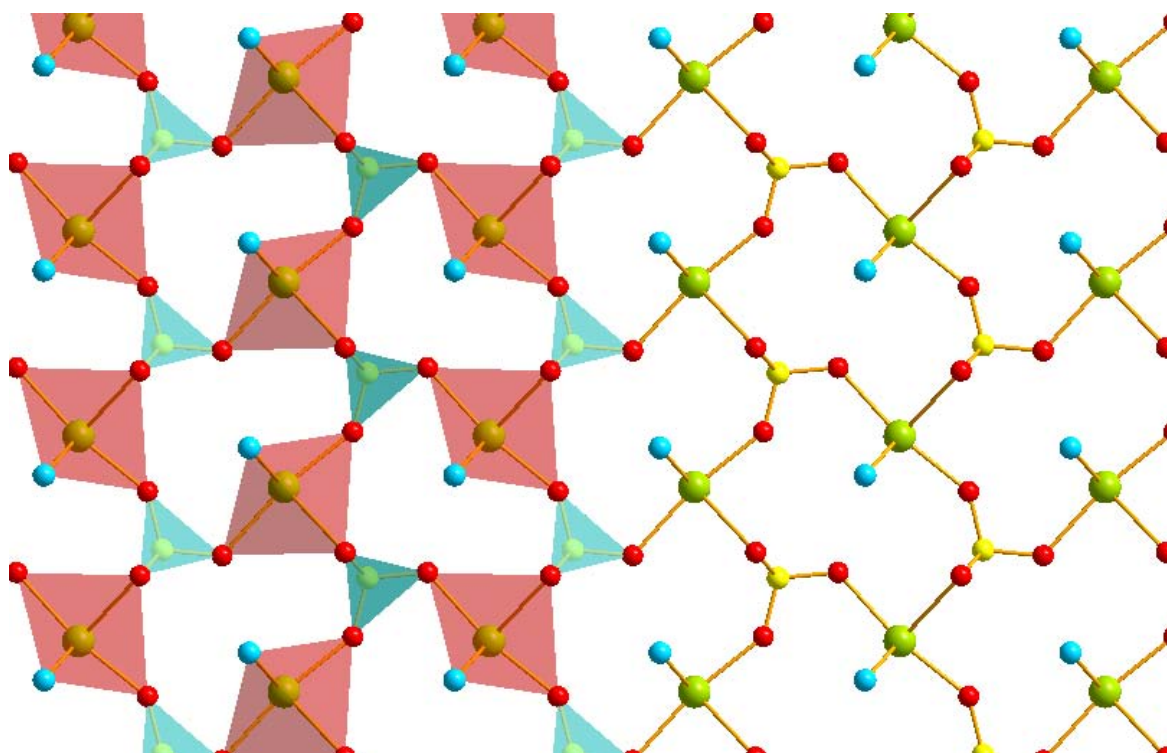


Figure 77. A  $-M-SO_4-$  layer ( $M$  – green, blue – nitrogen, red – oxygen, yellow – sulfur)

The type of space group in which compounds (amine)MSO<sub>4</sub> crystallize depends on the amines used in the synthesis. Thus, all compounds with PXDA crystallize in space group Pnma, whereas compounds with MXDA crystallize in P2<sub>1</sub>ma. In this case this may be associated with the even and odd numbers of carbon atoms in the  $(CH_2)_n$  chain of the amine, which in turn is correlated with the mutual position of the NH<sub>2</sub> groups (trans or cis). Figure 78 presents the layered structures, the alignment of the diamines, and linking fragments in the structures of (MXDA)ZnSO<sub>4</sub> and (PXDA)ZnSO<sub>4</sub>.

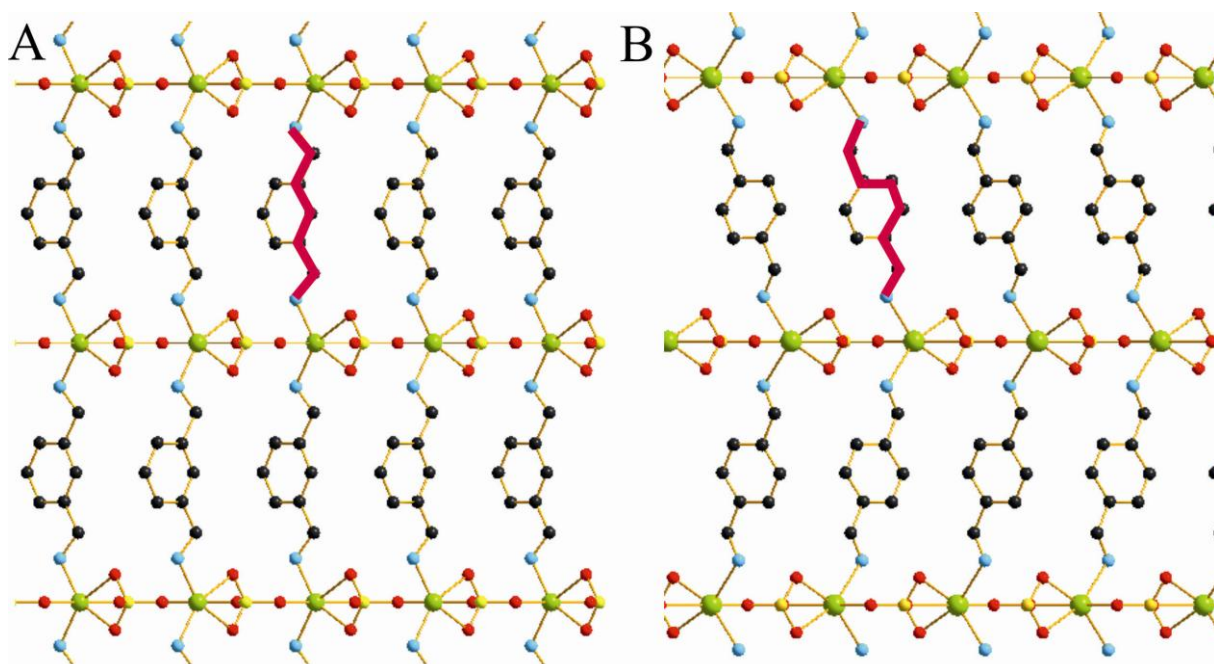


Figure 78. A) 'cis-amine' as a linker B) 'trans-amine' as a linker

In all structures diamine rings are perpendicular to each other, which is clearly visible in Figure 79.

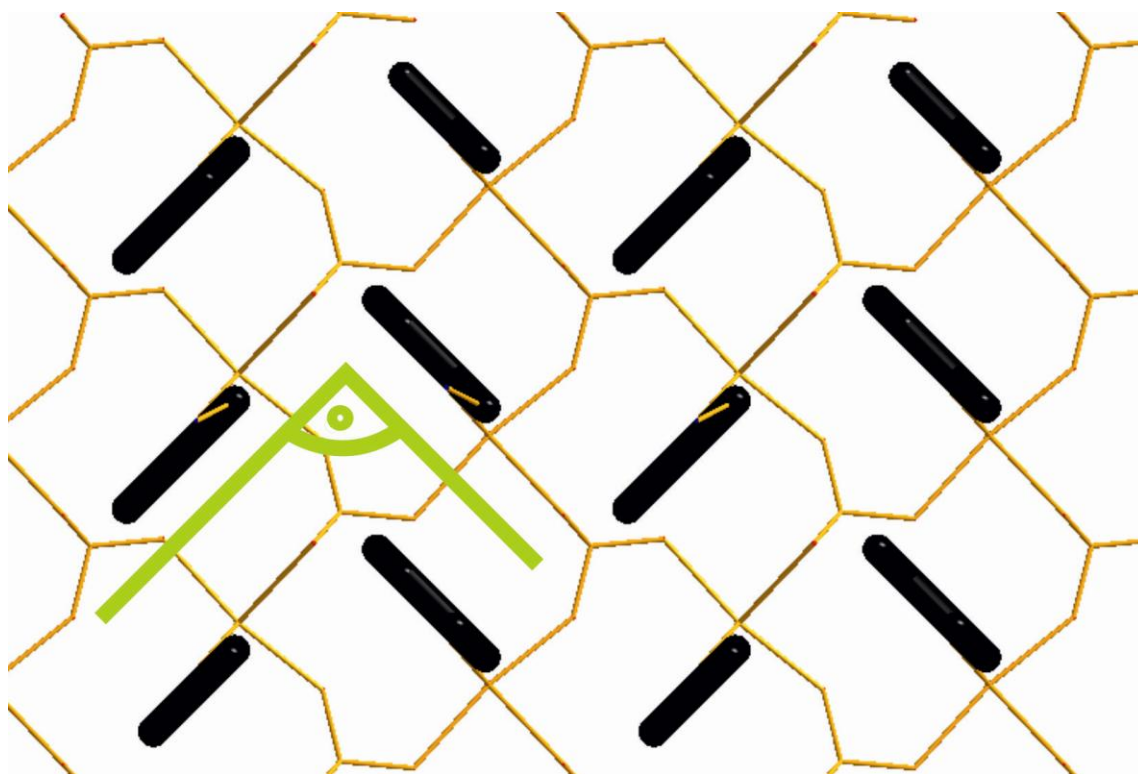


Figure 79. The orthogonal alignment of MXDA molecules (black bars) seen through  $-M-SO_4-$  layers

Furthermore, as can be seen, MXDA molecules are arranged orthogonally to  $-M-SO_4-$  layers. It lies exactly on the plane of symmetry  $m$ . Also, PXDA diamines are perpendicular to the layers; however, their long axes are arranged obliquely to them. This specific arrangement of both types of amines is presented in Figure 80.

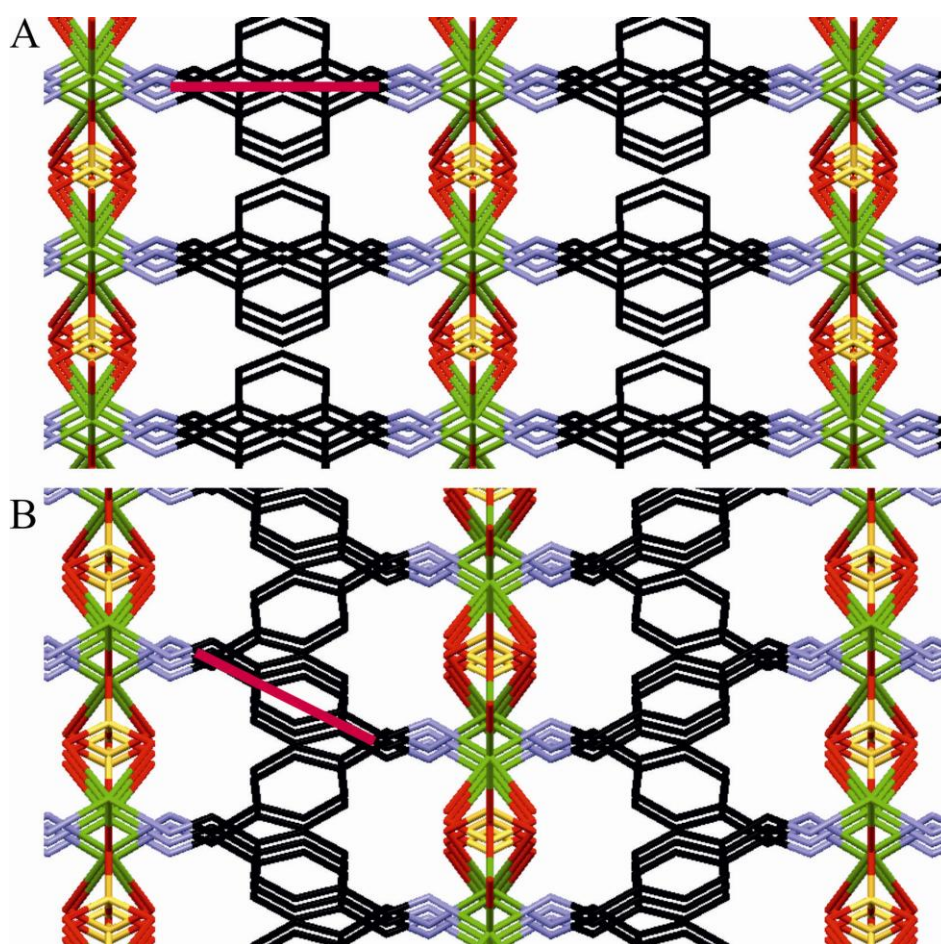


Figure 80. The alignment of amines between inorganic layers in **A)** compounds with amine – MXDA, **B)** compounds with amine – PXDA)

The (amine)MSO<sub>4</sub> materials are quite similar to recently-reported open-framework sulfates, mainly due to synthesis routes, structures (layered or linear), and the use of amines as a template. Nevertheless, some differences can also be observed. One of them is the method of linking organic components. In (amine)MSO<sub>4</sub> materials, the amine group is connected directly through a covalent bond to metal atoms, whereas in open-framework materials, ammonium fragments are bound by ionic forces and hydrogen bonds. Furthermore, compounds of the type (amine)MSO<sub>4</sub> are three-dimensional hybrid inorganic-organic materials. As an example of open-framework materials, [H<sub>3</sub>N(CH<sub>2</sub>)<sub>3</sub>NH<sub>3</sub>][Cd<sub>2</sub>(H<sub>2</sub>O)<sub>2</sub>(SO<sub>4</sub>)<sub>3</sub>] can be mentioned. This is a lamellar compound in which semiconducting layers are formed by two Cd atoms and two sulfate groups.<sup>80</sup> However, in (amine)MSO<sub>4</sub> materials three metal atoms and three sulfate groups are involved.

### 7.3.2 Chemical analysis

The chemical analyses correlate quite well with the structure solutions. However, they indicate that the samples (especially these with MXDA) are significantly contaminated by amorphous or liquid admixtures. The results are presented below.

For **(MXDA)ZnSO<sub>4</sub>** the empirical formula is ZnSO<sub>4</sub>C<sub>8</sub>H<sub>12</sub>N<sub>2</sub> (297.65 g/mol) and the obtained (and calculated) data are: C – 39.86% (32.28%), H – 5.33% (4.06%), N – 11.42% (9.41%), S – 7.10% (10.77%). As can be seen, an excess of amine is presented. **(MXDA)CdSO<sub>4</sub>** possesses the following chemical formula: CdSO<sub>4</sub>N<sub>2</sub>H<sub>12</sub>C<sub>8</sub> (344.57 g/mol). The obtained (and calculated) results are: C – 24.37% (27.88%), H – 3.22% (3.48%), N – 7.04% (8.12%), S – 9.47% (9.31%). This suggests the presence of synthesis substrates. For **(PXDA)ZnSO<sub>4</sub>** the empirical formula is ZnSO<sub>4</sub>C<sub>8</sub>H<sub>12</sub>N<sub>2</sub> (297.65 g/mol). The obtained (and calculated) results are: C – 33.92% (32.28%), H – 4.22% (4.06%), N – 9.61% (9.41%), S – 9.79% (10.77%). This data indicates a small excess of amine. Finally, the empirical formula of **(PXDA)CdSO<sub>4</sub>** is CdSO<sub>4</sub>N<sub>2</sub>H<sub>12</sub>C<sub>8</sub> (344.57 g/mol). The obtained (and calculated) data are: C – 29.70% (27.88%), H – 3.65% (3.48%), N – 8.35% (8.12%), S – 8.88% (9.31%). These slight differences can be explained by an excess of amine.

### 7.3.3 Thermal analysis

The thermal stability of (amine)MSO<sub>4</sub> materials were analyzed using TG/DSC (in an air atmosphere) and XRD as a function of temperature (in helium and air atmospheres). Two different atmospheres were used in measurement in order to compare their impact on the final product. (PXDA)MSO<sub>4</sub> compounds were analyzed in a helium-reducing atmosphere, whereas (MXDA)MSO<sub>4</sub> and (PXDA)CdSO<sub>4</sub> were measured in an air-oxidizing atmosphere.

Figure 81 presents the TG/DSC of (MXDA)ZnSO<sub>4</sub>.

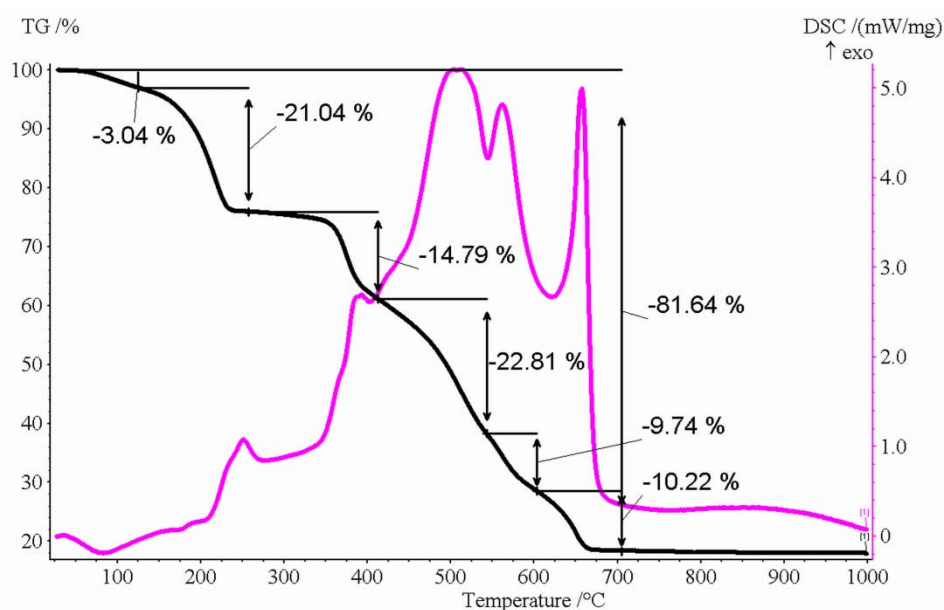


Figure 81. The TG/DSC analysis of (MXDA)ZnSO<sub>4</sub>

Three losses of weight (21.05%, 14.54%, and 23.10%) at a temperature range from 210 °C to 520 °C, are related to releases of amine. This result indicates a large excess of amines (about

8%) absorbed on the surface of crystallites, as well as confirming the chemical analysis. In turn, the last loss of mass which occurs, 23.10%, could be a combination of two effects: the release of amine and the decomposition of ZnSO<sub>4</sub> to ZnO. Finally, two losses of weight (9.45%, 10.51%) can be observed. They are related to the removal of SO<sub>3</sub>. The total loss of weight is 81.94% and the product is ZnO.

In Figure 82, XRD as a function of temperature in helium atmosphere is presented. In the range between 300–400 °C the amines are removed; at 400 °C the amorphous phase was obtained. Then, at 600 °C the ZnO (PDF 04-008-8198) appeared. This phase remains stable to 800 °C. The same final product was obtained in TG/DSC.

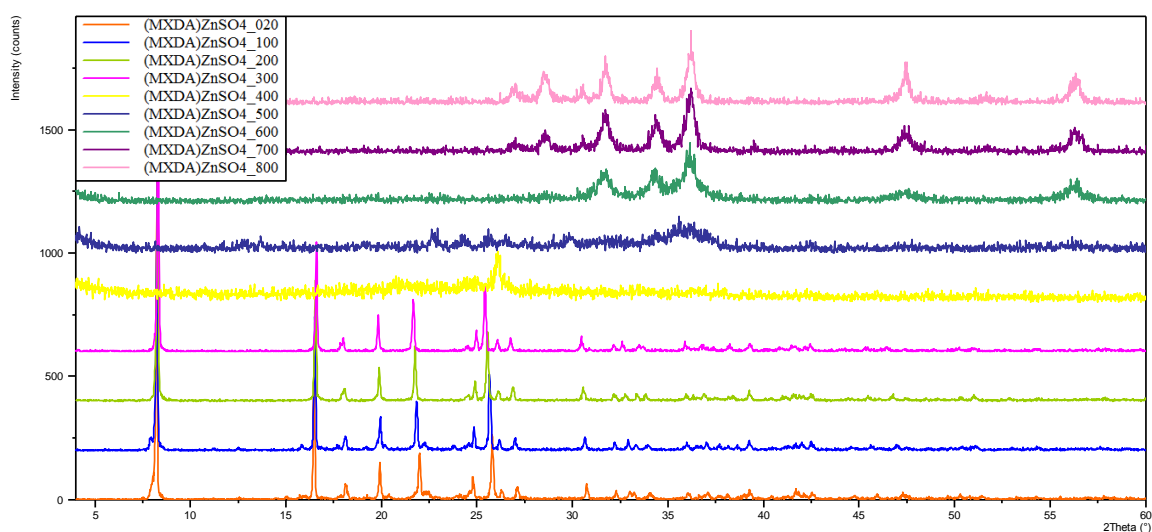


Figure 82. XRD patterns of (MXDA)ZnSO<sub>4</sub> vs. temperature (helium atmosphere)

Figure 83 presents the TG/DSC results.

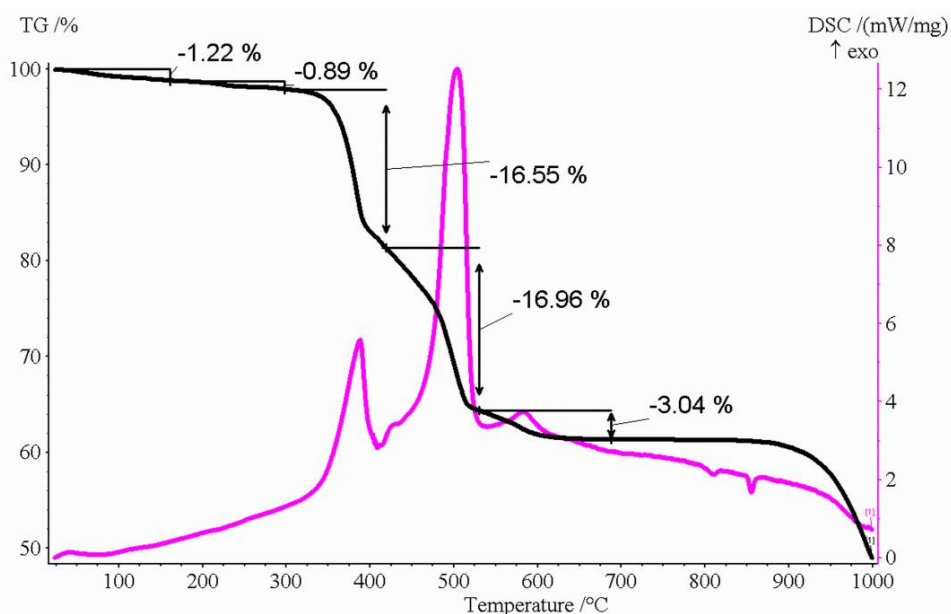


Figure 83. The TG/DSC analysis of (MXDA)CdSO<sub>4</sub>

The first small losses of weight (1.22% and 0.89%) can be related to the evaporation of hydration water. The next two (16.55%, 16.96%) are correlated to the release of nearly equal amounts of amines. The final product is CdSO<sub>4</sub>.

In Figure 84, XRPD patterns as a function of temperature in helium atmosphere are shown.

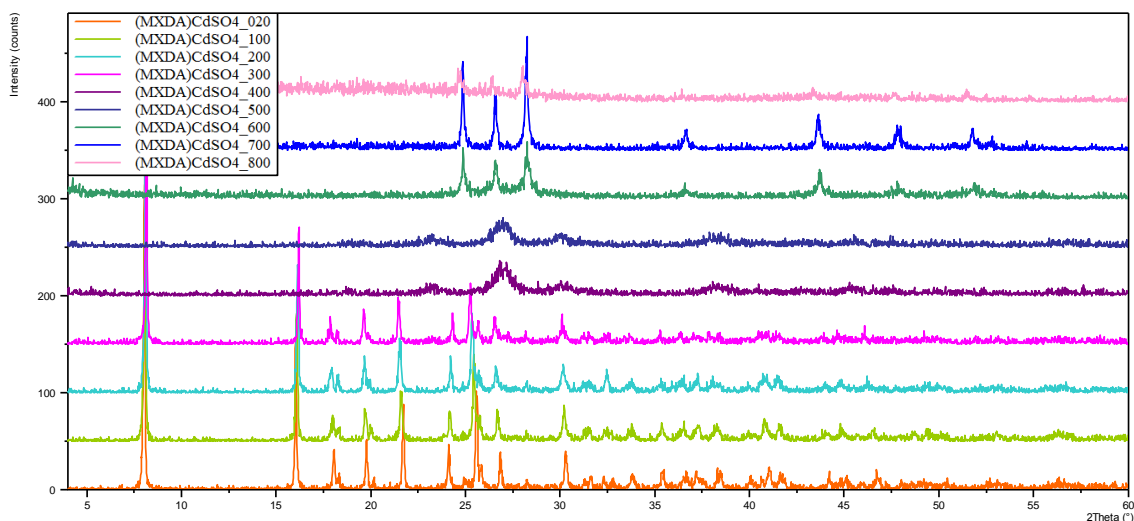


Figure 84. XRD patterns vs. temperature of (MXDA)CdSO<sub>4</sub> (helium atmosphere)

Hybrid materials are stable to 300 °C. At 400 °C the amine is released and CdS (PDF 04-003-6705) appears. This phase remains stable to 800 °C.

The TG-DSC results of (PXDA)ZnSO<sub>4</sub> are presented in Figure 85.

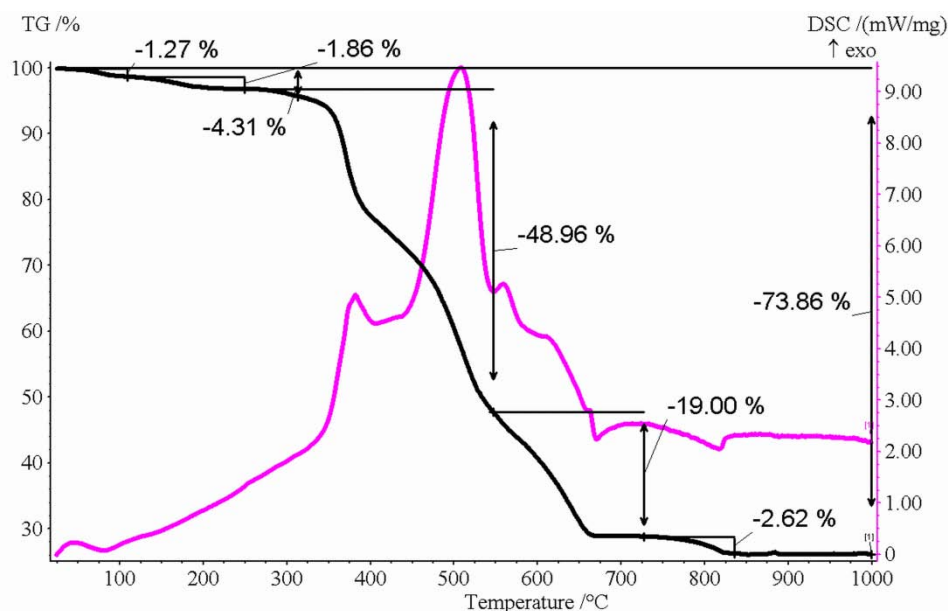


Figure 85. The TG/DSC analysis of (PXDA)ZnSO<sub>4</sub>

The compounds with PXDA amine, used as linkers, behave quite similarly to those with MXDA. In the case of (PXDA)ZnSO<sub>4</sub> the first two losses of weight (1.27%, 1.86%) can be explained by the evaporation of hydration water or by the release of unbonded amines

(PXDA). The weight losses around 300 °C to 510 °C (the first two exothermic peaks) are related to the loss of amines pertaining to (PXDA) $ZnSO_4$  as a result of its decomposition. Finally, the last exothermic peak that appears at 560 °C is correlated with zinc sulfate decomposition (release of  $SO_3$  – 19.00% loss of mass). The total mass lost is between 72–74%. The final product of the TG-DSC analysis is ZnO.

In the case of XRPD studies as a function of temperature in an air atmosphere (Figure 86), two final products are obtained: ZnO (PDF 04-008-8199) and  $Zn_3O(SO_4)_2$  (PDF 00-032-1476). Both are stable within a temperature range from 400 °C to 700 °C.

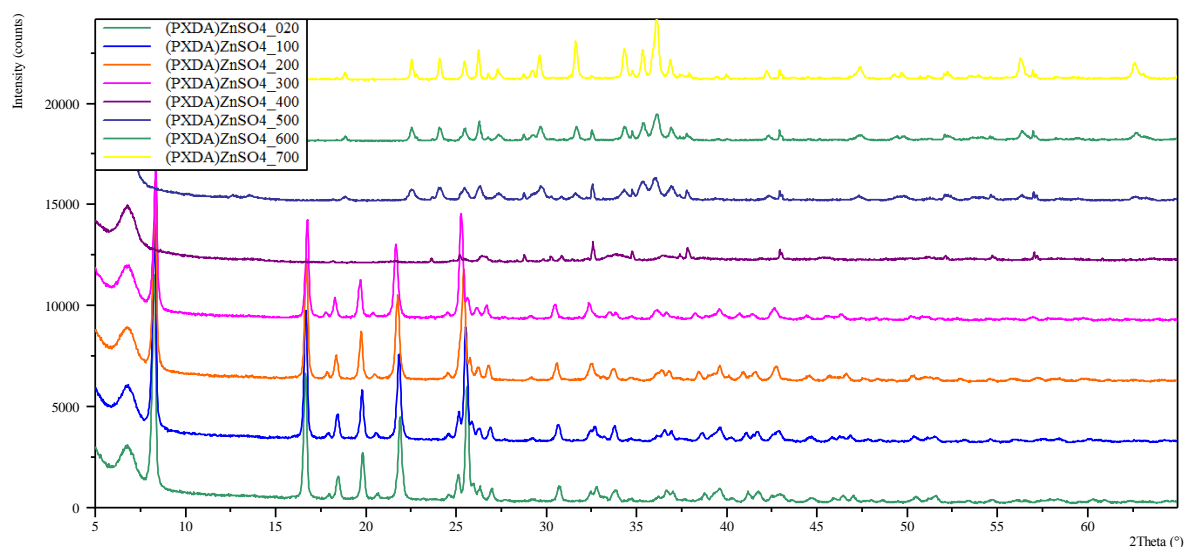


Figure 86. XRD patterns of (PXDA) $ZnSO_4$  vs. temperature (air atmosphere)

The results of TG/DSC for (PXDA) $CdSO_4$  are presented in Figure 87.

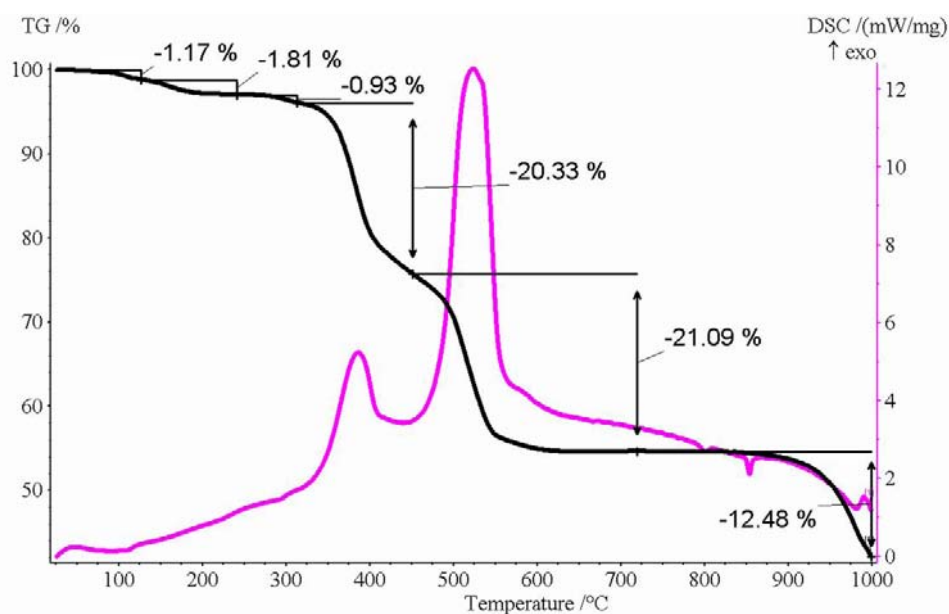


Figure 87. TG/DSC analysis of (PXDA) $CdSO_4$

First, the hydration water and amine absorbed on the sample surface are released. Then, the two weight losses (20.33% and 21.09%), from about 300 °C to 650 °C, are related to the complete loss of amine built in to the (PXDA)CdSO<sub>4</sub>. The last two exothermic peaks (at 800 and 850 °C) may be caused by the melting of products of thermal decomposition, for example, CdSO<sub>4</sub>. Finally, cadmium sulfate (CdSO<sub>4</sub>) remains.

In Figure 88 and 89, the XRD patterns of (PXDA)CdSO<sub>4</sub> as a function of temperature are presented.

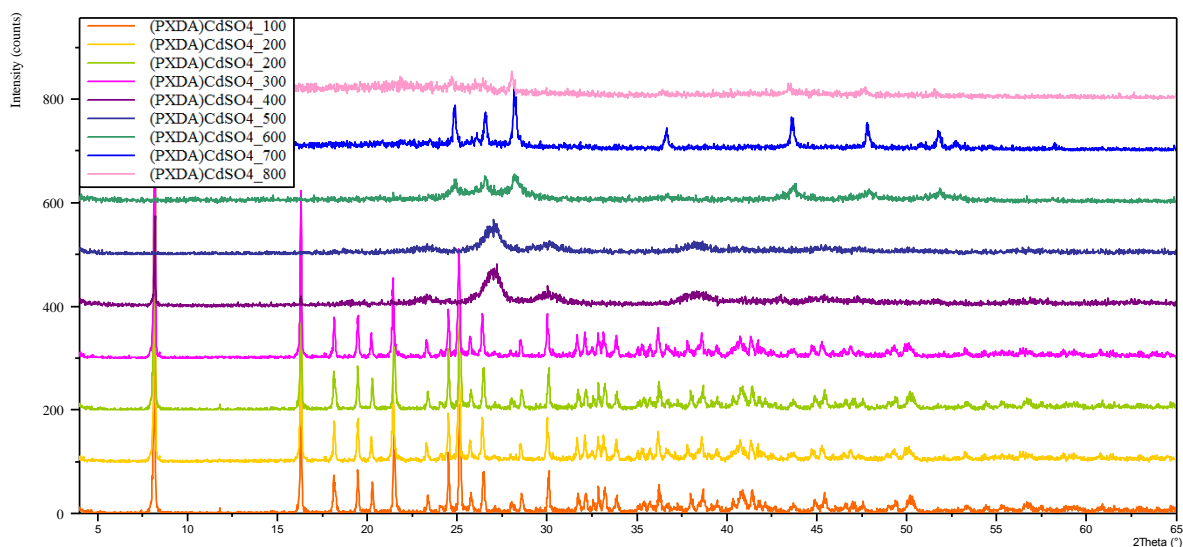


Figure 88. XRD patterns of (PXDA)CdSO<sub>4</sub> vs. temperature (helium atmosphere)

Hybrid materials are stable to 300 °C. At 400 °C all amines are removed and CdSO<sub>4</sub> (PDF 01-085-0673) appears. At 600 °C CdS (PDF 01-074-9663) is obtained. This phase remains stable to 800 °C.

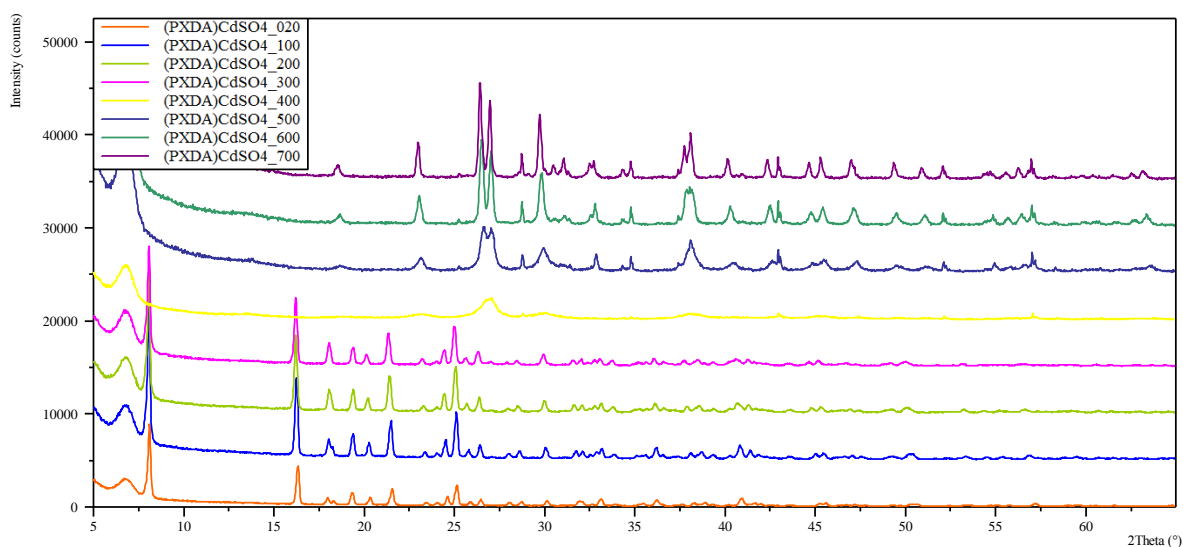


Figure 89. XRD patterns of (PXDA)CdSO<sub>4</sub> vs. temperature (air atmosphere)

As in the previous case, the amines are removed at 300 °C. At 500 °C CdSO<sub>4</sub> (PDF 01-085-0673) is obtained. This phase is stable to 700 °C.

Based on XRDP measurements vs. temperature (air atmosphere) for compounds (PXDA)ZnSO<sub>4</sub> and (PXDA)CdSO<sub>4</sub>, an intermediate product, crystallized in tetragonal crystal system, was detected at a temperature range of 300–400 °C. The cell parameters for (PXDA)ZnSO<sub>4</sub> compound are:  $a=b=9.661(5)$  Å,  $c=21.181(9)$  Å, while for (PXDA)CdSO<sub>4</sub>  $a=b=10.074(4)$  Å,  $c=21.864(8)$  Å. These results show that the initial orthorhombic structure ((PXDA)MSO<sub>4</sub>) recrystallizes into the tetragonal compounds of the type (PXDA)<sub>1/2</sub>MSO<sub>4</sub>, in which there is half of an amine molecule in each formal molecule. Because of the two-phase mixture, space group determination is very difficult, thereby hindering determination of the structure model.

#### 7.3.4 SEM analysis

SEM images of (MXDA)ZnSO<sub>4</sub> are presented in Figure 90. As can be seen, the obtained crystallites possess uniform morphology. The thin plates (thickness from 10 to 50 nm) with very uneven surfaces are the dominant phase. The crystallites are complex aggregates.

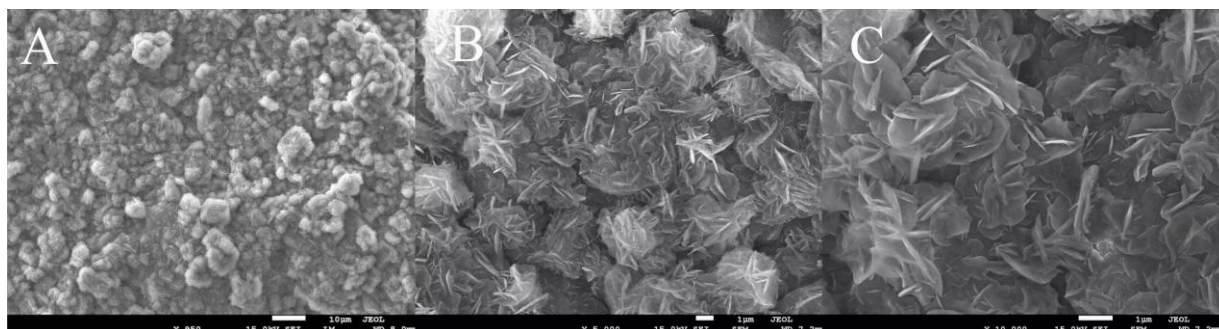


Figure 90. SEM images of (MXDA)ZnSO<sub>4</sub>

SEM images of (MXDA)CdSO<sub>4</sub> are presented in Figure 91. The aggregates of plate-like crystallites are clearly visible. They possess irregular edges and heterogeneous surfaces. The shape and thickness of crystallites vary greatly (from 0.1 µm to 1 µm).

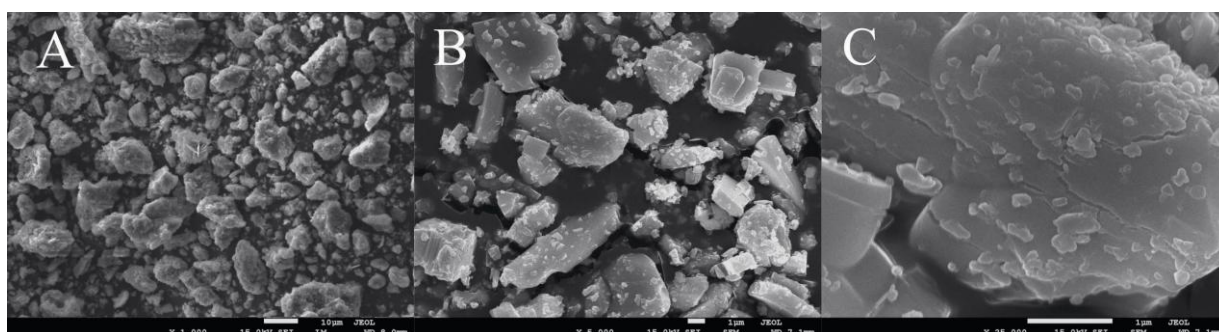


Figure 91. SEM images of (MXDA)CdSO<sub>4</sub>

In the case of (PXDA)ZnSO<sub>4</sub> (Figure 92) the crystallites are rectangular with different sizes. Their edges are regular and the surfaces are homogenous. The thickness of crystallites is about 0.1  $\mu\text{m}$ .

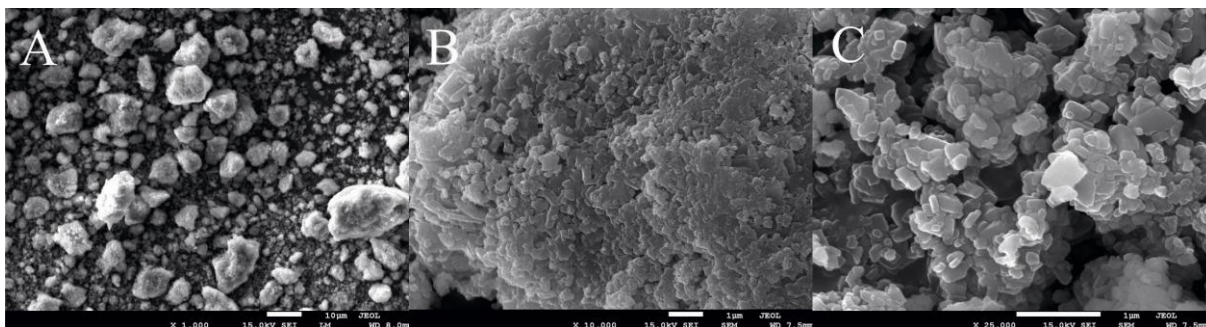


Figure 92. SEM images of (PXDA)ZnSO<sub>4</sub>

SEM images of (PXDA)CdSO<sub>4</sub> indicate that the crystallites are of very different sizes (from 0.1  $\mu\text{m}$  to several  $\mu\text{m}$ ) with thicknesses about 1  $\mu\text{m}$  or less. Their surfaces are quite homogenous and the edges are quite regular (Figure 93).

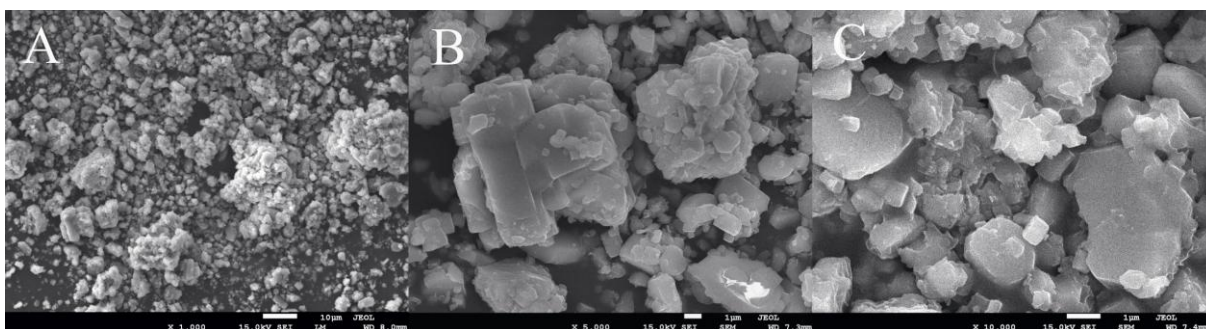


Figure 93. SEM images of (PXDA)CdSO<sub>4</sub>

## 7.4 Conclusion

Four materials of the type (diamine)MSO<sub>4</sub> (diamine – MXDA, PXDA; M-Zn, Cd) were synthesized using the solvothermal technique. All these materials crystallize in orthorhombic crystal system, but in different space groups: (PXDA)MSO<sub>4</sub> in Pnma, (MXDA)MSO<sub>4</sub> in P2<sub>1</sub>ma. Also, the cell parameters for compounds with the same amine but different metal atoms are quite similar (in the case of Cd atoms they are a little bit larger, which can be attributed to the ionic radii). These 3-D hybrid materials are built of diamines (MXDA, PXDA) forming coordination bonds with metal ions from infinite, parallel layers of the type –M–(SO<sub>4</sub>)–. Interesting, inorganic layers in “typical” MQ(amine)<sub>1/2</sub> and (amine)MSO<sub>4</sub> compounds are similar from a topological point of view: 6<sup>3</sup> in both cases. The SEM images show that the obtained materials are aggregates of plate-like crystals, but with different sizes and thicknesses. The TG-DSC analyses show that all materials are stable to about 300 °C, at

which point the release of amine is observed. In the case of (MXDA)ZnSO<sub>4</sub> and (PXDA)ZnSO<sub>4</sub> the final product is ZnO, while for (PXDA)CdSO<sub>4</sub> and (MXDA)CdSO<sub>4</sub> the final product is CdSO<sub>4</sub>. The results of XRPD vs. temperature are related to the atmosphere of measurement. In an air atmosphere, ZnO and CdSO<sub>4</sub> are the main products; in helium, ZnO and CdS.

## Chapter 8

## Obtaining pure semiconducting nanostructures from hybrid organic-inorganic precursors

### 8.1 Method of formation of semiconducting nanostructures

To form pure semiconducting nanostructures from hybrid organic-inorganic precursors, boiling in different solvents, mainly alcohols at various boiling points, were used. In this method, the synergic effect between temperature and reactant medium is sufficient to form aggregates of pure semiconductor II-VI. Two hybrid precursors,  $\text{ZnS}(1,3\text{-pda})_{1/2}$  and  $\text{ZnSe}(\text{MXDA})_{1/2}$ , were used in the formation of pure II-VI semiconductors.

#### *8.1.1 Synthesis methods with the use of different solvents*

Since different results can be obtained depending on the formation substrates used, these syntheses were carried out in three different variants: **1)** 40 ml of solvent and 0.005 mol of hybrid precursors were mixed and boiled about 3h under reflux; **2)** 40 ml of solvent, 0.005 mol of hybrid precursors and 10 ml of acetic acid were mixed and boiled about 3h under reflux; **3)** finally, 40 ml of solvent, 0.005 mol of hybrid precursors, 10 ml of acetic acid and 5 ml of formic acid were mixed and boiled about 3 h under reflux. As reaction mediums, acetonitrile [ $\text{CH}_3\text{CN}$ ], 1-octanol (abbreviated as octanol) [ $\text{C}_8\text{H}_{17}\text{OH}$ ], 1,6-hexanodiol (abbreviated as heksanodiol) [ $\text{C}_6\text{H}_{12}\text{OH}_2$ ], and paraffin oil were used.

The formation of pure semiconductors was also performed using microwave radiation. In the first experiment, the pure 40 ml of 1-octanol as a reaction medium and 0.005 mol of  $\text{ZnSe}(\text{MXDA})_{1/2}$  were used. In the second, 40 ml of octanol, 10 ml of acetic acid and 0.005 mol of  $\text{ZnSe}(\text{MXDA})_{1/2}$  were mixed. The suspensions were placed in a domestic microwave oven and heated 3 min. Then the precipitations were washed in propanol with water and dried at room temperature.

### 8.2 XRDP analysis of obtained II-VI semiconductors

The obtained samples were tested using the XRDP method. In Figure 94 and 95, the XRD patterns of  $\text{ZnS}(\text{pda})_{1/2}$  and  $\text{ZnSe}(\text{MXDA})_{1/2}$  after boiling in **(1)** acetonitrile **(2)** acetonitrile and acetic acid **(3)** acetonitrile, acetic acid and formic acid were presented.

The boiling temperature of acetonitrile is 81.6 °C. The use of acetonitrile as the only reaction medium does not cause the removal of amine in either case ( $\text{ZnS}(\text{pda})_{1/2}$  or  $\text{ZnSe}(\text{MXDA})_{1/2}$ ).

The precursors remain unchanged. However, the addition of acetic acid to the solution is sufficient to form ZnSe from  $\text{ZnSe}(\text{MXDA})_{1/2}$ .  $\text{ZnS}(\text{pda})_{1/2}$  is more resistant. The creation of pure ZnS occurs only if both acids (formic acid and acetic acid) are present in the reaction mixture. The size of crystallites was evaluated based on XRPD patterns. For ZnS (PDF 04-013-5951), it is about 6 nm. For ZnSe obtained by boiling in acetonitrile and acetic acid, it is about 8 nm (PDF 00-015-0105), while the addition of formic acid reduces the size to about 7 nm (PDF 01-08-0008).

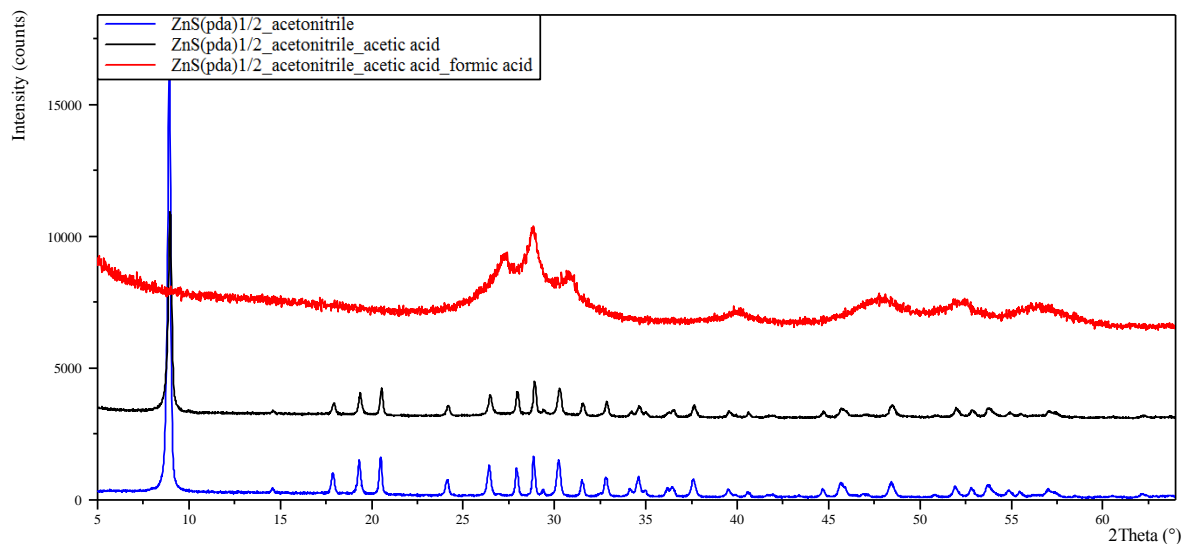


Figure 94. The results of treatment of  $\text{ZnS}(\text{pda})_{1/2}$  in acetonitrile; acetonitrile+acetic acid; acetonitrile+acetic acid+formic acid

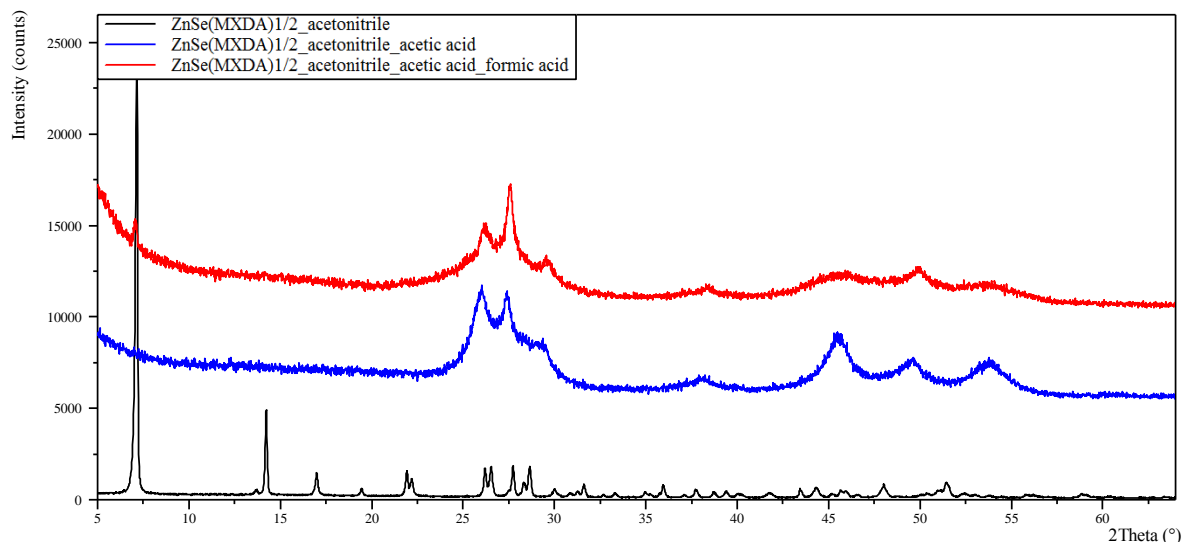


Figure 95. The results of formation of  $\text{ZnSe}(\text{MXDA})_{1/2}$  in acetonitrile; acetonitrile+acetic acid; acetonitrile+acetic acid+formic acid

Next, 1-octanol was tested as the reaction medium for the formation of a pure semiconductor. The same variants of mixed solvent were used as in the previous cases. In Figure 96, the XRD patterns of  $\text{ZnS}(\text{pda})_{1/2}$  after treatment with (1) octanol (2) octanol and acetic acid (3) octanol,

acetic acid and formic acid are presented. In Figure 97, the XRD patterns of  $\text{ZnSe}(\text{MXDA})_{1/2}$  under the same conditions of formation are shown.

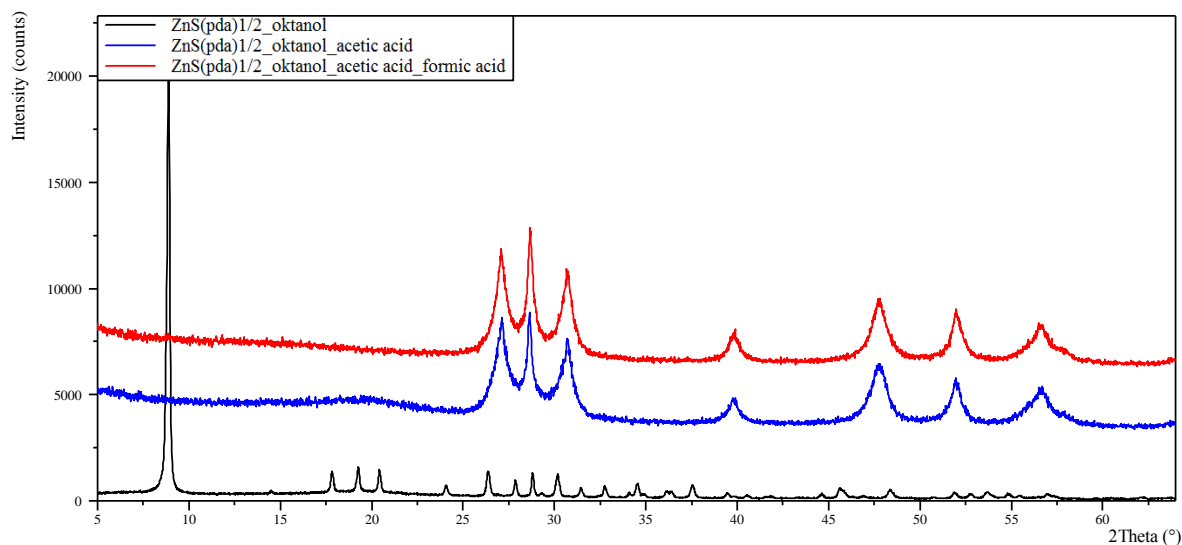


Figure 96. The results of treatment of  $\text{ZnS}(\text{pda})_{1/2}$  in octanol; octanol+acetic acid; octanol+acetic acid+formic acid

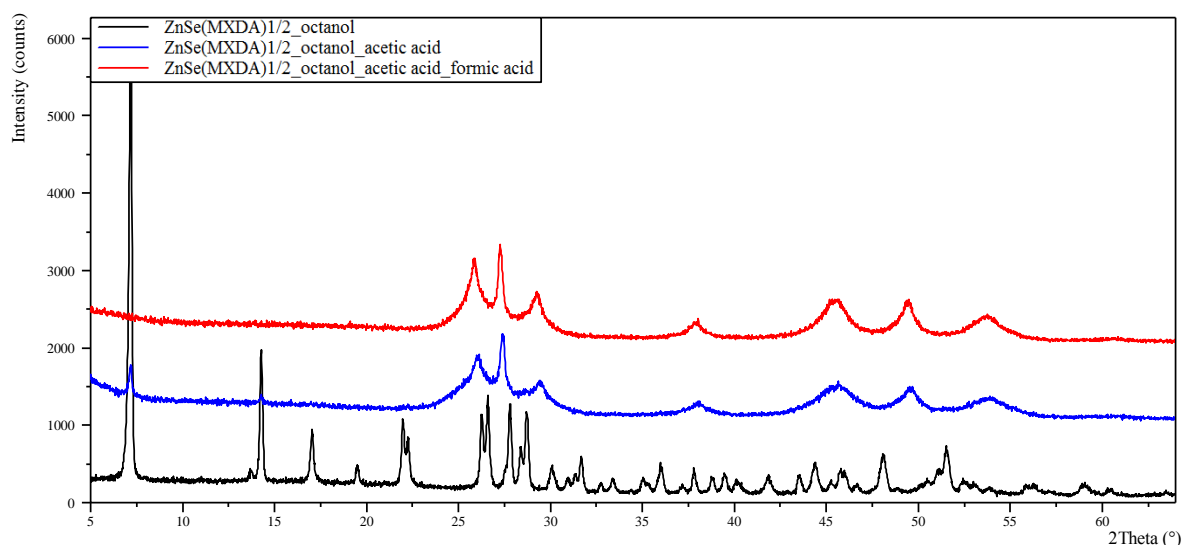


Figure 97. The results of treatment of  $\text{ZnSe}(\text{MXDA})_{1/2}$  in octanol; octanol+acetic acid; octanol+acetic acid+formic acid

The boiling point of octanol is 195 °C. Both hybrid precursors remain stable after boiling in octanol. However, both decompose to pure semiconductors of the type II-VI, even if only acetic acid is added to the reaction mixture. The calculated size of grains for ZnS, obtained by treatment in octanol and acetic acid (PDF 01-075-1534), is about 13 nm; for ZnS obtained by boiling in octanol, acetic acid and formic acid (PDF 01-075-1534), about 12 nm. The crystallite size of ZnSe formed in octanol and acetic acid (PDF 04-006-2041) is about 20 nm; for ZnSe obtained by formation in octanol, acetic acid and formic acid (PDF 04-006-2041), about 10 nm.

In Figure 98, the XRD patterns of samples obtained by treatment of  $\text{ZnS}(\text{pda})_{1/2}$  in hexanodiol (three variants) are presented.

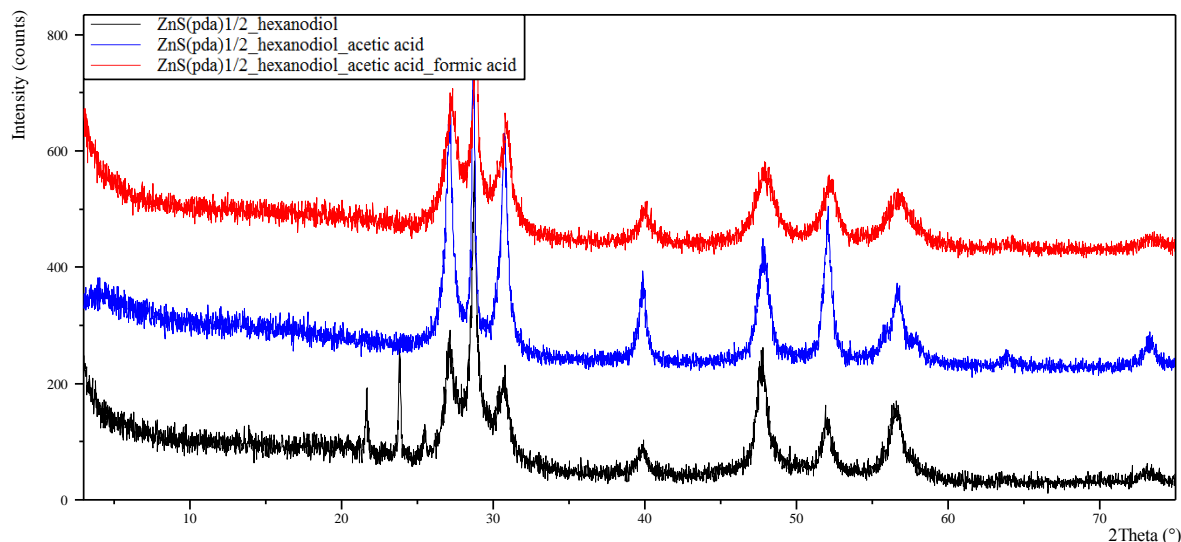


Figure 98. Results of treatment of  $\text{ZnS}(\text{pda})_{1/2}$  in hexanodiol; hexanodiol+acetic acid; hexanodiol+acetic acid+formic acid

In Figure 99, the XRD patterns of samples obtained after boiling  $\text{ZnSe}(\text{MXDA})_{1/2}$  in hexanodiol (three variants) are presented.

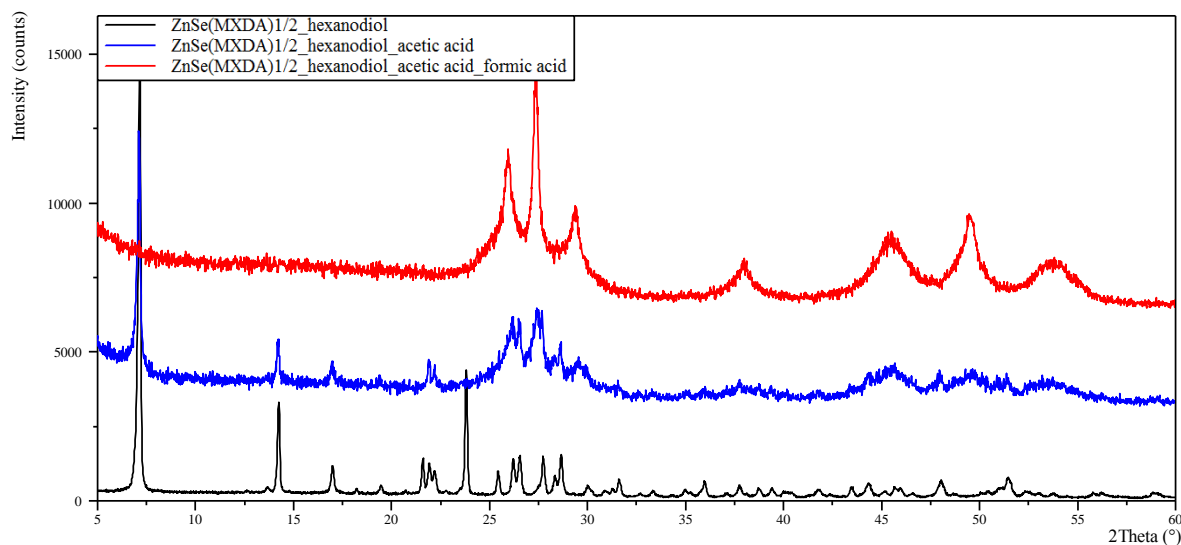


Figure 99. Results of treatment of  $\text{ZnSe}(\text{MXDA})_{1/2}$  in hexanodiol; hexanodiol+acetic acid; hexanodiol+acetic acid+formic acid

The boiling point of hexanodiol is 250 °C. In the case of  $\text{ZnS}(\text{pda})_{1/2}$ , boiling in hexanodiol alone is sufficient to form a pure ZnS semiconductor. However,  $\text{ZnSe}(\text{MXDA})_{1/2}$  seems much more resistant; even after boiling in acetic acid and hexanodiol, a small amount of initial (unreacted) compound is clearly visible. The estimated sizes of crystallites are: for ZnS boiled in hexanodiol (PDF 01-075-1534) 14 nm, for ZnS treated by hexanodiol and acetic acid (PDF 01-075-1534) 13 nm, and finally for ZnS boiled in hexanodiol, acetic acid and formic acid

(PDF 01-075-1534) 9 nm. The size of crystallites for ZnSe formed in hexanodiol and acetic acid (PDF 01-080-0008) is about 10 nm; for ZnSe treated in hexanodiol, acetic acid and formic acid (PDF 01-080-0008), about 8 nm.

In Figures 100 and 101, the XRD patterns for samples obtained after boiling in paraffin oil (three variants) are depicted. The boiling temperature of paraffin oil is 280 °C.

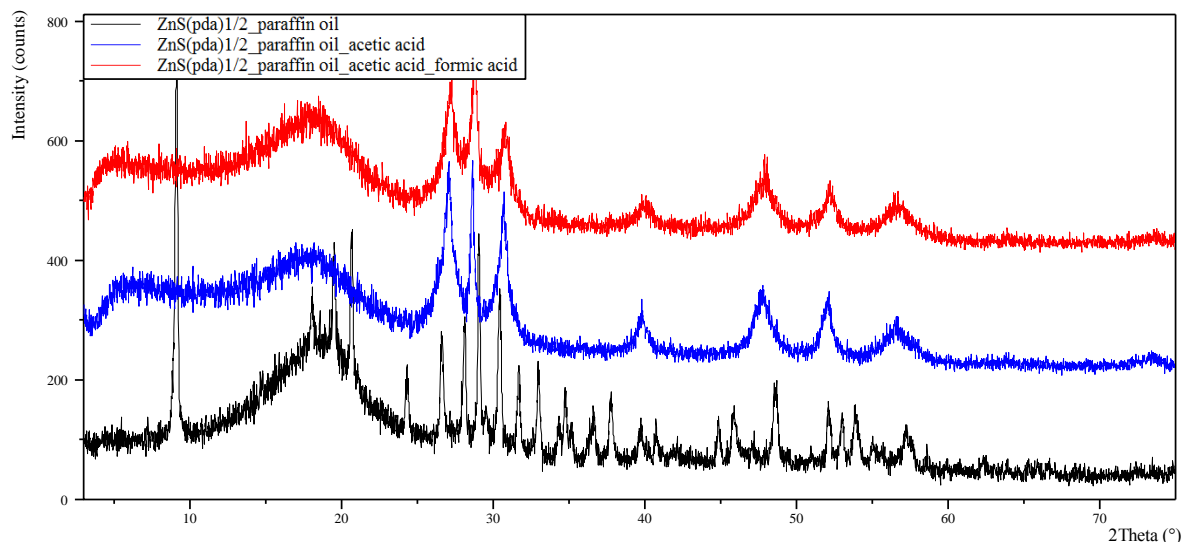


Figure 100. Results of treatment of ZnS(pda)<sub>1/2</sub> in paraffin oil; paraffin oil+acetic acid; paraffin oil+acetic acid+formic acid

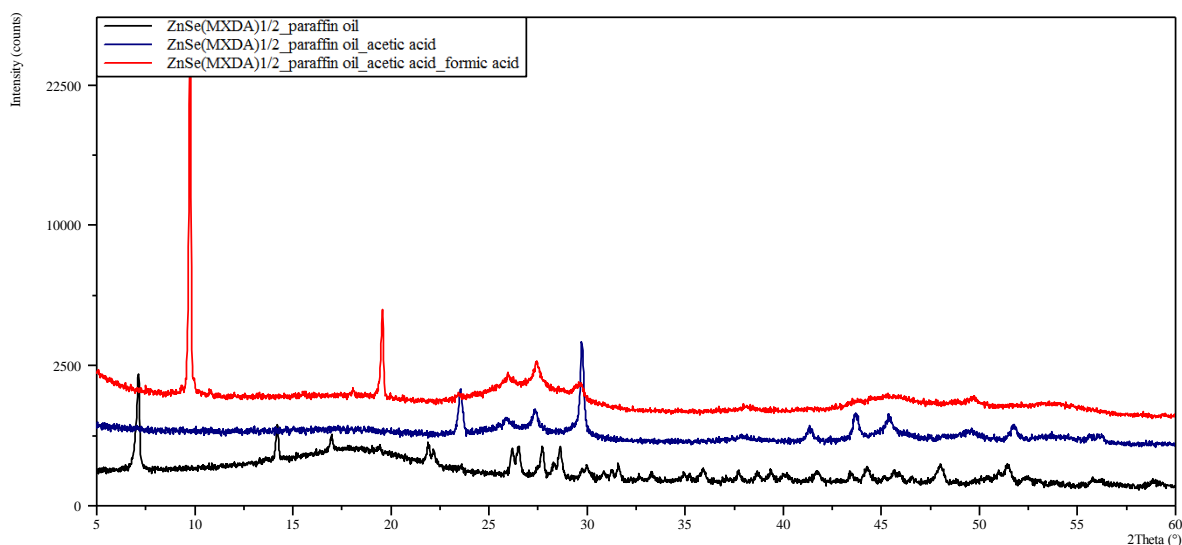


Figure 101. Results of treatment of ZnSe(MXDA)<sub>1/2</sub> in paraffin oil; paraffin oil+acetic acid; paraffin oil+acetic acid+formic acid

ZnS(pda)<sub>1/2</sub> is resistant to boiling in paraffin oil. However, the addition of acetic acid is sufficient to remove amines, and pure ZnS is obtained (PDF 04-006-2556) with a crystallite size of 10 nm. The size of ZnS crystallites (PDF 04-001-6854) obtained by treatment in paraffin oil, acetic acid and formic acid is about 7 nm. In the case where ZnSe(MXDA)<sub>1/2</sub> was used as a precursor, the pure phase of ZnSe is not obtained. Simple treatment in paraffin oil

does not change the precursor. However, by boiling in paraffin oil and acetic acid ZnSe (PDF 01-080-0008) and Se (PDF 00-042-1425) are obtained. The calculated size of ZnSe grains is about 5 nm. Formation in paraffin oil, acetic acid and formic acid causes the removal of amines from between adjacent layers and ZnSe (PDF 01-080-0008) and zinc formate (PDF 08-076-8283) are obtained.

Also, the formation of pure nanometer semiconductors was performed by boiling only in acetic acid and formic acid (Figure 102). As it turned out in these cases too, pure ZnS and ZnSe crystallites were obtained with sizes of 5 and 8 nm, respectively.

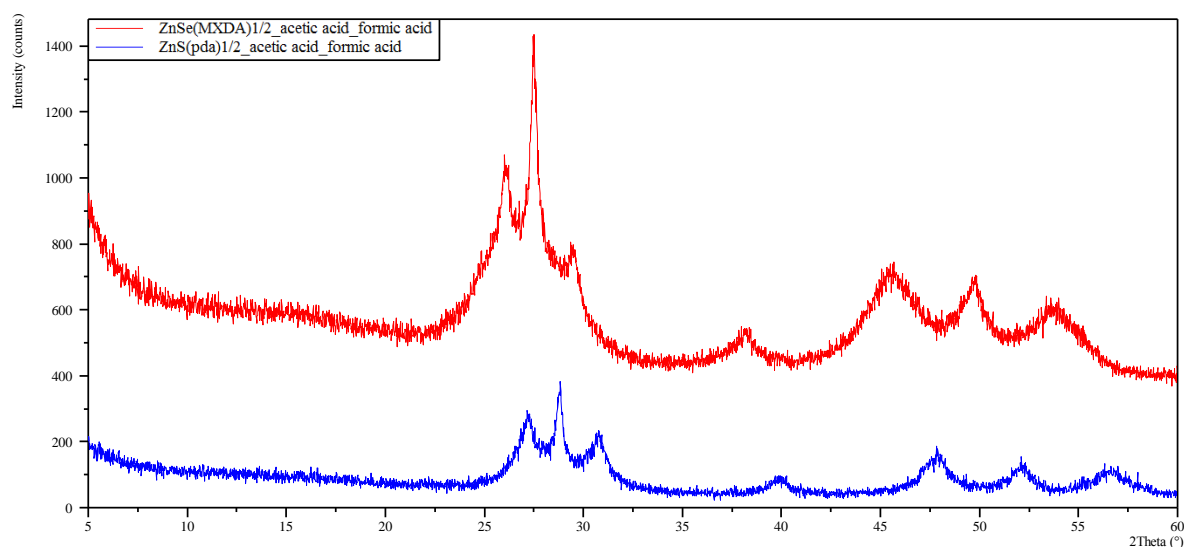


Figure 102. Results of treatment of ZnS(pda)<sub>1/2</sub> and ZnSe(MXDA)<sub>1/2</sub> in acetic acid and formic acid

In Figure 103, the XRD patterns for samples obtained by microwave radiation are presented.

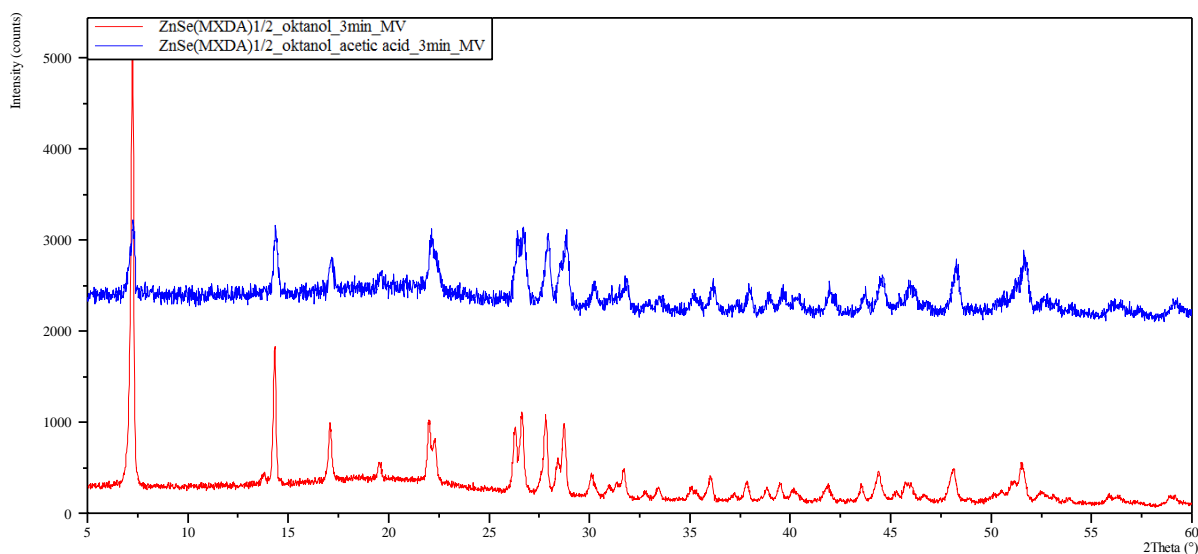


Figure 103. Results of treatment of ZnSe(MXDA)<sub>1/2</sub> in octanol; octanol and acetic acid using microwave radiation

As can be seen, the use of microwave radiation together with octanol and octanol with acetic acid to remove amines from  $\text{ZnSe}(\text{MXDA})_{1/2}$  causes no chemical changes (regardless of the formation of a spongy product). The precursor remains stable, regardless of the presence of acid in the reaction medium.

For better understanding of the impact of the reactant mixture on the size of crystallites, all obtained results are presented in Table 29.

Table 29. Results of formation of pure ZnS and ZnSe by boiling in different reaction mediums

Substrates	acetonitrile	octanol	hexanodiol	paraffin oil
<b>Precursor- <math>\text{ZnS}(\text{pda})_{1/2}</math></b>				
<b>Pure solvent</b>	precursor	precursor	14nm	precursor
<b>+acetic acid</b>	precursor	13 nm	13 nm	10 nm
<b>+acetic acid+formic acid</b>	6 nm	12 nm	9 nm	7 nm
<b>Precursor- <math>\text{ZnSe}(\text{MXDA})_{1/2}</math></b>				
<b>Pure solvent</b>	precursor	precursor	precursor	precursor
<b>+acetic acid</b>	8 nm	21 nm	10 nm	15 nm
<b>+acetic acid+formic acid</b>	7 nm	10 nm	8 nm	5 nm

As can be seen, the addition of acetic acid and then formic acid to the solvent affects the size of crystallites, which decreases along with increases in strength of the added acid. Also, in most cases, boiling in solvent is insufficient to removing amines. Analysis of diffraction patterns shows that the wurtzite phase was obtained.

### 8.3 Optical properties of obtained semiconductors

UV-vis spectroscopy studies were performed to investigate the optical properties of the obtained samples. As was observed in the case of  $\text{ZnS}(\text{pda})_{1/2}$ , the band gaps of most of the obtained semiconductors were almost the same as that of the bulk phase, which suggest that the bulk phase was reproduced. However, significant changes were observed for semiconductors obtained from  $\text{ZnSe}(\text{MXDA})_{1/2}$ . This can be correlated with aromatic amines which are not removed from the structures

Most surprising is that even in cases when amines were not removed, the band gaps changed. In Figures 104 and 105, the band gaps for samples obtained by boiling  $\text{ZnS}(\text{pda})_{1/2}$  and  $\text{ZnSe}(\text{MXDA})_{1/2}$ , respectively, in acetonitrile are presented.

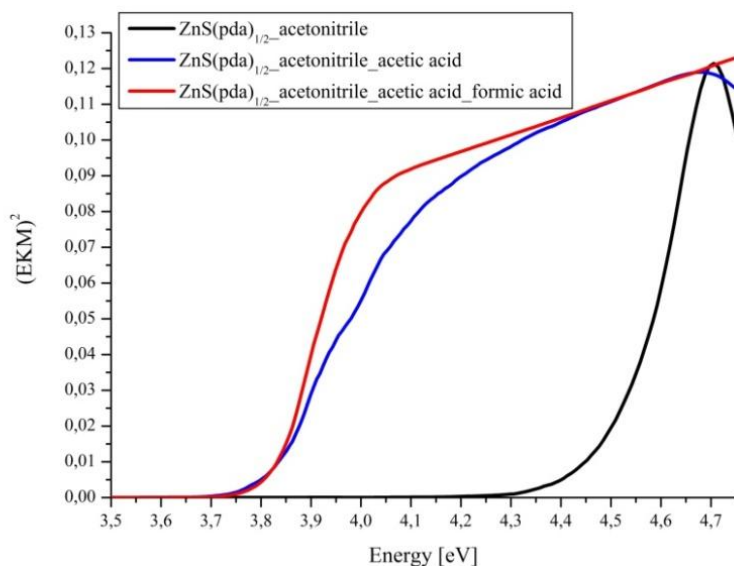


Figure 104. UV-vis spectra for samples obtained from  $\text{ZnS(pda)}_{1/2}$  by boiling in acetonitrile; acetonitrile and acetic acid; acetonitrile, acetic acid and formic acid

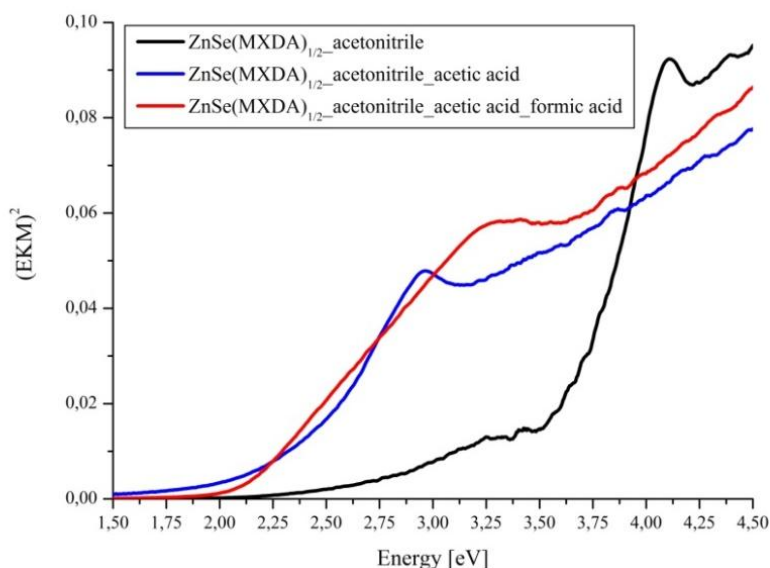


Figure 105. UV-vis spectra for samples obtained from  $\text{ZnSe(MXDA)}_{1/2}$  by boiling in acetonitrile; acetonitrile and acetic acid; acetonitrile, acetic acid and formic acid

In the case of  $\text{ZnS(pda)}_{1/2}$ , boiling in acetonitrile causes a decrease in the band gap from 4.75 eV to 4.5 eV (the amines **remain** in the structure). The same effect is observed in the case of formation of semiconductor in acetonitrile and acetic acid: the band gap decreases to about 3.85 eV. This value is closer to that typical for bulk phase. Finally, treatment in acetonitrile, acetic acid and formic acid removes the amines from the space between adjacent semiconductor layers; however, the volume phase is reconstructed and the band gap is 3.8 eV. In the case of  $\text{ZnSe(MXDA)}_{1/2}$ , after boiling in acetonitrile the band gap is 3.55 eV. Formation in acetonitrile with addition of organic acids results in a pure semiconductor with band gaps of 2.30 eV (acetonitrile, acetic acid) and 2.10 eV (acetonitrile, acetic acid and formic acid). As can be seen, the red shift is clearly visible and the band gaps are much

smaller than that in bulk materials (2.70 eV). Also, for  $\text{ZnSe}(\text{MXDA})_{1/2}$  treated in acetonitrile (1) and acetonitrile and both acids (3) the Urbach tail is clearly visible.

In Figure 106, the UV-vis spectra for samples obtained by boiling  $\text{ZnS}(\text{pda})_{1/2}$  precursor in three different variants of octanol-based solutions are presented.

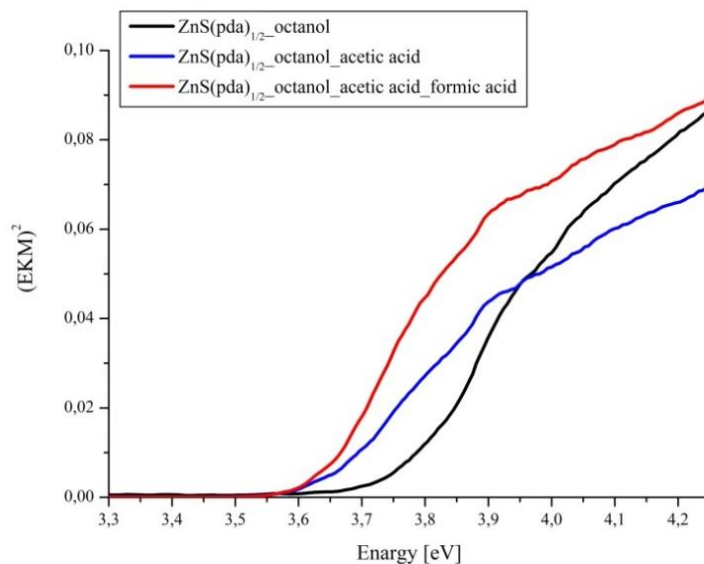


Figure 106. UV-vis spectra for samples obtained from  $\text{ZnS}(\text{pda})_{1/2}$  by boiling in octanol; octanol and acetic acid; octanol, acetic acid and formic acid

In each case, the band gap changes. For the sample obtained by boiling in octanol only, the band gap is 3.85 eV; for the sample obtained from octanol and acetic acid, 3.65 eV. The same value (3.65 eV) is obtained in the case of formation in octanol, acetic acid and formic acid.

In Figure 107, the UV-vis spectra for samples obtained by boiling  $\text{ZnSe}(\text{MXDA})_{1/2}$  in octanol (1); octanol and acetic acid (2); octanol, acetic acid and formic acid (3) are presented.

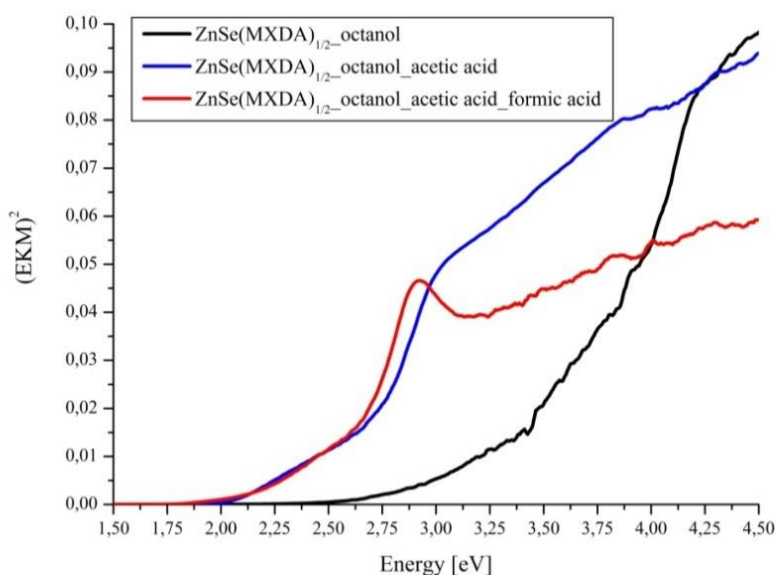


Figure 107. UV-vis spectra for samples obtained using  $\text{ZnSe}(\text{MXDA})_{1/2}$  by boiling in octanol; octanol and acetic acid; octanol, acetic acid and formic acid

Treatment of  $\text{ZnSe}(\text{MXDA})_{1/2}$  in octanol does not cause removal of amine; however, it changes the band gap, which just after synthesis is about 3.25 eV. After boiling in octanol and acetic acid, the band gap can be measured at 2.50 eV. After boiling in octanol, acetic acid and formic acid it is 2.60 eV, which is close to the typical value for bulk phase.

In Figure 108, the UV-vis spectra for samples obtained by boiling  $\text{ZnS}(\text{pda})_{1/2}$  in hexanodiol, hexanodiol and acetic acid, and hexanodiol, acetic acid and formic acid are presented.

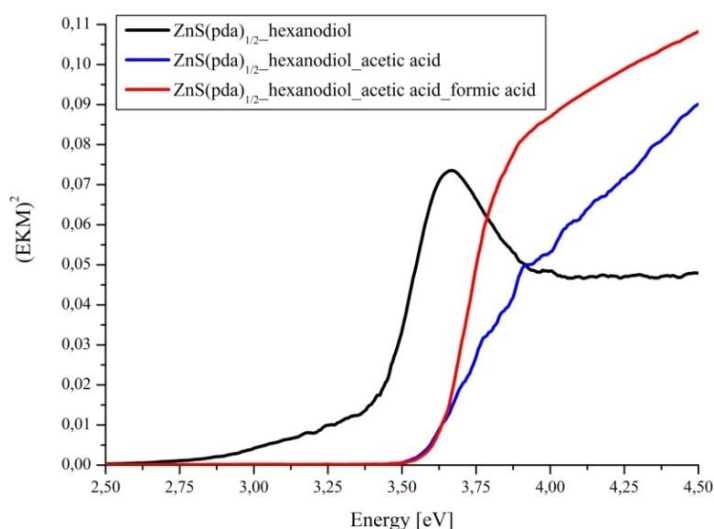


Figure 108. UV-vis spectra for samples obtained from  $\text{ZnS}(\text{pda})_{1/2}$  by boiling in hexanodiol; hexanodiol and acetic acid; hexanodiol, acetic acid and formic acid

Boiling of  $\text{ZnS}(\text{pda})_{1/2}$  in hexanodiol changes its optical properties; the band gap is 3.35 eV. The Urbach tail is clearly visible. Formation in hexanodiol and acetic acid changes the band gap to 3.50 eV; boiling in hexanodiol, acetic acid and formic acid changes the band gap to 3.60 eV.

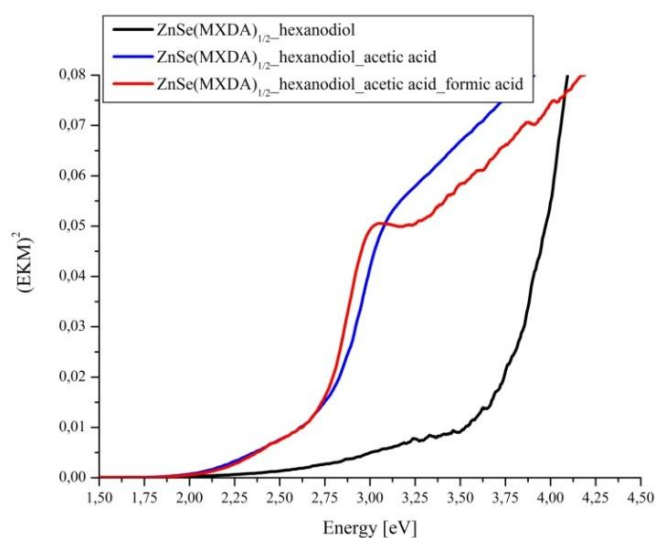


Figure 109. UV-vis spectra for samples obtained from  $\text{ZnSe}(\text{MXDA})_{1/2}$  by boiling in hexanodiol; hexanodiol and acetic acid; hexanodiol, acetic acid and formic acid

As a result of boiling  $\text{ZnSe}(\text{MXDA})_{1/2}$  in hexanodiol (Figure 109) the value of the band gap is 3.75 eV. After boiling in hexanodiol and acetic acid it is 2.70 eV, and after boiling hexanodiol, acetic acid and formic acid, a band gap of 2.75 eV is obtained. As can be seen, after removal of amines the optical properties are similar to those observed for bulk phase.

The UV-vis spectra obtained by boiling of  $\text{ZnS}(\text{pda})_{1/2}$  and  $\text{ZnSe}(\text{MXDA})_{1/2}$  in paraffin oil are presented in Figures 110 and 111.

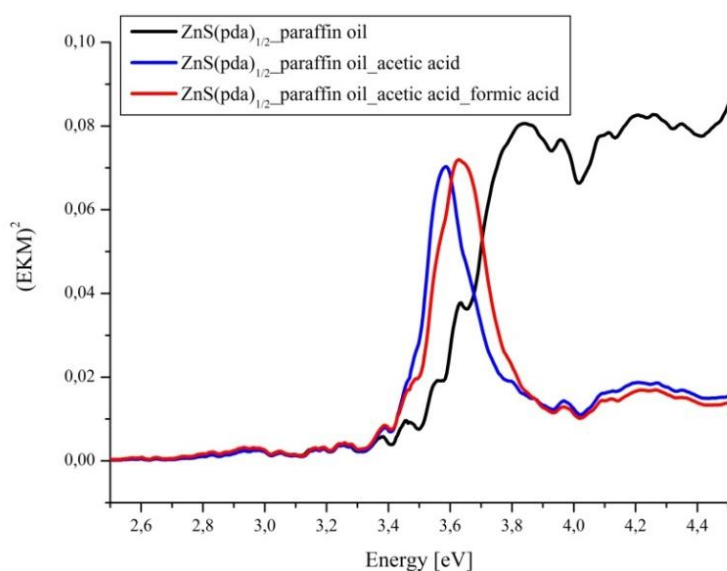


Figure 110. UV-vis spectra for samples obtained from  $\text{ZnS}(\text{pda})_{1/2}$  by boiling in paraffin oil; paraffin oil and acetic acid; paraffin oil, acetic acid and formic acid

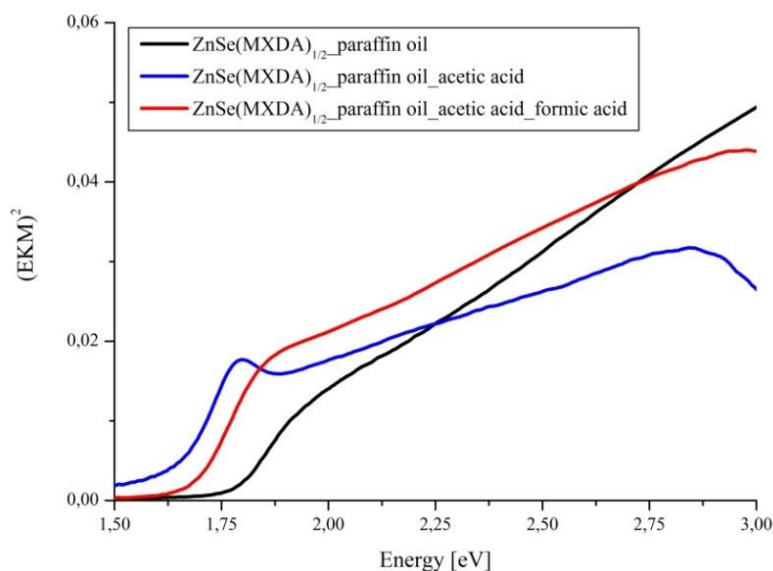


Figure 111. UV-vis spectra for samples obtained from  $\text{ZnSe}(\text{MXDA})_{1/2}$  by boiling in paraffin oil; paraffin oil and acetic acid; paraffin oil, acetic acid and formic acid

For  $\text{ZnS}(\text{pda})_{1/2}$  boiled in paraffin oil (1), the band gap is 3.50 eV. When  $\text{ZnS}(\text{pda})_{1/2}$  is boiled in paraffin oil, acetic acid (2), or paraffin oil, acetic acid and formic acid (3) the band gaps are similar, 3.40 eV. In both cases a very small red shift is visible. Nevertheless, interestingly, the

UV-vis curve is shaped like a Gaussian curve (also observed for  $\text{ZnS(pda)}_{1/2}$  boiled in hexanodiol). This may be related to the thickness of the conduction band, which in these cases seems to be thin. For  $\text{ZnSe(MXDA)}_{1/2}$  boiled in paraffin oil and organic acids, huge changes in optical properties were observed. The band gap calculated for the sample obtained by boiling in paraffin oil is 1.75 eV. Therefore, the red shift is about 1 eV. Smaller values of band gaps are found for samples formed in paraffin oil, acetic acid (2), and paraffin oil, acetic acid and formic acid (3), 1.55 eV and 1.65 eV, respectively. Such a large red shift may be caused by amines, which were not removed from the structures. Also, the layered structure might be preserved, as suggested by the XRD patterns.

The next two UV-vis spectra (Figure 112 and 113) present the results for  $\text{ZnS(pda)}_{1/2}$  and  $\text{ZnSe(MXDA)}_{1/2}$  boiled in acetic acid and formic acid.

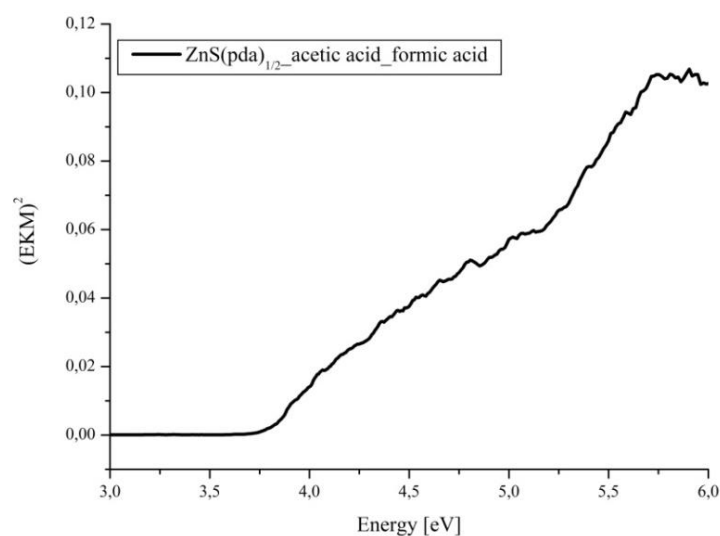


Figure 112. UV-vis spectra for samples obtained from  $\text{ZnS(pda)}_{1/2}$  by boiling in acetic acid and formic acid

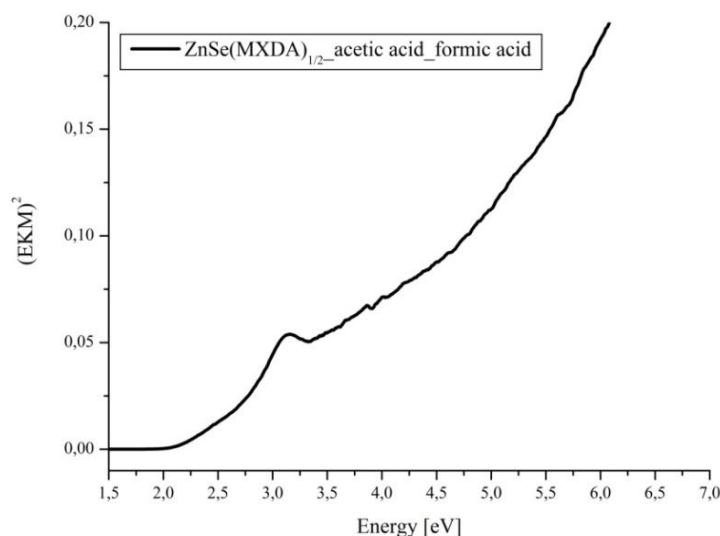


Figure 113. UV-vis spectra for samples obtained from  $\text{ZnSe(MXDA)}_{1/2}$  by boiling in acetic acid and formic acid

Treatment of  $\text{ZnS}(\text{pda})_{1/2}$  with acetic acid and formic acid causes removal of amines. Based on UV-vis spectra, two band gaps can result: 4.5 eV and 3.6 eV. The first value is quite similar to those obtained for hybrid materials, the second to bulk phase of ZnS. These results indicate that one part of the sample decomposes to bulk ZnS while another part remains unchanged. Analysis of UV-vis spectra of  $\text{ZnSe}(\text{MXDA})_{1/2}$  formed in acetic acid and formic acid shows a band gap about 2.5 eV, which is less than the typical value for bulk phases at 2.7 eV.

Also, UV-vis spectra were measured for  $\text{ZnSe}(\text{MXDA})_{1/2}$  treated with microwave radiation and octanol (Figure 114).

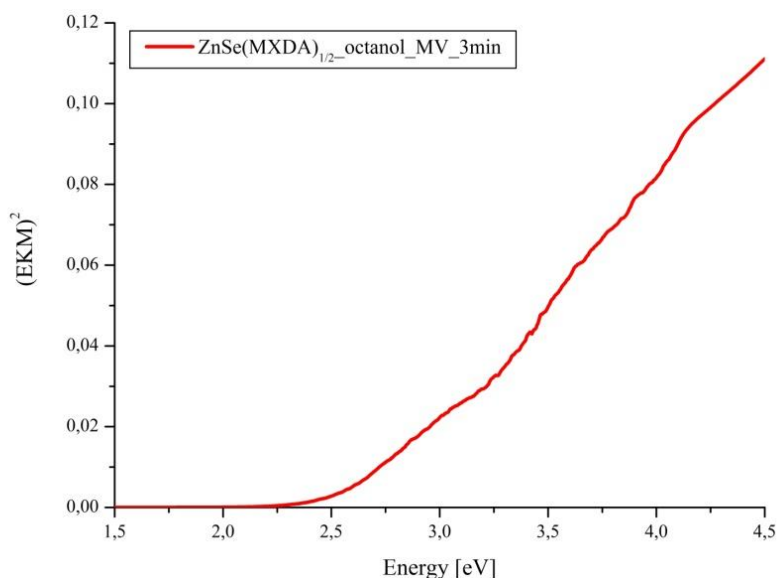


Figure 114. UV-vis spectra for samples obtained from  $\text{ZnSe}(\text{MXDA})_{1/2}$  formed in octanol and acetic acid using microwave radiation

Even though XRD analysis shows that amines are not removed, the band gap obtained for sample treated with microwave irradiation and octanol is 2.70 eV, which is a typical value for bulk phase.

### 8.3.1 Conclusion for optical properties of obtained samples

As indicated by UV-vis spectra, in most cases removing amines causes the collapse of semiconducting layers and re-obtaining bulk phase with the typical band gap. This process is unintentional. However, in a few cases, an interesting modification of optical properties can be observed. For example, boiling in pure reaction medium does not cause removing of amines; nevertheless, the band gap changes slightly in comparison to “normal hybrid materials.” Also very interesting is the “red shift,” which occurs mostly for samples formed from  $\text{ZnSe}(\text{MXDA})_{1/2}$ . Such phenomena can be caused by single aromatic amines preserved

in the structures or by numerous vacancies or defects which could arise in the course of formation of pure semiconductors. The presence of the rest of the amines may cause the charge transfer effect. The band gaps calculated from UV-vis spectra are presented in Table 30.

Table 30. Band gaps of obtained compounds (blue indicates “blue shift,” red “red shift” in comparison to bulk phases of the semiconductor\*)

Substrates	acetonitrile	octanol	hexanodiol	paraffin oil
<b>Precursor- ZnS(pda)<sub>1/2</sub></b>				
Pure solvent	4.50 eV	3.85 eV	3.35 eV	3.50 eV
+acetic acid	3.85 eV	3.65 eV	3.50 eV	3.40 eV
+acetic acid+formic acid	3.80 eV	3.65 eV	3.60 eV	3.40 eV
<b>Precursor- ZnSe(MXDA)<sub>1/2</sub></b>				
Pure solvent	3.55 eV	3.25 eV	3.75 eV	1.75 eV
+acetic acid	2.30 eV	2.50 eV	2.70 eV	1.55 eV
+acetic acid+formic acid	2.10 eV	2.60 eV	2.75 eV	1.65 eV

\*ZnS – band gap of bulk phase is 3.6eV (zinc blende phase), 3.8 eV (wurzite phase), ZnSe – band gap of bulk phase is 2.7 eV.

One more question needs to be considered regarding the optical properties of semiconductors obtained from hybrid organic-inorganic materials: namely, in the UV-vis spectra of many samples, Urbach tails<sup>80</sup> are clearly visible. This phenomenon can be regarded as a measure of disorder in the system, which has two sources: in crystalline phase it is related to thermal disorder due to atomic vibrations (at a high temperature), and in the general case is accounted for by structural disorder. In a single material both disorders were additive. In my samples, mainly due to the low temperature of measurement (room temperature), the greater contribution is made by structural disorder caused by the noncrystalline location of the atoms. However, the temperature factor cannot be excluded.<sup>81</sup>

#### 8.4 SEM images of obtained materials

The morphology of the samples was investigated using a scanning electron microscope. Unfortunately, the materials obtained by treatment in paraffin oil as a reaction medium were wet (even after being washed in n-hexane and dried at 80 °C for 6 days), which prevented this type of analysis. For the others, the obtained images are presented below.

Figure 115 presents SEM images of samples obtained by boiling  $\text{ZnS}(\text{pda})_{1/2}$  in acetonitrile as a reaction medium.

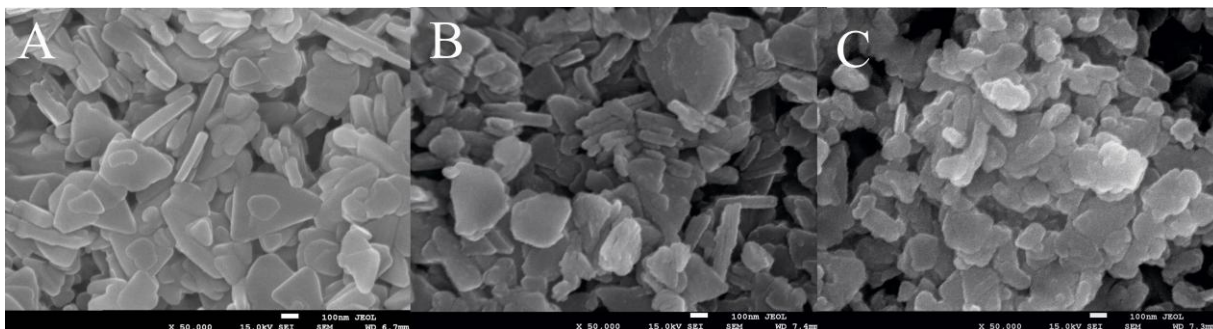


Figure 115. SEM images of samples obtained of  $\text{ZnS}(\text{pda})_{1/2}$  by boiling in: **A)** acetonitrile **B)** acetonitrile and acetic acid **C)** acetonitrile, acetic acid and formic acid

After boiling in pure acetonitrile, the crystallites are in the form of a prism. Their surface is homogenous and the edges are smooth. The thickness of the crystallites is less than 50 nm. Along with the increasing acidity of the reaction medium (through adding an acid), the edges become more rugged and irregular, while the surface becomes rougher.

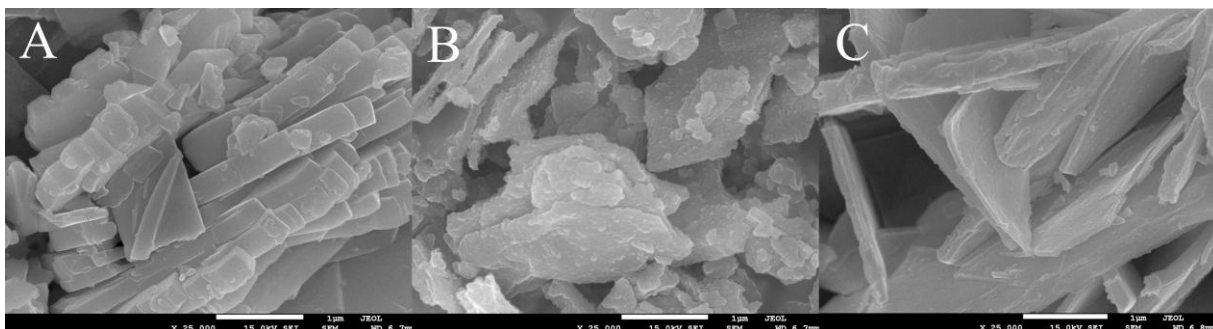


Figure 116. SEM images of samples obtained of  $\text{ZnSe}(\text{MXDA})_{1/2}$  by boiling in: **A)** acetonitrile, **B)** acetonitrile and acetic acid, **C)** acetonitrile, acetic acid and formic acid

In the case of  $\text{ZnSe}(\text{MXDA})_{1/2}$  boiled in acetonitrile (Figure 116) the crystallites have a platey form. Their thickness decreases along with the increasing acidity of the solutions. Therefore, after boiling in acetonitrile, this thickness is about 0.5  $\mu\text{m}$ ; after treating in acetonitrile and acetic acid it is about 100 nm; and finally, crystallites obtained by formation in acetonitrile, acetic acid and formic acid range from 0.5  $\mu\text{m}$  to 10 nm thick, with predominantly thinner forms. Simple treatment with acetonitrile does not impact morphology. However, the addition of acid causes the surface to become more heterogeneous and the edges more ragged (the same effect was observed in the previous case).

To compare the impact of the reaction mediums on morphology, the samples obtained by boiling in acetonitrile, octanol, hexanediol (with both acids) were analyzed. The results are presented in Figure 117 for  $\text{ZnS}(\text{pda})_{1/2}$  and in Figure 118 for  $\text{ZnSe}(\text{MXDA})_{1/2}$ .

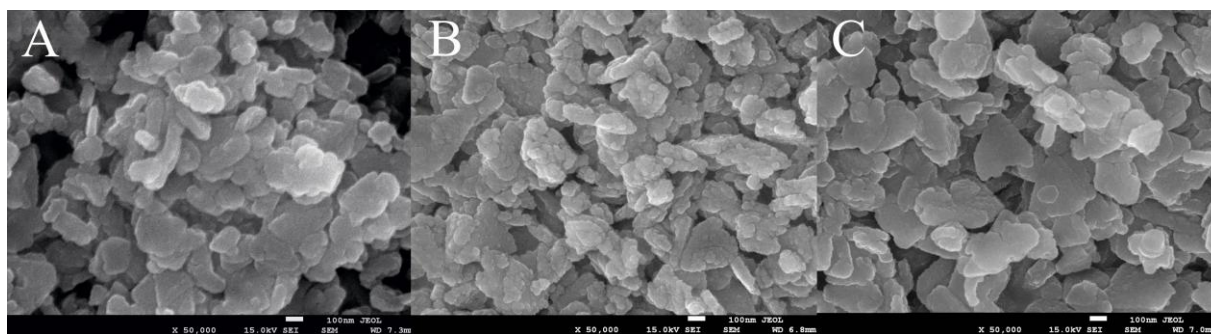


Figure 117. SEM images of  $\text{ZnS}(\text{pda})_{1/2}$  boiled in: **A)** acetonitrile, acetic acid and formic acid, **B)** octanol, acetic acid and formic acid, **C)** hexanodiol, acetic acid and formic acid

The crystallites adopt the form of a prism with irregular edges and a rough surface. However, as can be seen, the most heterogeneous morphology is possessed by crystallites treated with octanol, acetic acid and formic acid.

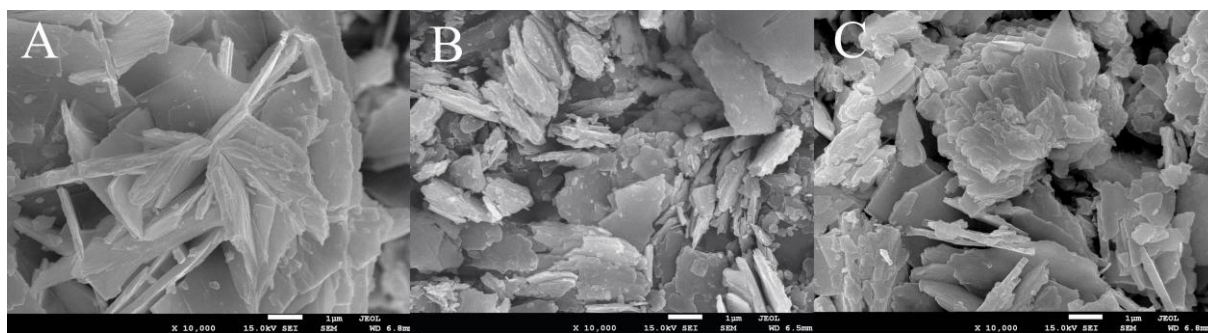


Figure 118. SEM images of samples obtained by boiling of  $\text{ZnSe}(\text{MXDA})_{1/2}$  in: **A)** acetonitrile, acetic acid and formic acid, **B)** octanol, acetic acid and formic acid, **C)** hexanodiol, acetic acid and formic acid

As can be seen, the crystallite surface is heterogeneous and the edges are ragged. The crystallites possess layered structures and are aggregated.

Separate analysis was performed for both samples boiled only in acetic and formic acid. The images are presented in Figures 119 and 120.

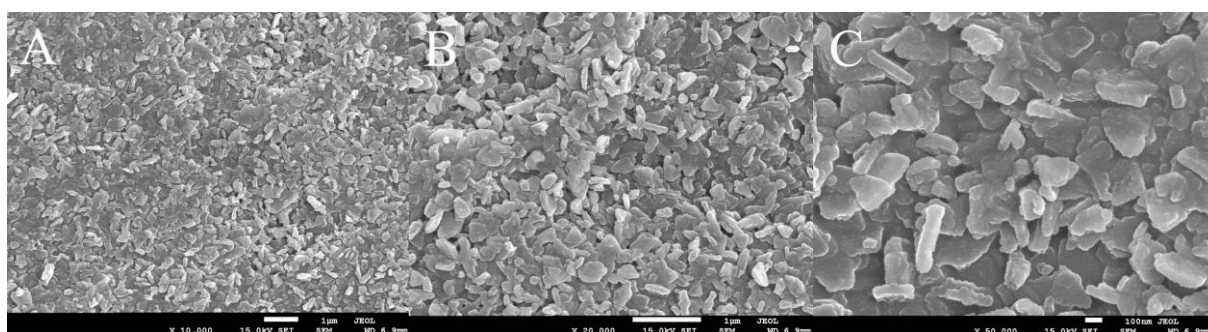


Figure 119. SEM images of samples obtained by boiling  $\text{ZnS}(\text{pda})_{1/2}$  in acetic acid and formic acid

The obtained crystallites, as in the previous cases, are prisms with a thickness about 50 nm. The edges are irregular and the surface is heterogeneous.

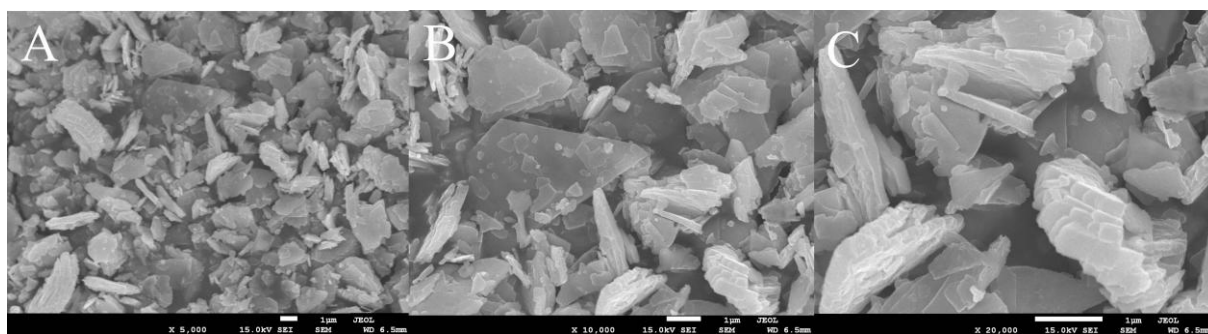


Figure 120. SEM images of samples obtained by boiling  $\text{ZnSe}(\text{MXDA})_{1/2}$  in acetic acid and formic acid

The crystallites possess a platy habit and are aggregated. It seems as though two phases were obtained, the first with regular edges and homogenous surfaces and the second more heterogeneous with jagged edges and surfaces.

The morphology of sample obtained by treating with microwave radiation (Figure 121) is quite interesting. Two different phases are clearly visible: layered and porous forms.

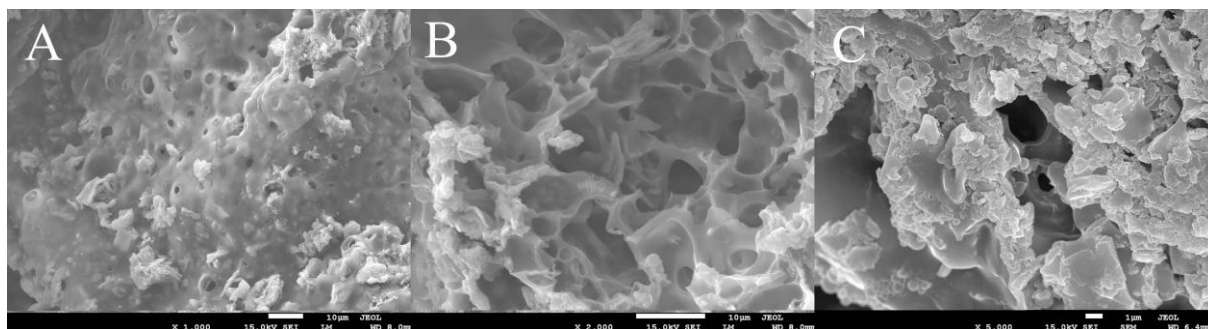


Figure 121. SEM images of samples obtained by boiling  $\text{ZnSe}(\text{MXDA})_{1/2}$  in octanol using microwave radiation

#### 8.4.1 Conclusion

In both cases, boiling in different reaction mediums does not cause drastic morphology transformations. However, some changes in comparison to hybrid precursors can be observed, in particular in the case of  $\text{ZnSe}(\text{MXDA})_{1/2}$ . To better illustrate this phenomenon, Figure 122 A, B shows the precursors ( $\text{ZnS}(\text{pda})_{1/2}$  and  $\text{ZnSe}(\text{MXDA})_{1/2}$ ).

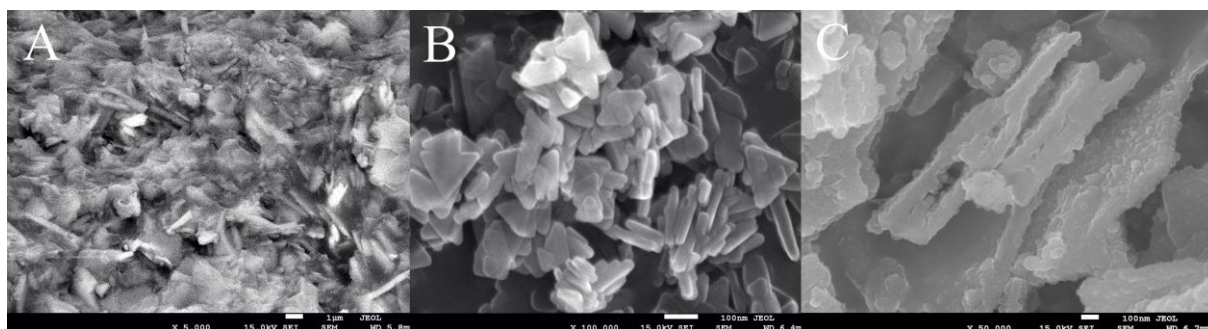


Figure 122. SEM images of A) precursor of  $\text{ZnSe}(\text{MXDA})_{1/2}$  B) precursor of  $\text{ZnS}(\text{pda})_{1/2}$  C) sample obtained by boiling in acetonitrile and acetic acid

As can be seen, the  $\text{ZnSe}(\text{MXDA})_{1/2}$  precursor looks quite different than after formation – the crystallites possess a platy habit (as they do after boiling) but are aggregated. However, even simple treatment in pure solvent causes them to separate. Along with the increasing acidity of the reaction medium, the crystallites become thinner and simultaneously more heterogeneous, a phenomenon clearly visible in Figure 122C. Such behavior can be correlated with removing amines from the structure. In the case of  $\text{ZnS}(\text{pda})_{1/2}$  the general shape of crystallites remains stable; however, the surface and the edges become rougher.

Despite the fact that the most significant changes in morphology were observed in the case of microwave radiation use, the amines were not removed. This suggests that in the next step, more drastic measures need to be employed to obtain pure semiconductor. In my opinion, however, formation using microwaves is worth further examination.

## **8.5 Conclusion**

Four different solvents in three different variants were used to form pure semiconducting nanostructures. Only in one case, using pure solvents as a reaction medium (boiling  $\text{ZnS}(\text{pda})_{1/2}$  in octanol) was pure semiconductor obtained; in others, treatment by pure solvent alone was not sufficient to remove amines. Adding acids (formic and acetic acids) to the reaction medium enabled the formation of semiconducting nanostructures. The size of obtained crystallites was strongly related to the type of reaction medium. As was observed, along with the increasing acidity of the mixture, the size of crystallites decreases. Such method can be used to control the size of semiconducting nanocrystallites.

The optical properties of the obtained samples strongly depended on the type of amine built in the hybrid precursors. Specifically, in the case of  $\text{ZnS}(\text{pda})_{1/2}$ , in most cases the bulk phase was reconstructed, with typical band gap values. However, in the case of  $\text{ZnSe}(\text{MXDA})_{1/2}$  the optical properties changed significantly. The red shift was clearly visible, even at about 1 eV. This phenomenon can be explained by the presence in the structure of a small amount of amines with aromatic rings, which were not removed. Such change of optical properties can bring new potential application of these semiconductors.

Finally, SEM investigations, show that the morphology of the samples did not change drastically in comparison to the hybrid precursor (mostly in the case of  $\text{ZnS}(\text{pda})_{1/2}$ ). In general, the shape of crystallites was preserved; however, they became more heterogeneous: the surface became rougher and the edges more irregular. It should be also emphasized that size of crystallites calculated based on XRD patterns are different than values obtained by

SEM investigation. That is due to the fact that in SEM images the aggregates of crystallites are visible.

The trials of using microwave radiation to remove amines were performed. The XRD patterns suggest that the precursors are stable. Probably the more chemically active ingredients may improve morphology and properties of obtained materials.

## Chapter 9

### Synthesis of nanometric ZnS using microwave radiation

#### 9.1 Materials and synthesis procedure

Zinc sulfate monohydrate [ZnSO<sub>4</sub>·H<sub>2</sub>O] was purchased from Mach Chemikálie spol. s r.o.; thiourea [CS(NH<sub>2</sub>)<sub>2</sub>], 25 wt.% solution of ammonia in water [NH<sub>3</sub>·H<sub>2</sub>O] and ethanol [C<sub>2</sub>H<sub>5</sub>OH] were bought from Lach-Ner, s.r.o.; thioacetamide [CH<sub>3</sub>CSNH<sub>2</sub>] was purchased from Sigma-Aldrich. All reactants were used without purification.

##### 9.1.1 Method of synthesis

The samples were obtained using microwave irradiation, by two different synthesis routes. In both, zinc sulfate monohydrate was the source of zinc cations, but in the first route the source of sulfur was thioacetamide and in the second thiourea. The use of thiourea instead of thioacetamide was dictated by its lower price, which is particularly important for potential applications.

In the first synthesis route (**I**), the sample was obtained using 0.025 mol of zinc sulfate monohydrate, 0.05 mol of thioacetamide and 40 ml of distilled water. All reactants were homogenized using a magnetic stirrer (time: about 2 h). Then the mixture was heated in a domestic microwave oven (3 min, at microwave power about 350 W). Finally the precipitate was filtered and washed several times using ethanol. The resulting product was white.

In the second synthesis route (**II**), 0.02 mol of zinc sulfate monohydrate and 0.02 mol of thiourea were placed in separate beakers and both were dissolved in 12 ml of 25% ammonia. The solutions were separately stirred using an electromagnetic stirrer (about 1 min), after which they were combined and heated for 6 min in the microwave oven. At the end of this time, the ammonia had evaporated and a solid yellow product remained in the vessel. The product was washed several times with ethanol. Finally the sample changed to a white powder. Because of the lower cost of synthesis and thus a higher probability of potential application, the sample based on thiourea, as a source of sulfur, became the subject of wide-ranging analysis.

##### 9.1.2 Photodegradation activity: the preliminary tests.

The discoloration of acid orange 7 (AO7) solution was used as a measure of the photodegradation activity of the obtained ZnS nanoparticles. The experiment was prepared as

follows: 0.05 g of ZnS photocatalyst and 5 ml of AO7 aqueous solution with a concentration equal to  $6.259 \times 10^{-4} \text{ mol dm}^{-3}$  were dissolved in 65 ml of distilled water. Then this suspension was stirred in the dark for 1 h, after which absorbance  $A_0$  at 480 nm was measured using a CINTRA 303 UV-Vis spectrometer. Finally, the solution was irradiated by radiation with a wavelength of 254 nm and, at selected time intervals, absorbance at 480 nm was measured to give the value  $A_T$ . The photocatalytic activity (PA) of ZnS in AO7 degradation was calculated using the equation:

$$PA = \left[ 100 - \left( \frac{A_T}{A_0} \right) * 100 \right] \quad (52)$$

## 9.2 Analysis of the samples

In Figure 123, the XRD patterns of obtained materials are presented. The results clearly indicate that ZnS nanoparticles (zinc blende type) were obtained. Three peaks are associated with planes (111), (220) and (311). The crystallite sizes were calculated using the Scherrer equation. For sample (I) the calculated value is 4 nm, while for sample (II) it is 3 nm.

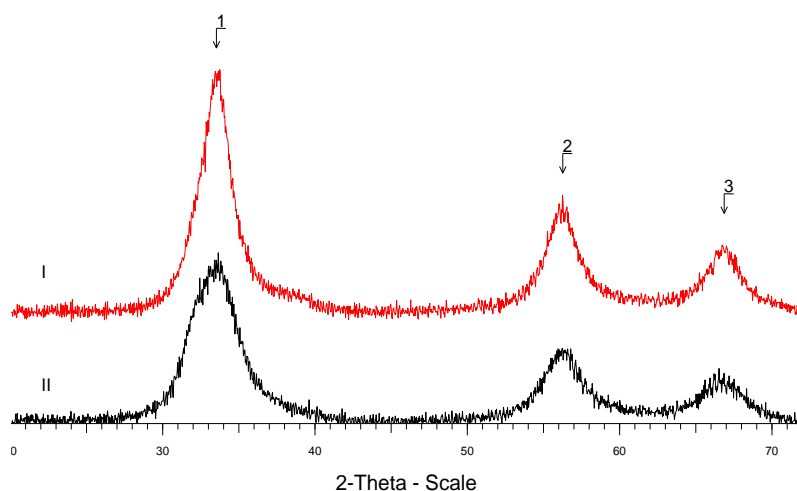


Figure 123. X-ray powder diffraction patterns of samples: (I)- ZnS\_thioacetamide and (II)- ZnS\_thiourea (1...ZnS (111), 2...ZnS (220) and 3...ZnS (311))

The SEM investigation shows that the crystallites are aggregated (Figure 124). As can be seen, they are very small, with a somewhat spherical shape.

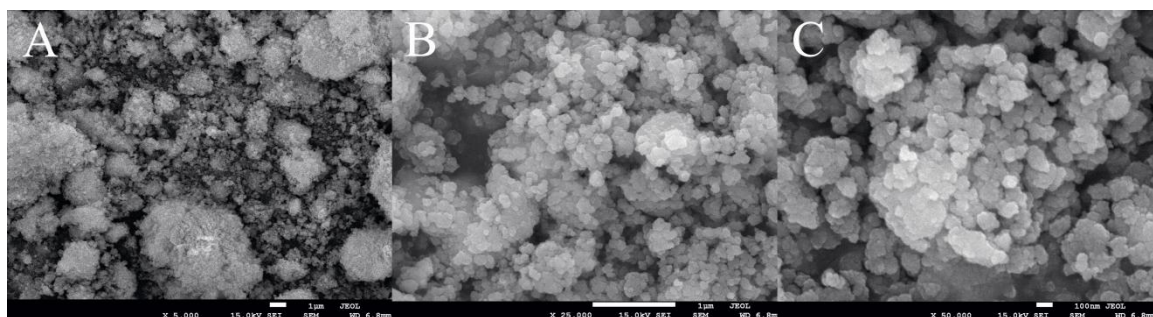


Figure 124. SEM images of the ZnS obtained by the use of thiourea

The optical properties of both samples were also studied using UV-vis spectroscopy. The obtained results (Figure 125 and 126) are presented below. The values of band gaps of both samples are quite similar to those typical for bulk semiconductors. Thus, ZnS obtained with thioacetamide as a source of sulfur is about 3.55 eV, and ZnS obtained with thiourea about 3.50 eV. In both cases the Urbach tail is clearly visible.

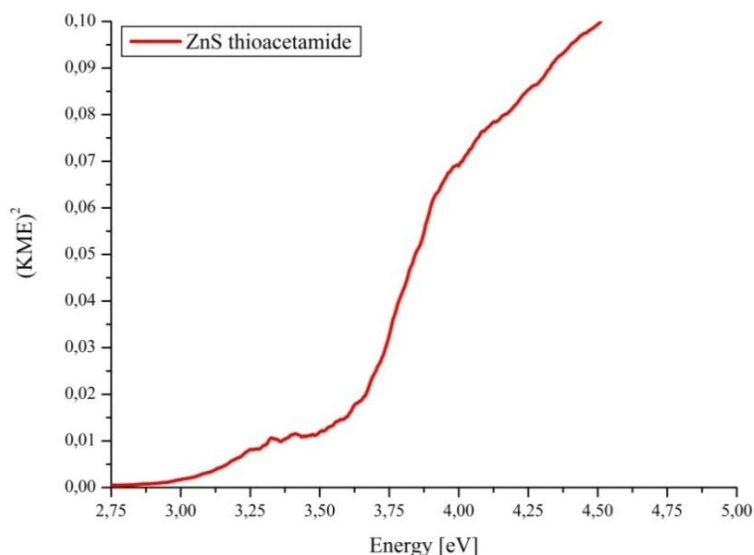


Figure 125. UV-vis spectra of ZnS obtained with thioacetamide

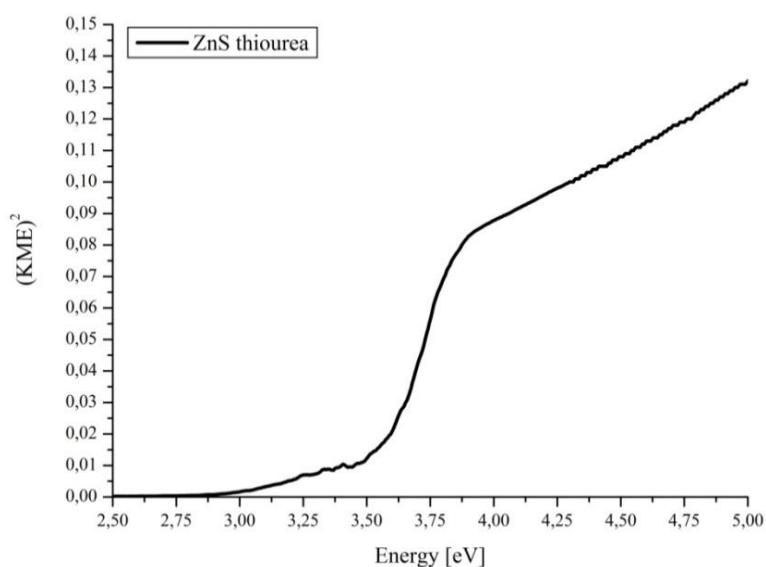


Figure 126. UV-vis spectra of ZnS obtained with thiourea

### 9.3 Preliminary tests of photodegradation activity

As was mentioned, the photodegradation activity of both samples (ZnS after being treated with thiourea and thioacetamide) was tested using discoloration of AO7. In Figure 127, the time dependency of the changes in AO7 absorption maxima as a result of UV irradiation is presented for both samples.

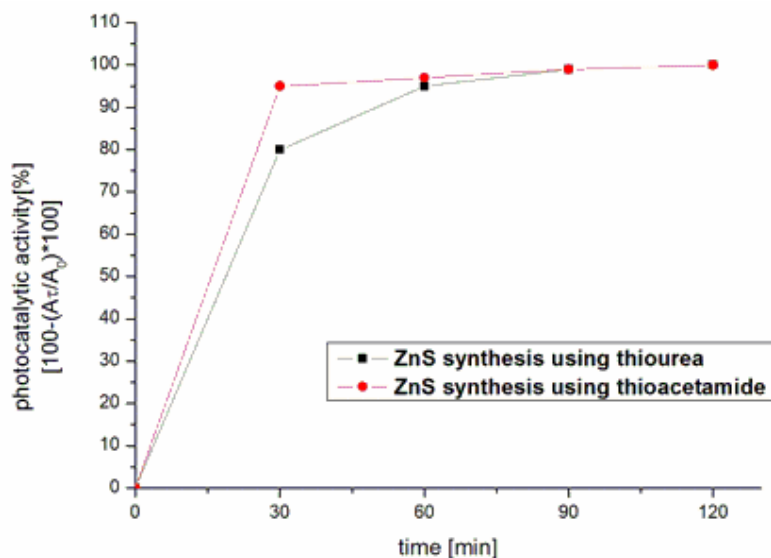


Figure 127. Time dependency of photocatalytic activity for pure ZnS synthesized using thioacetamide and thiourea

As can be seen, in both cases, after 2 h, the dye was completely degraded (more than 99%); however, ZnS with thioacetamide exhibited higher photocatalytic activity during the first 30 min of UV irradiation.

ZnS synthesized using thiourea was calcinated at 300, 400 and 500 °C. The XRD patterns of ZnS obtained in room temperature and the sample heated at 500 °C are presented in Figure 128. As is clearly visible, at 500 °C the second phase, ZnO (PDF 00-003-0888), occurs.

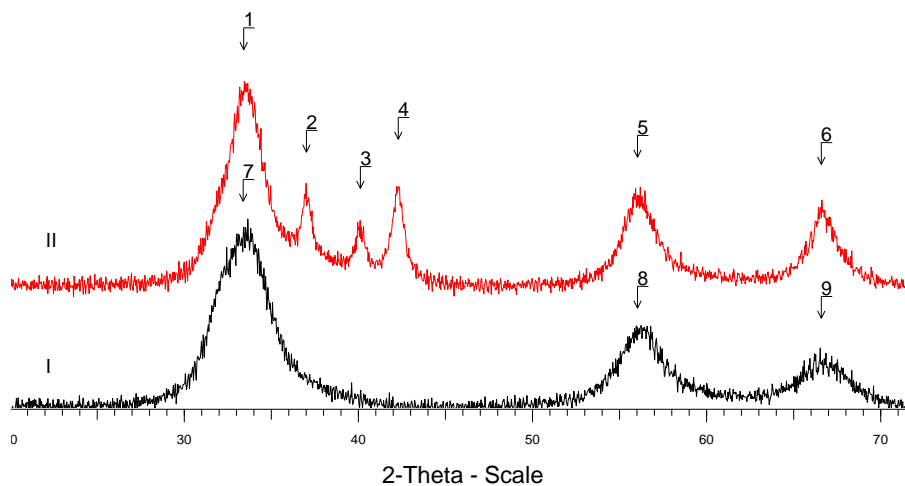


Figure 128. X-ray powder diffraction pattern of samples: ZnS at room temperature and ZnS calcinated at 500°C. (1, 7, 8, 9) ZnS and (2, 3, 4) ZnO and (5, 6) ZnS, ZnO

Furthermore, based on those diffraction patterns, the crystallite sizes of the ZnS were evaluated once again. The following values were obtained: for ZnS at 100 °C, 3 nm; for the calcinated sample, 5 nm.

Also, the time dependency of AO7 absorption maxima as a result of the UV irradiation measured for the calcinated samples was analyzed (Figure 129).

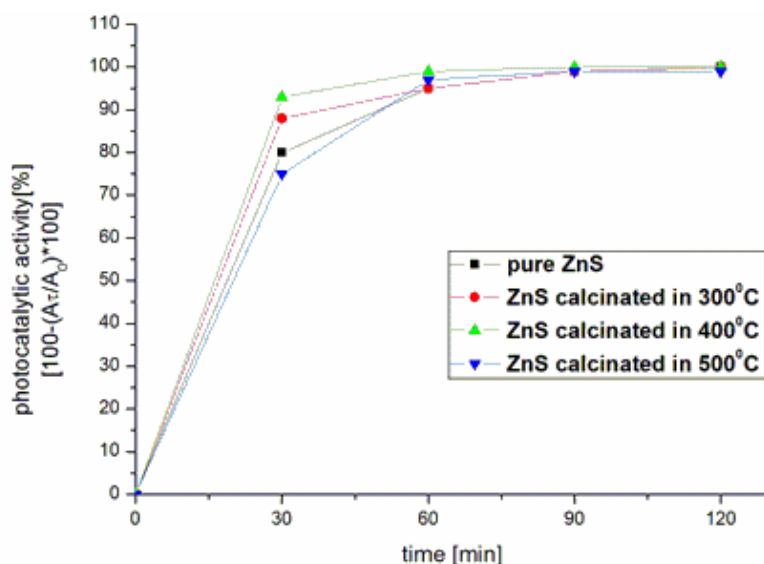


Figure 129. Time dependency of photocatalytic activity for pure ZnS synthesized using thiourea and calcinated at 300, 400 and 500 °C

The results show that the calcinations at 300 and 400 °C cause an increase in photodegradation activity (30 min of UV irradiation). However, after heating to 500 °C, photodegradation activity decreased (after 30 min of activity, photodegradation of AO7 reached only 75%). In all cases, after 2 h the AO7 was almost completely photodegraded.

The increased degradation efficiency at 400 °C and 300 °C may be caused by a decrease in the number of defects of the crystals. At 500 °C the ZnS started to oxidize to ZnO, which caused a weaker photodegradation effect in the first 60 min of UV irradiation.

#### 9.4 Conclusion

ZnS nanoparticles were successfully synthesized using microwave irradiation methods and two different sources of sulfur, thioacetamide and thiourea. However, as regards future applications, thiourea seems to be more promising, mainly due to its price, which is approximately one-tenth that of thioacetamide. Furthermore thioacetamide is also more toxic. Our preliminary test of photocatalytic degradation shows that the obtained compounds are promising photocatalysts. Following 2 h of UV irradiation, degradation of AO7 had reached almost 100%.

Such synthesis method were used to obtain semiconductor deposited on the surface of clay mainerals, this may lead to some practical applications.

## Summary

Hybrid organic-inorganic materials with the general formulae  $\text{MQ(L)}_{1/2}$  were the main subject of my research. All aspects, including synthesis, structure determination, characterization and finally preliminary application as a precursor for pure nanometric semiconductors, were studied and the obtained results presented in this dissertation.

At the beginning of my research, I synthesized materials such as  $\text{MQ(amine)}_{1/2}$  with the use of aliphatic amines. A new, cheaper and shorter synthesis route under reflux was elaborated as a method competitive with the commonly-used solvothermal technique. Furthermore, the influence of the reaction mixture on the growth, shape and structure of the obtained compounds was analyzed in detail. As it turns out, amines can act as directing agents for the alignment of inorganic fragments. Depending on the type of organic molecule used (1-ap, 1,2-pda and 1,3-pda), different hybrid materials were obtained (two- or three-dimensional). All of these studies were performed based on “ZnS semiconducting layer – organic linkers system”.

In addition to synthesis conditions, the properties of hybrid organic-inorganic materials needed to be analyzed in detail. Therefore, thermal and optical properties, morphology and structure were determined, summarized and discussed. Such compounds turn out to be stable to about 300 °C, at which point the amines are removed. Depending on the atmosphere, air or helium, different final products can be obtained. Because of the quantum confinement effect which occurs in such materials, the value of the band gap increases by about ~1 eV in comparison to the bulk counterpart.

An interesting point was the dependence of optical properties on the composition of the semiconducting monolayers. Thus, two different group of compounds,  $\text{Zn}_x\text{Cd}_{1-x}\text{Se(pda)}_{1/2}$  and  $\text{ZnS}_x\text{Se}_{1-x}\text{(pda)}_{1/2}$ , were synthesized and their optical properties tested. In the first group, the most significant modification was observed: two different band gaps instead of one.

Furthermore, a new class of hybrid materials of the type  $(\text{amine})\text{MSO}_4$  were obtained and characterized. Similarities and differences between the two classes were found. As the results of structure determination show, such materials are similar to “typical”  $\text{MQ(amine)}_{1/2}$  hybrid organic-inorganic materials. They also possess layered structures and, as in previous cases, amines are connected to the metal atom by covalent bonds. Furthermore, the topology of the  $-\text{M}-\text{SO}_4-$  layers in both classes of compounds is exactly the same:  $-6^3$ .

Finally, the formation of a pure semiconductor in different reaction mediums was performed. As the results show, the amines can be removed even at low temperatures (80 °C). However, the presence of acids is required for this result. In a few cases, unusual optical properties were obtained. Interestingly, red shift is clearly visible. Such behavior is extraordinary and suggests new potential functionalities for the analyzed semiconductor, which can serve as the subject of future studies.

Also, the synthesis of pure semiconductors (precipitated on the surface of clay materials) using microwave radiation was elaborated. Preliminary photocatalytic tests were performed on the obtained materials.

The results of the investigations described in this work have been already published in scientific journals of international circulation and have been presented at conferences in the form of oral presentations or posters.

## List of Figure

Figure 1. Bragg law .....	5
Figure 2. Ewald's construction .....	6
Figure 3. X-ray reflection from a polycrystalline sample .....	7
Figure 4. Application of Fourier transform and inverse Fourier transform in diffraction .....	8
Figure 5. The structure determination graph .....	9
Figure 6. Geometry of a Bragg-Brentano diffractometer .....	12
Figure 7. Spectrum of the X-ray diffraction tube .....	13
Figure 8. Schematic construction of synchrotron .....	14
Figure 9. Synchrotron Radiation Spectrum emitted by SURF III.....	15
Figure 10. Classification of structure solution methods .....	20
Figure 11. Relation between structure factor amplitudes, phases and electron density .....	21
Figure 12. The probability density of $\varphi(\mathbf{H}_1, \mathbf{H}_2)$ .....	22
Figure 13. Operation used in programs based on the direct method.....	23
Figure 14. N-hypersurface with local and global minimum .....	25
Figure 15. Applying a global optimization to crystal structure determination .....	26
Figure 16. Schematic structures of hybrid organic inorganic materials, where organic and inorganic ligands are presented in the structure. E', E can be O, N, S, Se.....	31
Figure 17. Schematic structures of hybrid organic inorganic materials, where inorganic and terminal organic ligands are presented in the structure. E', E can be O, N, S, S .....	31
Figure 18. Semiconducting package.....	32
Figure 19. 1D hybrid organic-inorganic materials with <b>A</b> ) monoamines, <b>B</b> ) diamines.....	33
Figure 20. Structure of ZnTe(pda).....	33
Figure 21. 2D hybrid organic-inorganic hybrid materials .....	34
Figure 22. 3D-MQ(L) <sub>1/2</sub> hybrid organic inorganic materials – schematic representation .....	35
Figure 23. 3D-MQ(L) <sub>1/2</sub> <b>A</b> ) $\alpha$ -ZnTe(hda) <sub>1/2</sub> <b>B</b> ) $\gamma$ -ZnTe(hda) <sub>1/2</sub> <b>C</b> ) $\delta$ -ZnTe(hda) <sub>1/2</sub> .....	36
Figure 24. The semiconducting layers typical for compound $\alpha$ -ZnTe(en) <sub>1/2</sub> and $\beta$ -ZnTe(en) <sub>1/2</sub> .....	37
Figure 25. Excitation in the case of <b>A</b> ) a direct semiconductor, <b>B</b> ) an indirect semiconductor.....	41
Figure 26. Zinc blende structure of ZnS: <b>A</b> ) zinc blende structure <b>B</b> ) wurtzite structure. Colors: Zn – pink, S – yellow .....	47
Figure 27. Schematic of the photocatalytic effect in a semiconductor. ....	50
Figure 28. A set of equipment for synthesis under reflux used in the synthesis of hybrid organic-inorganic materials .....	56
Figure 29. XRD-pattern of ZnS(1-ap) .....	57
Figure 30. Model of the 2D- Zn <sub>2</sub> S <sub>2</sub> (1-ap) – double semiconductor layer (n=2) .....	58
Figure 31. XRD patterns of (ZnS) <sub>n</sub> 1-ap obtained during heat treatment in air .....	58
Figure 32. SEM images of (ZnS) <sub>n</sub> 1-ap .....	59
Figure 33. UV-vis spectra of (ZnS) <sub>n</sub> 1-ap, compared with spectrum of ZnS.....	59
Figure 34. XRD pattern of (ZnS) <sub>n</sub> 1,2-pda .....	60
Figure 35. XRD patterns of (ZnS) <sub>n</sub> 1-ap obtained during heat treatment in air.....	61
Figure 36. SEM images of (ZnS) <sub>n</sub> 1,2-pda .....	61
Figure 37. UV-vis spectra of (ZnS) <sub>n</sub> 1,2-pda, compared with spectrum of ZnS.....	62
Figure 38. Rietveld plot of ZnS(pda) <sub>1/2</sub> .....	63
Figure 39. Layer of ZnS <b>A</b> ) view along the a-axis <b>B</b> ) view along the b-axis <b>C</b> ) view along the c-axis; (Zn-pink, S-yellow) .....	64
Figure 40. <b>A</b> ) Tetrahedral coordination of Zn atom <b>B</b> ) amine as a linker between two zinc atoms; (Zn-pink, S-yellow, N-blue, C-black) .....	64
Figure 41. Layered structure of ZnS(pda) <sub>1/2</sub> ; (Zn-pink, S-yellow, N-blue, C-black).....	65
Figure 42. XRD patterns of ZnS(pda) <sub>1/2</sub> obtained during heat treatment in air .....	65
Figure 43. XRD patterns of ZnS(pda) <sub>1/2</sub> obtained during heat treatment in helium .....	66
Figure 44. TG/DSC analysis of ZnS(pda) <sub>1/2</sub> .....	66
Figure 45. SEM images of ZnS(pda) <sub>1/2</sub> .....	67

Figure 46. UV-vis spectra of $\text{ZnS}(\text{pda})_{1/2}$ .....	67
Figure 47. Amine used in synthesis: 1-aminopropane (1-ap), 1,2-propanediamine (1,2-pda), 1,3-propanediamine (1,3-pda), respectively .....	68
Figure 48. Autoclave used for synthesis.....	71
Figure 49. XRD patterns of $\text{Zn}_x\text{Cd}_{1-x}(\text{pda})_{1/2}$ .....	71
Figure 50. Obtained volumes as a function of the amount of zinc and cadmium ( $x = 0, 0.25, 0.5, 0.75, 1$ ) in compounds type $\text{Zn}_x\text{Cd}_{1-x}\text{Se}(\text{pda})_{1/2}$ (pink line – calculated volumes).....	72
Figure 51. UV-vis spectra of $\text{Zn}_x\text{Cd}_{1-x}\text{Se}(\text{pda})_{1/2}$ compounds.....	73
Figure 52. XRD patterns as a function of temperature of $\text{ZnSe}(\text{pda})_{1/2}$ obtained in helium atmosphere.....	74
Figure 53. TG/DSC analysis for $\text{ZnSe}(\text{pda})_{1/2}$ .....	75
Figure 54. XRD patterns at the function of temperature of $\text{Zn}_{0.5}\text{Cd}_{0.5}\text{Se}(\text{pda})_{1/2}$ obtained in helium atmosphere.....	76
Figure 55. TG/DSC analysis for $\text{Zn}_{0.5}\text{Cd}_{0.5}\text{Se}(\text{pda})_{1/2}$ .....	76
Figure 56. XRD patterns as a function of temperature of $\text{CdSe}(\text{pda})_{1/2}$ obtained in helium atmosphere .....	77
Figure 57. TG/DSC analysis for $\text{CdSe}(\text{pda})_{1/2}$ .....	77
Figure 58. SEM images of $\text{ZnSe}(\text{pda})_{1/2}$ .....	78
Figure 59. SEM images of $\text{Zn}_{0.75}\text{Cd}_{0.25}\text{Se}(\text{pda})_{1/2}$ .....	78
Figure 60. SEM images of $\text{Zn}_{0.5}\text{Cd}_{0.5}\text{Se}(\text{pda})_{1/2}$ .....	79
Figure 61. SEM images of $\text{Zn}_{0.25}\text{Cd}_{0.75}\text{Se}(\text{pda})_{1/2}$ .....	79
Figure 62. SEM images of $\text{CdSe}(\text{pda})_{1/2}$ .....	79
Figure 63. The data collection area of $\text{Zn}_{0.5}\text{Cd}_{0.5}\text{Se}(\text{pda})_{1/2}$ .....	80
Figure 64. XRD patterns of $\text{ZnS}_x\text{Se}_{1-x}(\text{pda})_{1/2}$ .....	80
Figure 65. Obtained volumes as a function of the number of sulfur and selenium atoms ( $x = 0, 0.25, 0.5, 0.75, 1$ ) in compounds of the type $\text{ZnS}_x\text{Se}_{1-x}(\text{pda})_{1/2}$ (violet line – calculated volumes).....	81
Figure 66. UV-vis spectra of $\text{ZnS}_x\text{Se}_{1-x}(\text{pda})_{1/2}$ compounds .....	82
Figure 67. XRD patterns as a function of temperature of $\text{ZnS}_{0.5}\text{S}_{0.5}\text{e}(\text{pda})_{1/2}$ obtained in helium atmosphere .....	83
Figure 68. TG/DSC analysis for $\text{Zn}_{0.5}\text{Cd}_{0.5}\text{Se}(\text{pda})_{1/2}$ .....	83
Figure 69. SEM images of $\text{ZnS}_{0.75}\text{Se}_{0.25}(\text{pda})_{1/2}$ .....	84
Figure 70. SEM images of $\text{ZnS}_{0.5}\text{Se}_{0.5}(\text{pda})_{1/2}$ .....	84
Figure 71. SEM images of $\text{ZnS}_{0.25}\text{Se}_{0.75}(\text{pda})_{1/2}$ .....	84
Figure 72. Rietveldt plot for (MXDA) $\text{ZnSO}_4$ .....	89
Figure 73. Rietveldt plot for (MXDA) $\text{CdSO}_4$ .....	89
Figure 74. Rietveldt plot for (PXDA) $\text{ZnSO}_4$ .....	91
Figure 75. Rietveldt plot for (PXDA) $\text{CdSO}_4$ .....	92
Figure 76. Basic structure fragments of: <b>A</b> ) (MXDA) $\text{MSO}_4$ , <b>B</b> ) (PXDA) $\text{MSO}_4$ .....	93
Figure 77. A – $\text{M-SO}_4$ - layer (M – green, blue – nitrogen, red – oxygen, yellow – sulfur).....	94
Figure 78. <b>A</b> ) ‘cis-amine’ as a linker <b>B</b> ) ‘trans-amine’ as a linker .....	95
Figure 79. The orthogonal alignment of MXDA molecules (black bars) seen through – $\text{M-SO}_4$ - layers.....	95
Figure 80. The alignment of amines between inorganic layers in <b>A</b> ) compounds with amine – MXDA, <b>B</b> ) compounds with amine – PXDA).....	96
Figure 81. The TG/DSC analysis of (MXDA) $\text{ZnSO}_4$ .....	97
Figure 82. XRD patterns of (MXDA) $\text{ZnSO}_4$ vs. temperature (helium atmosphere) .....	98
Figure 83. The TG/DSC analysis of (MXDA) $\text{CdSO}_4$ .....	98
Figure 84. XRD patterns vs. temperature of (MXDA) $\text{CdSO}_4$ (helium atmosphere) .....	99
Figure 85. The TG/DSC analysis of (PXDA) $\text{ZnSO}_4$ .....	99
Figure 86. XRD patterns of (PXDA) $\text{ZnSO}_4$ vs. temperature (air atmosphere) .....	100
Figure 87. TG/DSC analysis of (PXDA) $\text{CdSO}_4$ .....	100
Figure 88. XRD patterns of (PXDA) $\text{CdSO}_4$ vs. temperature (helium atmosphere) .....	101
Figure 89. XRD patterns of (PXDA) $\text{CdSO}_4$ vs. temperature (air atmosphere) .....	101
Figure 90. SEM images of (MXDA) $\text{ZnSO}_4$ .....	102
Figure 91. SEM images of (MXDA) $\text{CdSO}_4$ .....	102
Figure 92. SEM images of (PXDA) $\text{ZnSO}_4$ .....	103
Figure 93. SEM images of (PXDA) $\text{CdSO}_4$ .....	103

Figure 94. The results of treatment of ZnS(pda) <sub>1/2</sub> in acetonitrile; acetonitrile+acetic acid; acetonitrile+acetic acid+formic acid.....	106
Figure 95. The results of formation of ZnSe(MXDA) <sub>1/2</sub> in acetonitrile; acetonitrile+acetic acid; acetonitrile+acetic acid+formic acid .....	106
Figure 96. The results of treatment of ZnS(pda) <sub>1/2</sub> in octanol; octanol+acetic acid; octanol+acetic acid+formic acid .....	107
Figure 97. The results of treatment of ZnSe(MXDA) <sub>1/2</sub> in octanol; octanol+acetic acid; octanol+acetic acid+formic acid.....	107
Figure 98. Results of treatment of ZnS(pda) <sub>1/2</sub> in hexanodiol; hexanodiol+acetic acid; hexanodiol+acetic acid+formic acid.....	108
Figure 99. Results of treatment of ZnSe(MXDA) <sub>1/2</sub> in hexanodiol; hexanodiol+acetic acid; hexanodiol+acetic acid+formic acid.....	108
Figure 100. Results of treatment of ZnS(pda) <sub>1/2</sub> in paraffin oil; paraffin oil+acetic acid; paraffin oil+acetic acid+formic acid.....	109
Figure 101. Results of treatment of ZnSe(MXDA) <sub>1/2</sub> in paraffin oil; paraffin oil+acetic acid; paraffin oil+acetic acid+formic acid.....	109
Figure 102. Results of treatment of ZnS(pda) <sub>1/2</sub> and ZnSe(MXDA) <sub>1/2</sub> in acetic acid and formic acid .....	110
Figure 103. Results of treatment of ZnSe(MXDA) <sub>1/2</sub> in octanol; octanol and acetic acid using microwave radiation.....	110
Figure 104.UV-vis spectra for samples obtained from ZnS(pda) <sub>1/2</sub> by boiling in acetonitrile; acetonitrile and acetic acid; acetonitrile, acetic acid and formic acid .....	112
Figure 105.UV-vis spectra for samples obtained from ZnSe(MXDA) <sub>1/2</sub> by boiling in acetonitrile; acetonitrile and acetic acid; acetonitrile, acetic acid and formic acid .....	112
Figure 106.UV-vis spectra for samples obtained from ZnS(pda) <sub>1/2</sub> by boiling in octanol; octanol and acetic acid; octanol, acetic acid and formic acid .....	113
Figure 107. UV-vis spectra for samples obtained using ZnSe(MXDA) <sub>1/2</sub> by boiling in octanol; octanol and acetic acid; octanol, acetic acid and formic acid.....	113
Figure 108.UV-vis spectra for samples obtained from ZnS(pda) <sub>1/2</sub> by boiling in hexanodiol; hexanodiol and acetic acid; hexanodiol, acetic acid and formic acid.....	114
Figure 109.UV-vis spectra for samples obtained from ZnSe(MXDA) <sub>1/2</sub> by boiling in hexanodiol; hexanodiol and acetic acid; hexanodiol, acetic acid and formic acid .....	114
Figure 110. UV-vis spectra for samples obtained from ZnS(pda) <sub>1/2</sub> by boiling in paraffin oil; paraffin oil and acetic acid; paraffin oil, acetic acid and formic acid .....	115
Figure 111. UV-vis spectra for samples obtained from ZnSe(MXDA) <sub>1/2</sub> by boiling in paraffin oil; paraffin oil and acetic acid; paraffin oil, acetic acid and formic acid .....	115
Figure 112. UV-vis spectra for samples obtained from ZnS(pda) <sub>1/2</sub> by boiling in acetic acid and formic acid... 116	116
Figure 113. UV-vis spectra for samples obtained from ZnSe(MXDA) <sub>1/2</sub> by boiling in acetic acid and formic acid .....	116
Figure 114. UV-vis spectra for samples obtained from ZnSe(MXDA) <sub>1/2</sub> formed in octanol and acetic acid using microwave radiation .....	117
Figure 115. SEM images of samples obtained of ZnS(pda) <sub>1/2</sub> by boiling in: <b>A)</b> acetonitrile <b>B)</b> acetonitrile and acetic acid <b>C)</b> acetonitrile, acetic acid and formic acid .....	119
Figure 116.SEM images of samples obtained of ZnSe(MXDA) <sub>1/2</sub> by boiling in: <b>A)</b> acetonitrile, <b>B)</b> acetonitrile and acetic acid, <b>C)</b> acetonitrile, acetic acid and formic acid .....	119
Figure 117. SEM images of ZnS(pda) <sub>1/2</sub> boiled in: <b>A)</b> acetonitrile, acetic acid and formic acid, <b>B)</b> octanol, acetic acid and formic acid, <b>C)</b> hexanodiol, acetic acid and formic acid.....	120
Figure 118. SEM images of samples obtained by boiling of ZnSe(MXDA) <sub>1/2</sub> in: <b>A)</b> acetonitrile, acetic acid and formic acid, <b>B)</b> octanol, acetic acid and formic acid, <b>C)</b> hexanodiol, acetic acid and formic acid.....	120
Figure 119. SEM images of samples obtained by boiling ZnS(pda) <sub>1/2</sub> in acetic acid and formic acid .....	120
Figure 120. SEM images of samples obtained by boiling ZnSe(MXDA) <sub>1/2</sub> in acetic acid and formic acid .....	121
Figure 121. SEM images of samples obtained by boiling ZnSe(MXDA) <sub>1/2</sub> in octanol using microwave radiation .....	121

Figure 122. SEM images of <b>A)</b> precursor of $\text{ZnSe}(\text{MXDA})_{1/2}$ <b>B)</b> precursor of $\text{ZnS}(\text{pda})_{1/2}$ <b>C)</b> sample obtained by boiling in acetonitrile and acetic acid .....	121
Figure 123. X-ray powder diffraction patterns of samples: <b>(I)</b> - $\text{ZnS}_{\text{thioacetamide}}$ and <b>(II)</b> - $\text{ZnS}_{\text{thiourea}}$ ( <b>1</b> ... $\text{ZnS}$ (111), <b>2</b> ... $\text{ZnS}$ (220) and <b>3</b> ... $\text{ZnS}$ (311)) .....	125
Figure 124. SEM images of the $\text{ZnS}$ obtained by the use of thiourea .....	125
Figure 125. UV-vis spectra of $\text{ZnS}$ obtained with thioacetamide.....	126
Figure 126. UV-vis spectra of $\text{ZnS}$ obtained with thiourea .....	126
Figure 127. Time dependency of photocatalytic activity for pure $\text{ZnS}$ synthesized using thioacetamide and thiourea .....	127
Figure 128. X-ray powder diffraction pattern of samples: $\text{ZnS}$ at room temperature and $\text{ZnS}$ calcinated at $500\text{ }^{\circ}\text{C}$ . (1, 7, 8, 9) $\text{ZnS}$ and (2, 3, 4) $\text{ZnO}$ and (5, 6) $\text{ZnS}$ , $\text{ZnO}$ .....	127
Figure 129. Time dependency of photocatalytic activity for pure $\text{ZnS}$ synthesized using thiourea and calcinated at $300$ , $400$ and $500\text{ }^{\circ}\text{C}$ .....	128

## List of Tables

Table 1. A list of the most common problems which could reduce the quality of powder diffraction data and the possible solution .....	11
Table 2. Length of X-rays depending on anode type.....	13
Table 3. Algorithm for finding the cell parameters .....	17
Table 4. Proposed classification of dimensionality hybrid organic-inorganic materials .....	31
Table 5. 2D-MQ(L) hybrid organic-inorganic materials .....	34
Table 6. 2D-(MQ) <sub>2</sub> L hybrid organic-inorganic materials.....	34
Table 7. Crystallographic data of 3D-MQ(L) <sub>1/2</sub> hybrid organic-inorganic materials .....	36
Table 8. The band gap energy for selected 3D-MQ(L) <sub>1/2</sub> compounds.....	41
Table 9. The blue shifts for selected 2D-(MQ) <sub>n</sub> L hybrid organic-inorganic materials.....	42
Table 10. Potential applications of semiconductors II-VI .....	46
Table 11. Detailed information about measurement parameters .....	54
Table 12. Crystallographic data for ZnS(pda) <sub>1/2</sub> .....	63
Table 13. Atomic parameters .....	63
Table 14. Selected interatomic distances.....	64
Table 15. Indexing results of powder X-ray diffraction of Zn <sub>x</sub> Cd <sub>1-x</sub> Se(pda) <sub>1/2</sub> (x = 0, 0.25, 0.5, 0.75, 1) .....	72
Table 16. The calculated band gaps of hybrid materials of the type Zn <sub>x</sub> Cd <sub>1-x</sub> Se(pda) <sub>1/2</sub> .....	73
Table 17. Indexing results of powder X-ray diffraction of ZnS <sub>x</sub> Se <sub>1-x</sub> (pda) <sub>1/2</sub> (x = 0, 0.25, 0.5, 0.75, 1).....	81
Table 18. The calculated band gaps of hybrid materials of the type ZnS <sub>x</sub> Se <sub>1-x</sub> (pda) <sub>1/2</sub> .....	82
Table 19. Crystallographic data for (MXDA)ZnSO <sub>4</sub> and (MXDA)CdSO <sub>4</sub> .....	90
Table 20. Selected interatomic distances for (MXDA)ZnSO <sub>4</sub> .....	90
Table 21. Selected interatomic distances for (MXDA)CdSO <sub>4</sub> .....	90
Table 22. Atomic positions of (MXDA)ZnSO <sub>4</sub> .....	90
Table 23. Atomic positions of (MXDA)CdSO <sub>4</sub> .....	91
Table 24. Crystallographic data for (PXDA)ZnSO <sub>4</sub> and (PXDA)CdSO <sub>4</sub> .....	92
Table 25. Selected interatomic distances for (PXDA)ZnSO <sub>4</sub> .....	92
Table 26. Selected interatomic distances for (PXDA)CdSO <sub>4</sub> .....	92
Table 27. Atomic positions of (PXDA)ZnSO <sub>4</sub> .....	93
Table 28. Atomic positions of (PXDA)CdSO <sub>4</sub> .....	93
Table 29. Results of formation of pure ZnS and ZnSe by boiling in different reaction mediums .....	111
Table 30. Band gaps of obtained compounds (blue indicates “blue shift,” red “red shift” in comparison to bulk phases of the semiconductor*) .....	118

## List of References

1. W. Friedrich, P. Knipping and M. Laue, *Sitzungsber. K. Bayer. Akad. Wiss.* (1912) 303
2. C. Davies, S. E. Gerchman, J. H. Kycia, K. McGee, V. Ramakrishnan and S. W. White, *Acta Cryst. D Biol. Cryst.* (1994) 790
3. Wlodawer, M. Miller, M. Jaskolski, B.K. Satyanarayan, E. Baldwin, I.T. Weber, L.M. Selk, L. Clawson, J. Schneider, S.B.H. Kent, *Science*, **245** (1989) 616
4. D. Shechtman, *Acta Cryst.* **A43** (1987), C3
5. <http://www.iucr.org/people/nobel-prize>, 03.04.2013
6. W.I.F. David, K. Shankland, L.B. McCusker and Ch. Berlocher, “*Structure Determination from Powder Diffraction Data*”, Oxford University Press, (2002)
7. H.M. Rietveld, *J. Appl. Cryst.* **2**, (1969) 65
8. T. Wessels, Ch. Baerlocher, L.B. McCusker, *Science* **284** (1999) 477
9. W. Clegg, “*Crystal Structure Analysis: Principles and Practice*”, Oxford Science Publications, (2009)
10. Z. Bojarski, H. Habla, M. Surowiec, „*Krystalografia*”, Państwowe Wydawnictwo Naukowe, Warszawa, (1986)
11. W. Borchart-Ott, “*Crystallography*”, Springer, (2011)
12. M. Ladd, R. Palmer, “*Structure determination by X-ray Crystallography*”, Kluwer Academic/Plenum Publishers, New York, (2003)
13. M. Van Meerssche, J. Feneau-Dupont, „*Krystalografia i Chemia Strukturalna*”, Państwowe Wydawnictwo Naukowe, Warszawa, (1984)
14. H. Swanson, M. C. Morris, E.H. Evans, L. Ulmer, *Natl. Bur. Stand. (US)*, Monography, **25** (1964) 1–3
15. W. Łasocha, H. Schenk, *J. Appl. Cryst.* **30** (1997) 561
16. R. Hedel, H.J. Bunge, G. Reck, *Tectures Microstruct.* **29** (1997) 103
17. E. Guilmeau, *Mat. Sci. Eng.* **B104** (2003) 107
18. M. Morales, *J. Magn. Magn. Mat.* **257** (2003) 258
19. S. Mackiewicz, *Conf. mat. Popów*, (2005)
20. J.A. Bearden, *Rev. Mod. Phys.* **39** (1967) 78
21. Lecture materials of Prof. B. Oleksyn (2012)
22. <http://www.synchrotron.uj.edu.pl/> 05.05.2013
23. <http://www.esrf.eu/about/synchrotron-science/synchrotron> 05.04.2013
24. <http://physics.nist.gov/MajResFac/SURF/SURF/sr.html> 11.04.2013
25. Lecture materials Prof. W. Łasocha, (2011)
26. A. Altomare, C. Caliendo, C. Camalli, C. Cuocci, G. Giovacazzo, A. G. G. Moliterni, and R. Rizzi, *J. Appl. Cryst.* **37** (2004) 1025
27. V. Favre-Nicolin and R. Cerny, *J. Appl. Cryst.* **35** (2002) 734
28. V. Petricek, M. Dusek, and L. Palatinus, *Jana2006 – The Crystallographic Computing System* (Institute of Physics, Praha, Czech Republic, 2006).
29. X. Huang, H.R. Heulings IV, V. Le, J. Li, *Chem. Matter*, **13** (2001) 3754.
30. X. Huang, J. Li, *J. Am. Chem. Soc.* **122** (2000) 8789.
31. K. Rurack, R. Martinez-Mañez, “*Supramolecular Chemistry of Organic-Inorganic Hybrid Materials*”, A John Wiley and Sons Inc., New Jersey (2010)
32. C. Janiak, *Dalton Trans.* (2003) 2781
33. A.K. Cheetham, C.N.R. Rao, R.K. Feller, *Chem. Commun.* (2006) 4780
34. S. Spornic, T. Becker, K. Wright, W.R. Richmond, *J. Inc. Phenom. Macroc. Chem.* **65** (2009) 89
35. B. Gawel, W. Łasocha, *J. Alloy. Comp.* **442** (2007) 77
36. X. Huang, J. Li, Y. Zhang, A. Mascarenhas, *J. Am. Chem. Soc.* **125** (2003) 7049
37. X. Huang, J. Li, *J. Am. Chem. Soc.* **129** (2007) 3157
38. Z.-X. Deng, L. Li, Y. Li, *Inorg. Chem.* **42** (2003) 2331
39. J. Li, W. Bi, W. Ki, X. Huang, S. Reddy, *J. Am. Chem. Soc.* **129** (2007) 14141
40. C.-Y. Moon, G.M. Dalpian, Y. Zhang, S.-H. Wei, *J. Am. Chem. Soc.* **18** (2006) 2805
41. X. Huang, M. Roushan, T. J. Emge, W. Bi, S. Thiagarajan, J. Cheng, R. Yang, J. Li, *Angew. Chem. Int. Ed.* **48** (2009) 7871
42. H.R. Heulings IV, X. Huang, *J. Li, Nano Lett.* **1** (2001) 521
43. J. Lu, S. Wei, Y. Peng, W. Yu, Y. Qian, *J. Phys. Chem.* **B 107** (2003) 3427
44. J. Lu, S. Wei, W. Yu, H. Zhang, Y. Qian, *Chem. Mater.* **17** (2005) 1698
45. J. Li, Y. Xu, D. Wu, Yuhuan Sun, *Solid State Commun.* **130** (2004) 619
46. L. Fan, H. Song, H. Zhao, G. Pan, H. Yu, X. Bai, S. Li, Y. Lei, Q. Dai, R. Qin, T. Wang, B. Dong, Z. Zheng, X. Ren, *J. Phys. Chem.* **B 110** (2006) 12948
47. X. Ouyang, T.-Y. Tsai, D.-H. Chen, Qi.-J. Huang, W.-H. Cheng, A. Clearfield, *Chem. Commun.* (2003) 886

48. W.-T. Yao, S.-Y. Yu, *Adv. Funct. Mater.* **18** (2008) 3357
49. T. Trindade, P. O'Brien, N.L. Pickett, *Chem. Mater.* **13** (2001) 3843
50. R.W. Kelsall, I.W. Hamley, M. Geoghegan, "Nanotechnologie", Wydawnictwo Naukowe PWN, Warszawa (2009) 138–148
51. Lecture materials of prof. W. Macyk (2010)
52. Z.-X. Deng, C. Wang, X.-M. Sun, Y.-D. Li, *Inorg. Chem.* **41** (2002) 869
53. S. Wei, J. Lu, Y. Qian, *Chem. Mater.* **20** (2008) 7220
54. X. Fang, S. Xiong, T. Zhai, Y. Bando, M. Liao, U.K. Gautham, Y. Koide, X. Zhang, Y. Qian, D. Goldberg, *Adv. Mater.* **21** (2009) 5016
55. H.-B. Yao, X. Zhang, X.-H. Wang, S.-H. Yu, J.Li, *Dalton Trans.* **40** (2011) 3191
56. J.W. Jang, S.H. Choi, J.S. Jang, J.S. Lee, S. Cho, K.-H. Lee, *J. Phys. Chem. C* **113** (2009) 20445
57. M. Zhang, Y. Lu, J.-F. Chen, T.-K. Zhang, Y.-Y. Liu, Y. Yang, W.-T. Yao, S.-H. Yu, *Langmuir* **26** (2010) 12882
58. W. Ki, J. Li, *J. Am. Chem. Soc.* **130** (2008) 8114
59. X. Fang, T. Zhai, U. K. Gutham, L. Li, L. Wu, Y. Bando, D. Golberg, *Progr. Mater. Sci.* **56** (2011) 175
60. L. Chen, W. Zhang, C. Feng, Z. Yang, Y. Yang, *Ind. Eng. Chem. Res.* **51** (2012) 4208
61. R. M. Blanchard, A. R. Noble-Luginbuhl, and R. G. Nuzzo, *Anal. Chem.* **72** (2000) 1365
62. K. D. Patel, G. K. Solanki, J. R. Gandhi, S. G. Patel, *Chalcogenide Lett.* **6** (2009) 393
63. D. Ke, S. Liu, K. Dai, J. Zhou, L. Zhang, and T. Peng, *J. Phys. Chem. C* **113** (2009) 16021
64. C. Liu, P. Wu, T. Sun, L. Dai, Y. Ye, R. Ma, and G. Qin, *J. Phys. Chem. C* **113** (2009) 14478
65. J.P. Borah, K.C. Sarma, *Act. Cryst. Pol. A* **114** (2008) 713
66. S. Miao, Z. Liu, B. Han, H. Yang, Z. Miao, Z. Sun, *J. Colloid Interf. Sci.* **301** (2006) 116
67. C.L. Torres-Martínez, R. Kho, O.I. Mian, and R.K. Mehra, *J. Colloid Interf. Sci.* **240** (2001) 525
68. V. Taghvaei, A. Habibi-Yangjeh, M. Behboudnia, *Physica E* **42** (2010) 1973
69. O. Kozak, P. Praus, K. Koci, M. Klementova, *J. Colloid Interf. Sci.* **352** (2010) 244
70. M. Chitkara, K. Singh, I. S. Sandhu, H.S. Bhatti, *Nanoscale Res Lett.* **6** (2011) 438
71. L. Zang, C.-Y. Liu, X.-M. Ren, *J. Photochem. Photobiol A: Chem.* **85** (1995) 239
72. <http://goldbook.iupac.org/P04580.html> 20.04.2013
73. J.-M. Herrmann, *Catal. Today* **53** (1999) 115
74. W. Łasocha and K. Lewiński, *J. Appl. Cryst.* **27** (1994) 437
75. BrukerAXS, TOPAS V.2.1: General Profile and Structure Analysis Software for Powder Diffraction Data. User Manual. Bruker AXS, Karlsruhe, Germany, 2003
76. Ed. R. Delhez and E.J. Mittenmeijer, *Proceedings of the Seventh European Powder Diffraction Conference (EPDIC 7)*, (2000), 118
77. Y.-P. Yuan, R.-Y. Wang, D.-Y. Kong, J.-G. Mao, A. Clearfield, *J. Solid State Chem.* **178** (2005) 2030
78. W. Zhou, Q. Chen, D. Zhu, Y. Xu, *Z. Anorg. Allg. Chem.* **351 635** (2009) 572
79. T. Bataille, D. Louër, *J. Solid State Chem.* **177** (2003) 1235
80. G. Paul, A. Choudhury, C. N. R. Rao, *J. Chem. Soc. Dalton Trans.* (2002) 3859
81. F. Urbach, *Phys. Rev.* **92** (1953) 1324
82. *Comments Cond. Mat. Phys.* **13** (1987) 35